Automated inversion of long period signals from shallow volcanic and induced seismic events

Dissertation

zur Erlangung des Doktorgrades

an der MIN-Fakultät, Fachbereich Geowissenschaften
der Universität Hamburg

vorgelegt von

Lars Ulrich Krieger

aus Dannenberg (Elbe)

Hamburg

2011

Als Dissertation angenommen
vom Fachbereich Geowissenschaften der Universität Hamburg

Auf Grund der Gutachten von **Prof. Dr. Torsten Dahm**
und **Prof. Dr. Matthias Hort**

Hamburg, den 17.05.2011

Prof. Dr. Jürgen Oßenbrügge

Leiter des Fachbereichs für Geowissenschaften

University of Hamburg – Faculty of Mathematics, Informatics and Natural Sciences

Institute of Geophysics

Dissertation

Automated inversion of long period signals from shallow volcanic and induced seismic events

Lars Ulrich Krieger

Dipl.-Phys., Bacc.-Math.

born in Dannenberg (Elbe)

Supervisor

Prof. Dr. Torsten Dahm

Second advisor

Prof. Dr. Matthias Hort

Hamburg

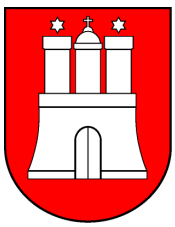

2011

Zusammenfassung

Vulkanische seismische Ereignisse, die langperiodische Signale erzeugen (sog. *LP-Events*), werden als wichtige Indikatoren für im Erdinneren stattfindende Fluid- und Magmabewegungen interpretiert. Ihre Untersuchung ist im Rahmen kontinuierlicher Überwachungen von Vulkangebieten essentiell, um Entwicklungen im Vulkan und damit einhergehende Gefährdungen für die Umgebung abschätzen zu können. LP-Events treten aber nicht nur an Vulkanen auf, sie sind unter anderem auch in der Umgebung von Fluid-Lagerstätten und Bergwerken zu beobachten. Dort werden sie als Anzeichen für das Auftreten langsam ablaufender Bruch- oder Deformationsprozesse gedeutet, welche in Zusammenhang mit strukturellen Inhomogenitäten stehen können und durch äußere Einwirkungen ausgelöst werden (*induzierte Ereignisse*). Die Interpretation solcher Ereignisse kann einen Beitrag zu lokalen oder regionalen seismischen Gefährdungsanalysen liefern.

Bei der Untersuchung von LP-Events hat man auf der einen Seite die bereits über einen langen Zeitraum erforschten lokalen vulkanischen Ereignisse, welche vulkantypische Charakteristika aufweisen können und in von starker Topographie und heterogenen Untergrundstrukturen geprägten Regionen vorkommen. Auf der anderen Seite findet man durch z.B. Erdölförderung oder Kohleabbau induzierte LP-Events, welche noch nicht der Gegenstand systematischer Untersuchungen waren, da sich die Auswertungen induzierter Ereignisse zumeist auf Daten mit höheren Frequenzen stützen.

Es existieren einerseits Computerprogramme, welche zur kontinuierlichen Überwachung und Auswertung von seismischen Signalen bei vulkanischen Krisen gedacht sind. Andererseits gibt es Programme, welche groß- und intermediärskalige seismische Ereignisse für bestimmte Regionen analysieren und auftretende Ereignisse katalogisieren. Bis zum aktuellen Zeitpunkt gibt es keinen systematischen Ansatz, die Untersuchungen von vulkanischen und induzierten seismischen LP-Events zu kombinieren.

Im Rahmen der vorliegenden Arbeit wurde ein Programm entwickelt, welches es erlaubt, langperiodische seismische Signale schnell und unabhängig von der vorliegenden Geometrie der betreffenden Region zu analysieren. Der zugrundeliegende Algorithmus basiert auf einer algebraischen Inversion seismischer Daten in einem Einschrittverfahren. Diese Inversion wurde mit einer dreidimensionalen räumlichen Gittersuche bezüglich möglicher Quellpositionen kombiniert. Um die Inversion ausführen zu können, wird ein Satz von 18 Green's-Funktionen (GFn) benötigt. Die GFn beinhalten Informationen über das lokale oder regional Geschwindigkeitsmodell. Sie werden für die betreffende Region im Voraus berechnet und in einer Dateistruktur bereitgestellt, was eine sehr schnelle Inversion der Daten ermöglicht. Im Gegensatz zu anderen Methoden für die Inversion seismischer Daten ist im vorliegenden Ansatz die vollständige dreidimensionale Untergrundstruktur in den GFn enthalten, dies beinhaltet auch Topographie oder Anisotropien.

Die seismischen Daten können zum einen ereignisbasiert analysiert werden. Hierbei invertiert der Algorithmus Daten für eine durch ein externes (Detektions-)Programm be-

stimmte Quellzeit, Die Bestimmung dieser Quellzeit kann durch eine weitere Gittersuche innerhalb eines gegebenen Zeitintervalls verfeinert werden. Unter Verzicht auf externe Detektion von Ereignissen kann das entwickelte Programm aum anderen auch zur schnellen Untersuchung eines kontinuierlichen Datanstroms verwendet werden. Dies wird durch die schrittweise Anwendung der Inversion in einem gleitenden Zeitfenster ermöglicht. Die für jedes Zeitfenster bestimmte Lösung erlaubt den Vergleich von eingelesenen Daten mit intern generierten Vergleichsspuren. Das Maß ihrer Übereinstimmung wird durch einen skalaren Wert ausgedrückt. Das Überschreiten eines anwendungsfallabhängigen Schwellenwerts markiert ein Ereignis.

Der neuentwickelte Algorithmus wurde mit synthetischen und echten Daten getestet, Daten für ein- und dreidimensionale Geschwindigkeitsmodelle wurden verwendet. Der Code ist lauffähig und auf Daten anwendbar. Die ermittelten Ergebnisse sind konsistent, sowohl mit Resultaten von bekannten methodischen Untersuchungen als auch im Fall der Echtdatenstudien mit den Parametern, die von anderen Inversionsprogrammen für die jeweiligen Ereignisse ermittelt wurden.

Es zeigte sich, daß die Topographie einen starken Einfluß auf den Signalgehalt der GFn hat. Darum müssen vor nachfolgenden Anwendungen auf Fälle mit komplizierter Geometrie weitere Tests durchgeführt werden, welche die genauen Auswirkungen verschiedener Topographien quantifizieren können.

In dieser Arbeit wurden Fallstudien für vulkanische und induzierte LP-Events bearbeitet. Die Ergebnisse dieser Studien legen nahe, daß numerische Verbesserungen sowie die Implementierung weiterer Regularisierungsparameter angeraten sind, um robuste Lösungen zu gewährleisten.

Die allgemeine Funktionsfähigkeit des Algorithmus' wurde demonstriert, sowohl für die statische Inversion eines zeitlich begrenzten Datensatzes als auch für die Anwendung auf kontinuierliche synthetische und reale Datensätze als selbständige Inversions- und Detektionsroutine.

Diese Anwendungen machen deutlich, daß eine Verringerung der Rechenzeit notwendig ist, um bei der Analyse echter Datensätze belastbare Ergebnisse zu erzielen. Unter Einbeziehung der aufgeführten Verbesserungsmöglichkeiten kann der vorgestellte Algorithmus im Rahmen eines automatisierten, echtzeitnahen Monitoring-Systems verwendet werden.

Abstract

Volcanic seismic events that emit long period signals (*LP-events*) are considered important indicators for current subsurface fluid or magma movement. The analysis of such events is crucial for the monitoring of volcanic regions in order to evaluate the evolution of volcanic unrest and the relative hazard assessment. In addition, *induced* LP-events occur near fluid reservoirs and mining sites, where they are interpreted as evidence for slow rupturing or deformation processes. The continuous long-term evaluation of LP-signals in such regions can allow to infer local or regional structural inhomogeneities, which again can contribute to seismic hazard estimations. So far, the analyses of volcanic and induced seismic LP-events are strictly separated. Software tools are available, which are either specialised on the monitoring of volcanic unrest or restricted to the continuous analysis of large and medium scaled seismic events on regions with a flat topography.

A new software tool has been developed in the scope of this thesis. It allows the fast and simple analysis of seismic LP-events, independent of the geometry and size of the source region. The algorithm is based on an algebraic one-step time-domain inversion of full waveform data, combined with a gridsearch for possible source locations. For conducting the inversion, a set of 18 Green's functions (GFs) is used that take into account the local or regional seismic velocity model. The GFs are generated in advance to allow a fast data processing. In contrast to other approaches, the complete infomation about the three-dimensional structure of the underground is contained within the GFs – this includes topography as well as anisotropies.

Seismic data can be analysed event-based, in which the source time can be determined by an additional gridsearch in time. Without the need for an external event detection routine it is furthermore possible to analyse continuous seismic data by applying a moving time-window approach. Data and estimated parameters are compared for successive overlapping time intervals. The level of agreement between them is expressed in one value and a pre-defined threshold is utilised for the detection of LP-events.

The new algorithm has been tested under several considerations using synthetic data sets for one- and three-dimensional geometries. The code is operational and yields results that are consistent with former findings existing event analyses. Topography has a large influence on the GFs, therefore special care has to be taken of the generation of GFs in case of complex geometries.

Case studies have been carried out for both volcanic and induced seismic LP-events. The results suggest that numerical improvements and the implementation of regularisation parameters are advisable.

The general capability of the inversion algorithm to act as an automated inversion detection routine on continuous data is demonstrated for both synthetic and real data. These tests show that further optimisation with respect to computational speed is required. Overcoming these limitations will allow to use the developed algorithm within the framework of an automated monitoring system.

Contents

List of Figures

1 Introduction

The Earth is permanently moving[1]. This movement comprises continuous processes on large scales (plate tectonics, eigenoscillations, tides), impulsive localised events (earthquakes, volcanic eruptions, explosions), as well as small scale processes (microearthquakes, fluid flows). All these processes emit seismic waves of specific amplitudes and frequencies, which propagate through the Earth. The seismic waves cause local displacements, which are recorded at or near the surface as seismic data. In seismology, these data are analysed in order to study the global and local inner structures of the Earth.

1.1 Inversion of seismic data

Depending on the aim of the analysis of seismic data, they can be interpreted in different ways. In this work, I focus on the study of distinct *seismic events*, i.e. source processes that are clearly localised in time and space. Aside a permanent indeterminable background of low-level displacement, originating from the continuous large scale movements (here regarded as *noise*), the seismic data contain information about these events. Inferring location and time, as well as the geometry and strength of such a source process, is called *event inversion of seismic data*[2].

Depending for instance on the quality of data or the detailedness of the respective study, more or less complex methods and algorithms exist for carrying out the inversion of seismic (event) data. For example, some tools invert only the onset polarity of the seismic signals for the source mechanism (Reasenberg and Oppenheimer, 1985). Other methods (e.g. Kanamori, 1970; Heimann, 2011), analyse specific seismic phases (P-waves, S-waves, surface-waves) in the data. Finally one can also invert the full waveforms. The inversion can be calculated not only directly from the time series of the recorded displacement (Tajima et al., 2002; Rößler, 2006; Lokmer et al., 2009), but also from its spectra, as for instance in (Lesage et al., 2002; Kawakatsu and Montagner, 2008; Cesca et al., 2010b).

Nowadays automated routines for the inversion of seismic data exist to some extent. This enables the fast generation of large catalogues of inversion results, for example the *Global CMT catalogue* (Dziewonski et al., 2000; Larson et al., 2010). Besides the automatic collection of information about large and globally detectable earthquakes in such a catalogue, there is large interest in identifying and analysing specific events in greater detail (Anderson et al., 2010). Therefore data are for instance analysed with respect to restricted source regions (Braunmiller et al., 2002; Pondrelli et al., 2002; Tsuruoka et al., 2009; Ford et al., 2009; Stich et al., 2010). Other restrictions are the analyses

[1] "Eppur si muove!" (prob. Giordano Bruno or Galileo Galilei)

[2] For the remainder of the work, I refer to it by the term *inversion*.

only of specific classes of events of interest, e.g. explosions and volcanic events (Legrand et al., 2000; Dreger and Woods, 2002; Minson and Dreger, 2008), landslides (Kawakatsu, 1989), or microseismic events (Rodriguez et al., 2010). Most of the inversion methods are event-based, i.e. they are used for analysing finite data from seismic events, whose origin time is roughly confined. However, some methods can be applied to the analysis of a continuous stream of data (Kawakatsu, 1995; Tajima et al., 2002).

The seismic data contains information about the source process, as well as the parts of the Earth, which the seismic waves have passed. Unfortunately, these two parts of information cannot be easily separated.

1.2 Green's functions

The influence of the Earth onto the signal must be accurately determined in order to invert the data for the source process (Šílení et al., 1992). This is achieved by including an Earth model into the inversion algorithms.

The Earth structure is modelled using approximations, partly because of a limited knowledge, and partly as a consequence of applying simplifying assumptions for reducing the numerical cost of the analysis (e.g. one-dimensional approximations). The main parameters for describing the model are the depth-depending values of wave velocities and their damping, as well as the model's densities. From that, a simplified (one-dimensional) structural model of the Earth can be defined, which is the most common assumption for the analysis of seismo-tectonic events in regional and global catalogues.

Carrying out a more sophisticated analysis for strongly inhomogeneous regions, e.g. volcanic areas, subduction zones or geothermal research sites, however, the three-dimensional subsurface structure must be resolved in greater detail. Therefore the model of the medium is extended to a full three-dimensional description of the known composition of the underground. A full three dimensional model of the medium includes the variation of the elastic parameters in all spatial dimensions, possible anisotropy of the medium and the topography of the Earth surface.

On the one hand, the detailedness of the Earth model depends on the conscious restriction of desired information density im combination with the signal's wavelengths under consideration. On the other hand, the model's accuracy is restricted by the a-priori information about the Earth's interior; the model cannot be more complex than the knowledge about the structure itself.

Modelling the wave propagation through a medium can be conveniently achieved by introducing the concept of Green's functions (GFs), which reflect the answer of a medium to impulsive excitation. The latter can be described either by single forces or by the more complex *seismic moment tensor* (Gilbert, 1971). The GFs contain all information about the Earth model, they describe the impact of a seismic source within the medium onto a seismometer at any given position. Thus, they contain the full information of the wavefield propagation properties, including the particularly interesting near- and far-field terms (Aki and Richards, 2002). The generation of Green's functions, which suit the necessities of a given geometrical setup, is an essential step for setting up a stable inversion routine (Bean et al., 2008).

1.3 Long period events

The sources processes that I will focus my analysis on are local ruptures and deformations, as well as volcanic seismic events. The latter are related to volcanic activity (magma motion through the the Earth crust) thus their occurrence is restricted to the vicinity of active volcanic areas. Their sources are localised in small regions around or inside volcanic edifices, and their mechanisms can be manifold in type, occurrence, and signal characteristics. Thus an improved insight into the source processes of volcanic seismic signals leads to a better understanding of the volcanoes' inner structure and dynamics.

In contrast to impulsive single fracturing events, as it is widely the case for tectonic events, volcanic source dynamics can be persisting for long times due to a temporally extended source mechanism, e.g. fluid movements (McNutt, 1996). A correct interpretation of these dynamics as sources of seismic waves provides information about the chronological development of the state inside and below the volcanic edifice, thus the expansion of magma reservoirs or even the movement of magma can be studied. A comprehensive analysis of these dynamics at specific volcanoes is necessary for developing a broad conceptual picture of the general volcanic processes. In addition, this knowledge can help to improve estimating volcanic hazards, which is important for inhabited volcanic areas.

Seismic signals at volcanoes differ from each other in many characteristic ways. For instance they show different amplitudes, times of persistence, periods of occurrence, and power spectral densities. Signals from different volcanic areas can vary quite strongly, but there are techniques to classify events (Neuberg, 2000). Classifications are mainly based on the frequency content of the seismic signals. Beside other classes like tremor, silent slip, or rockfall events, the class of the low frequency *long-periodic* or *long period events (LP-events)* is of great importance. The LP-signals are characterised by a significant content of low frequencies following an abrupt onset (asymmetric waveform envelope). In contrast to other seismic events, which show strong signal amplitudes in the frequency band above 2 Hz, the LP-events have main signal contents below that. The volcanic LP-events are suspected to directly reflect fluid movements in the interior of the edifice (e.g. Gilbert and Lane, 2008); thus their occurrence initiated several attempts to infer their source mechanism.

The observation of low frequency signals is not restricted to volcanic areas. Shallow tectonic events can generate surface waves with a significant low frequency content. Long period signals can also originate from so-called *induced seismic events* (McGarr et al., 2002), which are indirectly generated by human action or strong natural transient phenomena generally involving a sub-surface movement of fluids, e.g. persisting subsurface drainage or rainfall (e.g. Hainzl et al., 2006; Dahm et al., 2010). In contrast to direct human engagement, as it is the case for example at nuclear explosions, induced events stem indirectly from a change of the local stress field by means of fluid extraction (gas and oil fields) or injection (hydro fracturing), or around excavated cavities (mining areas). All these changes in the local stress field can lead to spontaneous stress release by fracturing. If these fracturing processes run sufficiently slowly, LP-signals can be generated.

The analysis of LP-signals has a long history (Kanamori and Given, 1981; Kuge and Kawakatsu, 1990), which often is related to the survey of volcanic LP-events (e.g.

Hasegawa et al., 1991; Chouet, 2003) or to the analysis of tectonic LP-events (e.g. Tajima et al., 2002). Besides the general analysis of the relation between the strength of events and the frequency content of their emitted signals (Kagan, 1999) inversion routines have been developed for the manual or automated determination of source mechanisms of regional LP-events (Ritsema and Lay, 1995; Kawakatsu, 2003; Ford et al., 2009). With regard to induced seismic events one can find a variety of analyses (Trifu et al., 2000; Lasocki and Orlecka-Sikora, 2008; Malovichko, 2005; Gibowicz, 2009; Li et al., 2010), which show that the determination of the source mechanism is in most cases neither easy nor unique.

Methods dealing with the source determination in mining areas are often restricted to estimating the source location. Often they only take into account the onset times on a large number of high frequency stations detecting acoustic emissions (Spies and Eisenblätter, 2001) or microseismicity (Young et al., 1989). The same holds for the survey of micro fractures in the surrounding of hydro-fracturing areas (Nolen-Hoeksema and Ruff, 2001). An enhancement of the analysis of full waveform information from low frequency seismic data in the framework of mining surveys is subject to ongoing research (Rodriguez et al., 2010; Cesca, 2011).

The general concepts of seismic moment tensor inversion (Dziewonski et al., 1981) have been used to develop inversion routines. Besides the methods and applications mentioned above, several publications have concentrated on different topics: Automated inversions for source mechanisms have been systematically carried out on a global (Ferreira and Woodhouse, 2006; Larson et al., 2010; USGS, 2010; Heimann, 2011) and regional scale (Bernardi et al., 2004; Pondrelli et al., 2002; Brandt and Saunders, 2011). Induced events have been subject to investigations (Dreger and Kaverina, 2000; Dahm et al., 2010), as well as shallow events (Forbriger, 2003a,b; Cesca et al., 2006). Furthermore, a broad set of independent approaches has been developed to detect volcanic LP-events and infer their sources (McNutt, 2005; Chouet, 2003, 1996).

1.4 Scope and structure of this work

Altogether, there are many independent methods for the inversion of LP-events for specific setups. Unfortunately, no algorithm exists so far, which combines the different capabilities that are needed for the general study of shallow LP-events. Furthermore, if such an algorithm were able to analyse a continuous seismic data stream sufficiently fast, it could be used for real-time monitoring of volcanoes, as well as fluid reservoirs or mining regions. This requires a near real-time processing.

In order to allow a fast analysis of shallow LP-signals, originating from volcanic as well as induced seismic sources, I have developed a software algorithm, which allows to invert for a seismic source mechanism causing long period signals: *ARCTIC* – **A***utomated* **R***eal-time* **C***MT* **T***ime-domain* **I***nversion* **C***ode*. Following the method described in (Sipkin, 1982), an algebraic inversion in the time domain is combined with a four-dimensional grid search for determining a *centroid moment tensor* solution. By making use of pre-

calculated Green's functions, the speed of the algorithm is sufficiently high to justify the term *real-time*.

As a specific improvement over existing similar methods (Tajima et al., 2002; Kawakatsu, 2003; Ford et al., 2009), my development includes the use of the full information of the three-dimensional source region (e.g. velocity structure, damping, topography). It is contained in the 18 components of the Green's function. No a-priori one-dimensional or far-field approximations are necessary.

The final inversion solution contains the estimations of the full moment tensor, the energy release, the location in three dimensions, as well as the source time for a seismic event. This solution can be provided to a database system, which is suited to successively build a catalogue of seismic LP-events (Barsch, 2009).

Successful examples of continuous seismic survey algorithms (Pasyanos et al., 1996; Takanami et al., 2003; Kawakatsu, 2003) encouraged for extending the event-based inversion routine of *ARCTIC* to act optionally on a continuous data stream. The data are continuously analysed and inverted in the application of this extension of the algorithm. Possible high correlations of the real data and the inversion results can be used to detect events automatically. This setup allows to use *ARCTIC* as an independent detection routine for LP-events in addition to the use as a pure event based inversion algorithm.

I will present the structure of the algorithm, as well as the feasibility studies for the aforementioned development in the following chapters of this work. In order to introduce the general and basic concepts, which the inversion routine and its applications are based on, I present the general description of an arbitrary seismic source in the second chapter. Furthermore, I introduce the important concept of the *centroid* (Backus, 1977; Doornbos, 1982; Dahm and Krüger, 1999). As already mentioned, the use of pre-calculated Green's functions is a crucial step for achieving the inversion in near real-time. Therefore, I dedicate the third chapter to a careful introduction of their definitions and notation.

In the fourth chapter, I introduce models of seismic sources that generate LP-signals. There I also give the definition of LP-events and show examples of characteristic seismic data traces. As the last step of the theoretical part, I describe the inversion approach and its implementation in the *ARCTIC* software in chapter five.

To demonstrate the general technical functionality of *ARCTIC*, several tests with synthetic data samples have been carried out, which will be discussed in chapter six. Finally I present the results of applying the newly developed tool to several sets of real data on a local and regional scale. I have processed and analysed a set of induced seismic events as well as a volcano seismic data sample. These I present in chapter seven together with an example of an extension of *ARCTIC*, acting here as an automatic detection routine on a continuous data set. This work closes with the discussion of the presented results of the applications on real and synthetic data.

2 Seismic sources

Seismic sources occur in a large diversity of sizes, geometries, and strengths. Their spatial scale varies over several ranges of magnitudes. On large scales, it includes for instance large scale plate boundary tectonic movement which generates tectonic earthquakes, mass movements within plates due to large interior stresses, as well as localised magma movement inside and beneath volcanic areas. On small spatial scales there are earthquakes related to man-made and natural fluid injections, construction failures in buildings and caverns, and finally the initiation of microcracks, resulting in micro earthquakes and acoustic emissions respectively. All these sources span a broad set of mechanisms: they can for instance represent pure shear movement, tensile crack openings, or isotropic explosions. Therefore the seismic signals exhibit distinctly different characteristics with respect to amplitudes, frequencies, durations, and so on.

In the following, I will provide a consistent compilation of necessary theoretical concepts for the description of seismic sources. In this brief overview, the concept of the seismic moment tensor to describe arbitrary sources will be introduced. The differences between point and finitely extended sources will motivate the formulation of the *source centroid*. In addition, I will explain and validate the use of the *point source approximation* and the definition of the *centroid moment tensor*. I will give a small introduction into the visualisation of a seismic source mechanism with the aid of *focal sphere diagrams* at the end of this chapter. These visualisations are often used for evaluation and interpretation of source geometries.

2.1 A general seismic source

The endeavours to describe the excitation of Earth's normal modes (eigenoscillations) by tectonic shear crack events led to the development of the concept of the *seismic moment tensor*. It has been designed to model and characterise general seismic sources, and it is applied since its introduction and discussion in (Gilbert, 1971) and (Backus and Mulcahy, 1976a,b). Deeper insight can be gained and a vast set of examples apart from this work can be found in standard textbooks (e.g. Lay and Wallace, 1995; Udıas, 1999; Stein and Wysession, 2003).

The seismic moment tensor provides a convenient way to describe not only shear cracks, but an arbitrary seismic source in a very general form, including e.g. explosive events. This brief introduction to the seismic moment tensor follows the definitions given in (Stein and Wysession, 2003).

As a general assumption I take the seismic source as free of net forces and torques, as stated for instance in (Aki and Richards, 2002) and (Jost and Herrmann, 1989). This has become the most accepted approach in seismological methods, see for instance

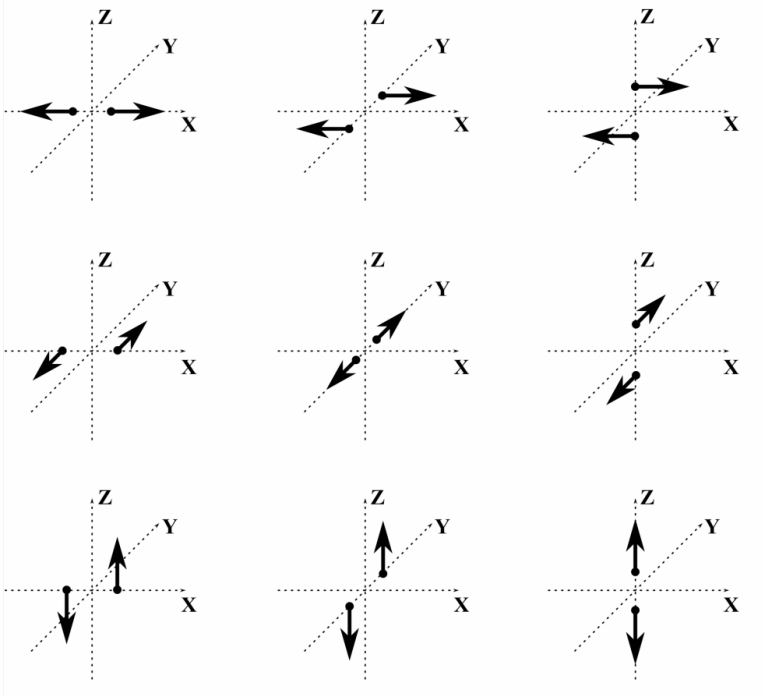

Figure 2.1:
Illustration of the nine basis force couples contained in the seismic moment tensor. The coordinate system is an arbitrary orthogonal basis of the $\mathbb{R}^3$. The positions of the force couples in this graphic represent their respective positions inside the 3×3 structure of the seismic moment tensor $\mathbf{M}$.

(Stein and Wysession, 2003; Knopoff and Randall, 1970; Dahm et al., 1999; Udıas, 1999; Shearer, 1999). For the sake of completeness it shall be mentioned, that there can be found alternative concepts, that take into account asymmetric moment tensors (Takei and Kumazawa, 1994, 1995).

2.1.1 The seismic moment tensor

In this section, the seismic moment tensor is introduced in accordance with (Jost and Herrmann, 1989). The general concept and the description of a seismic source are presented. Its profound theoretical development is highly entangled with the definition of *Green's functions*, therefore it will be carried out later on in chapter 3.

In three spatial dimensions, a combination of six basis shear cracks can describe every possible shear source. These basis elements are defined by force couples, which are perpendicular to three basis vectors of the $\mathbb{R}^3$. Three additional basis elements are given by pairs of forces aligned along each basis vector (*vector dipoles*). All together they set up a nine-elementary basis system, by which all possible point source geometries can be described. Each element of this basis is defined at the spatial center point of the acting forces' levers, thus they represent rather force dipoles than distinguishable pairs. The rotational force dipoles are interpreted as a torque.

The basis elements' orientations are shown in figure 2.1. The coordinates XYZ are arbitrary and denote an orthogonal basis system of the $\mathbb{R}^3$. The torques of this set are more commonly denoted with the term *seismic moment*. They are commonly assembled in a two dimensional matrix structure $\mathbf{M}$, ordered according to the chosen spatial basis.

The orientation of the applied forces can be found in the rows, the column defines the lever arm direction.

$$\mathbf{M} := \begin{pmatrix} M_{11} & M_{12} & M_{13} \\ M_{21} & M_{22} & M_{23} \\ M_{31} & M_{32} & M_{33} \end{pmatrix} , \tag{2.1}$$

where the $\{M_{ij} \,|\, i,j \in 1,2,3\}$ are the seismic moments of the shear cracks and vector dipoles orientated according to some basis of the $\mathbb{R}^3$.

Since this real valued matrix shows the transformation properties of a tensor of rank two (Shearer, 1999), $\mathbf{M}$ is called *seismic moment tensor*. With this tensor as a collection of linear coefficients for the chosen basis, we already have set up a convenient concept to describe all types of seismic sources with symmetric forcing (free of net forces).

A general mechanism $\mathbf{M}$ consists of a superposition of the basis vectors, so the detailed source geometry may not always be obvious. To allow a direct human interpretation of the source mechanism, $\mathbf{M}$ can be transformed and decomposed into smaller parts, which themselves describe different types of source mechanisms. Following (Jost and Herrmann, 1989), a standard decomposition of $\mathbf{M}$ has been established which provides information about the relative amounts of isotropic action, a main shear crack orientation, and the remaining non-shear part of the source.

$\mathbf{M}$ is a real-valued symmetric matrix, therefore a set of three orthonormal eigenvectors $\{\boldsymbol{v_i} \,|\, i \in \{1,2,3\}\}$ and their respective eigenvalues λ_i can be found, with which $\mathbf{M}$ can be written in fully diagonalised form:

$$\mathbf{M} = (\boldsymbol{v_1}, \boldsymbol{v_2}, \boldsymbol{v_3}) \cdot \mathrm{Diag}(\lambda_1, \lambda_2, \lambda_3) \cdot \begin{pmatrix} \boldsymbol{v_1}^T \\ \boldsymbol{v_2}^T \\ \boldsymbol{v_3}^T \end{pmatrix} . \tag{2.2}$$

To carry out the decomposition of $\mathbf{M}$, I will stay in this reference eigenvector system. As an abbreviative notation for the dyadic (outer) product of two eigenvectors, I define

$$\langle \boldsymbol{v_m} \rangle := \boldsymbol{v_m} \otimes \boldsymbol{v_m}^T . \tag{2.3}$$

The *isotropic* component $\mathbf{M}^{\mathrm{iso}}$ of $\mathbf{M}$contains only information about the volumetric changes at the source, where the impact of the change is described by the value of the trace $\mathrm{Tr}(\mathbf{M})$ of $\mathbf{M}$. As the first step of the decomposition of $\mathbf{M}$, $\mathbf{M}^{\mathrm{iso}}$ is separated from the non-volumetric or *deviatoric* part $\mathbf{M}^{\mathrm{devi}}$:

$$\mathbf{M} = \mathbf{M}^{\mathrm{iso}} + \mathbf{M}^{\mathrm{devi}} = \frac{1}{3} \cdot \begin{pmatrix} \mathrm{Tr}(\mathbf{M}) & 0 & 0 \\ 0 & \mathrm{Tr}(\mathbf{M}) & 0 \\ 0 & 0 & \mathrm{Tr}(\mathbf{M}) \end{pmatrix} + \mathbf{M}^{\mathrm{devi}} \tag{2.4}$$

For the next steps, I need the reduced eigenvalues λ_i^*:

$$\lambda_i^* = \lambda_i - \frac{1}{3} \mathrm{Tr}(\mathbf{M}) . \tag{2.5}$$

Let these eigenvalues be sorted $|\lambda_3^*| \geq |\lambda_2^*| \geq |\lambda_1^*|$. Then a factor ε can be defined, which gives information about the deviation of the source mechanism from a pure shear crack:

$$\varepsilon := -\frac{\lambda_1^*}{\lambda_3^*}\,, \tag{2.6}$$

where $\varepsilon = 0$ for a pure shear and $\varepsilon = 0.5$ for no distinct shear component existing in $\mathbf{M}$.

Now I can write the deviatoric part of $\mathbf{M}$ as

$$\mathbf{M}^{\mathrm{devi}} = \underbrace{\lambda_3^* \cdot (1-2\varepsilon) \cdot (\langle \boldsymbol{v_3} \rangle - \langle \boldsymbol{v_2} \rangle)}_{=:\mathbf{M}^{\mathrm{DC}}} + \underbrace{\lambda_3^* \cdot \varepsilon \cdot (2 \cdot \langle \boldsymbol{v_3} \rangle - \langle \boldsymbol{v_2} \rangle - \langle \boldsymbol{v_1} \rangle)}_{=:\mathbf{M}^{\mathrm{CLVD}}}\,. \tag{2.7}$$

The $\mathbf{M}^{\mathrm{DC}}$ describes a pure shear action, orientated normal to $\boldsymbol{v_1}$, $\mathbf{M}^{\mathrm{CLVD}}$ describes the deforming action of a *compensated linear vector dipole (CLVD)* (Knopoff and Randall, 1970).

Besides the information about the source geometry, one is also interested in the overall strength of a seismic source. This strength is described in units of a torque by the *scalar seismic moment* M_0. That attribute of $\mathbf{M}$ is defined according to Bowers and Hudson (1999) by

$$M_0 := \frac{1}{3}\,|\mathrm{Tr}(\mathbf{M})| + |\lambda_3^*|\,. \tag{2.8}$$

2.1.2 The *centroid moment tensor* (CMT) as an approximative description of sources with finite spatial extent

Up to this point, the description of a seismic source is restricted to a single source point. In case of a finite shear failure, the vicinity of this point has to be included in the definition of the non-zero shear surface and the finite displacement of the rupture. For to obtain a consistent framework for the handling of real extended sources, the concept of the seismic moment tensor must be further developed. This can be carried out in either of the two following ways.

2.1.2.1 The finite source and the seismic moment tensor density

The first approach to extend the pointwise defined moment tensor to a finite source is the definition of a *seismic moment tensor density* $\mathbf{m}$. This is the distribution of seismic moment tensors per unit volume within a three dimensional source region V. An overall definition of the source mechanism $\mathbf{M}$results then from a spatial integration of $\mathbf{m}$ over the source volume. In case of a non-impulsive source, an integration over the finite duration of the rupture τ_{r} for the inclusion of the temporal evolution of the full source has to be taken into account in addition to the spatial integration:

$$\mathbf{M} = \int_V \int_{\tau_{\mathrm{r}}} \mathbf{m}(\boldsymbol{\xi}, \tau)\ \mathrm{d}\tau\, \mathrm{d}\boldsymbol{\xi}\,. \tag{2.9}$$

These steps can be calculated either in an analytical way in case of theoretical developments, or by the introduction of a finite sampling of the source volume, where the single moment tensor density entries are weighted with the sampling size and afterwards are summed up. This discretisation of the extended source volume is sketched in figure 2.2. The finite partition of the source region is a usual method for the analysis of real, non analytical setups (e.g. Heimann, 2011).

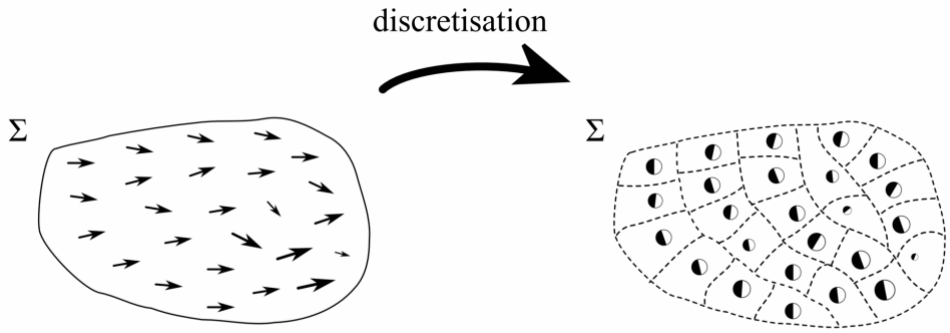

Figure 2.2:
Approximation of an extended source by discretisation into a finite set of smaller subvolumes of the source. Arrows indicate local movements of the volume in front of the image plane. Local source mechanisms are illustrated by focal sphere diagrams. Their size reflects the seismic moment.

This ansatz of generalising the application of the moment tensor to an extended source is the natural way to make the true continuous behaviour of the source volume accessible to numerical descriptions. The finitely sampled time and space representation of the process is of course only an approximation of the real process. Nevertheless, for our practical purposes even this approximation raises a (sampling dependent) high demand on computational effort. Hence it is advantageous to derive a simpler alternative concept.

2.1.2.2 The centroid

When looking for a simpler, yet valid concept for the inclusion of the spatial extension of the source region, one finds a very intuitive setup. Instead of studying standard parameters as e.g. nucleation point and rupture propagation within the source region, one reduces the investigation to the average source mechanism, that describes the mean behaviour of the full contemplable source region. A sketch of this scheme is given in figure 2.2.

By this definition the influence of every single source location point is included within the overall source mechanism, but its explicit contribution to the signal is not used as vital single information. Instead it is just an implicit part of the integral over the volume. In other words, if the source region can be assumed as a finite volume which is comparably small in relation to the seismic signal's main wavelengths, it is a valid approach to restrict the full analysis on one hypocentral point of the whole source volume, the so-called

centroid (see figure 2.3). Therefore this approach must be understood as a *point source approximation* for the source volume. In opposite to the partition of the source region (section 2.1.2.1), this method has the advantage, that the source can be described by a far smaller set of parameters; the danger of spurious results due to overparametrisation is averted.

This method was introduced and discussed in (Backus and Mulcahy, 1976a; Dziewonski et al., 1981; Doornbos, 1982). Its temporal and spatial location is implicitly obtained by taking the weighted arithmetic mean value of all points inside the source region, the absolute value is based on the size of the complete source region. The centroid as the dynamic seismic source is described by the *centroid moment tensor* (CMT). All further considerations of the seismic source region will be done with respect to this mean hypocentral source point.

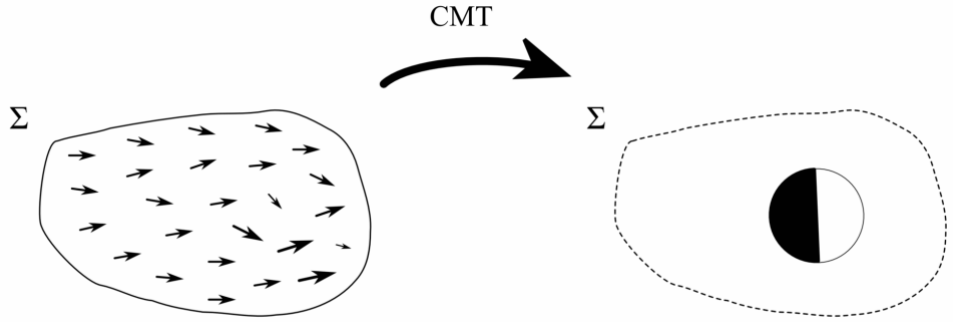

Figure 2.3:
Approximation of an extended source by a point source, the *centroid*. Arrows indicate local movements of the volume in front of the image plane. The centroid source mechanism is illustrated by a focal sphere diagram. The size and angle reflect the seismic moment and orientation of the complete extended source

This simple approximation can be justified by some basic theoretical thoughts, which I present in the following; they can be found in (Stump and Johnson, 1982) or (Lay and Wallace, 1995; Dahm and Krüger, 1999). As a start we have to leave the concept of the moment tensor as a source of signals and take a look at the action of single forces instead. The observed signal $\boldsymbol{u}_j$ caused by impulsive force impacts $\boldsymbol{F}_i$ at a time t_0 in i-direction inside a source volume V is given by

$$\boldsymbol{u}_j(\boldsymbol{x}, t) = \int_V \tilde{\boldsymbol{G}}_{\boldsymbol{ji}}(\boldsymbol{x}, \boldsymbol{\xi}; t, t_0) * \boldsymbol{F}_i(\boldsymbol{\xi})\ \mathrm{d}\boldsymbol{\xi}\,, \tag{2.10}$$

where the $\tilde{\boldsymbol{G}}_{\boldsymbol{ji}}$ is some transfer function of the signal (Aki and Richards, 2002). At this point the exact definition of this function is not of great importance. It is only assumed to be an analytical function, therefore it can be expanded into a Taylor series up to second order around the source point ξ_0. Higher order terms are neglected under the assumption that these transfer functions do not vary significantly in space, if the spatial dimensions are much smaller than the wavelengths of the emitted signals. The explicit

time dependence is dropped for readability. So the expansion of the transfer function equates to

$$\begin{aligned}\tilde{\boldsymbol{G}}_{\boldsymbol{ji}}(\boldsymbol{x_0},\boldsymbol{\xi}) = \tilde{\boldsymbol{G}}_{\boldsymbol{ji}}(\boldsymbol{x_0},\boldsymbol{\xi_0}) + \sum_{k=1}^{3} \frac{\partial}{\partial \xi_k} \tilde{\boldsymbol{G}}_{\boldsymbol{ji}}(\boldsymbol{x_0},\boldsymbol{\xi})\Big|_{\boldsymbol{\xi_0}} \cdot \delta\xi_k + \\ + \frac{1}{2} \sum_{k,l=1}^{3} \frac{\partial^2}{\partial \xi_k \partial \xi_l} \tilde{\boldsymbol{G}}_{\boldsymbol{ji}}(\boldsymbol{x_0},\boldsymbol{\xi})\Big|_{\boldsymbol{\xi_0}} \cdot \delta\xi_k \delta\xi_l + \mathcal{O}(\boldsymbol{\delta\xi}^3)\,,\end{aligned} \tag{2.11}$$

with the spatial variation $\delta\xi_k := (\boldsymbol{\xi} - \boldsymbol{\xi_0})_k$.

From here on, the abbreviative notation for partial spatial derivatives of functions applies:

$$h_{i,j}(\boldsymbol{y}) := \frac{\partial}{\partial y_j} h_i(\boldsymbol{y})\,. \tag{2.12}$$

Using the expansion of the transfer function from eq.(2.11), where terms of third and higher orders in eq. (2.10) are neglected, the observed signal is approximated by

$$\begin{aligned}\boldsymbol{u}_j(\boldsymbol{x},t) \approx \int_V \Bigg(\tilde{\boldsymbol{G}}_{\boldsymbol{jk}}(\boldsymbol{x},\boldsymbol{\xi_0}) + \sum_{k=1}^{3} \tilde{\boldsymbol{G}}_{ji,k}(\boldsymbol{x},\boldsymbol{\xi})\Big|_{\boldsymbol{\xi_0}} \cdot \delta\xi_k + \\ + \frac{1}{2} \sum_{k,l=1}^{3} \tilde{\boldsymbol{G}}_{ji,kl}(\boldsymbol{x},\boldsymbol{\xi})\Big|_{\boldsymbol{\xi}_0} \cdot \delta\xi_k \delta\xi_l \Bigg) * \boldsymbol{F}_i(\boldsymbol{\xi},t_0)\ \mathrm{d}\boldsymbol{\xi} \\ = \tilde{\boldsymbol{G}}_{\boldsymbol{ji}}(\boldsymbol{x},\boldsymbol{\xi_0}) * \int_V \boldsymbol{F}_i(\boldsymbol{\xi},t_0)\ \mathrm{d}\boldsymbol{\xi} + \\ + \tilde{\boldsymbol{G}}_{ji,k}(\boldsymbol{x},\boldsymbol{\xi_0}) * \sum_{k=1}^{3} \int_V \boldsymbol{F}_i(\boldsymbol{\xi},t_0) \cdot \delta\xi_k\ \mathrm{d}\boldsymbol{\xi} + \\ + \tilde{\boldsymbol{G}}_{ji,kl}(\boldsymbol{x},\boldsymbol{\xi_0},\boldsymbol{x}) * \frac{1}{2} \sum_{k,l=1}^{3} \int_V \boldsymbol{F}_i(\boldsymbol{\xi},t_0) \cdot \delta\xi_k \delta\xi_l\ \mathrm{d}\boldsymbol{\xi}\end{aligned} \tag{2.13}$$

or

$$\begin{aligned}\boldsymbol{u}_j(\boldsymbol{x},t) = \left\{ \tilde{\boldsymbol{G}}_{\boldsymbol{ji}}(\boldsymbol{x},\boldsymbol{\xi_0}) * \int_V \boldsymbol{F}_i(\boldsymbol{\xi},t_0)\ \mathrm{d}\boldsymbol{\xi} \right\} + \left\{ \tilde{\boldsymbol{G}}_{ji,k}(\boldsymbol{x},\boldsymbol{\xi_0}) * \sum_{k=1}^{3} \mathbf{M}'_{ik} \right\} + \\ + \left\{ \tilde{\boldsymbol{G}}_{ji,kl}(\boldsymbol{x},\boldsymbol{\xi_0}) * \frac{1}{2} \sum_{k,l=1}^{3} \mathbf{M}'_{ikl} \right\}\end{aligned} \tag{2.14}$$

for $\boldsymbol{\xi} \in V$. Here $\mathbf{M}$' is defined as the mechanical rotational moment (torque) of (n+1)-th order:

$$M'_{il_1\ldots l_n} := \int_V (\boldsymbol{\xi} - \boldsymbol{\xi_0})_{l_1} \ldots (\boldsymbol{\xi} - \boldsymbol{\xi_0})_{l_n} \cdot \boldsymbol{F}_i(\boldsymbol{\xi}, t_0)\ \mathrm{d}\boldsymbol{\xi}\,. \tag{2.15}$$

Referring to the requirement that the action of seismic sources is caused only by force double-couples instead of single forces (see section 2.1), the first summand in eq. (2.14) must be equal to zero:

$$\tilde{\boldsymbol{G}}_{\boldsymbol{ji}}(\boldsymbol{\xi_0}, \boldsymbol{x}) * \int_V \boldsymbol{F}_i(\boldsymbol{\xi}, t_0)\ \mathrm{d}\boldsymbol{\xi} \stackrel{!}{=} 0\,. \tag{2.16}$$

The second summand is the description of the point source geometry. This will be described in detail in chapter 3.1.3. The handling of the third summand, including the $\mathbf{M}'_{ikl_1l_2}$ of third order, follows the axiomatic demand that the centroid shall describe a *mean* source point. So one can write this moment as

$$\mathbf{M}'_{il_1l_2} = \int_V (\boldsymbol{\xi} - \boldsymbol{\xi_0})_{l_1} (\boldsymbol{\xi} - \boldsymbol{\xi_0})_{l_2} \cdot \boldsymbol{F}_i(\boldsymbol{\xi})\ \mathrm{d}\boldsymbol{\xi} = \int_V (\boldsymbol{\xi} - \boldsymbol{\xi_0})_{l_1} \cdot m_{il_2}(\boldsymbol{\xi}, \boldsymbol{\xi_0})\ \mathrm{d}\boldsymbol{\xi}\,, \tag{2.17}$$

with the pointwise acting torque

$$m_{il_2}(\boldsymbol{\xi}, \boldsymbol{\xi_0}) := (\boldsymbol{\xi} - \boldsymbol{\xi_0})_{l_2} \cdot \boldsymbol{F}_i(\boldsymbol{\xi})\,. \tag{2.18}$$

The centroid's position as the effective centre point $\boldsymbol{\xi_0}$ of the source volume is now defined as the location, where all the pointwise torques $m(\boldsymbol{\xi})$, weighted by their distance to the centre point $(\boldsymbol{\xi} - \boldsymbol{\xi_0})$ cancel out each other. This is equivalent to the demand that all third order torques $\mathbf{M}'_{abc}$ equate to identically zero for all tuples $\{abc\}$.

With the aid of this argumentation it is shown that the introduction of the source centroid is a formally valid approximation of an extended source volume by means of the centroid moment tensor, so it is consistent to handle the centroid itself as a single point source.

In (Knopoff and Randall, 1970) the authors show that the use of only the first elements of the multipole expansion is a valid approach for describing the point source. This holds under the conditions that the main content of the signals observed from the source has longer wavelengths than the real spatial extent of the source, and that the characteristic times of these signals are larger than the *rise time* τ_r of the factual source. The rise time is the temporal extent, within which the *source time function* is not constant: $\tau_r = \max(t_r) - \min(t_r)\ ;\ t_r = \{\, t \mid \frac{\partial}{\partial t}\mathrm{stf}(t) \neq 0\}$ (c.f. chapterr 3.1.6). All these conditions are fulfilled in my approach of inverting LP-events. Thus all moment tensor solutions which occur throughout this work are to be understood as *centroid moment tensors*.

2.2 Graphical representation of the seismic moment tensor - the focal sphere diagram

The description of seismic source mechanisms with the help of the seismic moment tensor is not only very convenient for the theoretical treatment of problems, it also has the benefit that most of the source mechanisms can be visualised in a very intuitive way, which allows for direct human interpretation. Besides some non-standard approaches (e.g. Neeman, 2004), the *focal sphere diagram* is the most common method to illustrate source mechanisms. It is based on a virtual sphere around the source point – the *focal sphere* – on whose surface the sign of the pressure signal stemming from the source mechanism at this point is visualised.

This graphical representation is called *focal sphere diagram*, due to its shape it is sometimes referred to as *beachball diagram*. Its generation is described in (Riedesel and Jordan, 1989; Udıas, 1999; Krieger and Heimann, 2011). In the following, I illustrate its definition with two sketches that show the systematics of a focal sphere diagram. In addition I present some example plots for different source types to clarify the systematics.

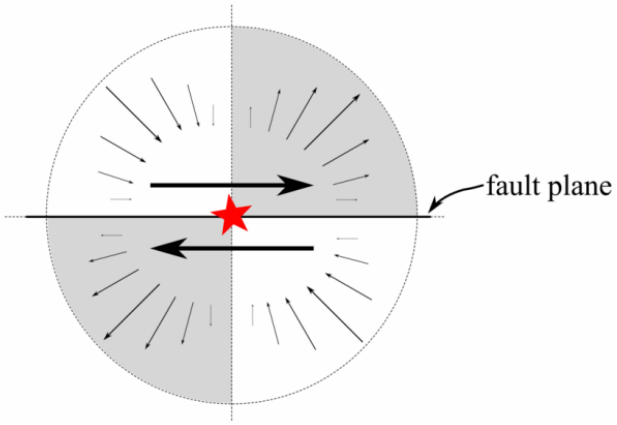

Figure 2.4:
Two dimensional vertical cross section through a medium. It sketches a horizontal fault plane, approximated as a point source. Small arrows show the pressure signal of the source. The dashed circular line defines the focal sphere. Its colouring is defined by the radial sign of the pressure signal: dark colour denotes positive pressure in outwards direction.

In figure 2.4, a horizontal rupture plane is sketched in a vertical cross sectional view. The source is interpreted as a point source. The sign of the P-wave signal that is generated by this source is called *P-wave radiation pattern*. Although in most cases it is represented in two dimensions, it is a three dimensional characteristic of the source mechanism. A virtual sphere is set around the source point. On the surface of this sphere there are distinct connected areas which represent the radiation pattern: the parts of the surface in which the P-wave signal points radially outwards (compression signal) and inwards

(dilatation signal) respectively. These areas are uniquely coloured with respect to the polarity of the P-wave signal.

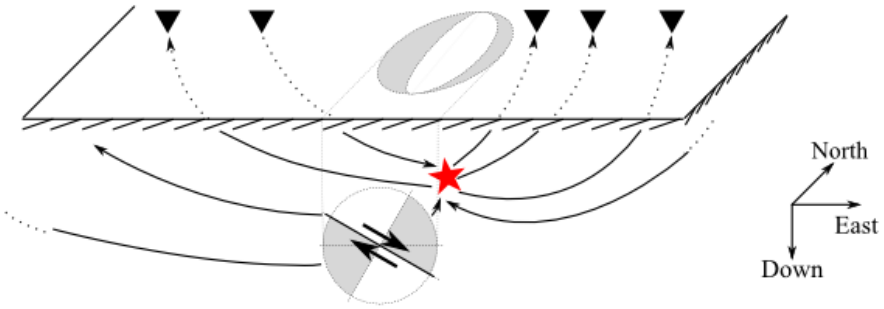

Figure 2.5:
The 3-dimensional sketch of a subsurface fault mechanism with strike 0°, dip $30°$, and slip-rake $-90°$. The source location is marked by the red star. The emitted signals including their polarities are indicated by bent arrows. Seismic stations are denoted by black triangles. The focal sphere is projected in two ways: Below it is shown in the vertical back-projection in the two dimensional cross section. Above, the planar horizontal mapping of the lower hemisphere of the focal sphere is shown in the North-East plane. In both cases the colouring shows the P-wave signals' onset polarities (dark colouring marks areas of compressional polarity).

In figure 2.5 the principle of a focal sphere diagram at a buried seismic source is shown. The source represents a dip-slip shear crack and it can be seen directly from the focal sphere plot, which are the onset polarities of the P-wave signal arriving at the seismic stations. In the most common application for this construction of a illustration of the source mechanism, a two dimensional projection of the focal sphere diagram onto a horizontal surface is used. The basis for the projection is a viewpoint vertically above the source. In such a view most commonly the lower hemisphere of the focal sphere is plotted in a standard planar mapping. This is the standard graphical representation of a seismic source on geographical maps.

An example for this projection is also shown in the upper part of figure 2.5. The choice of visualising the lower hemisphere of the focal sphere accommodates the fact that most observations from regional and tele-seismic earthquakes are from rays leaving the source downwards. In accordance to this setup, most focal sphere diagrams show the projection of the back-hemisphere of the sphere, also if the setup does not contain the vertical view on the projection surface.

I present three examples of focal sphere diagrams to clarify their orientation, as well as the interrelation of moment tensor entries and the respective visualisation.

Figure 2.6 shows a shear crack that represents oblique faulting. The visualisation of a pure CLVD is shown in figure 2.7, and a composite source mechanism is illustrated in 2.8; the overall mechanism is a combination of a shear-, a CLVD-, and an explosive

source in arbitrary orientations. The basis system of the provided moment tensors is (*North, East, Down*). The orientation of the plots follows the geographical orientation: *North* is pointing upwards, *East* to the right. The *Down* is located at the center of the plots, because the lower hemispheres are projected. All plots in figures 2.6 to 2.8 use standard stereographic projection. They have been generated with *MoPaD* (Krieger and Heimann, 2011).

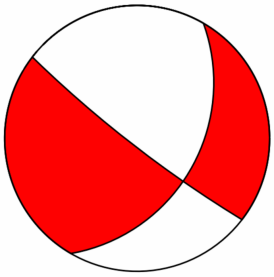

Figure 2.6:
Example of a focal sphere diagram. The source mechanism is a shear crack with the parameters strike: 30°, dip: 40°, slip-rake: −30°. Red denotes the tensional area.

$$\mathbf{M} = \begin{pmatrix} -36 & 7 & -53 \\ 7 & 85 & -41 \\ -53 & -41 & -49 \end{pmatrix}$$

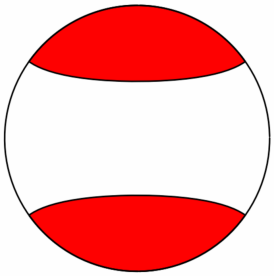

Figure 2.7:
Example of a focal sphere diagram. The source mechanism is a compensated linear vector dipole (CLVD) in North-South orientation.

$$\mathbf{M} = \begin{pmatrix} 2 & 0 & 0 \\ 0 & -1 & 0 \\ 0 & 0 & -1 \end{pmatrix}$$

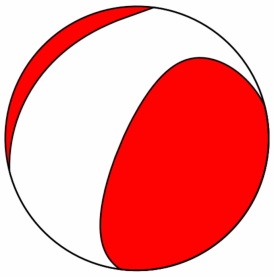

Figure 2.8:
Example of a focal sphere diagram. The source mechanism is an arbitrary combination of shear- (37.4%), CLVD- (49.6%), and explosive isotropic (13%) components.

$$\mathbf{M} = \begin{pmatrix} 1 & -4 & -5 \\ -4 & 2 & 10 \\ -5 & 10 & 3 \end{pmatrix}$$

3 Green's functions

One vital point in the structure of the inversion algorithm developed in this thesis is the application of a pre-calculated database of Green's functions (GFs). This chapter is dedicated to the introduction of the general ideas of this method. Although no new methods or concepts will be developed in this chapter, it seems meaningful to provide a collection[1] of the properties of GFs in a consistent notation and structure.

Including the formal definition, I will show how seismic data traces generated by acting forces inside a medium can be described using GFs. This concept will be expanded to the description of *double-couples* of rotational moments, which will lead to a complemental and more formal definition of the seismic moment tensor. The handling of the time dependency of the GFs will be shown and the usage of elementary seismograms will be illucidated. Finally I will give a short overview of the handling of GFs within the *ARCTIC* software.

3.1 Theory of Green's functions and elementary seismograms

In this section I give a short review on the development and application of GFs. Unfortunately the nomenclature in available literature is non-unique, therefore I define a consistent terminology to avoid misunderstandings.

3.1.1 General background

The general concept of GFs has been developed to describe and derive fundamental solutions for linear differential equations (e.g. Jackson and Fox, 1999). The Green's function G^* is defined by

$$\mathcal{L}\{G^*(x)\} = \delta(x)\,, \tag{3.1}$$

where $\mathcal{L}$ is an arbitrary linear differential operator, which describes the evolution of the system under consideration. The x is an arbitrary variable, and the δ denotes the Dirac distribution (Bronstein et al., 1989). Thus the respective GFs are implicitly defined, if a problem can be formulated by an essential differential equation.

Assuming now that the G^* exists, one may find the general solution $y(x)$ for an arbitrary excitation of the system of equation (3.1) by a simple convolution. This is shown in the following for an arbitrary system-exciting right hand side $f(x)$:

$$\mathcal{L}\{y(x)\} = f(x)\,. \tag{3.2}$$

[1] following mainly (Lay and Wallace, 1995; Aki and Richards, 2002; Stein and Wysession, 2003)

Since

$$f(x) * \mathcal{L}\{G^*(x)\} = \mathcal{L}\{G^*(x) * f(x)\} \tag{3.3}$$

and

$$\delta(x) * f(x) = f(x) \tag{3.4}$$

hold, one can convolve both sides of equation (3.1) with the $f(x)$

$$\mathcal{L}\{G^*(x)\} * f(x) = \delta(x) * f(x)\,, \tag{3.5}$$

and obtains the final solution $y(x)$ as

$$y(x) = G^*(x) * f(x)\,. \tag{3.6}$$

The above derivation illustrates the two main features of the GFs: they are a theoretical construction based upon the assumption of singular ("impulsive") input, and their knowledge enables the solution of eq. (3.2) for any arbitrary source function.

The second property makes for the frequent application of this concept for the solution of physical problems. In the framework of seismology, the GFs represent the transfer properties of the Earth in the sense that a variable source (an earthquake) leads to a determined measurable temporal function at a distinct spatial location (seismogram). In most cases, an exact determination of the GFs cannot be achieved, because the differential equations are not solvable analytically, but only numerically. Additionally, neither a perfect impulsive source can be generated, nor are the numerical solutions for the differential equations perfectly accurate. This has always to be kept in mind when handling Green's functions.

Focussing on the application to two- and three-dimensional problems in this thesis, the concept of GFs is sketched in figures 3.1 and 3.2. In figure 3.1 an impulsive source and the propagation of the resulting seismic waves to two seismic stations are shown. The medium is homogeneous to the left side of the source location and layered to the right. Figure 3.2 shows the temporal evolution of the source signal and the signals as observed at the stations 1 and 2. Already in this simple case one can see that the structure of the inner medium is contained and imaged in the observed data. The traces shown in 3.2 represent Green's functions for this specific geometric setup. It is clear that they are functions in time, as well as in space. For better understanding, these GF are denoted by $\tilde{G}(\boldsymbol{x}, \boldsymbol{\xi}; t, t_0)$ from now on. The $\boldsymbol{\xi}$ is the source location, the $\boldsymbol{x}$ is the position of the recording. The time variable is t, and the source time is given by t_0.

Fortunately, assuming that the media which are penetrated by the signals are not changing significantly during the signal's runtime, the time dependence of the functions can be reduced to the relative source time. Hence one is only interested in the time span Δt defined by the start t_0 of the impulsive source and observation time t:

$$\tilde{G}(\boldsymbol{x}, \boldsymbol{\xi}; t, t_0) = \tilde{G}(\boldsymbol{x}, \boldsymbol{\xi}; \Delta t) \quad , \quad \Delta t := t - t_0\,. \tag{3.7}$$

Nevertheless, within this theory chapter, the time dependence of the GFs will be explicitly stated for a better understanding of the systematics.

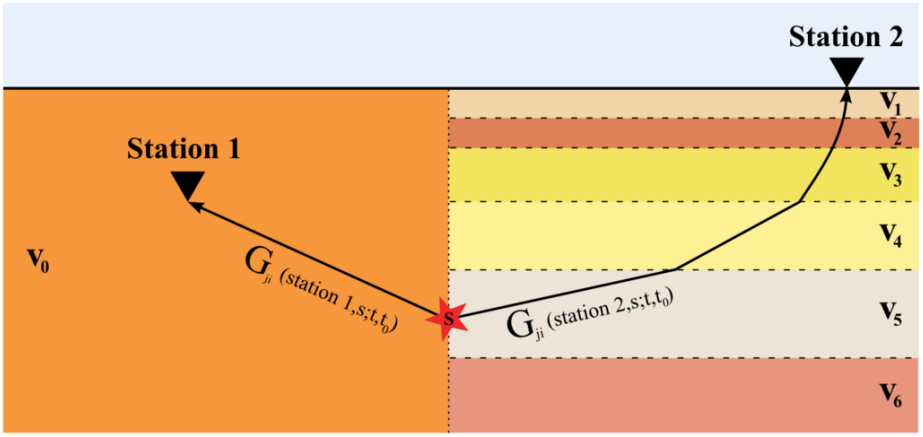

Figure 3.1:
Sketch of the propagation of seismic signals from a source s inside a medium (red star). The medium is homogeneous to the left and layered to the right. The arrows represent the signal paths from the source to the respective station, described by the Green's functions G (reflected and converted parts of the complete signal to the right side are not plotted explicitly). All effects of the medium's structure are contained in the Green's functions.

3.1.2 The reciprocity of Green's functions

From a theoretical point of view, a dynamical problem is solved, if only the GFs are known. However, the direct forward computation of the GFs for real seismic data inversion problems requires a too high numerical and computational effort for many practical applications. So a very important property of the GFs proves beneficial: the GFs show symmetry with respect to their arguments:

$$\tilde{G}_{ji}(\boldsymbol{x}, \boldsymbol{\xi}; t, t_0) = \tilde{G}_{ij}(\boldsymbol{\xi}, \boldsymbol{x}; -t_0, -t)\,. \tag{3.8}$$

This feature is called *reciprocity* of the GFs (Knopoff and Gangi, 1959; Aki and Richards, 2002). It means that GFs for a pair of spatial components $\boldsymbol{x}$ or $\boldsymbol{\xi}$ can be expressed by GFs with exchanged spatial and temporal indices after their complete calculation.

In the setup of a grid search for several possible source positions, one is in need of a huge dataset, that contains information of many source locations but a limited number of receiver coordinates. Unfortunately, numerical codes for the generation of GFs are mainly capable of the opposite behaviour: they model the forward propagation of a seismic signal from some defined source, that is fixed in position and mechanism. These codes calculate a seismic signal for every time (step) on every position (potential receiver position) on their numerical grid, this is shown in figure 3.3.

The concept of reciprocity allows for transforming the output of these codes into the desired datasets by defining given receiver coordinates as source points and using the dense grid of "receivers" as a set of possible source points for a grid search. This is

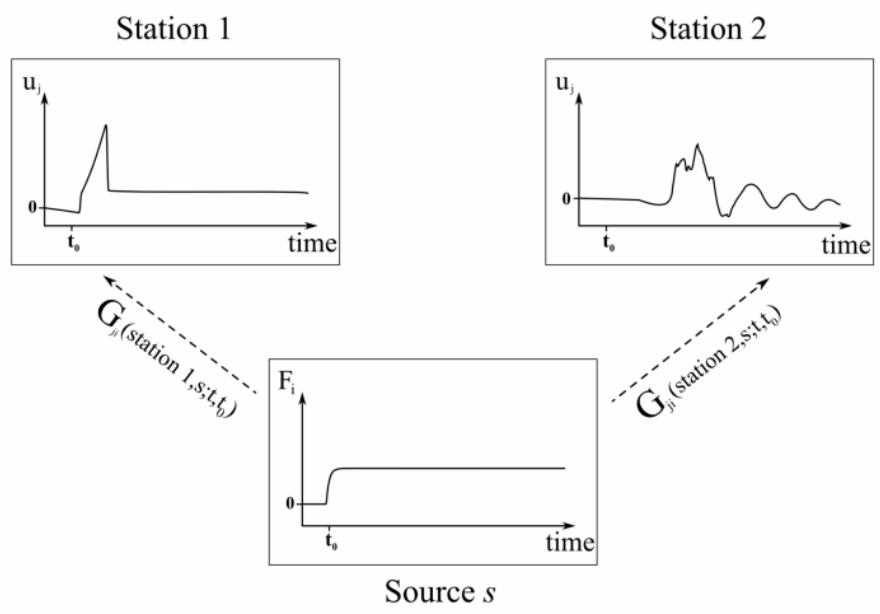

Figure 3.2:
Schematic explanation of the temporal evolution of the signals at the source s and stations 1 and 2 in figure 3.1. The source is characterised by a step like excitation at some source time t_0. The synthetic displacement signals at the stations follow retarded in accordance to the waves' travelling time. The two time traces of the stations signals mirror the complexity of the structure of the medium, the seismic waves have passed through.

illustrated in figure 3.4. By making use of this concept, single CPU computers are capable of generating a set of GFs for a real data application.

3.1.3 Single forces excitation

The source f of the signal described by the solution y of the differential equation (3.2) can be any well-defined function from a purely mathematical point of view. For physical problems, the source function is in the majority of cases the temporal evolution of a force, driving a temporally and spatially dynamic system. For setting up a consistent framework, the impulsive right hand side in (3.1) must be accordingly defined in units of a force. In (Burridge and Knopoff, 1964) the authors show that the use of the term *force* is justified, since one can describe every dislocation source with the help of *body force equivalents*, which have the same temporal evolution as the dislocation itself. By this we know additionally that if we continue to describe our seismic sources by means of impulsively acting forces, we have to consider the *Heaviside step function* $\Theta(t)$ (see eq. (3.27)) as the source time function and not a *delta-peak* like function, as one would assume due to the phrasing "impulsive". All mentions of the term *force* in the scope of this work are referring to *body force equivalents*.

In the standard terminology within seismology (c.f. Aki and Richards, 2002, ch. 4),

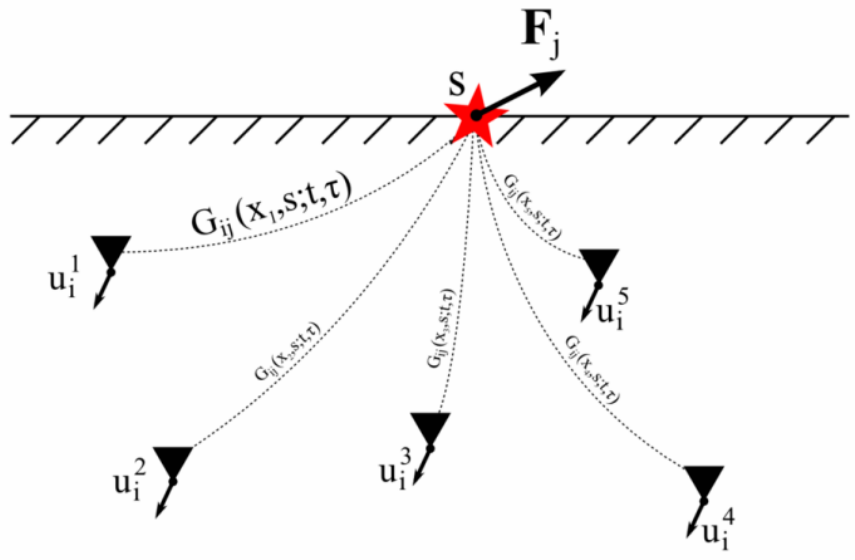

Figure 3.3:
Applying the principle of reciprocity of the Green's functions G, step 1. The point S is the desired position of the station in the later application, thus here it is the location of a single force impact in j-direction as the seismic source. Signals of this source are recorded at points 1 to 5 on the i-components.

the desired solution function y is the observational displacement $\boldsymbol{u}_j(\boldsymbol{x_0}, t)$ of the Earth in j-direction at position $\boldsymbol{x_0}$ and time t. The GFs are defined with respect to a single force $\boldsymbol{F}_i(\boldsymbol{\xi}, t_0)$ in i-direction at a source location $\boldsymbol{\xi}$ at the time t_0. An index is given to the GF for the spatial orientations of both signal and source, the GFs are labelled $\tilde{G}_{ji}$. Therewith the description of a seismic signal by means of a GF is given by the simple (yet important) equation

$$\boldsymbol{u}_j(\boldsymbol{x_0}, t) = \tilde{G}_{ji}(\boldsymbol{x}, \boldsymbol{\xi}; t, t_0) * \boldsymbol{F}_i(\boldsymbol{\xi}, t_0)\,. \tag{3.9}$$

The respective GFs contain implicit information about parameters of the medium, mainly density $\rho(\boldsymbol{x})$, damping $Q(\boldsymbol{x})$, and stress-strain relation $\boldsymbol{C}_{klmn}$ (Udıas, 1999). For all practical purposes in seismology, the Green's functions, imaging the complex interior of the Earth, are obtained by numerical algorithms!

Only in few approximative and theoretical cases the respective GF can be calculated analytically. One example is the wave propagation through a homogeneous, isotropic medium, like the signal path for station 1 in figure 3.1 (e.g. Udıas, 1999, chs. 2 and 16):

$$\begin{aligned}\tilde{G}_{ji}(\boldsymbol{x}, \boldsymbol{\xi}; t, t_0) = \frac{1}{4\pi\rho} \Bigg[& \frac{1}{r^3}(3\gamma_i\gamma_j - \delta_{ij}) \int_{r/v_P}^{r/v_S} \tau\delta(t-\tau)\,\mathrm{d}\tau + \dots \\ & \dots + \frac{1}{rv_P^2}\gamma_i\gamma_j\delta(t - r/v_P) - \frac{1}{rv_S^2}(\gamma_i\gamma_j - \delta_{ij}\delta(t - r/v_S)) \Bigg]\,,\end{aligned} \tag{3.10}$$

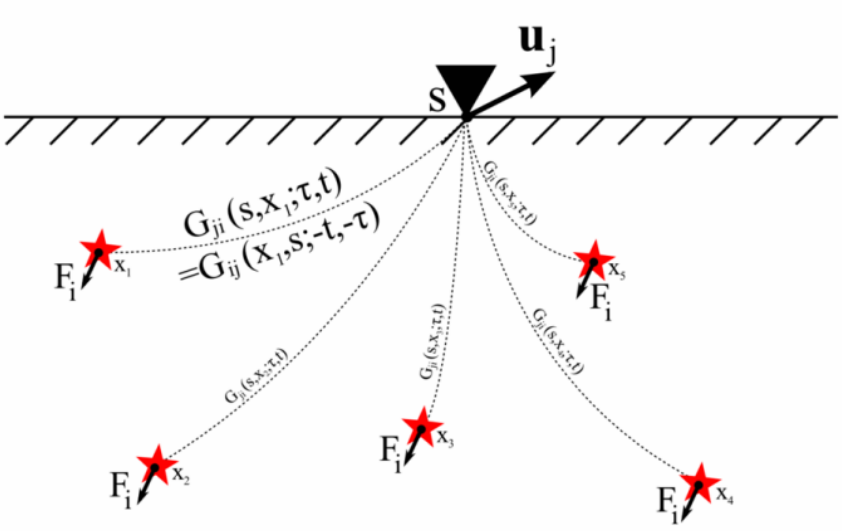

Figure 3.4:
Applying the principle of reciprocity of the Green's functions G, step 2. The desired Green's functions G follow from the interchange of source and station locations and components, as well as from the flipping of time axis.

with $r = |\boldsymbol{x} - \boldsymbol{\xi}|$, $t_0 = 0$, $\delta(t)$ as the Dirac delta distribution, and δ_{ij} the Kronecker symbol. The γ_i are the projections onto basis elements $\{\boldsymbol{e_1}, \boldsymbol{e_2}, \boldsymbol{e_3}\}$ of the $\mathbb{R}^3$, also called *direction cosines*:

$$\gamma_i = \frac{\langle \boldsymbol{x}, \boldsymbol{e_i} \rangle}{||\boldsymbol{x}|| \cdot ||\boldsymbol{e_i}||} = \cos(\angle(\boldsymbol{x}, \boldsymbol{e_i}))\,. \tag{3.11}$$

The seismic velocities v_P, v_S contain structural information in terms of the Lamé-parameters λ and μ:

$$v_P = \sqrt{\frac{\lambda + 2\mu}{\rho}} \qquad \text{and} \qquad v_S = \sqrt{\frac{\mu}{\rho}}\,. \tag{3.12}$$

The formulation of equation (3.9) describes a theoretically valid solution of an abstract differential equation for the basic assumption of a single, directed force as the source mechanism. Earthquakes are described by generalised force dipoles. Single forces as seismic sources may only occur, if their oppositely directed counterpart does not have any contribution to the observed signal by means of the geometry, e.g. for some volcanic events, where the counteracting part of the force can be distributed into the free air, or in case of active seismic experiments. According to this argumentation, the standard seismic source is described in a different way, which will be described in the next section.

3.1.4 The seismic moment and spatial derivatives of the Green's functions

As mentioned before, only on very rare occasions a seismic source is composed of unilateral single forces. In this section I concentrate on earthquakes, which mainly appear

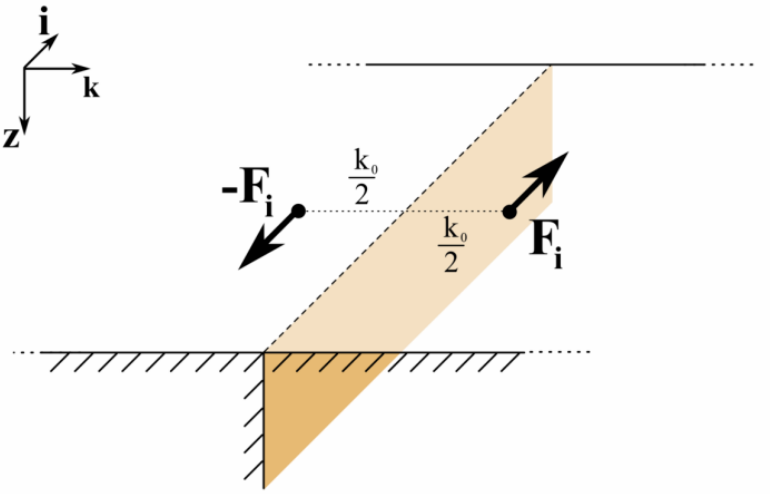

Figure 3.5:
Sketch of a horizontal sinistral strike-slip shear in i-direction on a vertical fault plane caused by a force couple $\pm\mathbf{F}_i$.

as shear cracks. These are intuitively described by a couple of forces rather than only a single one, as may be obvious when looking at figure 3.5. Although not explicitly stated, the values of force and moment as introduced here still show a time dependency; the respective argument of the functions is omitted for better readability in this section.

The forces of this couple have the distance $\frac{k_0}{2}$ in $\boldsymbol{k}$-direction from the rupturing surface; the tuple $(\boldsymbol{F}_i, \frac{k_0}{2} \cdot \boldsymbol{e_k})$ with $\boldsymbol{e_k}$ being a unit vector of the $\mathbb{R}^3$ in k-direction defines a rotational moment (torque) $\tilde{M}_{ik}$:

$$\tilde{M}_{ik} = \boldsymbol{F}_i \times \frac{k_0}{2} \boldsymbol{e_k} \,. \tag{3.13}$$

From equation (3.9) it follows that the j-component of the signal $\boldsymbol{u}$ resulting from the force couple is given by

$$\begin{aligned} \boldsymbol{u}_j(\boldsymbol{x}, t) = \tilde{G}_{ji}(\boldsymbol{x}, \boldsymbol{\xi_0} + \frac{k_0}{2}\boldsymbol{e_k}; t, t_0) * \boldsymbol{F}_i(\boldsymbol{\xi_0} + \frac{k_0}{2}\boldsymbol{e_k}, t_0) - \\ - \tilde{G}_{ji}(\boldsymbol{x}, \boldsymbol{\xi_0} - \frac{k_0}{2}\boldsymbol{e_k}; t, t_0) * \boldsymbol{F}_i(\boldsymbol{\xi_0} - \frac{k_0}{2}\boldsymbol{e_k}, t_0) \,. \end{aligned} \tag{3.14}$$

To describe a spatial point source rather than a spatially separated force couple, I take the limit process of vanishing lever arm length in the force dipole $k_0 \to 0$, whereupon the absolute moment is kept constant. This yields the dipole

$$M_{ik} := \lim_{\substack{k_0 \to 0 \\ M_{ik}=\text{const}}} 2 \cdot \tilde{M}_{ik} = \lim_{\substack{k_0 \to 0 \\ M_{ik}=\text{const}}} \boldsymbol{F_i} \times k_0 \boldsymbol{e_k} \,. \tag{3.15}$$

The $\boldsymbol{u}$ originating from this dipole source mechanism is

$$\begin{aligned}\boldsymbol{u}_j(\boldsymbol{x},t) = \lim_{\substack{k_0\to 0\\ M_{ik}=\text{const}}} \Big[&\tilde{G}_{ji}(\boldsymbol{x},\boldsymbol{\xi_0}+\frac{k_0}{2}\boldsymbol{e_k};t,t_0) * \boldsymbol{F}_i(\boldsymbol{\xi_0}+\frac{k_0}{2}\boldsymbol{e_k},t_0) - \\ &-\tilde{G}_{ji}(\boldsymbol{x},\boldsymbol{\xi_0}-\frac{k_0}{2}\boldsymbol{e_k};t,t_0) * \boldsymbol{F}_i(\boldsymbol{\xi_0}-\frac{k_0}{2}\boldsymbol{e_k},t_0)\Big] \,, \\ = \lim_{\substack{k_0\to 0\\ M_{ik}=\text{const}}} &\left[\left(\tilde{G}_{ji}(\boldsymbol{x},\boldsymbol{\xi_0}+\frac{k_0}{2}\boldsymbol{e_k};t,t_0) - \tilde{G}_{ji}(\boldsymbol{x},\boldsymbol{\xi_0}-\frac{k_0}{2}\boldsymbol{e_k};t,t_0)\right) * \frac{1}{k_0}M_{ik}(\boldsymbol{\xi_0},t_0)\right] \\ = &\frac{\partial}{\partial \boldsymbol{e_k}}\tilde{G}_{ji}(\boldsymbol{x},\boldsymbol{\xi_0};t,t_0) * M_{ik}(\boldsymbol{\xi_0},t_0) \,, \\ = &\tilde{G}_{ji,k}(\boldsymbol{x},\boldsymbol{\xi_0};t,t_0) * M_{ik}(\boldsymbol{\xi_0},t_0) \,,\end{aligned} \tag{3.16}$$

where the derivative $\tilde{G}_{ji,k}$ must be continuous in a surrounding of $\boldsymbol{x_0}$, and $\boldsymbol{e_k}\perp\boldsymbol{e_i}$. The latter is assumed to hold, since this action of a rotational moment dipole describes a shearing strain.

If this strain causes a structural failure of the medium, a local displacement on a rupture surface of area A_Σ occurs as a spatial discontinuity in the ik-plane. The two fronts of this shearing plane are mutually displaced by the mean distance $\overline{\Delta d}$. Following (Gilbert, 1971; Randall, 1971), the seismic moment M_{ik} is equivalently described by the slip vector $\boldsymbol{s}$ on the rupture plane and the vector normal to the plane $\boldsymbol{n}$:

$$M_{ik} = \mu A_\Sigma \overline{\Delta d} = \mu A_\Sigma (s_k \cdot n_i + s_i \cdot n_k) \,, \tag{3.17}$$

where μ is the shear modulus of the medium. The M_{ik} is to be identified with the entries of the seismic moment tensor $\mathbf{M}$ as introduced in section 2.1.1. Note the symmetry between the interchangeable components i and k, which reflects the non-uniqueness of the definition of the rupture plane orientation; this effect is discussed in the following section.

For a single shear event, the absolute value of M_{ik} directly represents the strength of this event, expressed by the scalar seismic moment $M_0 = M_{ik}$. For more complex source mechanisms, all contributions of the respective cracks must be summed up to M_0. The general formula for the scalar seismic moment M_0 of an arbitrary moment tensor $\mathbf{M}$ is given by equation (2.8). This scalar seismic moment can be transformed into a comparable event moment magnitude M_w by (Kanamori, 1977):

$$M_w = \frac{2}{3}\log_{10}(M_0 \cdot 10^7/\text{Nm}) - 10.7 \,. \tag{3.18}$$

3.1.5 Force double-couples and the symmetric seismic moment tensor

Unlike the former more or less obvious steps, it may not seem very clear that even this extended description of the source mechanism is not sufficient. But let's assume, a shear crack could be simply described by only one couple of two forces as stated above. This again would induce a net torque (artificial/spurious static angular momentum) onto the medium, that would cause a resulting change of tension in the vicinity of the source location. Such a torque and its consequences are not observable in reality (Aki and Richards, 2002; Stein and Wysession, 2003).

Not only this obvious contradiction, but also the fact that seismic signals show a geometric symmetry that is more likely related to a quadrupole source rather than a single dipole calls for a revised model: The source model is extended one step further from a pair of forces. The source is described by a combination of two perpendicular shear cracks: a net torque free *double-couple*. This implies that no shear crack resulting from a source moment M_{ik} can exist without its symmetric counterpart that belongs to the source mechanism M_{ki} of same strength as shown in figure 3.6. Following this path,

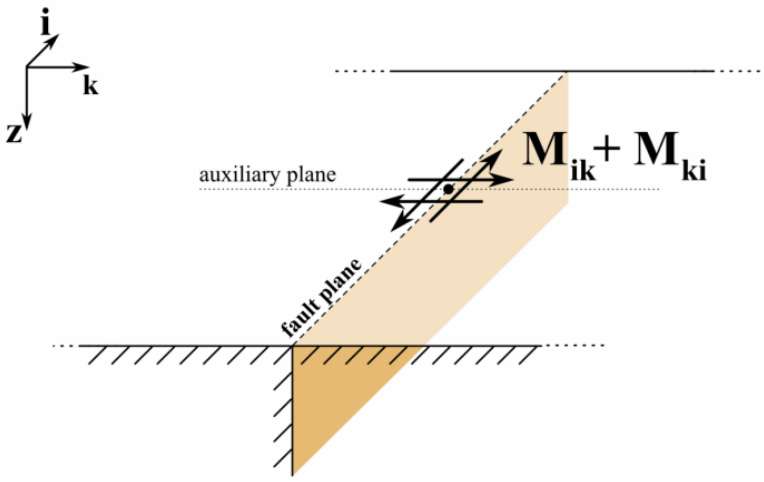

Figure 3.6:
Sketch of a horizontal sinistral strike-slip shear in i-direction on vertical fault plane caused by a force double-couple, which is acting as a combination of two torques at the centre point (black dot). The symmetry causes an ambiguity of the fault plane's orientation, illustrated by the auxiliary plane.

one obtains

$$M_{ik} = M_{ki} \quad \forall\, i,k \in \{1,2,3\}\,, \tag{3.19}$$

and by this the number of independent entries of $\mathbf{M}$ reduces from nine to six.

The evidence of the symmetry of the seismic moment tensor is hitherto derived only theoretically. Following this concept means that every shear crack – and so every earthquake – can solely be described by defining two slipping surfaces rather than a single surface. However, only one crack forms during a real shear displacement in the medium.

The surface in orientation of the crack is called *fault plane*; the perpendicularly orientated plane, which theoretically would yield the same seismic signals, is named *auxiliary plane* (as labelled in figure 3.6). Both planes cannot be separated by the exclusive analysis of seismic signals in case of a pure shear crack event; additional information is needed for their final discrimination.

For the sake of further convenience, I introduce a mapping from the space of the symmetric matrices $\mathbb{M}^{\text{sym}}$ to the $\mathbb{R}^6$, accommodating the aforementioned symmetry:

$$\mathbb{M}^{\text{sym}}_{3\times 3}(\mathbb{R}) \rightarrow \mathbb{R}^6 \quad , \quad \mathbf{M} \mapsto \mathbf{M}^* = (M_{11}, M_{22}, M_{33}, M_{12}, M_{13}, M_{23})\,. \tag{3.20}$$

According to this bijection, $\mathbf{M}$ and $\mathbf{M}^*$ are identified; they are used synonymously from now on. This identification will be used for the scope of this work, $\mathbf{M}$ will be used symbolically for matrix- and vector-notation. The ordering of the indices is the same in all cases. Taking into account the doubled entries of $\mathbf{M}$ due to the symmetry, this factor has to be included in an appropriate transformation of $\tilde{\mathbf{G}}$:

$$\boldsymbol{u}_j(\boldsymbol{x}, t) = \sum_{i,k=1}^{3} \tilde{G}_{ji,k} * M_{ik} = \sum_{k_*=1}^{6} \bar{G}_{jk_*} * M_{k_*}\,, \tag{3.21}$$

$$\bar{G}_{jk_*} = \begin{cases} 2 \cdot \tilde{G}_{ji,k} & \forall\ k_* = i \ \wedge\ i \neq k \\ \tilde{G}_{ji,i} & \text{else} \end{cases}\,. \tag{3.22}$$

From now on, the methodological setup for defining an arbitrary source of seismic data is available. In most cases, a description by a linear combination of seismic moments in directions of an arbitrary basis of the $\mathbb{R}^3$ is appropriate. For generating seismic signals from this basis representation, equation (3.16) is adapted by adding a summation over all moment tensor components:

$$\boldsymbol{u}_j(\boldsymbol{x}, t) = \sum_{i=1}^{6} \bar{G}_{ji}(\boldsymbol{x}, \boldsymbol{\xi_0}; t, t_0) * M_i(\boldsymbol{\xi_0}, t)\,. \tag{3.23}$$

If the action of isolated single force components is considered in the source mechanism, the latter relation is extended to

$$\boldsymbol{u}_j(\boldsymbol{x}, t) = \sum_{i=1}^{6} \bar{G}_{ji}(\boldsymbol{x}, \boldsymbol{\xi_0}; t, t_0) * M_i(\boldsymbol{\xi_0}, t) + \sum_{i=1}^{3} \tilde{G}_{ji}(\boldsymbol{x}, \boldsymbol{\xi_0}; t, t_0) * F_i(\boldsymbol{\xi_0}, t)\,. \tag{3.24}$$

3.1.6 Time dependencies and elementary seismograms

So far I have described the static concept of the seismic moment tensor ignoring the time dependencies of all involved quantities. In the majority of cases, the time dependence of

$\mathbf{M}$ can be set to be equal for all components

$$\mathbf{M}(t) = (M_{11}, M_{22}, M_{33}, M_{12}, M_{13}, M_{23}) \cdot \mathrm{stf}(t)\,, \tag{3.25}$$

with some general *source time function* $\mathrm{stf}(t)$ including the temporal evolution (Aki and Richards, 2002; Stein and Wysession, 2003). All source descriptions in this work are reduced to an approximated seismic point source by the definition of the centroid in section 2.1.2.2. Thus the event durations *rupture time* (total duration of movement in the source volume) and *rise time* (duration of movement of a single point inside the source volume), which are different in case of a finitely extended source volume, cannot be separated.

For any practical purposes, the theoretical calculation of the Green's functions and their generation itself should not become an issue. Following section 3.1.4, it is clear that for a description of a seismic trace only combinations of spatial derivatives of the GFs are needed. So in the following I show how the GFs are transformed into functions (*elementary seismograms*), which can be directly convolved (or even just multiplied) with the respective moment tensor entries or single force components, which on their part describe an arbitrary seismic source.

Following equations (3.23) and (3.25), a seismic displacement signal component $\boldsymbol{u}_j$ is obtained by:

$$\begin{aligned} \boldsymbol{u_j}(\boldsymbol{x}, t) &= \sum_{i=1}^{6} \bar{G}_{ji}(\boldsymbol{x}, \boldsymbol{\xi_0}; t, t_0) * M_i(\boldsymbol{\xi_0}, t) \\ &= \sum_{i=1}^{6} \left[\bar{G}_{ji}(\boldsymbol{x}, \boldsymbol{\xi_0}; t, t_0) * \mathrm{stf}(t)\right] \cdot M_i(\boldsymbol{\xi_0})\,. \end{aligned} \tag{3.26}$$

This provides a simple possibility to construct a seismic signal for a source described by $\mathbf{M}$, as long as $\bar{\mathbf{G}}$ and $\mathrm{stf}(t)$ are known. One standard approach for modelling the latter in numerical programs for the generation of GFs is given by the temporal development, which one naturally expects for the displacement at the source location:

$$\mathrm{stf}(t) = \Theta(t) := \begin{cases} 1 & \text{if} \quad t \geq 0 \\ 0 & \text{else} \end{cases}\,. \tag{3.27}$$

Thus $\boldsymbol{u}$ is expressed by

$$\begin{aligned} \boldsymbol{u}_j(\boldsymbol{x}, t) &= \sum_{i=1}^{6} \underbrace{\left[\bar{G}_{ji}(\boldsymbol{x}, \boldsymbol{\xi_0}; t, t_0) * \Theta(t)\right]}_{=:\boldsymbol{G}} \cdot M_i \\ &= \sum_{i=1}^{6} G_{ji}(\boldsymbol{x}, \boldsymbol{\xi_0}; t, t_0) \cdot M_i\,. \end{aligned} \tag{3.28}$$

The **G** is implicitly defined in this juncture, its entries are basis functions, which are summed and weighted by the entries of **M**. For each source described by an M_i, they consist of the respective measurable signal at the seismic station component j. These functions of time and space are called *elementary seismograms*. For all practical purposes in the further scope of this work, I will use them instead of the "pure" Green's functions. Since the G_{ji} likewise provide a system's answer to an impulsive source, I will refer to these functions as Green's functions as well for the rest of this thesis. Consistently, they are (yet virtually) arranged in a multi-dimensional array, which I will denote with *Green's tensor* **G** from now on. Although not necessarily holding the transformation properties of a tensor, the denotation is chosen for convenience.

By introducing the elementary seismograms **G** instead of the GFs, and using equation (3.28) we obtained a simple algorithm for describing the displacement signal, which is generated by a spatial and temporal point source. The latter is a low order approximation for a real seismic source defined by an arbitrary seismic moment tensor (Backus and Mulcahy, 1976a). This is valid as long as the dominating wavelengths of the considered signals are significantly larger than the spatial extensions of the source volume, and the signals periods are outweighing the rupture time of the event (the time interval of actual movement within the source volume). Within this work, these assumptions hold in most cases due to the focus on LP-events (chapter 1)

If the temporal evolution of a seismic source cannot be satisfactorily described by the aforementioned approximation, it is necessary to include the influence of the source time function in equation (3.28). The handling of such an alternative arbitrary source time function $\mathrm{stf}^{\mathrm{alt}}(t)$ will be explained in the following[2].

As a first step, we take the velocity signal $\boldsymbol{v}$ generated by an impulsive source. It can be expressed according to the former equations:

$$\boldsymbol{v}_j = \dot{\boldsymbol{u}}_j = \sum_{i=1}^{6} M_i \cdot \dot{G}_{ji}(t)\,. \tag{3.29}$$

This temporal derivative of the displacement signal can be further decomposed into[3]

$$\dot{G}_{ji}(t) = \dot{\Theta}(t) * \bar{G}_{ji}(\boldsymbol{x}, \boldsymbol{\xi_0}; t, t_0) = \delta(t) * \bar{G}_{ji}(\boldsymbol{x}, \boldsymbol{\xi_0}; t, t_0) = \bar{G}_{ji}(\boldsymbol{x}, \boldsymbol{\xi_0}; t, t_0)\,. \tag{3.30}$$

Furthermore we know, that the arbitrary source time function $\mathrm{stf}^{\mathrm{alt}}(t)$ results in a displacement signal $\boldsymbol{u}^{\mathrm{alt}}(t)$:

$$\boldsymbol{u}_j^{\mathrm{alt}}(\boldsymbol{x}, t) = \sum_{i=1}^{6} \mathbf{M}_i \cdot \mathrm{stf}^{\mathrm{alt}}(t) * \bar{G}_{ji}(\boldsymbol{x}, \boldsymbol{\xi_0}; t, t_0)\,. \tag{3.31}$$

[2] An overview over the notation can be found in appendix A.2

[3] Note that the step function Θ is not differentiable, so that its temporal derivative is only well defined in the sense of distribution theory!

And by a combination of equations (3.29), (3.30), and (3.31) we obtain

$$\boldsymbol{u}_j^{\mathrm{alt}}(\boldsymbol{x},t) = \mathrm{stf}^{\mathrm{alt}}(t) * \boldsymbol{v}_j \ . \tag{3.32}$$

Thus, the seismograms for every desired temporal source evolution can be modelled by the convolution of a given source time function with the temporal derivative of the elementary (displacement) seismograms from an impulsive source.

Assuming, the source time function for a given source region is known in advance, it is beneficial to include this information already in the Green's tensor:

$$\boldsymbol{u}_j^{\mathrm{alt}}(\boldsymbol{x},t) = \sum_{i=1}^{6} \mathbf{M}_i \cdot \underbrace{\mathrm{stf}^{\mathrm{alt}}(t) * \bar{G}_{ji}(\boldsymbol{x},\boldsymbol{\xi_0};t,t_0)}_{=:\check{G}_{ji}} \ . \tag{3.33}$$

Then the $\check{\mathbf{G}}$ is set as the array of elementary seismograms instead of the original $\mathbf{G}$. This method is applied in section 7.2.

Calculation of elementary seimograms using the principle of reciprocity

For a small number of combinations $\{(\boldsymbol{\xi_0},\boldsymbol{x}) \,|\, \boldsymbol{\xi_0} \in S \ , \ \boldsymbol{x} \in R\}$, the elementary seismograms $G(\boldsymbol{x},\boldsymbol{\xi_0})$ can be calculated directly by applying a well-defined source at numerical tools, which generate synthetic seismograms for a given Earth model. In later parts of this work, the calculation of $\mathbf{G}$ for an arbitrary large set of observation points and especially source locations is needed, so a grid search algorithm can be applied.

Although some numerical tools are able to do simultaneous calculations of synthetic seismograms at different observation points $\boldsymbol{x_n}$ induced by one single source point, this does not directly fit the needs of the mentioned setup with a large amount of source points. Here the GFs' property of reciprocity (s. section 3.1.2) proves beneficial. If the number of potential source points $|S|$ is larger than the number of observational locations, it may be advisable to carry out the numerical calculations of elementary seismograms for the inverted setup in the beginning. Afterwards the results are transformed in a way that the needed set of GFs is obtained.

Assuming a static Earth model, I may reduce the time dependency of $\mathbf{G}$ to one parameter (c.f. eq. (3.9)). Successively, single forces with unity amplitude

$$\boldsymbol{F}_j(t) = F_0 \cdot \boldsymbol{e}_j \cdot \Theta(t) \qquad , \qquad |F_0| = 1 \tag{3.34}$$

are applied at every observation point $\boldsymbol{x}$, and the respective synthetic seismograms $\boldsymbol{u}^{j,\boldsymbol{x}}(\boldsymbol{\xi})$ at the points $\boldsymbol{\xi} \in S$ are calculated

$$\boldsymbol{u}_i^{j,\boldsymbol{x}}(\boldsymbol{\xi},\Delta t) = \tilde{G}_{ij}(\boldsymbol{\xi},\boldsymbol{x},\Delta t) * \boldsymbol{F}_j(t) \ . \tag{3.35}$$

Since the convolution with the Heaviside function is equivalent to an integration, this can also be read as

$$\boldsymbol{u}_i^{j,\boldsymbol{x}}(\boldsymbol{\xi}, \Delta t) = \int_0^{\Delta t} \tilde{G}_{ij}(\boldsymbol{\xi}, \boldsymbol{x}, t')\,\mathrm{d}t' \ . \tag{3.36}$$

Applying now the reciprocity of $\tilde{G}_{ij}$, one obtains

$$\boldsymbol{u}_i^{j,\boldsymbol{x}}(\boldsymbol{\xi}, \Delta t) = \int_0^{\Delta t} \tilde{G}_{ji}(\boldsymbol{x}, \boldsymbol{\xi}, -t')\,\mathrm{d}t' \ . \tag{3.37}$$

The elementary seismograms for the non-interchanged setup ($\tilde{G}_{ji}(\boldsymbol{x}, \boldsymbol{\xi})$ for a force in i-direction) are obtained by

$$\tilde{G}_{ji}(\boldsymbol{x}, \boldsymbol{\xi}, \Delta t) = \frac{\partial}{\partial t} \boldsymbol{u}_i^{j,\boldsymbol{x}}(\boldsymbol{\xi}, -\Delta t)\,. \tag{3.38}$$

So one obtains a set of $\tilde{G}_{ji}$ which are defined on a finite source point grid. The final $\tilde{G}_{ji,k}(\boldsymbol{x}, \boldsymbol{\xi}, \Delta t)$ as spatial derivatives in k-direction at the respective source points $\boldsymbol{\xi}$ can be calculated by finite difference schemes on this grid (e.g. Conte and Boor, 1980; Moczo et al., 2004; Press et al., 2007).

For example assume a regular grid with a spacing Δd. Then the fourth order central finite difference approximation for the derivative yields

$$\begin{aligned}\tilde{G}_{ji,k}(\boldsymbol{x}, \boldsymbol{\xi}, \Delta t) \approx \frac{1}{\Delta d} \Bigg[\frac{2}{3} \cdot \Big(\tilde{G}_{ji}(\boldsymbol{x}, \boldsymbol{\xi} + \Delta d \cdot \mathbf{e_k}, \Delta t) - \tilde{G}_{ji}(\boldsymbol{x}, \boldsymbol{\xi} - \Delta d \cdot \mathbf{e_k}, \Delta t) \Big) - \\ - \frac{1}{12} \cdot \Big(\tilde{G}_{ji}(\boldsymbol{x}, \boldsymbol{\xi} + 2\Delta d \cdot \mathbf{e_k}, \Delta t) - \tilde{G}_{ji}(\boldsymbol{x}, \boldsymbol{\xi} - 2\Delta d \cdot \mathbf{e_k}, \Delta t) \Big) \Bigg] \ .\end{aligned} \tag{3.39}$$

3.1.7 The absolute size of the Green's tensor

As we know so far, Green's functions and elementary seismograms are generally time-dependent. Furthermore we know that they yield the medium's transfer function between a source point and a seismic station's location.

In the developed algorithm (*ARCTIC*), the source point position is determined by a grid search on a source point grid. In case of such a grid search for an unknown source location, an appropriate set of GFs has to be defined. Every point on the grid may be interpreted as a potential source point, and, in addition, fixed locations for seismic stations are given. Each channel of the stations is interpreted as a single station itself. No further restrictions with regard to the seismic moment tensor apply beforehand, so all six components must be taken into account.

For any arbitrary source-station-combination, the GF is a continuous function of time. Within the numerical handling, these traces must be suitably sampled. In the sampling process we face a trade off between the suppression of aliasing-effects and potentially too

high numerical costs. The numerical time steps depend firstly on the frequency boundaries of the LP-signals under consideration in the observed data, and secondly on the wavelengths of the signals which reflect only structures one is interested in and suppresses statistical noise.

The total number of GFs $\mathcal{N}_{GF}$ that is needed for carrying out a grid search is given by

$$\mathcal{N}_{GF} = \mathcal{N}_s \cdot \mathcal{N}_r \cdot 6 \text{ (components of } \mathbf{M}) \cdot 3 \text{ (channels)} \ , \tag{3.40}$$

with $\mathcal{N}_s$ potential source points on the grid and $\mathcal{N}_r$ stations. The memory *mem*, needed to handle this amount of data is

$$mem = \mathcal{N}_{GF} \cdot \text{trace length in } s \cdot \text{sampling rate} \cdot 4 \text{ byte per sample} \, . \tag{3.41}$$

Taking a look at a realistic example (c.f. section 7.1.1) with a trace length of 360 seconds, sampled at 2 Hz, reveals that a grid search on 363 gridpoints demands a memory of approximately 18 MB. This amount of data can be numerically handled without any problems on standard computers.

3.2 Generation of Green's functions

For all practical purposes the GFs and elementary seismograms cannot be calculated analytically, but require numerical solutions. As an impression of the GFs' quality following from this confinement, a comparison of an analytical GF – which is available in the special case of a homogeneous propagation medium – and its numerical equivalent are plotted in figure 3.7. The time series of the analytical solution, presented in part b) of this figure, clearly show the effects of the near-field terms contained in equation (3.10). The relative arrival time t_p of the P-wave signal at the station is given by

$$t_p = \frac{1}{v_p} \cdot \sqrt{30^2 + 20^2}\text{km} \approx 7.2\,\text{s} \, . \tag{3.42}$$

At this time, the first step function shows up in the seismogram. This step reflects the temporal behaviour of the source itself. A ramp function is added to the step in the following, until the S-wave arrives. At that point, a second step function is added and finally a static offset remains, after both wave types have arrived.

In the far-field domain, only two impulsive (delta-peak like) functions are observed in the signal at the arrival times of P- and S-waves respectively. These peaks are originating in the time derivative of the temporal evolution of the source (c.f. Aki and Richards, 2002).

Furthermore the graphical comparison of analytical and numerical solution shows a feature, which is characteristic for numerical methods that calculate solutions in spectral domain. Due to a finite temporal window, in which the solution is obtained, these codes are not able to handle the static offset of the seismogram. A spurious damping is included in order to obtain stable numerical results. This can lead to significant

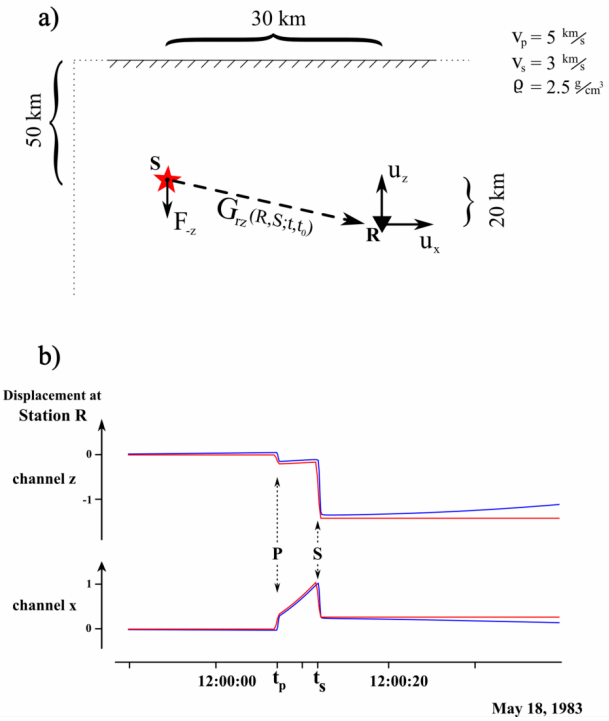

Figure 3.7:
Comparison of analytical solution and an elementary seismogram for a vertical single force excitation at point S, and a homogeneous fullspace medium. Synthetic trace generated with QSEIS. **a)** Geometrical setup with finite source depth 50 km (numerically necessary). The distances are chosen so that internal reflections are suppressed. The free surface correction applies in the numerical code. **b)** Data traces from two channels $\{x, z\}$ of the station at point R, displacement, overall scaling. The analytical solution is shown in red colour, the numerical solution in blue. The numerical solution shows an increasing deviation, which is systematically caused by the spectral method used for its calculation.

systematic deviations in the analysis of real data, if the used GFs are too short in time, or they are not corrected for this effect.

Several software tools are available to do the work of numerically generating GFs. One can generally distinguish between algorithms which are capable to calculate solutions on a full three-dimensional geometry (called *three-dimensional GFs*) and those that operate with one-dimensional modelling (*one-dimensional GFs*). Within the former examples, one can provide a detailed structural Earth model and the details of the results are only restricted by numerical boundary conditions. The latter codes generate solutions for a one dimensional geometry, their output has to be further transformed to be suitable for a three dimensional inversion routine as presented here. Of course they differ from the three-dimensional modelling codes also in terms of their internal calculation methods and computational requirements.

The advantages of the one-dimensional models are that they are numerically faster and a larger variety of them is available. Additionally the lateral inhomogeneities do not play a large roll in most of the geometries we face forr the inversion of non-volcanic LP-events, so one-dimensional codes provide sufficiently good results for our low frequency application.

In the following I will present the one-dimensional and three-dimensional codes I used for the generation of GFs. The non-mathematical expression *one-dimensional GFs* or *three-dimensional GFs* refers to the method the respective GFs have been generated with rather than to their real dimensionality. Independent of the generation method of the GFs themselves, in every application a set of gridpoints as possible source points S is defined in advance, and a set of fixed station positions R is provided. For each source-station

combination, the respective 18 elementary seismograms (six moment tensor components, three channels) are calculated. These are stored in a local database so they can directly be used within the inversion code.

3.2.1 Generation of Green's functions for three dimensional models

In theory, the 3D-codes return directly the respective 18 components of **G** for a given source-station pair as numerical time traces. For setting up the complete database, this calculation procedure has to be carried out over the whole numerical grid to cover all source-station pairs. But for most configurations only traces for a single moment tensor component can be calculated at a time. For generating a complete GF database for the full moment tensor information, the calculation has to be repeated successively for all single moment tensor entries. So the computational calculation time is mainly depending on the size of the source point grid, thus decreasing grid sizes to achieve a reasonable coverage or grid resolution is beneficial.

However, here the principle of reciprocity as discussed in section 3.1.2 can be exploited, since the computational costs of the codes rise slower than linear with the amount of station locations; the runtimes for calculations of GFs for 10 stations or 100 are nearly the same. To calculate the GFs the virtual source locations within the numerical code are set to the real station positions and the real grid points act as virtual signal receiving stations. The resulting GFs can afterwards be transformed with help of section 3.1.6 to the correct configuration.

The pseudo spectral method – *ct3dtopo*

The program *ct3dtopo* (Tessmer, 1995) simulates a seismic wave field on a three dimensional grid, where multiple station positions and also multiple simultaneously activated source locations can be defined. The latter is of use, if either active sources operating at the same time or extended source locations shall be modelled; in the setup of a grid search, we stick to a single source location.

I use this code to generate elementary seismograms for applications with full three dimensional media, including topography (see section 7.2).

The seismic source mechanism is defined either as a combination of single forces or a seismic moment tensor. I choose consecutively normalised single forces in three basis directions as the respective source mechanisms, and apply the program successively three times for generating the required elementary seismograms (c.f. section 3.1.6).

For each numerical calculation step, the wave-field is generated by a combination of calculations in the spatial spectral domain and the application of internal finite-difference schemes in time domain (c.f. Heimann, 2005). The temporary use of the spectral domain is characteristic for a class of codes, which are therefore named *pseudo spectral methods*.

In addition to the seismic signal for each gridpoint, *ct3dtopo* provides all the intrinsic spatial derivatives of the signals as a separate output. Their numerical precision is only restricted by the grid's spatial extension. With their help, the transformation to the desired setup as described above can be done precisely, whereas in any external approach these derivatives would have to be additionally calculated for each step in space and

time. This would result in a decrease in accuracy, since a nearest neighbour approximation would have to be used. For a more detailed description of the theoretical background of *ct3dtopo* see (Tessmer, 1995).

The grid, on which the program calculates the wavefield propagation is not regular. This leads to a problem in amplitude scaling. By applying the concept of reciprocity, one assumes, that the absolute value of the input force at the generation of the GF is the same as the output of the reciprocal GF. This assumption does not hold here, because the forces are handled rather in terms of force densities (force per unit cell), and the cell sizes vary along the grid, the required factor for scaling the respective force density cannot be determined directly. This leads to the loss of information about the absolute values of the GFs. The determination of the correct amplitudes is possible, if the overall dissipation on the numerical grid is known. Identical excitations of wavefields at different positions provide a fixed amount of energy to the system (grid) in each case. By a normalisation of the wavefield amplitudes with respect to the total energy, the GFs can be rescaled. This correction process has not been tested and is beyond the scope of this work. Here I use only the reasonable assumption, that the relative differences between the scalings of GFs for different station locations on the grid are small, if the differences between the distortions of the respective grid cells are sufficiently small.

Since the tool works on a full three dimensional grid space for all parameters, the complete structural information of the medium is contained in the GFs. This includes also the information about topography, which is handled as follows: in the initialisation the grid space is set up as a regular cuboid, upon which the velocity model is defined. Afterwards the whole grid gets linearly stretched in vertical direction fitting the given topography. This principle of handling is exemplified schematically with the help of a two dimensional slice of the grid in figure 3.8.

3.2.2 Generation of Green's functions for one dimensional models

If lateral variations of the medium can be neglected in comparison to the dominating wavelengths, the problem at hand can be approximated by a one dimensional modelling. Following (Udıas, 1999), a one dimensional layered velocity model is suitable for the analysis of seismic waves in all cases presented within this thesis. Here the velocity structure is held constant in the horizontal dimensions. In figure 3.9 the velocity structure of such an underground model is illustrated. This model is used in applications in chapters 6 and 7.

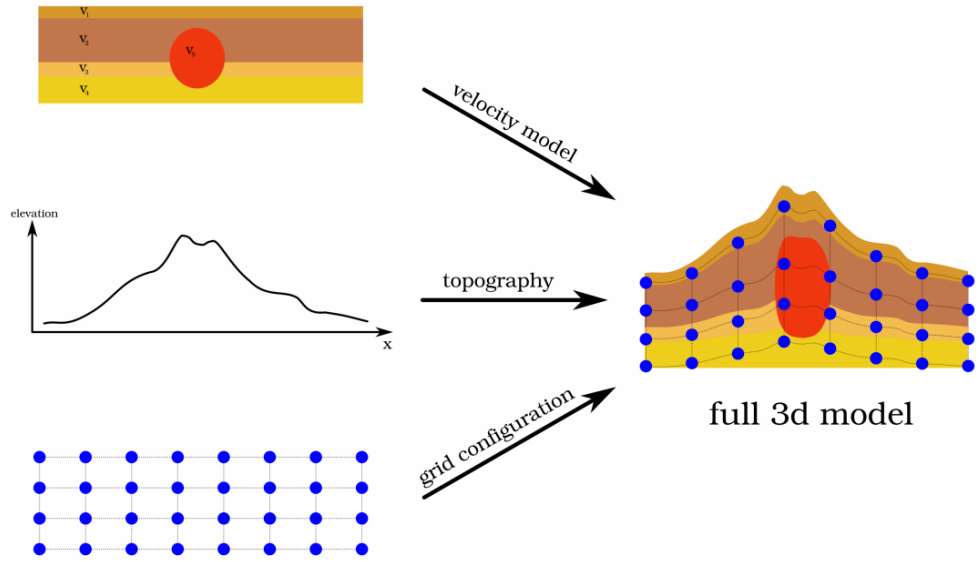

Figure 3.8:
Setup of the topography in *ct3dtopo*. The information about a two-dimensional velocity model (upper left) and the topography (center left) are combined to a full three dimensional velocity model. The medium is linearly stretched in vertical direction. The source point grid (lower left) is adopted to the new spatial structure.

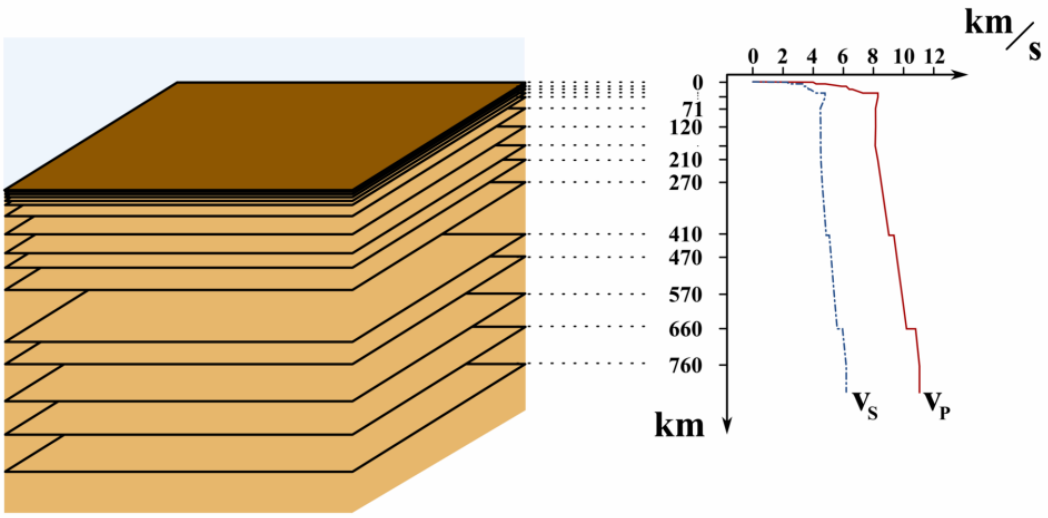

Figure 3.9:
Example for a one dimensional velocity model for the generation of GFs in QSEIS. **right:** The seismic wave velocities v_p and v_s are plotted against the depth. **left:** The layering dimensions are visualised for showing the relations of layer thicknesses. The model is used for the analysis in section 7.1.1. The model parameters are taken from (Dahm et al., 2007).

The coordinates within this setup reduce to one horizontal component h and one vertical z. However, the source mechanism can still be interpreted as a full moment tensor as well as the signals for three orthogonal components are available; mainly the inner calculations are simplified and all station positions are fixed at one angle with respect to the source geometry (azimuth $\varphi = 0$). After calculating the respective elementary seismograms for all combinations of source depths and station distances, the output has to be adjusted to the real geometry. That does not include effects of the Earth model but reflects the geometrical basis definition of $\mathbf{M}$. This transformation is described in the following section.

The reflectivity method – *QSEIS*

The routine mainly used for generating elementary seismograms throughout this work is the program *QSEIS* (Wang, 1999). It is based on a well tested, classical method that works with the reflection-transmission coefficient matrices of the horizontal interfaces of a stratified medium; the routine therefore belongs to the class of *reflectivity methods*.

The input of *QSEIS* is a single ASCII-formatted configuration file, containing all information regarding the source time function, location of source and station, numerical parameters (spatial and temporal samplings, accuracy and so on), the source mechanism ($\mathbf{M}$), and the velocities and elastic parameters of the medium. Effects of a free surface reflection and refraction can be included, just as an artificial curvature of the surface, reflecting Earth's spheric symmetry for large epicentral distances.

The output of *QSEIS* consists of elementary seismograms for internally defined source mechanisms. These can be set up in such a way that the output data can be easily transformed into the required basis functions. The output data are given as ASCII-formatted time series.

Unfortunately, the original *QSEIS* as a FORTRAN 77 program is not implemented to run in parallel on multi processor computers. With the help of an external wrapping software tool, which can parallelise the time consuming work of sequential/serial application of *QSEIS* for varying distances and depths in the geometrical configuration, the calculations can be speeded up significantly.

3.2.3 Geometrical expansion of Green's functions for one dimensional models – comparison of the general case and the far-field approximation

In the general case of a three-dimensional space, there are 18 elementary seismograms – they represent the signal content of the three components u_r, u_ϕ, u_z and each component is a priori influenced by all six moment tensor components. If the source-station geometry is restricted to a vanishing azimuth angle, as it is the case by definition in the one dimensional modelling setup, only a fraction of these 18 components is not identically zero. Therefore the codes for the generation of general GFs in one dimensional modelling return only a smaller number of independent basis functions. These can be transformed

into the desired elementary seismograms for the general three-dimensional case. The exact definition of the basis function depends on the application. In case of a full modelling, ten functions are generated, for a far-field approximation, there are only eight. The returned traces are transformed with geometric factors that depend on the azimuth angle φ between the epicentre and the respective station location. This geometrical correction is defined for the source-bound coordinate system with *radial* (r), *transversal* (ϕ), and *vertical* (z) components. The positive axis points away from the source for r and downwards for z; φ is chosen so that the basis system $r\varphi z$ is oriented right handed; an overview is given in figure 3.10.

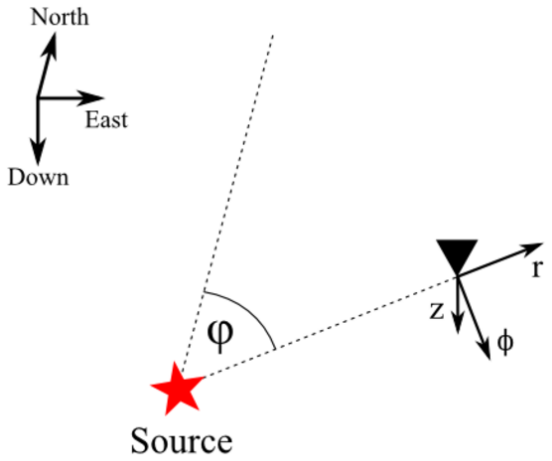

Figure 3.10:
Geometry of the $r\phi z$ basis as defined in 3.2.3. The epicentre is denoted with the red star, the seismic station location is given by the black triangle. The φ is the azimuth in the North-East-plane.

- **Geometrical correction for one-dimensional models – general form**

  In the most general case, no restrictions and approximations apply. The full information is contained within 10 independent basis functions $g_{1...10}$, which are identical to elementary seismograms G^0_{ji} for the case of azimuth angle $\varphi = 0$

$$g_1 = G^0_{r1} \quad , \quad g_2 = G^0_{r5} \quad , \quad g_3 = G^0_{r3} \quad , \quad g_4 = G^0_{\phi 5} \quad , \quad g_5 = G^0_{\phi 4},$$

$$g_6 = G^0_{z6} \quad , \quad g_7 = G^0_{z5} \quad , \quad g_8 = G^0_{z3} \quad , \quad g_9 = G^0_{r2} \quad , \quad g_{10} = G^0_{z2} \; .$$

  Including the necessary geometrical factors (for the derivation see for example (Müller, 1985; Heimann, 2011)), the 18 elementary seismograms G_{ji} are obtained as follows :

$$u_j = \sum_{i=1}^{6} M_i \cdot G_{ji}$$

$$\begin{aligned}
u_r = \quad & M_1 \cdot \left[\cos^2\varphi \cdot g_1 + \sin^2\varphi \cdot g_9\right] \\
\ldots + \quad & M_2 \cdot \left[\sin^2\varphi \cdot g_1 + \cos^2\varphi \cdot g_9\right] \\
\ldots + \quad & M_3 \cdot [g_3] \\
\ldots + \quad & M_4 \cdot [\sin 2\varphi \cdot (g_1 - g_9)] \\
\ldots + \quad & M_5 \cdot [\cos\varphi \cdot g_2] \\
\ldots + \quad & M_6 \cdot [\sin\varphi \cdot g_2] \\
u_\phi = \quad & M_1 \cdot \left[-\frac{1}{2}\sin 2\varphi \cdot g_5\right] \\
\ldots + \quad & M_2 \cdot \left[\frac{1}{2}\sin 2\varphi \cdot g_4\right] \\
\ldots + \quad & M_3 \cdot [0] \\
\ldots + \quad & M_4 \cdot [\cos 2\varphi \cdot g_4] \\
\ldots + \quad & M_5 \cdot [-\sin\varphi \cdot g_5] \\
\ldots + \quad & M_6 \cdot [\cos\varphi \cdot g_5] \\
u_z = \quad & M_1 \cdot \left[\cos^2\varphi \cdot g_6 + \sin^2\varphi \cdot g_{10}\right] \\
\ldots + \quad & M_2 \cdot \left[\sin^2\varphi \cdot g_6 + \cos^2\varphi \cdot g_{10}\right] \\
\ldots + \quad & M_3 \cdot [g_8] \\
\ldots + \quad & M_4 \cdot [\sin 2\varphi \cdot (g_6 - g_{10})] \\
\ldots + \quad & M_5 \cdot [\cos\varphi \cdot g_7] \\
\ldots + \quad & M_6 \cdot [\sin\varphi \cdot g_7] \; .
\end{aligned} \tag{3.43}$$

- **Geometrical correction for one-dimensional models – far-field approximation**

  The signal $\boldsymbol{u}$ contains contributions from near-field terms $\boldsymbol{u}^{\text{near}}$ as well as far-field terms $\boldsymbol{u}^{\text{far}}$:

  $$\boldsymbol{u} = \boldsymbol{u}^{\text{near}} + \boldsymbol{u}^{\text{far}}.$$

  If only signals from stations in large epicentral distances are considered for the analysis, the near field parts of the signals can be neglected. The term *large distance* is defined as several multiples of the dominant wavelengths of the considered signal (Aki and Richards, 2002). The inclusion of this assumption is quite common, therefore I briefly show its influence on the definition of elementary seismograms. In this far-field approximation, equation (3.26) can undergo another transformation, introducing the *slowness* $\boldsymbol{s}_k := \frac{\partial t}{\partial \boldsymbol{x}_k}$, where this includes a time independency of the travel time curves' derivatives $\boldsymbol{s}_k \neq \boldsymbol{s}_k(t)$:

  $$\begin{aligned} \boldsymbol{u}_j^{\text{far}}(\boldsymbol{x},t) &= \sum_{i=1}^{6} M_i(\boldsymbol{\xi_0}) \cdot \bar{G}_{ji}(\boldsymbol{x},\boldsymbol{\xi_0};t,t_0) * \text{stf}(t) \\ &= \sum_{i=1}^{6} M_i(\boldsymbol{\xi_0}) \cdot \text{stf}(t) * \frac{\partial}{\partial t}\left(\boldsymbol{s}_k \cdot \bar{G}_{ji}(\boldsymbol{x},\boldsymbol{\xi_0};t,t_0)\right) \\ &= \sum_{i=1}^{6} \underbrace{\left[M_i(\boldsymbol{\xi_0}) \cdot \frac{\partial}{\partial t}\text{stf}(t)\right]}_{=\dot{M}(t)} * \underbrace{\bar{G}_{ji}(\boldsymbol{x},\boldsymbol{\xi_0};t,t_0)\boldsymbol{s}_k}_{=:\breve{G}_{ji}^{\text{far}}} . \end{aligned} \tag{3.44}$$

  The $\dot{M}(t)$ is called the *moment rate tensor* in this connection. The $\breve{\mathbf{G}}^{\text{far}}$ contains the appropriate elementary seismograms. The construction of the latter is again carried out with the help of basis functions. Opposite to the general case introduced before, eight of them are sufficient ($\breve{g}_{1\ldots8}^{\text{far}}$). The basis functions of the full signal are connected with the basis of the far-field approximation via the five explicit

near-field terms $\breve{g}^{\text{near}}_{1\ldots5}$:

$$
\begin{aligned}
g_1 &= \breve{g}^{\text{far}}_1 - \frac{1}{2}\breve{g}^{\text{near}}_2 \,, \\
g_9 &= \frac{1}{2}\breve{g}^{\text{near}}_2 \,, \\
g_2 &= \breve{g}^{\text{far}}_2 + \breve{g}^{\text{near}}_1 \,, \\
g_3 &= \breve{g}^{\text{far}}_3 \,, \\
g_4 &= \breve{g}^{\text{far}}_4 + \breve{g}^{\text{near}}_4 \,, \\
g_5 &= \breve{g}^{\text{far}}_5 - \breve{g}^{\text{near}}_3 \,, \\
g_6 &= \breve{g}^{\text{far}}_6 - \frac{1}{2}\breve{g}^{\text{near}}_5 \,, \\
g_{10} &= \frac{1}{2}\breve{g}^{\text{near}}_5 \,, \\
g_7 &= \breve{g}^{\text{far}}_7 \,, \\
g_8 &= \breve{g}^{\text{far}}_8 \,.
\end{aligned}
\tag{3.45}
$$

So with the eight basis functions $\breve{g}^{\text{far}}_{1\ldots8}$ and neglecting the near-field terms, the signal $\breve{u}^{\text{far}}$ equates to

$$\begin{aligned}
\breve{u}^{\text{far}}_r = \quad & M_1 \cdot \left[\cos^2\varphi \cdot \breve{g}^{\text{far}}_1\right] \\
\ldots + \quad & M_2 \cdot \left[\sin^2\varphi \cdot \breve{g}^{\text{far}}_1\right] \\
\ldots + \quad & M_3 \cdot \left[\breve{g}^{\text{far}}_3\right] \\
\ldots + \quad & M_4 \cdot \left[\sin^2\varphi \cdot \breve{g}^{\text{far}}_1\right] \\
\ldots + \quad & M_5 \cdot \left[\cos\varphi \cdot \breve{g}^{\text{far}}_2\right] \\
\ldots + \quad & M_6 \cdot \left[\sin\varphi \cdot \breve{g}^{\text{far}}_2\right] \ , \\
\breve{u}^{\text{far}}_\phi = \quad & M_1 \cdot \left[-\frac{1}{2}\sin 2\varphi \cdot \breve{g}^{\text{far}}_4\right] \\
\ldots + \quad & M_2 \cdot \left[\frac{1}{2}\sin 2\varphi \cdot \breve{g}^{\text{far}}_4\right] \\
\ldots + \quad & M_3 \cdot [0] \\
\ldots + \quad & M_4 \cdot \left[\cos 2\varphi \cdot \breve{g}^{\text{far}}_4\right] \\
\ldots + \quad & M_5 \cdot \left[-\sin\varphi \cdot \breve{g}^{\text{far}}_5\right] \\
\ldots + \quad & M_6 \cdot \left[\cos\varphi \cdot \breve{g}^{\text{far}}_5\right] \ , \\
\breve{u}^{\text{far}}_z = \quad & M_1 \cdot \left[\cos^2\varphi \cdot \breve{g}^{\text{far}}_6\right] \\
\ldots + \quad & M_2 \cdot \left[\sin^2\varphi \cdot \breve{g}^{\text{far}}_6\right] \\
\ldots + \quad & M_3 \cdot \left[\breve{g}^{\text{far}}_8\right] \\
\ldots + \quad & M_4 \cdot \left[\sin 2\varphi \cdot \breve{g}^{\text{far}}_6\right] \\
\ldots + \quad & M_5 \cdot \left[\cos\varphi \cdot \breve{g}^{\text{far}}_7\right] \\
\ldots + \quad & M_6 \cdot \left[\sin\varphi \cdot \breve{g}^{\text{far}}_7\right] \ ,
\end{aligned} \tag{3.46}$$

where three basis functions are identical for the general case and the far-field approximation:

$$\breve{g}^{\text{far}}_3 = g_3 \quad , \quad \breve{g}^{\text{far}}_7 = g_7 \quad , \quad \breve{g}^{\text{far}}_8 = g_8.$$

If data are provided in an NEZ coordinate system, the components u_r and u_ϕ must be rotated into u_N and u_E respectively. The rotation angle α is determined by the backazimuth φ^* (see e.g. Stein and Wysession, 2003).

3.3 Handling of the Green's function within the *ARCTIC* code

Although the presented algorithm of ARCTIC and the applications are based on the analysis of very low frequencies, for which one could argue to restrict the demands of the GFs to the one-dimensional case, it handles the full information of the 18 component Green's tensor $\mathbf{G}$. On the one hand this allows for the possibility of improving the source inversion for approximately flat topographies (see chapter 7.1). On the other hand this

enables the inversion of data in case of complicated underground structures and topographies that have to be treated as a full three dimensional set of parameters without changing anything in the configuration (e.g. a volcanic area as it is the case in chapter 7.2)

For all practical purposes the number of station locations is assumed to be significantly smaller than the number of grid points, thus the GFs are sorted and organised with respect to the set of seismic stations. For each station-source combination one has to handle the 18 components of **G**, each of which representing a single time trace. These time traces are stored in single files, within which they are set in the structure that is sketched in figure 3.11.

On the one hand the chosen structure for storing the GFs allows for a clear structure inside the large set of time traces, which can be handled by human users. On the other hand it allows for the later extension of the GF's database without the need of a complete new setup. If the station geometry changes, the database can easily be updated. This case is much more likely than the change of assumptions on the source grid. However, in the latter case, a new setup has to be created.

In further development steps, the pure GFs, which describe the media's answer on single forces, can be stored equivalently in another file with similar structure, so that they can be generated and used independently and only if required from case to case.

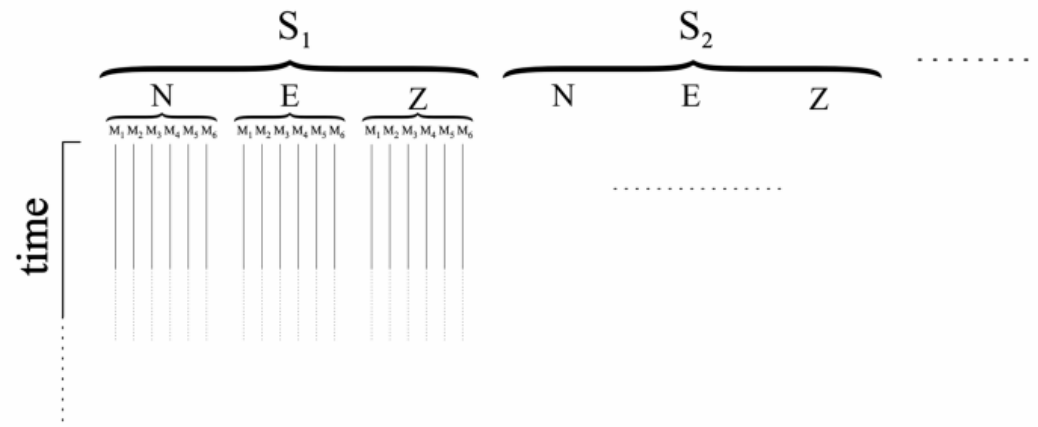

Figure 3.11:
Inner structure of the GFs inside each station-depending GFs-file. The time traces of the GFs are sorted successively by moment tensor component (M_i), station channel (NEZ) and source grid points (S_j).

Since for the application of *ARCTIC*, the local GF-collection has to be computed in advance and stored as files for the respective stations, a supplemental tool has been programmed to handle this task. It provides the transformation of basis functions of one-dimensional GF modelling into the general three-dimensional case as described in section 3.2.3. Additionally, it allows to set up a set of synthetic data based on this

collection of GFs, for instance for carrying out numerical tests for an arbitrary source mechanism. White noise can be added with different amplitudes.

Even if no explicit station geometry is provided, but only an arbitrary set of elementary seismograms is available, an artificial test geometry in form of a spiral or concentric circles can be set up with it, thus covering a range of different distances and azimuths. The synthetic data generated from the GFs are stored as miniSEED formatted files.

The format of NetCDF (*Network Common Data Form* – Rew and Davis, 2002) for storing the GFs-files has been chosen for convenience and performance; it is widely distributed for storing array style data, mainly in scientific fields like meteorology and oceanography. Software libraries for data handling are available for all important programming languages, just as further software tools (e.g. content viewer). Its usage helps to make the generation of the GFs completely independent from the inversion routine, providing a high portability not only for different programming languages, but even between different operating systems and hardware setups.

4 Long period events

In this work, I focus on the analysis of shallow seismic events that generate wave signals with a significant energy in low frequency regimes, the so-called *long period events (LP-events)*. There are no strict definitions for the terms *shallow event* and *long period event*, describing a distinct class of events. Therefore I give short definitions in this chapter. LP-signals, which I will study, can originate either from volcanic structures or from induced seismic events on local and regional scales. After a short introduction to LP-events, I briefly present examples of the LP-event characteristics and possible source mechanisms.

Besides the specific source mechanisms, the geometry of the propagation medium can influence the long period signals, as will be shown by an example.

4.1 What are *long period events* ?

The term LP-event is most widely used as a technical term within the subject of analysing volcano seismic data (Chouet, 1996). It describes a single volcanic event that emits signals, which show a significant energy content in frequency ranges that are well below the ones of volcano tectonic events (VT) (> 5 Hz (e.g. Hammer, 2007)). Opposite to the members of the latter event class, which may occur collaterally, the waveforms of the LP-events show highly repetitive characteristics. If a sufficiently high number of these single LP-events occur consecutively, their waveforms merge and the resulting overall waveform changes giving rise to a signal called *volcanic tremor* (Latter and Zealand, 1979; Fehler, 1983). This latter class shall not be of further interest in this thesis, only distinctively detectable events are considered. Therefore the requirement of a clear, event-related onset in the seismic data, combined with a coda, decreasing in signal amplitude, is part of the definition of an LP-event (Pitt and Hill, 1994; Chouet, 2003). This also holds in case of non-volcanic signal sources.

LP-events are well known through thoroughly analysing volcanic seismic signals (e.g. Chouet, 1988; Lahr et al., 1994; Neuberg et al., 1994; Kumagai and Chouet, 1999; Nishimura et al., 2000; Hidayat et al., 2000; Aster et al., 2003; Kumagai et al., 2005; Cannata et al., 2009) with different approaches for modelling the signal's source (s. appendix B). Due to the highly repetitive waveforms and in contrast to the destructive VT, a non-destructive source process is assumed to generate low frequency events. The source mechanisms are often related to fluid (gases or magma) movement in the interior of the volcanoes, possibly linking LP-events to a volcanic system that is either active or regains activity after a period of inactivity. Thus an analysis of volcanic LP-events is considered essential for developing a more thorough understanding and insight in precursory processes with regard to volcanic hazard (Havskov et al., 1983; Chouet, 1996). Any volcanic early warning system should therefore include the analysis of LP-events where available. One case study of the inversion of such a volcanic LP-event is carried out and presented

in chapter 7.2.

Seismic signals with significant energy content in low frequency bands are not only observed in volcanic areas, tectonic seismic events can also generate such a kind of long period signals. Take for instance a large, finitely extended fault, consisting of a combination of small cracks, that shows up somewhere inside the crustal or mantle. Each point on the fault's surface moves only for a very short time, the rise time (c.f. section 2.1.2.2). This time is significantly shorter than the characteristic times of the emitted wave signals; the source can be described as impulsive. Depending on the spatial extent of the fault, the consecutive movements of different areas of the fault can prolong the overall duration of the slip movement, the *rupture time*. This leads to an increase of low frequency content in the emitted signals. The larger the spatial extent of the seismic source or the lower the rupture velocity, the larger the low frequency content of the signal can be. Therefore sufficiently large tectonic events or shallow events with low rupture velocities can generate LP-signals.

Opposite to tectonic and volcanic events that are of pure natural origin, there is also the class of directly and indirectly human generated or anthropogenic seismic events, like explosive sources (e.g. nuclear test sites or mining). The indirect influence of man on natural processes leads to the so called *induced seismic events* (without drawing a distinction to *triggered events* (McGarr et al., 2002)). They are generated as consequences of human action: acoustic emissions or microearthquakes in case of *hydro-fracturing processes*, breakdowns of abandoned mining areas, stress change correlating with geothermal experiments, or subsidence of volumes above exploited oil-reservoirs are examples of this event class (McGarr et al., 2002).Examples from this class will be studied in the framework of this thesis later on (see section 7.1).

The *induced seismic events* differ from the natural seismic events also in the sense, that they cannot occur in great depths. Since the human range of influence is restricted by technical limits to the uppermost structures of the Earth's crust, depths below 15 km are excluded as source regions for this class of events (Kozlovsky, 1986). Therefore the *induced seismic events* and volcanic events are grouped under the term *shallow seismic events*.

Although finding some suggestions for definitions of the frequency range of volcanic LP-events (Chouet, 2003), no precise definition for general LP-events in terms of specified frequency bands has been given so far. In accordance with the aforementioned authors, I define LP-events as seismic events with signals containing a significant content in the frequency range below 2 Hz. In addition the signal has to show a clear impulsive onset to distinguish them not only from the volcanic tremor signals but also from silent slip events (Dragert et al., 2001). No further classification (for instance into *VLP-events* or *ULP-events* (Chouet, 2003)) will be used.

4.2 Characteristics of LP-signals

Before I focus on the presentation of possible source mechanisms, a few examples of representative waveforms of LP-signals in case of volcanic and induced seismic events are presented.

4.2.1 Volcanic events

Since LP-events are defined in a very broad sense, it is a challenging task to find a theoretical common ground theory that may explain the characteristics of the waveforms from general volcanic LP-events. Therefore it is useful to present a collection of volcanic example data containing LP-signals to get an impression of the common features within and the differences between the signals.

The data examples which are presented here are recordings from four volcanic areas: Mt. Erebus (Antarctica), Soufrière Hills (Montserrat), Mt. Yasur (Vanuatu), and Mt. Merapi (Indonesia). Many different data sets from these regions have been studied with respect to LP-events by various research groups and their extensive results can be found for instance in (Nabyl et al., 1997; Neuberg et al., 2000; Neuberg, 2000; Hidayat et al., 2002; Rowe et al., 2004; Aster et al., 2008).

The common characteristics of volcanic LP-events are:

- highly repetitive seismic signals for a long period, allowing for a standardisation of event types;
- variability of event types at one single volcano;
- clear differences between the waveforms from different volcanoes.

These features are visualised in figure 4.1. Therein, one example section of an original raw data trace, containing an LP-signal, is shown together with its frequency bandpass filtered equivalent for each volcano. Additionally, in all cases a visually stacked collection of different time sections that contain similar waveforms is plotted. This points out the systematic similarities within the signals of the same type at one source region. Additionally it shows up that the main period of the signals varies indeed from 1 to 8 seconds between the different locations, but it is constant for varying types at one and the same site.

As it can be seen in figure 4.1, LP-events at different volcanoes can vary quite strongly, which makes it difficult to extract common features for their analysis. However it is at least possible to clearly distinguish LP-events from other volcanic seismic events like VT (signal energy content mainly at high frequencies), tremors (no clear event onset in the signal), or rockfalls (neither significant energy at low frequencies nor an impulsive onset in the signal). In figure 4.2, an overview over signals that originate from different source types is presented, which allows the comparison and classification of volcanic seismic signals.

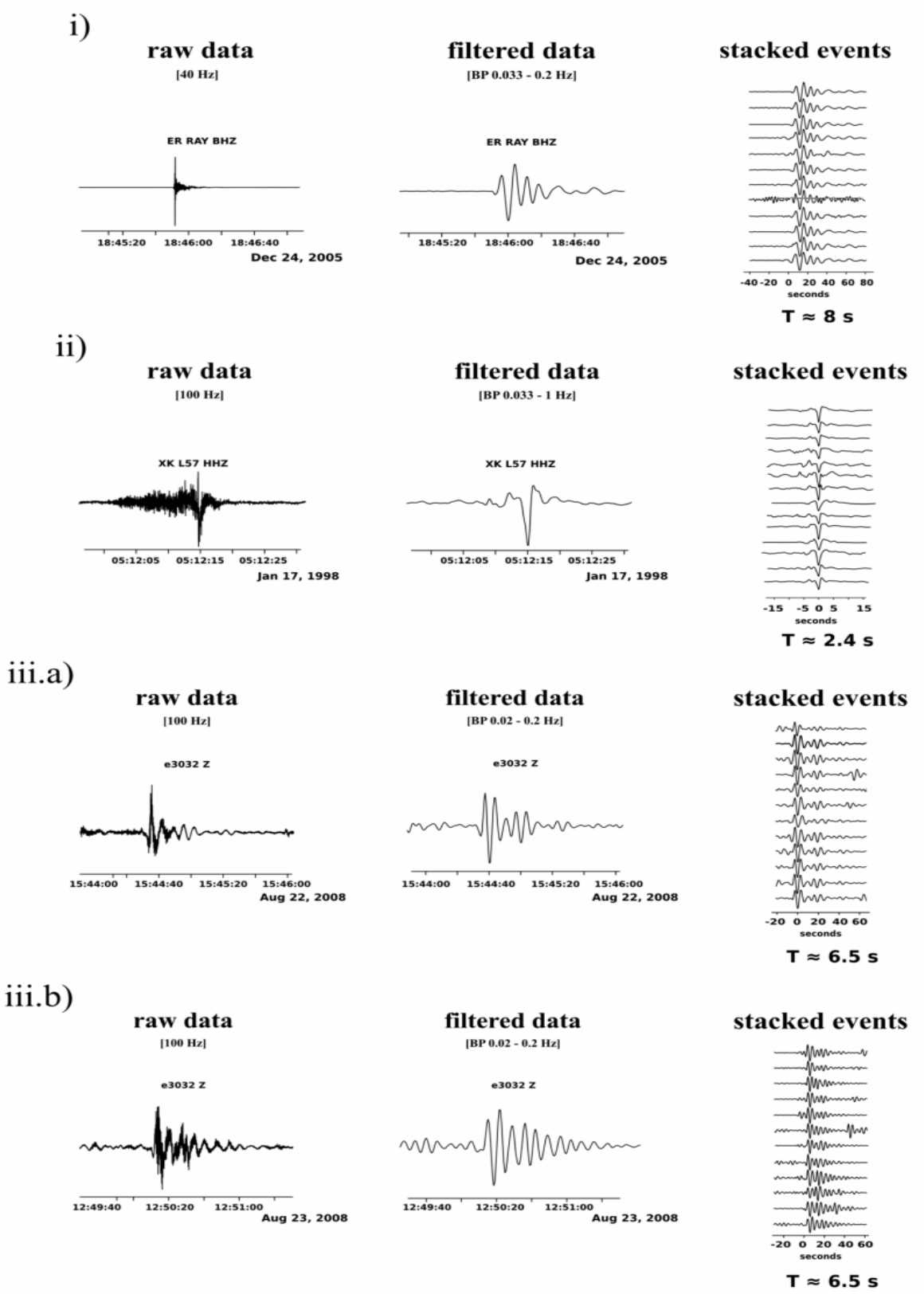

Figure 4.1: continued...

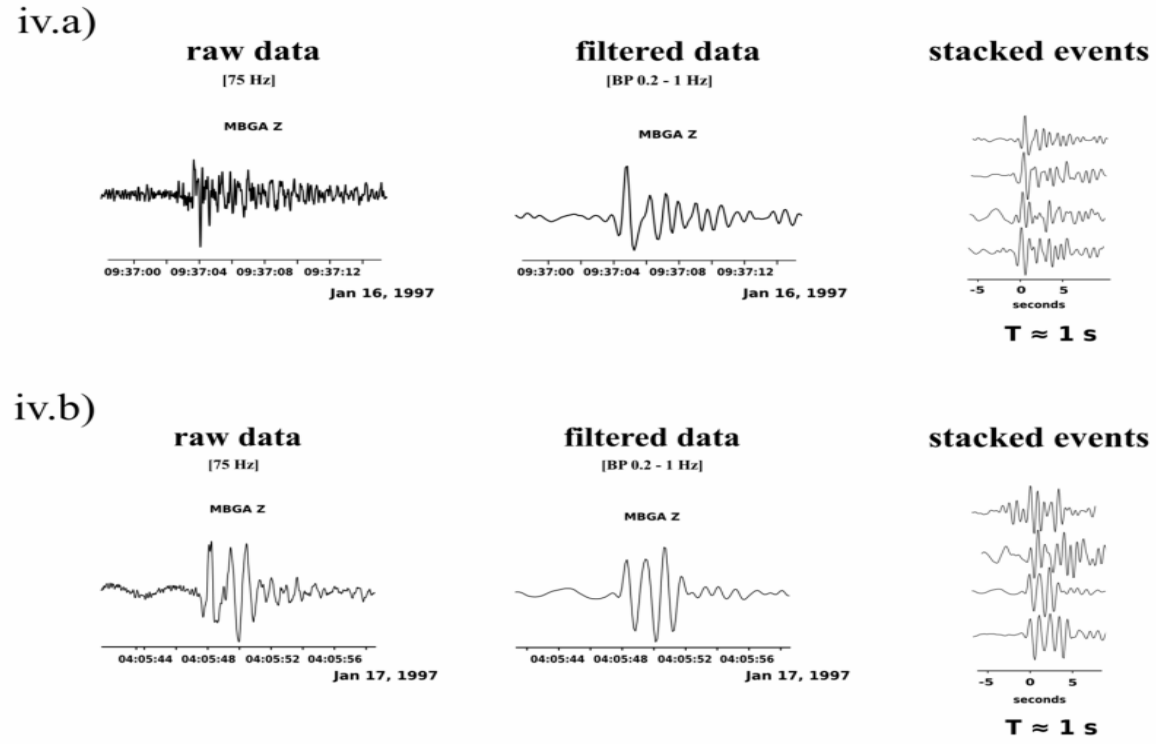

Figure 4.1:
Data examples for volcanic LP-events. Data traces from **i)** Mt. Erebus (IRIS Data Management System, 2010), **ii)** Mt. Merapi (c.f. Hidayat et al., 2002), **iii)** Mt. Yasur with two different signal types a) & b)(data provided by K. Meier), **iv)** Soufrière Hills with two signal types a) & b) (data provided by C. Hammer).
Sections of raw data traces (left), same sections of frequency filtered data (middle), and a collection of time sections, showing events with similar characteristics. T is the average of the main signal period. (right). All traces with individual scaling (c.f. A.1).
Comparison of i)-iv) shows the difference of signal types between different volcanoes. iii.a) and iii.b) give examples for different event types at the same volcano. iv.a) and iv.b) illustrate the problem to find clear distinction between different signal types.

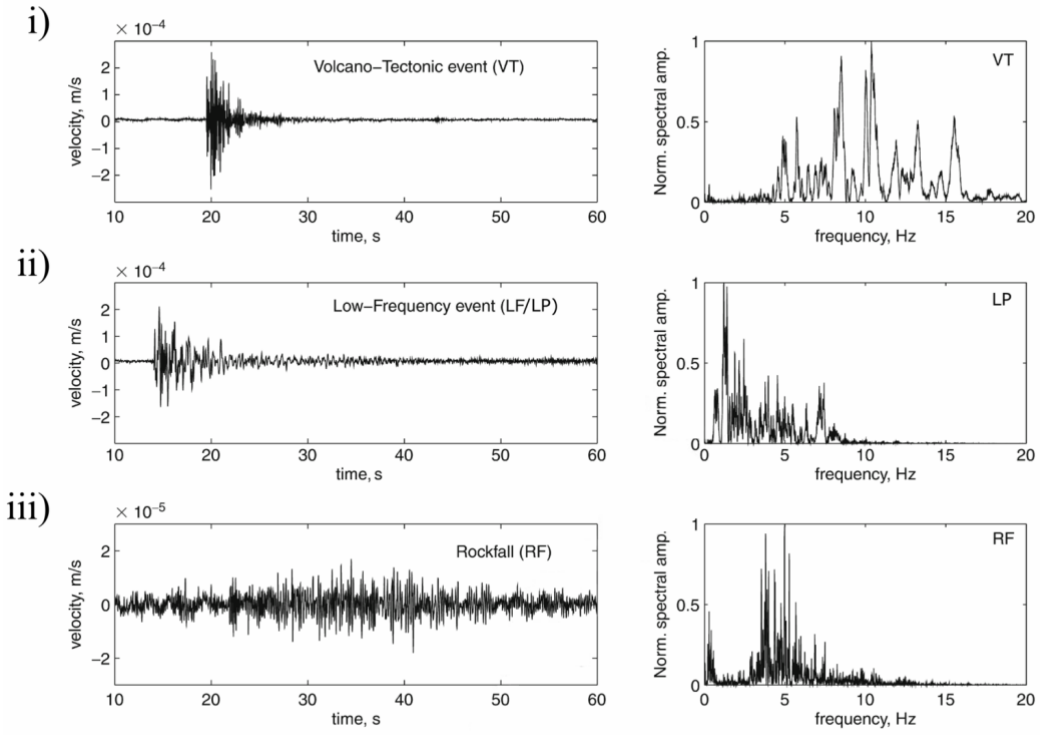

Figure 4.2:
Comparison of different volcanic seismic signals, distinguishing **i)** volcano tectonic events, **ii)** LP-events, and **iii)** rockfall events. Additionally, the respective frequency spectra are shown to the right of the data trace samples. (Modified from (Neuberg, 2011))

4.2.2 Induced seismic events

In contrast to the analysis of volcanic seismic events, long periodic signals of induced seismic events have not been subject to systematic studies hitherto. I present here one case of observed data in order to exemplify LP-signals from induced events.

Figure 4.3 shows data, observed in a mine region at seven stations at different epicentral distances. The source mechanism which generated these data is unknown. Together with the raw data, the frequency spectra are plotted; all spectra are in a limited amplitude band for the frequency range from 0 to 10 Hz. These spectra show clearly, that the data have strong signal content in the frequency range below 2 Hz, putting them into the class of LP-signals.

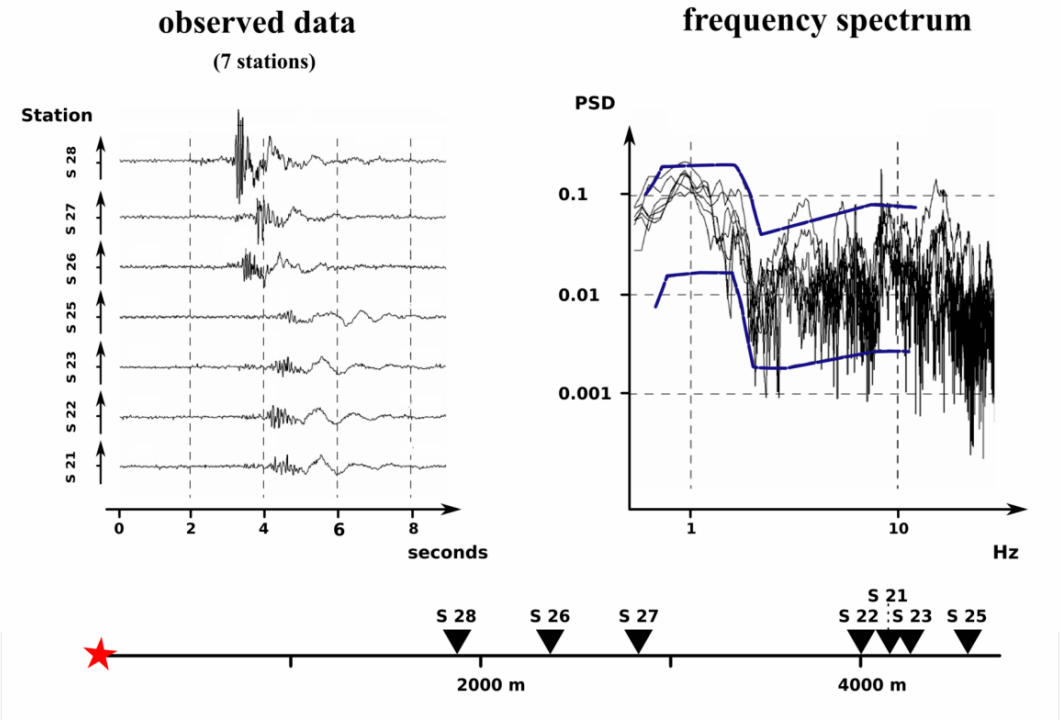

Figure 4.3:
Example data traces from a induced seismic event in a mining region. Velocity data (left) from vertical components of seven seismic stations are visualised in overall scaling together with the respective power spectral densities (right). The limited amplitude band between ∼0.1 Hz and ∼10 Hz is marked by the blue lines. Below, the epicentral distances of the stations are shown. (Modified from (Malovichko, 2005))

4.3 Source mechanisms

Although in most cases it is hard or even impossible to finally determine the correct source mechanism of an LP-signal, a few models of source processes and geometries are

presented below. Aside from the source process, the transmission of regular earthquake signals through the Earth can also give rise to LP-signals, which is known as *path-effects*.

4.3.1 Volcanic events

So far the mechanisms leading to LP-signals at volcanoes are not completely understood. The development of a consistent model is hindered by the facts, that firstly not all volcanoes generate LP-signals; and secondly LP-signals from different volcanic areas show large variability.

There are few volcanoes that are continuously monitored, which also show LP-events for long periods of time (e.g. Mt. Aetna, Mt. Vesuvius, Mt. Erebus, Mt. Kilauea, Mt. Aso, and Mt. Unzen). Not only the frequency content of their respective data varies strongly, also e.g. the amount of *calm* periods or *grouping* of events differ. Furthermore the large variety of types of volcanism (intra-plate, subduction zone, and hot spot volcanism) as well as their different magma compositions, their evolutionary history, and so on, suggest that the source mechanisms also may differ from each other (Aki et al., 1977; Ferrick et al., 1982; Chouet, 1985; Julian, 1994; Neuberg and Luckett, 1996; Kumagai and Chouet, 1999; Legrand et al., 2000; Kumagai and Chouet, 2000; Neuberg et al., 2000; Neuberg, 2000; Chouet et al., 2003; Iverson et al., 2006; Saccorotti et al., 2007; Gambino, 2006; Aster et al., 2008; Bean et al., 2008; Lokmer et al., 2008; O'Brien and Bean, 2008).

Most of these proposed source models have two important facts in common: they include the subsurface movement of fluids, and they accommodate the typical waveform style of a clear onset with the ringing coda by assuming the impulsive excitation of some resonating body. Thus the occurrence of volcanic LP-events is interpreted as reflecting the dynamics of magma and/or gas movement. This interpretation suggests that the current state of the volcanic edifice is changing, when LP-events are detected.

However, many models have been proposed to describe the physically meaningfull evolution of processes leading to the generation of LP-events. Two models are summarised below; the first one is a widely used approach, and the second one is essential for the analysis of the case study in chapter 7.2.

- **The rectangular crack**

  One of the oldest and most widely accepted approaches to explain LP-events has been proposed by Aki et al. (1977). An existing rectangular crack in the volcano is locally excited by some exterior forcing (see figure 4.4), as for instance brittle failure, local crack openings of the surrounding host rock, or impulsive fluid movement. The latter is sometimes referred to as *pumping* or *water-hammer* effect (Pearsall, 1965). As a first idea, it has been assumed that the propagating pressure waves inside the fluid generate standing waves inside the fluid itself and by this the whole crack is showing eigenoscillations. The characteristic time and length scales in this model are directly determined by the speed of sound in the fluid that fills the crack. In order to generate LP-signals with the observed frequencies, these cracks have to be very large (1×2 km^2)(Chouet and Julian, 1985).

Later this model has been modified by considering the propagation of slow waves at the boundary between the filled crack and the surrounding host rock, the so-called *crack-waves* (Chouet, 1986; Ferrazzini and Aki, 1987). This concept is an adaption of the long time known *tube-waves* (Biot, 1952; Ionov and Maximov, 1996). These crack-waves are propagating significantly slower than acoustic waves, hence this model allows for much smaller source geometries (100×0.5 m^2).

- **The bursting gas bubble**

  Under certain conditions, e.g. the size of the crater lake must be sufficiently large, detectable acoustic signals can be generated directly at the surface by the recoil of a bursting magmatic gas bubble, as shown in figure 4.5. This feature is described in (Gerst, 2010), and theoretically investigated in (Buckingham and Garcés, 1996) and (Vergniolle et al., 1996). On some occasions, LP-signals are generated at the same time as the bubble bursts. This effect can be seen in data recorded at Mt. Erebus, where the combined measurement of the lava lake's surface and the broadband recording of seismic signals have been carried out. One example of such an event can be studied in detail in section 7.2. The originating mechanism of the LP-signals is not known explicitly. The observed duration of the LP-signal of several seconds suggests that either the gas slug starts to emit oscillating signals already before bursting, or the signal stems from the relaxation process of the lava surface.

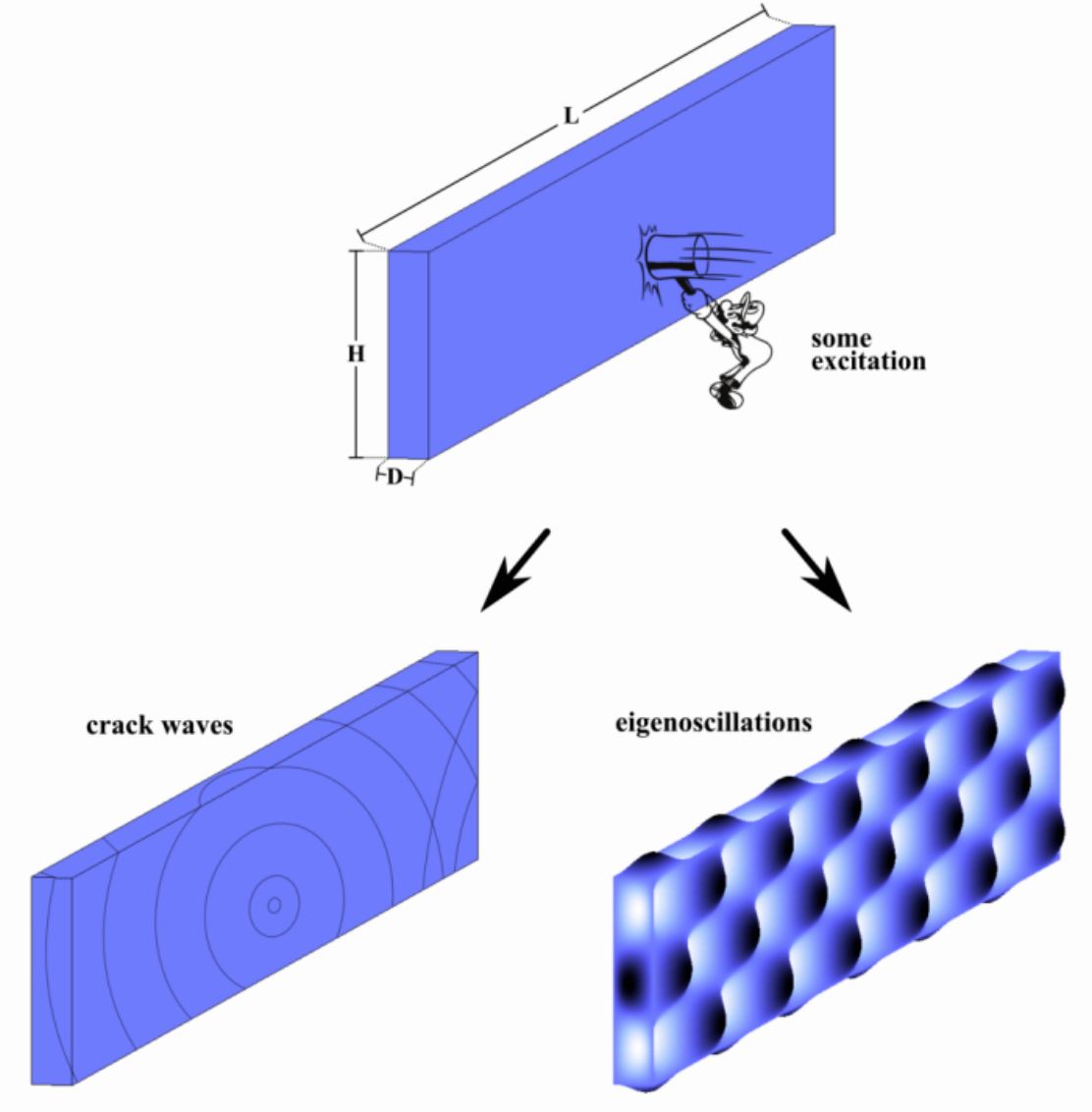

Figure 4.4:
Source model: resonating (static) rectangular crack with length L, width D and height H, $D \ll L$. **upper:** The fluid filled crack is excited (emblematised by impulsive hammer impact). **lower left:** Slow crack waves (propagation speed below acoustic velocities) at the surface between fluid and host rock are generated. **lower right:** Low frequency modes of the crack's eigenoscillations generate LP-signals (Frequencies limited by acoustic velocities).
(figure from (W., 2001))

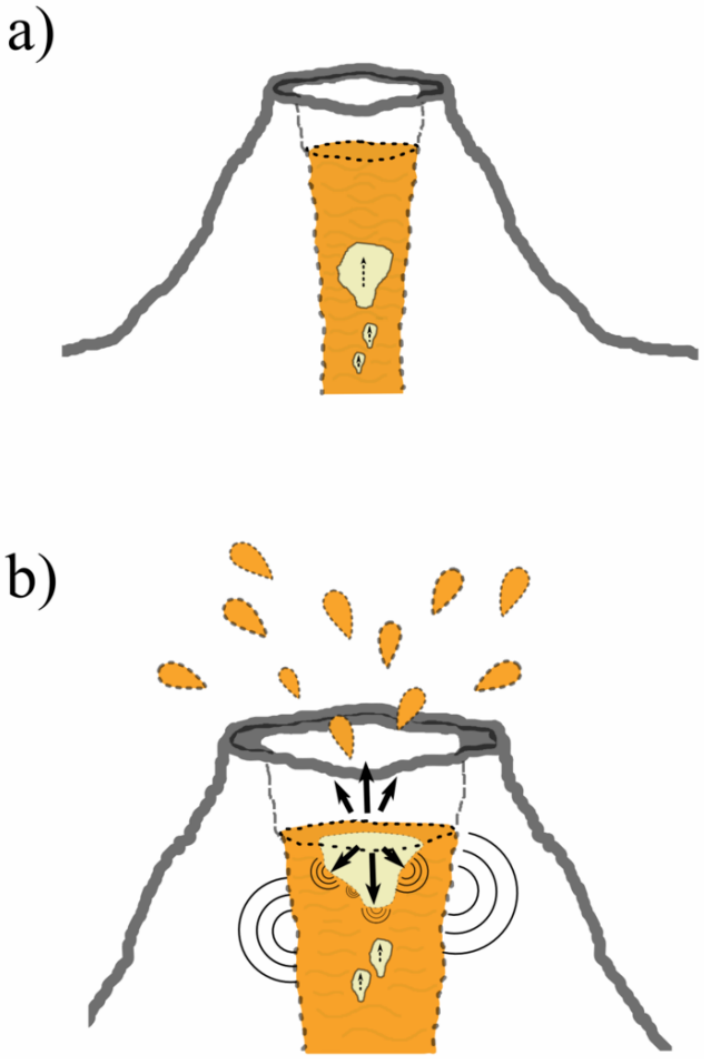

Figure 4.5:
Source model: bursting gas bubble. **a)** Ascending gas slug **b)** Bursted bubble. Emitted seismic waves are sketched at the borders of the gas volume.

4.3.2 Induced seismic events

Induced seismic events have often been subject to diverse analyses and modelling of their source mechanisms (e.g. Trifu and Radulian, 1985; Urbancic et al., 1996; Dahm et al., 1999; Feignier and Young, 1992; Dahm et al., 1998; Lasocki and Orlecka-Sikora, 2008; Julia et al., 2009). But in contrast to volcanic LP-events, unfortunately there is not a wide range of fundamental theories for the generation of LP-signals originating from induced seismic events (Bame and Fehler, 1986; Hasegawa et al., 1989; Trifu et al., 2000; Malovichko, 2005; Gibowicz, 2009), or systematic analysis of possibilities to distinguish between induced and natural events (Peppin and Bufe, 1980). Only some models exist that can explain the observed waveforms in different media, as for instance in salt or coal mining areas (Malovichko et al., 2010; Bischoff, 2010).

Similar to volcanic LP-events, several different source geometries can lead to the existence of induced LP-events. Some of these models are listed in (Braunmiller et al., 1994; Nolen-Hoeksema and Ruff, 2001; Šílení and Milev, 2006; Sílenı and Milev, 2008; Gibowicz, 2009; Julia et al., 2009). In figures 4.6 and 4.7 I sketch two of these models, which are frequently specified in publications: a sub-surface (partial) rockfall or -burst (McGarr, 1976; Hasegawa et al., 1989; Smith et al., 1995; Malovichko, 2005), and the contraction of an exploited fluid field inside host rock (reservoir compaction) (Segall, 1989; Hasegawa et al., 1989).

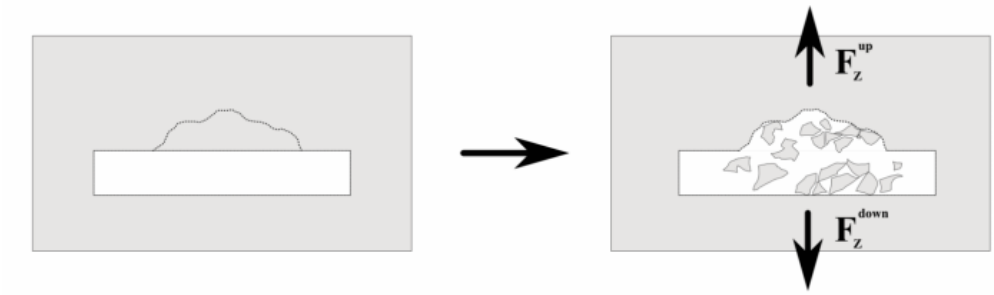

Figure 4.6:
Geometry of a rockfall/-burst as a potential source of LP-signals. Rocks are breaking (rockfall) or blasted (rockburst) from the ceiling of a cavity. The arrows indicate the dominating impulsive force impact.

Shallow induced events typically excite strong Rayleigh-waves and therefore emit long period signals. However, the characteristics of the signals evolving from the example events in figure 4.8 look quite different. As shown in part i) of this figure, the waveforms originating from a shear crack source do not contain significant energy in frequency ranges below 10 Hz, the energy is decreasing with decreasing frequency. Clear onsets of the P-wave and the surface-waves are visible in the seismograms of the different stations, but no clear dispersion can be observed. In case of an excitation by a simulated rockfall event (figure 4.8 ii)), the Rayleigh-waves show clear anomalous dispersion, with long periodic oscillations at the end of the seismic signal. The low frequency content of this signal leads to a good agreement of the power spectral densities of this simulated case and the

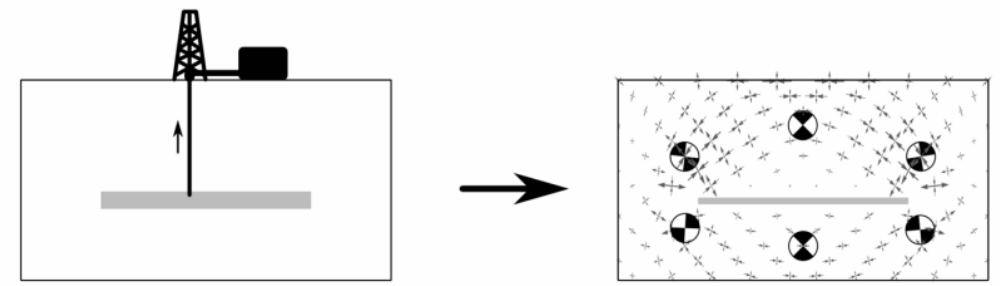

Figure 4.7:
Fluid extraction from a reservoir (grey) inside some host rock leads to localised contractions, stress changes and deformation. Stress field modelling yields determination of maximal shear stress orientation (arrows). This can lead to localised seismic events, exemplified by six FSDs. (Illustration of stress field modelling, non-isogonal, modified from T. Dahm)

observed data set. Very high energies show up in a frequency range around 1 Hz in the latter case. On the one hand the radiation of Rayleigh-waves from a vertical dipole or a CLVD source mechanism does not show angular dependence, so Rayleigh-waves can be observed for all azimuth angles. On the other hand, the Rayleigh-wave radiation pattern from a shear crack source contains nodal lines (Aki and Richards, 2002). If the observational position is set along such a nodal line, Rayleigh-waves cannot be present in the signals.

Up to now, no a priori boundary conditions can be implemented in the developed inversion algorithm, reflecting all characteristics, e.g. varying dispersion relations. However, the numerical inversion of the signals does not depend on their shape, rather than on other facts, like the abundance of a sufficiently well calculated model of the underground. One has to keep in mind, that the potential differences in source geometry have to be seriously considered later on in the interpretation of the (purely numerical) results of the inversion algorithm.

4.3.3 Path-effects

So far I have shown some examples of source models for volcano seismic and induced seismic events that are all suited to explain the generation of low frequency signals. However, it is important to keep in mind that not only the source mechanism itself can generate these LP-signals, but also the *path-effects* can contribute to long periodic oscillatory components within the seismic signals (Cesca et al., 2008).

In figure 4.9 I show how a simple two-layered medium can effect the measured signal with regard to the analysis of LP-events. One impulsively acting source mechanism generates seismic waves. Three seismic data traces of vertical components of receivers at the surface are shown. Their epicentral distances are 0, 200, and 400 km. The impulsive shape of the signal can be observed in the near field at the first receiver. The signals at the farthest station show oscillatory behaviour with main periods of approximately 12

seconds; the detection of such a signal suggests the occurence of an LP-event.

This brief example illustrates the possible ambiguity of *real* LP-events, which show non-impulsive source action, and contributing path-effects. That effect has to be considered within the signal analysis and the interpretation of the final inversion result.

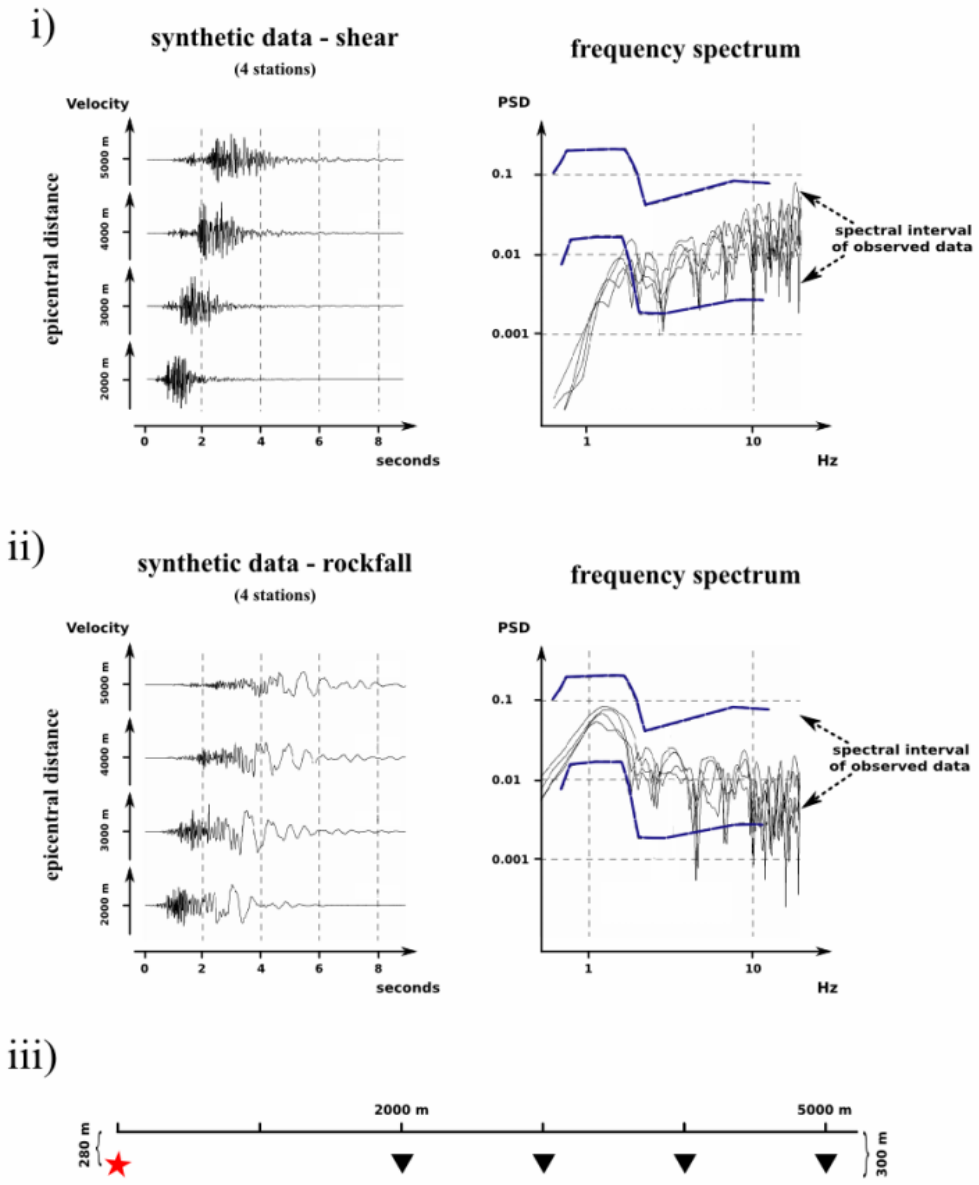

Figure 4.8:
Comparison of synthetic data from each of the two presented source mechanisms: **i)** (vertical) shear crack and **ii)** rockfall. Synthetic velocity data traces (vertical components in overall scaling) and the respective frequency spectra for four stations in different epicentral distances are shown. **iii)** Station geometry. The blue lines in the power spectral densities denote the amplitude range covered by real observed data (c.f. fig. 4.3). Synthetic data in part i) does not show significant signal content in frequency ranges below 2 Hz, data in part ii) has systematically less energy at higher frequencies above 10Hz. Strong dispersion of surface-waves can be observed. Rockfall is assumed to be the more likely source mechanism. (Modified from (Malovichko, 2005))

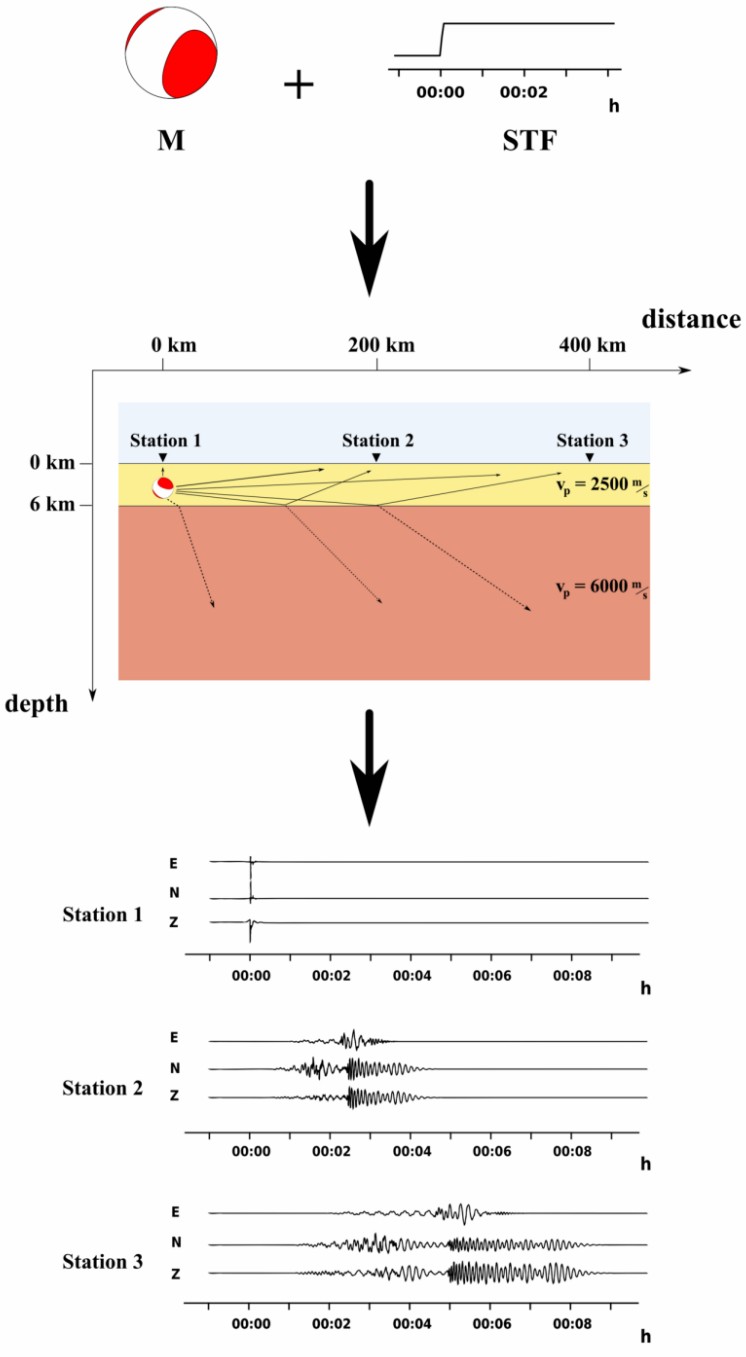

Figure 4.9:
Example for the generation of long periodic signals by path-effects. A seismic source M (visualised by the focal sphere diagrams) with the impulsive source time function STF is positioned in a low velocity layer over a homogeneous halfspace (source depth 3000 m), only the geomtery of two layers influences the wavefield. The signal is recorded at three stations (epicentral distances 0 km, 200 km, 400 km). The oscillatory behaviour (*ringing*) increases with distance, It is caused by the dispersion of Love-waves (channel E) and Rayleigh-waves (channels N and Z). The signals show strong low frequency contents with a main period of approximately 12 s. The underground model section shows the North-Down plane, amplitudes in individual scaling.

5 Inversion of long-periodic signals with *ARCTIC*

In this chapter, I describe the developed algorithm to determine the source mechanism from seismic data. After showing the single steps of the underlying general inversion scheme I will explain how they are practically implemented within the *ARCTIC* software tool.

The algorithm can be used to determine simultaneously the source mechanism and its localisation by a gridsearch method. Furthermore it is possible to extend the inversion scheme to an independent LP-event detection routine. This method is based on the approach described by Sipkin (1994), and it is comparable to the software implementations of Ford et al. (2009), Kawakatsu (1995), or Tajima et al. (2002). The used inverson scheme is a standard approach, which can be found in (e.g. Wang, 2004; Press et al., 2007)

5.1 Configuration of the inversion problem

5.1.1 Inversion scheme for the linear problem

A linear or linearised numerical problem can be written in matrix form

$$\boldsymbol{b} = \boldsymbol{A} \cdot \boldsymbol{x}\,, \tag{5.1}$$

with the sampled data $\boldsymbol{b}$, the mapping matrix $\boldsymbol{A}$ and the parameter set $\boldsymbol{x}$. In many cases one is interested in finding the optimal $\boldsymbol{x}$ to fit observed values, hence one needs an *inversion* of equation (5.1). If $\boldsymbol{A}$ is not a square matrix with full rank, it can not be trivially inverted, the problem is either *under-determined* or *over-determined*. At the handling of seimic data I deal with the latter case, for which a formal inversion can be stated. To do so, I use the *generalised* or *Moore-Penrose inverse* matrix $\tilde{\boldsymbol{A}}^{-1}$

$$\tilde{\boldsymbol{A}}^{-1} := (\boldsymbol{A}^T\boldsymbol{A})^{-1} \cdot \boldsymbol{A}^T\,. \tag{5.2}$$

If the entries of the observed data vector b_j shall be weighted additionally, equation (5.2) is extended to

$$\tilde{\boldsymbol{A}}^{-1} = (\boldsymbol{A}^T\boldsymbol{W}\boldsymbol{A})^{-1} \cdot \boldsymbol{A}^T\boldsymbol{W}\,, \tag{5.3}$$

where $\boldsymbol{W}$ is a diagonal matrix that contains the square-roots $\sqrt{w_i}$ of the respective station weight factors w_i.

The over-determined problem (5.1) has now a solution $\hat{\boldsymbol{x}}$, which is the best solution in the sense of a least-squares optimisation. It is obtained by

$$\hat{\boldsymbol{x}} = \tilde{\boldsymbol{A}}^{-1} \cdot \boldsymbol{b}\,. \tag{5.4}$$

5.1.2 The inversion in the present setup

Following the introduction of the the general concept of inversion, I present here the respective setup occurring in the analysis of seismic data sets. The vital assumptions and approximations are introduced and explained.

The low frequency approximation, as defined in section 3.1.6, is the basis for the setup of the linear inversion problem, but first some aspects of the occurring inversion problem are illucidated with respect to possible other solution algorithms.

If no further restrictions apply, all components of the moment tensor $\mathbf{M}$ have the same time dependency (c.f. equation (3.25)). Numerical calculations and finite sampling of the data lead to the discrete approximation of equation (3.23)

$$\begin{aligned} \boldsymbol{u}(t) &= \mathbf{G}(t) * \mathbf{M}(t) \\ &= \int_{-\infty}^{\infty} \mathbf{G}(t-\tau) \cdot \mathbf{M}(\tau)\ \mathrm{d}\tau \\ &\approx \sum_{i=-\infty}^{\infty} \mathbf{G}(t-\tau_i) \cdot \mathbf{M}(\tau_i) \cdot \Delta\tau_i \end{aligned}\,. \tag{5.5}$$

The spatial dependence as well as the summation over the six components i are dropped here for the sake of better readability; additionally the position of the second index of $\mathbf{G}$ components is shifted ($G^i_j = G_{ji}$) for the same reason in this subsection.

Under the valid assumption of causality, meaning that $\mathbf{M}$ is equal to zero until some source time τ_0 and acts only for a finite duration $N_T \cdot \Delta\tau$, one obtains for a finite observation time

$$\boldsymbol{u}(t) \approx \sum_{i=0}^{N_T} \underbrace{\mathbf{G}(t-\tau_i)\Delta\tau_i}_{=:\boldsymbol{G'}(t,\tau_i)} \cdot \mathbf{M}(\tau_i)\,. \tag{5.6}$$

This discretised linear problem can be written as a matrix equation

$$\begin{pmatrix} u_1(t_0) \\ u_2(t_0) \\ u_3(t_0) \\ \vdots \\ u_R(t_0) \\ u_1(t_1) \\ u_2(t_1) \\ \vdots \\ \vdots \end{pmatrix} = \begin{pmatrix} G'^1_1(t_0,\tau_0) & G'^2_1(t_0,\tau_0) & \cdots & G'^1_1(t_0,\tau_1) & G'^2_1(t_0,\tau_1) & \cdots \\ G'^1_2(t_0,\tau_0) & G'^2_2(t_0,\tau_0) & \cdots & G'^1_2(t_0,\tau_1) & G'^2_2(t_0,\tau_1) & \cdots \\ \vdots & \cdots & \ddots & & & \\ G'^1_R(t_0,\tau_0) & G'^2_R(t_0,\tau_0) & \cdots & G'^1_R(t_0,\tau_1) & G'^2_R(t_0,\tau_1) & \cdots \\ G'^1_1(t_1,\tau_0) & G'^2_1(t_1,\tau_0) & \cdots & G'^1_1(t_1,\tau_1) & G'^2_1(t_1,\tau_1) & \cdots \\ \vdots & \ddots & & & & \\ \vdots & & \ddots & & & \end{pmatrix} \cdot \begin{pmatrix} M_1(\tau_0) \\ M_2(\tau_0) \\ \vdots \\ M_6(\tau_0) \\ M_1(\tau_1) \\ M_2(\tau_1) \\ \vdots \\ \vdots \end{pmatrix}. \tag{5.7}$$

The size of the matrix $\boldsymbol{G'}$ is determined by the length T of the (observed) data trace $\boldsymbol{u}$, the number of data channels $\mathcal{N}_R$, the temporal samplings Δt and $\Delta\tau$ and the length of the temporal evolution of the source, the so-called source duration τ.

The dimensions of $\boldsymbol{G'}$ are $(\mathcal{N}_R \cdot T \cdot 1/\Delta t) \times (6 \cdot \tau \cdot 1/\Delta\tau)$. So if for instance 4 minutes of observational data, sampled with 10 Hz, from 11 channels are assumed to originate from a source mechanism which is defined for a duration of 30 s with sampling 2 Hz, the respective $\boldsymbol{G'}$ has the dimensions 2640×360.

One can see that this is an over determined system, if for every time sample independent data from seven channels[1] are available. This condition may fail in some cases of intrinsic statistical mutual dependence, which leads to systematic problems, so we use data from a larger number of stations in the applications. The equation (5.7) has now the linear form $\boldsymbol{u} = \boldsymbol{G'} \cdot \mathbf{M}$, so one can apply the concept of inversion (see eq. (5.4)) on this system.

The result $\mathbf{M}_i(t)$ represents six time traces, imaging the temporal evolution of the seismic moment tensor components. Assuming a common source time function for all moment tensor components (s. eq (3.25)), the weighted mean of the six components is an estimator of the final source time function.

Unfortunately, experiences with this setup in other software developments have shown that the result, the temporal evolution of the source for every single moment tensor component, cannot be determined in a stable way for all cases (e.g. Cesca, 2010). This ill-posed problem can only be solved under the consideration of further boundary conditions, which would need the implementation of sophisticated algorithms, which are mainly based on appropriate stepwise decompositions of the matrix. The numerical solvers for this inversion problem work iteratively, so I cannot use them for my purpose of *near real-time* analysis, that shall work in a one step process. Thus we have to proceed to an other approach.

Under the assumptions of a point source mechanism (c.f. section 2.1.2.2), whose tem-

[1] Valid under the assumptions, that full waveforms are analysed. If several phases of the waveform are analysed individually, fewer channels are necessary.

poral evolution is described by an impulsive Heaviside step function (c.f. section 3.1.3), I refer to equation (3.28) and the appropriate elementary seismograms as entries of the Greens tensor $\mathbf{G}$ for describing the problem:

$$\begin{pmatrix} u_1(t) \\ u_2(t) \\ \vdots \\ u_R(t) \end{pmatrix} = \begin{pmatrix} G_1^1(t) & G_2^1(t) & \cdots & G_6^1(t) \\ G_1^2(t) & G_2^2(t) & \cdots & G_6^2(t) \\ \vdots & \cdots & \ddots & \\ G_1^R(t) & \cdots & & G_6^R(t) \end{pmatrix} \cdot \begin{pmatrix} M_1 \\ M_2 \\ \vdots \\ M_6 \end{pmatrix} \tag{5.8}$$

or in short notation

$$\mathbf{u} = \mathbf{G} \cdot \mathbf{M} \,. \tag{5.9}$$

Here the entries $G_i^j(t)$ yield the displacement signal as response to a (stepwise) excitation with amplitude M_i at the source point. This formulation combines the advantages of calculation in time domain with the decreased size of the constituting matrices and vectors.

The use of the strong approximation of a localised, impulsive point source appears very rigid, but in the range of (very) low frequencies, to that I reduce the analysis, it works properly. This can be seen for instance in the experienced works of Kawakatsu (1995) or Tajima et al. (2002).

The weighted least squares solution $\hat{\mathbf{M}}$ of eq. (5.9) is given by eq. (5.3)

$$\hat{\mathbf{M}} = \left(\mathbf{G}^T\mathbf{W}\mathbf{G}\right)^{-1} \cdot \mathbf{G}\mathbf{W} \cdot \mathbf{u} \tag{5.10}$$

with the diagonal matrix $\mathbf{W}$ containing the station weights w_r. The latter can be defined for instance by the epicentral distance of the station or its average signal-to-noise ratio. Here the entries of $\mathbf{G}$ are known beforehand, so the non-singular term $\mathbf{G}^T\mathbf{W}\mathbf{G}$ can be calculated in advance. It shows the characteristic of a cross-correlation between GFs, hence it is called *correlation matrix* and it will be denoted $\mathbf{C}$,

$$\mathbf{C} = (C)_{ij} := \int_t \mathbf{G}^T\mathbf{W}\mathbf{G} \; \mathrm{d}t \,, \tag{5.11}$$

$$C_{ij} := \sum_{r=1}^{|R|} \sum_t w_r \cdot G_i^r \cdot G_j^r \cdot \Delta t \,. \tag{5.12}$$

In the latter step, an implicit integration over the time axis has been included. This reflects the samplewise interpretation of time traces for data and Greens functions. The $|R|$ is the total number of all single included channels.

Due to its definition, the correlation matrix $\mathbf{C}$ is a square matrix $\mathbf{C} \in \mathbb{M}_{6\times6}(\mathbb{R})$ with full rank, so its inverse is well-defined and can be directly calculated.

Equivalently the second part of the right hand side in equation (5.10) is interpreted

as a *correlation vector* $\mathbf{b}$

$$\mathbf{b} = (b)_j := \int_t \mathbf{GW} \cdot \mathbf{u} \, \mathrm{d}t \tag{5.13}$$

with the discretised integration in time domain

$$\mathbf{b}_j := \sum_{r=1}^{|R|} \sum_t G_j^r \cdot w_r \cdot u_r(t) \cdot \Delta t \,, \tag{5.14}$$

thus $\mathbf{b}$ is a vector $\mathbf{b} \in \mathbb{R}^6$.

The definition of $\mathbf{C}$ and $\mathbf{b}$ lead to the final and simple equation to solve:

$$\hat{\mathbf{M}} = \mathbf{C}^{-1} \cdot \mathbf{b} \,. \tag{5.15}$$

5.2 Setup of synthetic and real data

Following the approximations from the last section, the definition of the parameters of the elementary seismograms has become simple. By using only very low frequent data, information about local small scale inhomogeneities in the media, the seismic wave passed through, has been filtered out. So it is not necessary to include these spatial features in the underground model. The velocity structure is given by a horizontal stratification of the known main layers of the shallowest regions of the Earth's interiour as shown in section 3.2.2. For all the induced seismic events presented in this work, these velocity models have been used to generate the Green's functions.

In the presence of significant topography and complicated velocity structures, a one-dimensional velocity model is not a valid assumption any more. Therefore a full three dimensional modelling of the underground has been carried out in case of volcanic seismic data, assuming a geometry with the correct surface structure.

The input data consist of seismic displacement traces. These traces are of finite length T, which depends on the specific geometric setup. The data are checked for their general quality in advance, stations that provide data in bad quality (e.g. gaps, systematic problems, or low signal-to-noise ratio) are manually excluded form the inversion process. In figure 5.1 examples for data traces with bad quality are illustrated.

Opposite to other automatic inversion routines (e.g. Dahm, 1996; Heimann, 2011), that are focussed on the analysis of special phases of the seismic traces, I use the full waveform information for the analysis. On the one hand this may introduce spurious deviations from the internally calculated synthetic data with respect to the observed data, due to an imperfect modelling of the medium *Earth*. On the other hand, no potentially misleading picking algorithms, identifying the phases, are used. This would be a source of systematic errors, which is hard to evaluate. In figure 5.2, the parts of seismic data, used for the full waveform analysis are marked in comparison to the choice of distinct phases.

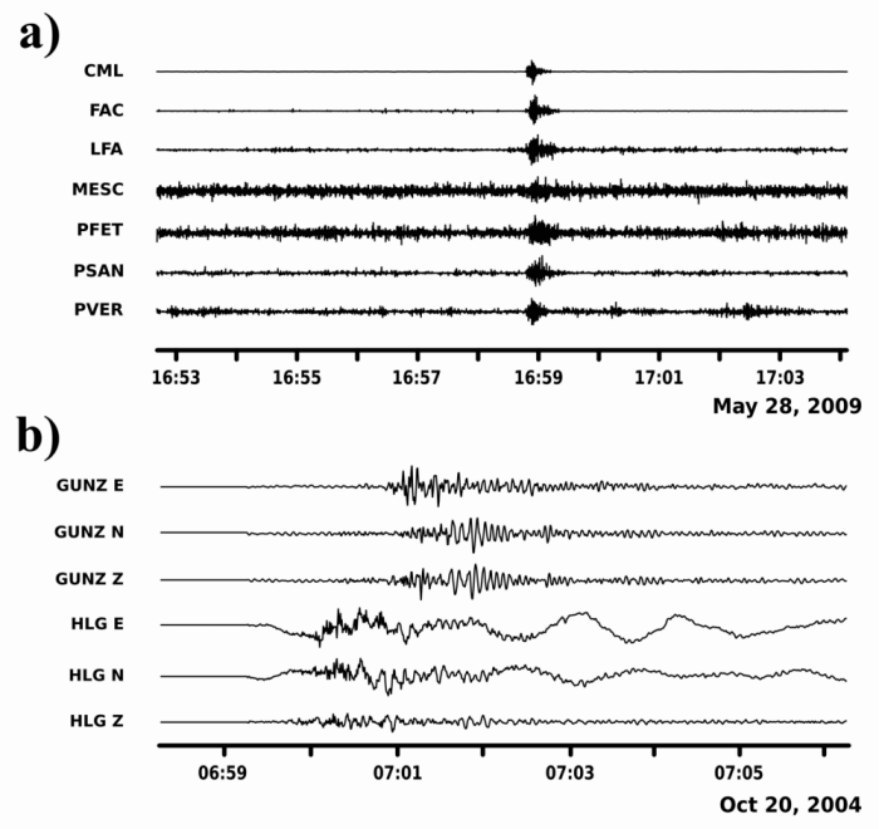

Figure 5.1:
Examples for traces with bad quality. **a)** Data traces with bad signal-to-noise ratio. Traces from stations MESC and PFET are excluded from further processing (Data from azores permanent network, vertical components, frequency filtered with bandpass 1-5 Hz, individual scaling). **b)** Data traces with systematic problems. Horizontal components E and N of station HLG are excluded due to low frequency background signal (Data from GRSN, sampling 4 Hz, signals originate from induced seismic event *Rotenburg*, c.f. section 7.1.1, individual scaling).

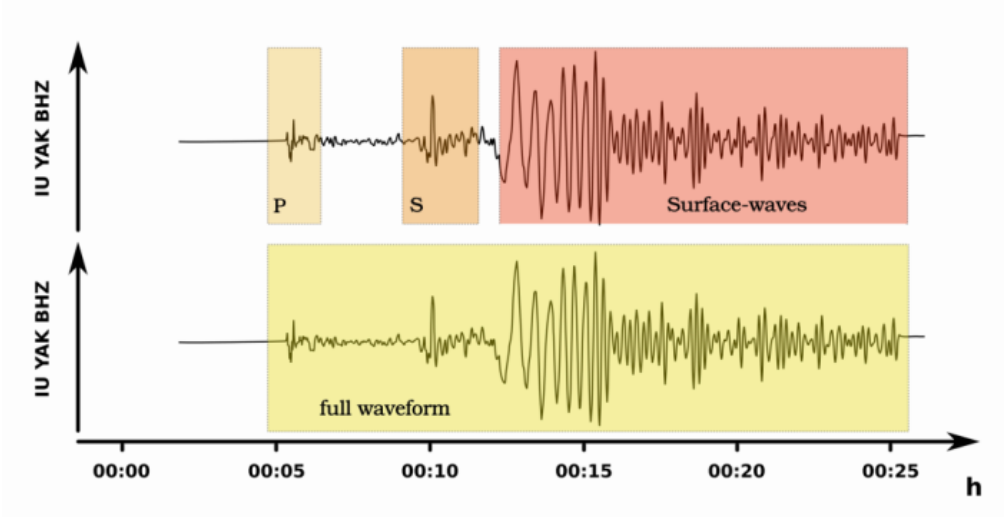

Figure 5.2:
Parts of the waveform, used for inversion algorithms. **upper:** time windows around identified seismic phases within the waveform. Other inversion routines depend on the definition of such time windows. **lower:** time window containing the full waveform information, which is used for the inversion in *ARCTIC*.
The data trace shows the normalised displacement signal of the vertical channel BHZ of station YAK (network IU); the signal originates from an M_w6.7 earthquake in Japan (25° epicentral distance) on 16/7/2007 01:13:27. Time axis is given w.r.t. source time.

In some parts of the data traces, systematically no event-data can be present due to the finite traveltimes of the signals from the source to the stations. To avoid the spurious interpretation of these parts, only subsections of the full data window are considered for the analysis. The temporal limits of these sections are defined by an estimation of the minimal and maximal signal arrival times, based on a linear extrapolation of signal propagation using the lowest and highest wave propagation velocities of the given underground model together with a geometry depending stretch factor. This setup is clarified by the visualisation of the travel time curves in figure 5.3.

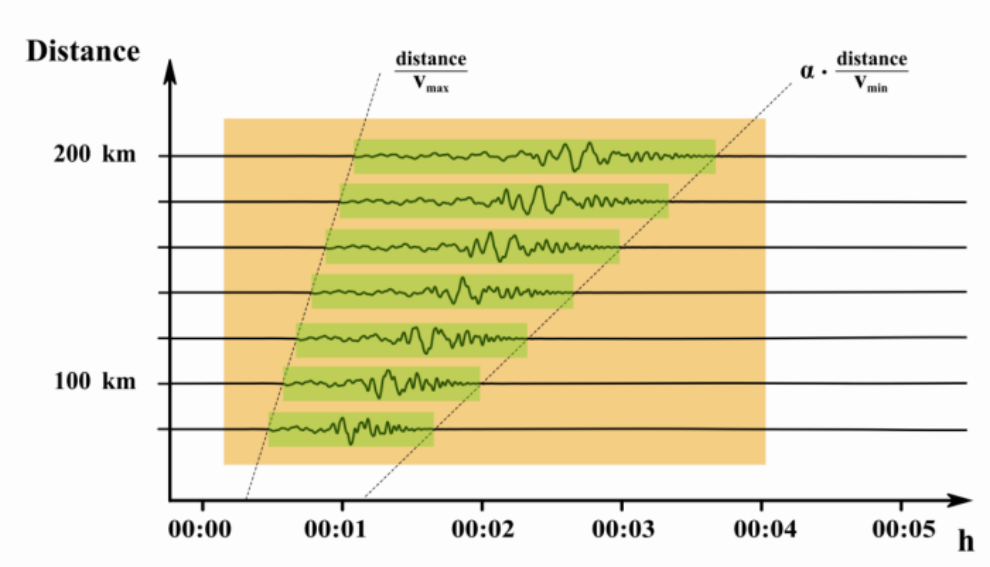

Figure 5.3:
Signals at stations in variable epicentral distances (y-axis) from an event at time zero. Not all information of the signals within the outer time window (saffron yellow) is related to the event. Due to finite traveltimes of the signals, only sections of the main window are chosen to contribute to the analysis (green). The sections are chosen by an estimate of the fastest (left dotted line) and scaled slowest (right dotted line) propagation velocity, leading to estimations of arrival times for the signals. The scaling factor $\alpha > 1$ depends on the respective application (here $\alpha = 1.6$). The traces shown represent individually normalised synthetic data, based on the velocity model in figure 4.9.

One has to be aware that the focussing on long periodic full waveforms leads to a suppression of the body wave content and an overweighting of the surface waves. This includes the fact that the three components of the seismic data traces cannot be interpreted as completely independent regarding their information content, mainly only two independent channels are existing. If one chooses to handle data provided in the orientation *NED*, as done here, no problem arises, if the full data sets are used. For not obtaining an under-determined system (eq. (5.1)), one has to assert that data from at least three stations is used in the analysis, not only two as one may think at a first glance.

A dataset in the orientation (*radial, transversal, vertical*), or (r, ϕ, z), could be reduced to the two components *transversal, vertical*, still holding full information of the surface waves and by this reducing the overall amount of data. In this work I use data in the orientation *NED*. I decided to take the full three channel data, since I want to include all 3D-effects potentially contained in the data, and because it is the native orientation for most of my data sets. So in case of missing data in some horizontal channels, a station is still usable, whereas an additional rotation into the (r, ϕ, z) would be impossible. Furthermore I eliminate the general potential source of errors due to failures in the reorientation process.

5.3 Finding the optimal solution in space and time

5.3.1 The source grid

All theoretical content of this chapter hitherto has been focussing on the solution of equation (5.1) which is describing the seismic signal caused by some seismic source mechanism. Of course this concept is valid, independent of the absolute location of the source centroid. For the analysis of our data the second important task is the estimation of the source centroid position in addition to the mechanism.

This problem is handled by a gridsearch algorithm. So the setup of the analysis starts with the definition of a potential source region. This region is spanned by a three dimensional grid with appropriate spacing, the *source point grid*, as it is sketched in figure 5.4. The grid does not necessarily need to be regular, but in most cases with flat topography and stratified underground, that is the easiest setup and no disadvantages arise from this choice. For the analysis of an area with strong inner heterogenieties and significant surface structure (as for volcanic areas, c.f. section 7.2), more complex grids are set, sometimes intrinsically by the programs that generate the Green's functions databases (s. 3.2.1).

The parameters of the grid are determined by the velocity model of the specific region and the frequency range of the observed data. The Nyquist-Shannon sampling criterion (Shannon, 1949) yields the outer spatial conditions, the grid has to fulfill. This means that the grid-spacing must not exceed the half of the smallest wavelength in the analysed signals.

For every point s of the $\mathcal{N}_s$ grid points the inversion (eq. (5.15)) is carried out. With the obtained parameters $\hat{\boldsymbol{m}}_s$, a forward modelling of the data $\hat{\boldsymbol{d}}_s$ is computed according to eq. (5.8)

$$\hat{\boldsymbol{d}}_s = \mathbf{G} \cdot \hat{\boldsymbol{m}}_s \,. \tag{5.16}$$

The summed squared deviation of the modelled data $\hat{\boldsymbol{d}}_s$ from the observations $\boldsymbol{u}$, summed over all channels $\mathcal{N}_r$ is defined as *residuum* Res_s for this source point

$$\mathrm{Res}_s := \sum_{\mathcal{N}_r} \sum_{t} (\hat{\boldsymbol{d}}_s(t) - \boldsymbol{u}(t))^2 \cdot \Delta t \,. \tag{5.17}$$

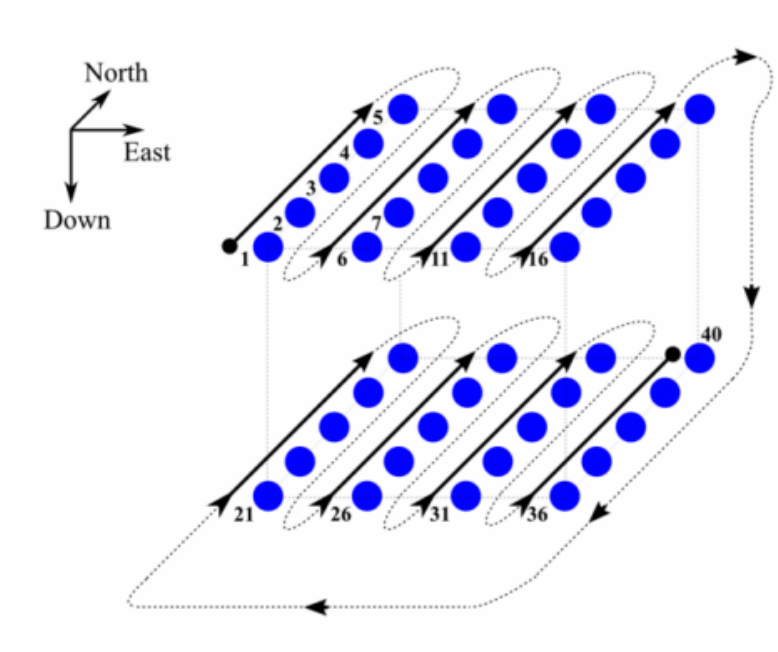

Figure 5.4:
Structure of the source point grid in case of a regular, cuboidal setup. The source points are sorted successively in the sorting order North, East, Down .

For normalisation, this value is divided by the summed square of the observations, afterwards, subtracting this value from unity is defining the *variance reduction* VR_s

$$\mathrm{VR}_s := 1 - \frac{\mathrm{Res}_s}{\sum_{\mathcal{N}_r} \sum_t \boldsymbol{u}(t)^2 \cdot \Delta t} \,. \tag{5.18}$$

The source point with the highest value of VR_s is assumed to be the best estimator for the source centroid location.

5.3.2 The moving time window – correction mechanism and allowing for continuous inversion and detection

In the given setup as described before, the algorithm is designed for the inversion of a data set of pre-defined length. This functionality is now slightly extended in two steps. The first step includes the variation of the data traces in time, by shifting them within a given range from the externally estimated source time. The second step enables the continuous handling of data streams allowing to use the developed algorithm as a detection routine.

For the first step, the time window of data is separated into smaller sub-windows, each of them belonging to one specific time of origin. All the sub-windows are fully analysed subsequently, for each single window an optimal solution is calculated. This procedure is

illustrated in figure 5.5. The highest occurring value of the respective VR values in total

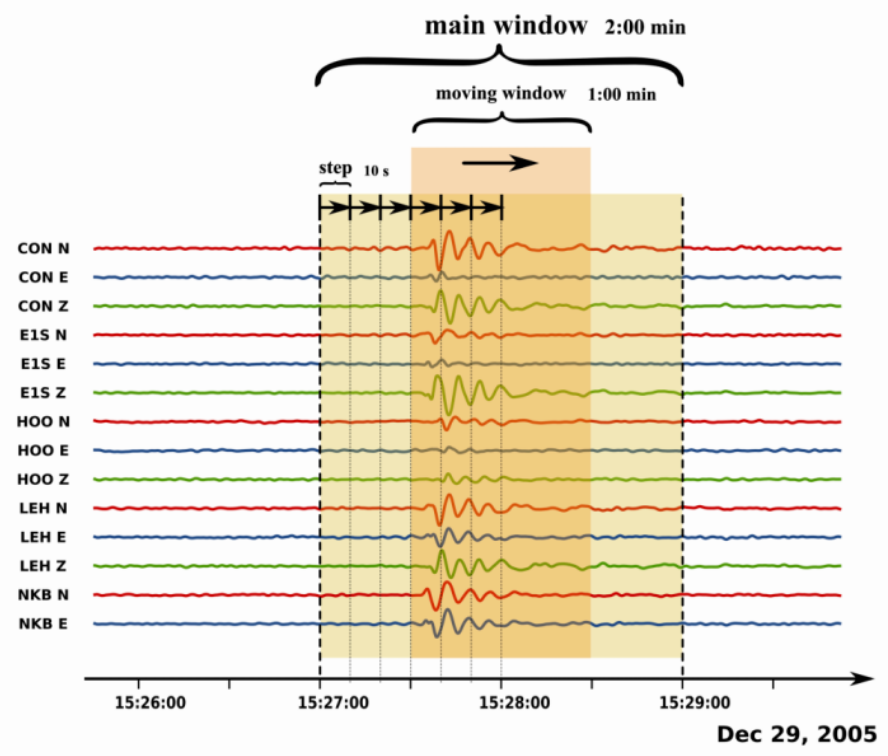

Figure 5.5:
The moving time window principle: A main time window (yellow-greenish, 2:00 minutes long) is defined. Therein a smaller sub-window (dark yellow, 1:00 minute) is set. The latter moves in defined steps (10 seconds) through the main window. For each position of the sub-window, the data contained in it are analysed. Traces are data from Mt. Erebus, frequency filtered with bandpass 0.033 - 0.2 Hz, modified amplitudes (c.f. section 7.2).

is interpreted as the indicator for the best estimation of the source mechanism. This defines the best absolute solution within the search algorithm, which now also includes the hypothetical correction for the source time. Figure 5.6 illustrates this estimation of the best solution for different time windows. By applying this systematic process, potential time shifts in the GFs due to wrong velocity models are considered in first order.

The size of the step between the consecutive time windows has to be chosen as small as possible in order to avoid under-sampling with respect to the dominant periods in the signal. If the step size exceeds the duration of half a period, a possible correct origin time with a high VR value is skipped, but two sub-windows where the signals are almost exactly out of phase are analysed instead, both yielding low VR values for the wrong origin times. In reality the step size is mainly determined by the duration of the inversion calculation within each window. This can be influenced by the setup of the source grid, the lengths of the time windows, and the respective computing hardware.

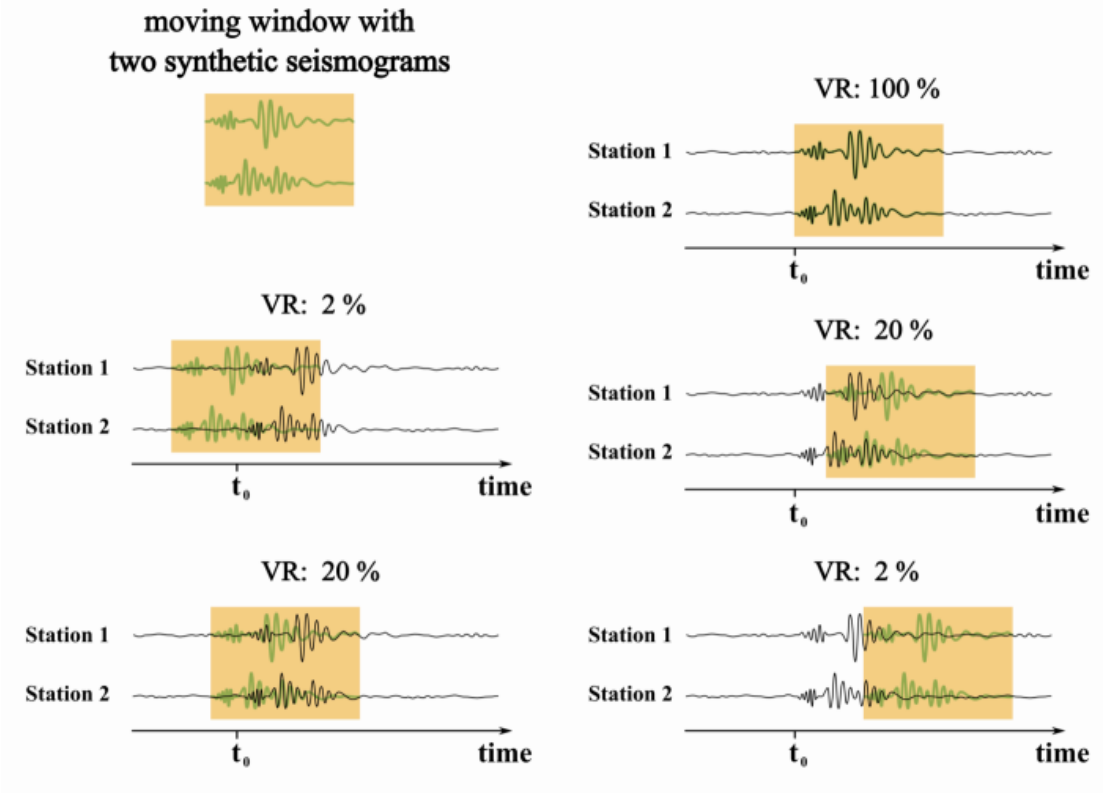

Figure 5.6:
Visualisation for the interpretation of the variance reduction VR. In the upper left, a yellow time window is sketched. It contains two synthetic seismograms for the stations 1 and 2. From the mid-left to the lower right sub-figure, sorted in vertical order, the yellow window moves along the real data observations (black). By the correlation between the synthetic and the real seismograms the VR is determined. The better the correlation within the respective time window position the higher is the value of VR. In case of complete agreement (upper right), VR reaches the maximum value of 100%.

An extended application of the approach of successively inverting moving time windows allows for achieving one main goal of the presented algorithm: the combination of the inversion of seismic data from a distinct event with an automatic detection of the latter. The setup is following the idea shown in (Tajima et al., 2002; Kawakatsu, 2003).

For the analysis of a continuous stream of seismic data, successively overlapping time windows are defined. Within these the combination of inversion routine and gridsearch as described before are carried out. Therefore also data not originating in seismic events are inverted; their shape does not suit any of the event-related elementary seismograms, thus the respective maximal variance reduction VR_{max} of these time windows is very low. In case of a real seismic event, the analysis will yield a significantly higher value for

the VR_{max}. By defining a threshold value VR_{ev}, an event is defined to be occurred, if $VR_{max} > VR_{ev}$. The exact definition of the value VR_{ev} is depending on the respective application. For instance the continuous analysis of synthetic noisy data (c.f. section 6.5) yields a distinct time series of values $VR(t)$. In that case, the VR_{ev} is defined to be 60%, which is significantly above the average level of approx. 2%. The schematics of the event-detection with this setup are shown in figure 5.7.

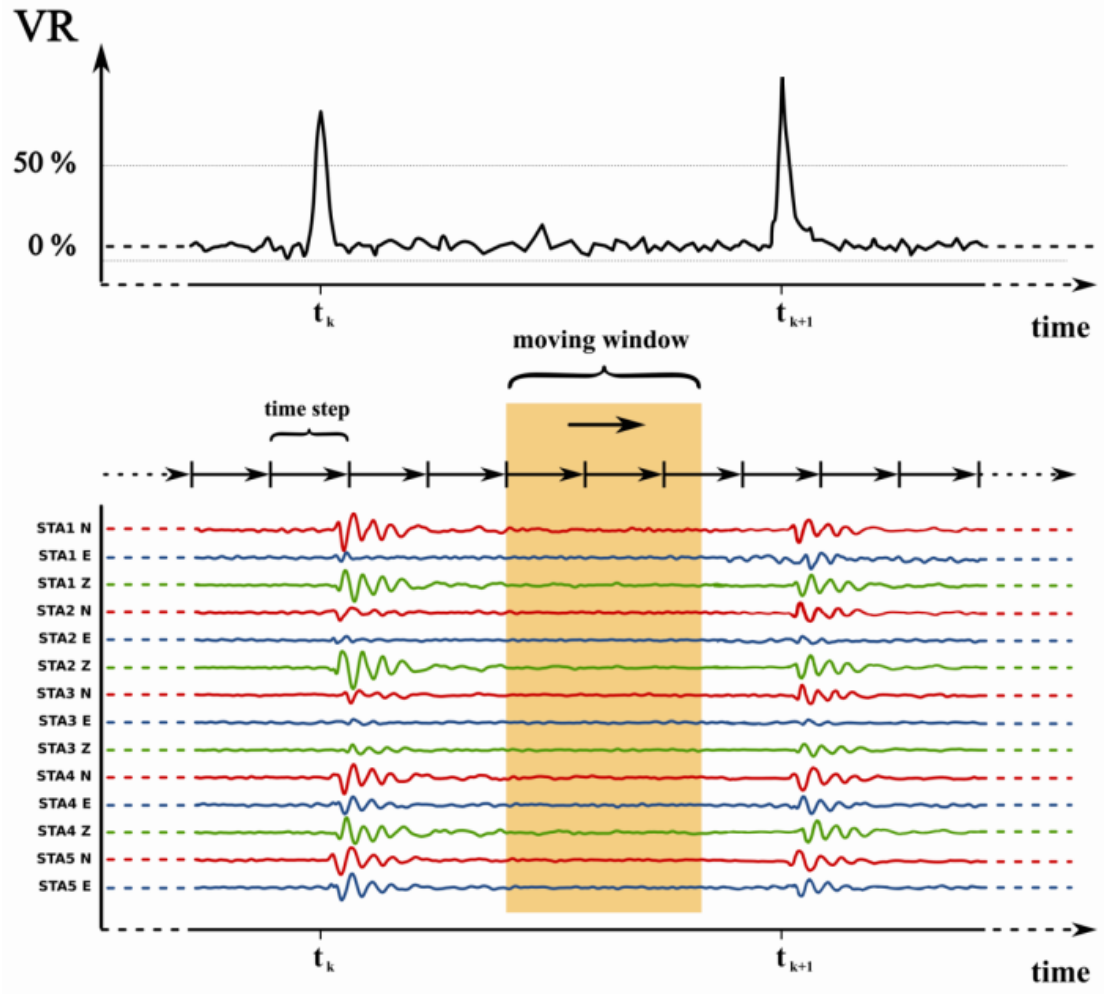

Figure 5.7:
The moving time window principle for the analysis of a continuous data stream. The analysis window (yellow) moves on the time axis in steps of pre-defined length. Data are analysed within the window for each position. Successively the full data stream is analysed, therefore at some time signals from events (at t_k and t_{k+1}) lie within the window. The application of the inversion yields high values VR (upper part), this defines the detection of the events. (Traces are modified data from Mt. Erebus, names of channels are arbitrarily set).

5.4 Implementation in ARCTIC

This section shows the numerical implementation of the successive inversion steps within the *ARCTIC* software. At the beginning, a general overview is given, which is followed by the description of two steps in the application, one is required for the setup of the routine in advance and the second one is the actual processing of the data.

The *ARCTIC* software is written in Python (Van Rossum, 2003; Lutz, 2006; Oliphant, 2006), thus a high portability between different hardware configurations and operating systems is guaranteed. The chosen programming language enables the use of a modular structure, as well as the nested definition of classes and functions. The computational speed of routines in this language is sufficiently high for most practical applications.

ARCTIC is designed as a command line tool. All parameters for the processings are given in two configuration files; one for the setup of geometry and Green's functions, another for the inversion itself. As input data, miniSEED formated traces have to be provided. The output consists of information about source location, focal mechanism solution and source time.

An overview over the structural processing is provided in figure 5.8, it will be described in the following in greater detail.

5.4.1 Setting the geometry and data structures

As a first step, the geometrical setup of the problem is implemented. The region of interest is defined, which is sampled by a grid of possible source points. The grid point positions can be given either directly by external information, or it can be set in a regular three dimensional lattice around a defined centre point. The grid spacing and the absolute extension in all directions has to be provided in the configuration file in the latter case.

Afterwards, information about the stations' positions is collected. If desired, an optional set of stations weights can be provided. In the case of synthetic tests, an arbitrary station configuration can be generated.

After having set up the source-station geometry, the GFs files must be set up. Its spatial and temporal parameters must suit the demands of the respective datasets, especially with respect to sampling rate and duration. These vary from case to case, so a rough knowledge of the present configuration is needed.

Two possibilities show up for this purpose. In case of a one dimensional velocity model and the use of tools like QSEIS (c.f. section 3.2.2), their result is a gridded set of GF for a sufficiently large set of source depths and epicentre-station distances, which are generated in advance. From this set, the respective GFs for the given geometry are read out and reassembled according to the data structure shown in section 3.3. Since of course not every real station distance can be covered exactly within this database, I use the entries corresponding to the distance which is nearest to the real one rather than an interpolation approach, this is again justified by the restriction to long periodic signals.

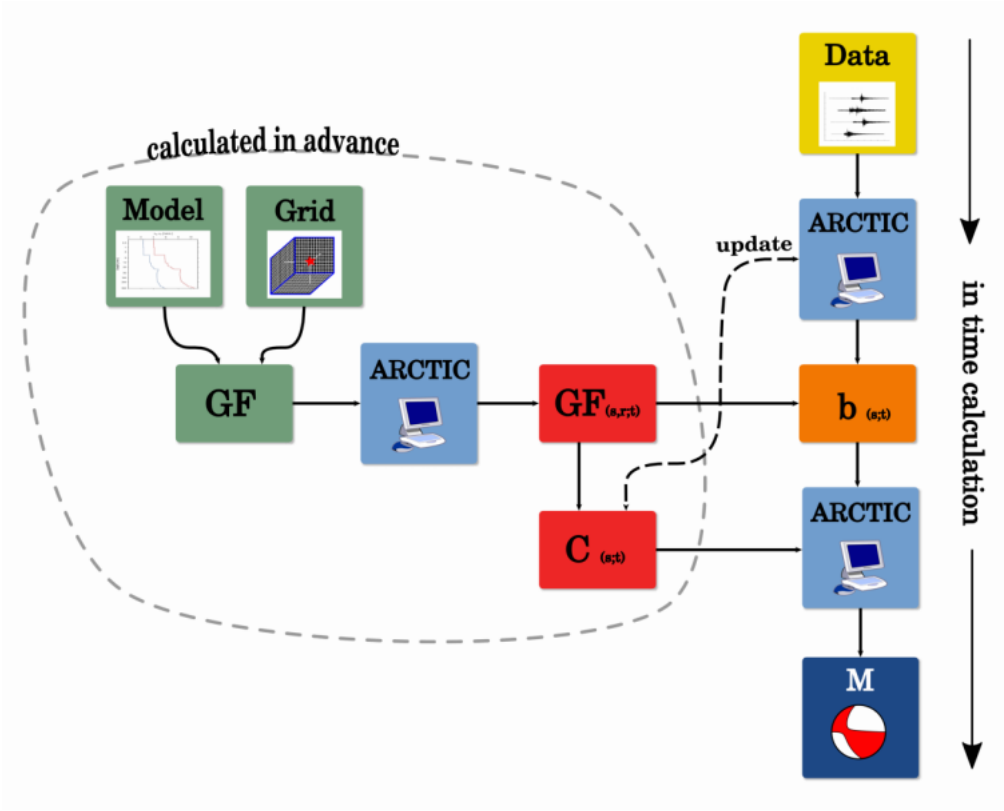

Figure 5.8:
Flow chart diagram that shows the general processing steps of ARCTIC. The part which is enclosed by the dashed line is calculated in advance; the remaining part to right is describing the in-time calculation steps. Colour coding is defined as: yellow for direct data involvement, light blue for calculation steps of ARCTIC, dark blue showing the output; orange and red mark the involvement of the structured GF database.

For the application of GF generation tools, which include three-dimensional modelling, the final source-station geometry must be known in advance of the generation. Therefore the calculation of GFs can be initiated earliest at this step of the processing. The GFs files are setup either directly from the output of the generating tools or accordingly reassembled in a second step.

So far I have the ready to use GFs files, files containing information about the source grid position, the stations' location, and their weights. Especially the first two information do not vary during the analysis of several datasets at one and the same site.

In the next steps, I show how the analysis of a given dataset is carried out. To do so I stick to the handling of data with finite length, on which consecutive time windows are defined, within which the results are obtained.

Data are read in from miniSEED format files. This format has the advantages that it is easy to handle thanks to wide spread standardisation, software for the (yet manual)

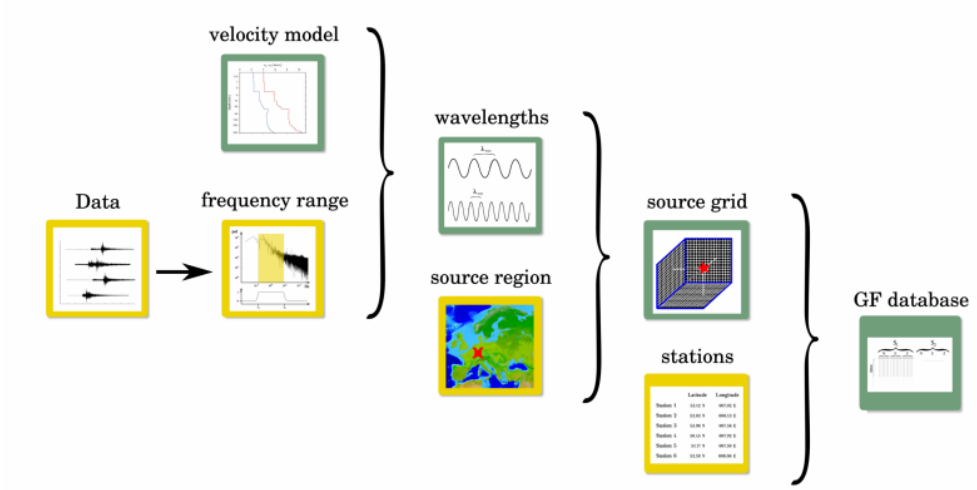

Figure 5.9:
Setup of the GF database. Information about data (yellow) and structural modelling (green) are combined to the GF database files, prepared to be read in for inversion. Assumptions on the internal structure of the Earth are combined with the frequency range under consideration, leading to an estimation of the maximal and minimal wavelengths of the signals. Together with the spatial extension of the possible source region this again enables the definition of a reasonable source point grid. The Green's functions for each pairwise combination of source grid point and station location are calculated or read from external databases.

handling and checking of the data quality is available (Aster et al., 2005; Lomax, 2008; Heimann, 2009; Beyreuther et al., 2010), obtaining data from online resources (IRIS Data Management System, 2010) or data loggers (Earth Data) is uncomplicated, and finally it holds the required meta-data. The latter includes station identification, sampling, time spans, and occurrence of data gaps (SEED, manual, 2010). Data can be stored in some standard database file structure, and for each analysis time window the appropriate data streams are found therein automatically according to their header information.

For the initialisation of the inversion, it must be assumed that the source time of an event is approximately known, for instance by detection of some external routine (Ohrnberger, 2001; Beyreuther and Wassermann, 2008). Data are given in files of arbitrary length around this source time; the location of the data files is an important parameter in the configuration file. Then a main time window is defined, within which data must be completely available. This full dataset is covered by a set of smaller time windows as sketched in section 5.3.2. The lengths of these small time windows, as well as the step size between two successive ones, are given in the configuration file.

As already stated, I restrict the analysis to LP-events. There are no exact definitions for frequency boundaries, thus they are manually set in accordance to the given dataset. It is assumed that this frequency band is not depending on the single event, but it can be

held constant for a given geometry. Two corner frequencies for a bandpass are given as parameters.

Furthermore it can be chosen, wether data shall be weighted or notr. Weighting can be carried out either by information provided in an external file or just by distance of the station; if the latter applies, the square root of the distance in metres is taken as weighting factor for counterbalancing the geometrical damping.

The last vital information contained in the configuration file is the structure of the file storage. A base directory is needed to be defined, within which respective paths for the data, the GFs, temporal files, and the results are created.

5.4.2 Running the analysis

As the first internal step of the inversion procedure, the configuration file is read in. All its information is stored inside a dictionary structure, and it will be available throughout all processing steps. The desired file structure is set if not yet present.

Then the GF database is read into an array; the GFs are downsampled in time if suitable. Additionally, they are tapered and frequency bandpass filtered (c.f. section 5.4.4). This process has to be carried out, if the setup has changed in some regard, thus in the optimal case it happens only once in the beginning of the first run. To avoid the time consuming setup of this array in further applications, the resulting array is written to a file, so it can easily and fast be re-read later on.

From the GFs, the correlation matrix $\mathbf{C}_s$ for each source point $s \in$ is calculated (see eq. (5.12)), and its inverse $\mathbf{C}_s^{-1}$ is generated. Both the matrices and their inverses are stored in an array $\mathbf{C}$ and $\mathbf{C}^{-1}$. The former one is written to file, too.

The tensor $\mathbf{G}$ is internally indexed by G_{rs}^{ci} with

$$\begin{aligned} \text{source index } s \quad &, \quad s \in S \\ \text{station index } r \quad &, \quad r \in R \\ \text{channel index } c \quad &, \quad c \in \{1,2,3\} \\ \text{moment tensor component } i \quad &, \quad i \in \{1,2,3,4,5,6\}\,. \end{aligned} \tag{5.19}$$

The definition of $\mathbf{C}^{-1}$ is now followed by the setup of the input data traces. The software searches inside the given locations for data available for the length of the full time window. From the header information of the mini-Seed format data files, the appropriate files are chosen. The appropriate data are read into an array ($\mathbf{u}$ in eq. (5.9)), where incomplete data traces are ignored. If necessary, data can be integrated (restituted). Tapering and filtering are applied to the data identically to the handling of the GFs. Stations that shall not be taken into account for the analysis – for whatever reasons – can be provided in the configuration file, their data will not be read in. All stations that have been implied in the setup of the GFs array, but do not contribute with analysable data are reason to spurious entries in the correlation matrix and its inverse. The matrices are corrected with regard to the missing channels. The same holds in principle for a adaption of weighting factors: if they have changed after the last run, $\mathbf{C}^{-1}$ is updated, too.

From the arrays containing the GFs and the data, the correlation vectors $\mathbf{b}_s$ are set up according to eq. (5.14) for each possible source point.

With all the data necessary for the inversion in memory, the estimation of the solution can start. For every source point, the calculation of the source mechanism is done by equation (5.15). The variance reduction value (5.18) belonging to each solution is stored, so that after the run over the complete source grid one overall best solution can be determined. The source grid can be reduced to a subset in advance, so that the computation time can be decreased. This is a useful option, if the source points of subsequent events show up to be confined in space, so that unnecessary calculations can be avoided.

The final result of the inversion is given on the one hand as a list of data, describing the result of the inversion. So one obtains the full moment tensor information for the estimated source location and time. On the other hand the tool yields a set of meta data which contains the information about the outer setup. For instance the list of stations whose data were used, the temporal spacing, the exact storage location of the used data traces within the database and so on. All information is additionally collected in an output file in `xml`-format. This is stored locally and can be read out by an appropriately designed style-sheet. Finally, this information can be sent to and collected in some (external) event based database for further analysis of the specific event (Barsch, 2009).

The steps described in this section are illustrated in the flow chart map in figure 5.10. Furthermore a visualisation of pointwise inversion results on the grid points, given by focal sphere diagrams for the horizontal layer of the source grid around the estimated optimal source point, can be generated (Wessel and Smith, 1999) and stored. Synthetic data traces based on parameters of the the estimated source mechanism are generated and stored in mini-Seed format files, so they can be visually compared with the real input data set very easily.

5.4.3 Application of the moving time window approach

For the standard application of the algorithm, an event and its origin time is needed to be detected by some external software (Withers et al., 1998; Ohrnberger, 2001; Beyreuther and Wassermann, 2008). This time stamp is provided at the initialisation of *ARCTIC* as a calling argument. A time span around the given time stamp is assumed to hold the true event time. Thus, depending on the parameter setup, a sufficiently large main data window is chosen within which the analysis is carried out, and the raw data are read in from the file system. The time spans of the sub windows are determined from the parameter configurations, and a loop is set up to invert every subset of the data as described in section 5.3.2. The tapering and bandpass filtering are subsequently applied to these subsets according to section 5.4.4. This is done identically for the GFs, whose length is determined by the sub-window duration rather than the length of the overall time span.

In order to use the *ARCTIC* as a detection routine in the case of a continuous data

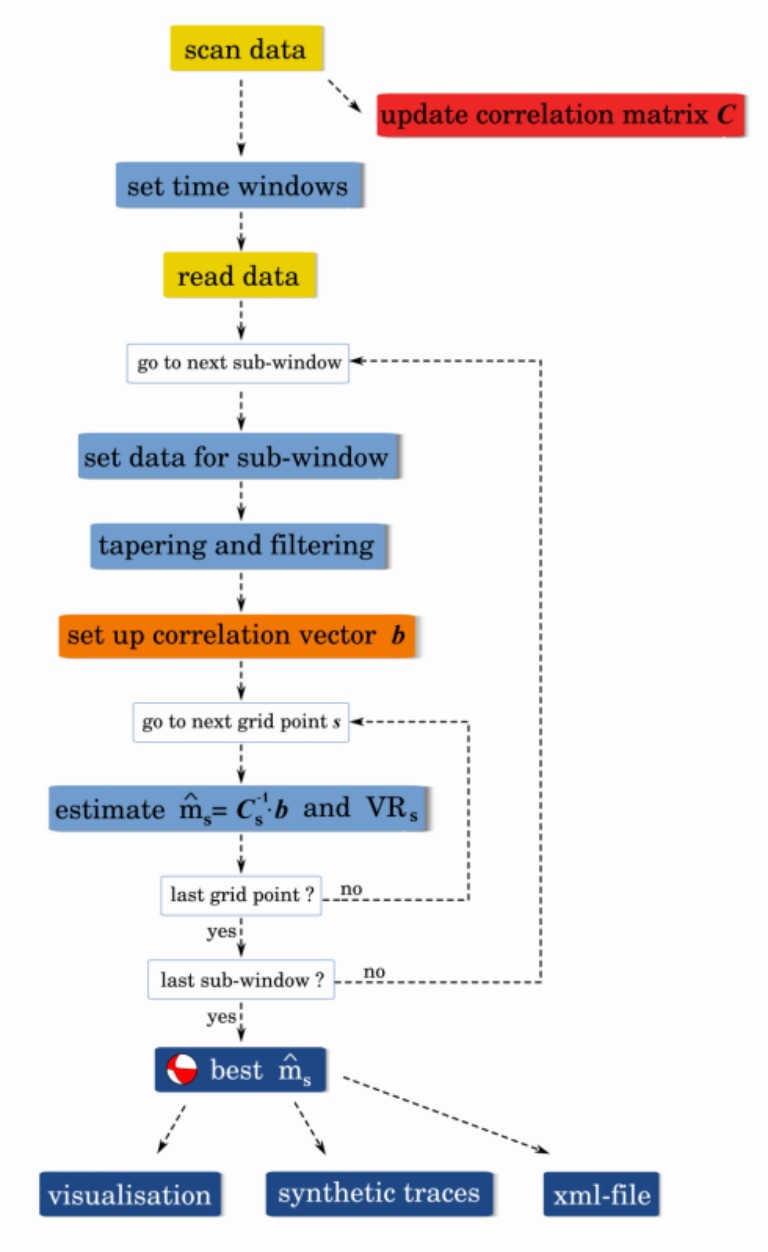

Figure 5.10:
Flowchart map for the single steps of the inversion. Colouring is in accordance to figure 5.8. From top to bottom: data are read in for a pre-defined time window; for every sub-window, data and GF are prepared and combined to set up the correlation vector, with which the inversion is carried out; after the loop over all source grid points and all sub-windows, the best inversion result is taken as final result; all parameters are stored and visualisations of the solution are plotted.

stream, the lengths of the moving time windows as well as the step size in-between them have to be adjusted to fulfill the needs of a (near) real time coverage of the data stream, as shown in fig. 5.7. A crucial point is that the data traces must be analysed within a short time which allows to work on the data stream in overlapping time windows, so that one is on the safe side, not to miss events due to too long jumps in the reading of the data. Therefore the chosen time window must not be too short, so that the analysis takes shorter time than the real time actually passed.

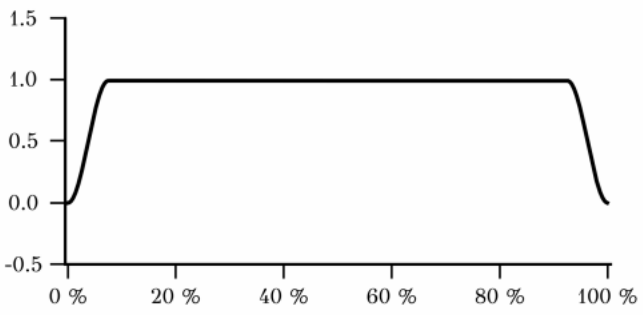

Figure 5.11:
Tukey window function with steepness factor 0.85, used for time domain tapering throughout ARCTIC. The x-axis shows relative values of data trace length.

The scope of running *ARCTIC* continuously, and by this independently detecting LP-events, does not require many modifications of the basic inversion algorithm. Data coming into the local system by some data stream, as for instance via SEISCOMP3 (Weber et al., 2007), are read in and stored into a data file structure by some external algorithmr. In parallel, the continuously running *ARCTIC* software successively defines analysis time windows. Their respective end times are delayed with respect to the current real time to some extent, so that the saving process of incoming data is asserted to be finished. The exact delay is constant for a given setup, and it depends on the external method used for streaming and saving the data. The beginning of the respective analysis window is defined by its end time and the given window length. Data are analysed within this time window as described before. If an event is detected by a VR value that exceeds the pre-defined threshold, all information and meta-information are sent to an event database. The incoming data file is therein handled as an event-trigger and can be further processed, e.g. for visualisation. After the analysis of the current window has been finished, a new analysis window is set, and the inversion scheme restarts.

The feasibility and utilisation of this concept in general is shown in section 6.5 based on synthetic data tests. Finally, an example event is analysed in section 7.3 as a first application on real data.

5.4.4 Some technical steps

The taper function and the frequency bandpass filter

All data sets included in the analysis steps are of finite length. So to avoid spurious frequency filter effects, data as well as elementary seismograms are tapered with a *Tukey window* tapering function $T_\alpha(x)$:

$$T_\alpha(x) = \begin{cases} \frac{1}{2}\left[1+\cos\left(\pi\left(\frac{2x}{\alpha N}-1\right)\right)\right] & \text{when } 0 \leqslant x \leqslant \frac{\alpha N}{2} \\ 1 & \text{when } \frac{\alpha N}{2} \leqslant x \leqslant N(1-\frac{\alpha}{2}) \\ \frac{1}{2}\left[1+\cos\left(\pi\left(\frac{2x}{\alpha N}-\frac{2}{\alpha}+1\right)\right)\right] & \text{when } N(1-\frac{\alpha}{2}) \leqslant x \leqslant N \end{cases} , \tag{5.20}$$

with $0 \leqslant x \leqslant N$ and $\alpha \in [0,1]$ describing the steepness of the window flanks. The general shape is shown in figure 5.11.

The frequency filtering is carried out by a recursive Butterworth filter of fourth order in time domain, which is a causal digital IIR filter (Allen and Mills, 2004). It will be seen in the analysis of synthetic and real data (chapters 6 and 7) that the estimation of the correct source time of a seismic event is an important parameter, which influences the stability and robustness of the overall inversion and gridsearch solution. In order to suppress spurious influences of the choice of filtering algorithm, GFs and data are frequency filtered identically.

However, the Rayleigh-wave content of the signal is dominant in the low frequency ranges of the signals of the presented case studies, and these waves can show strong dispersion. There may be an unresolved influence by frequency depending phase shifts due to the applied filter. It is necessary to test other filters instead, which preserve the correct phase position rather than the causality of the signal. An optimised solution would consist of a filter routine, which includes both the conservation of phases and causality. This could be achieved by a combined forward- and backward-filtering of both the GFs and the respective data section (e.g. Buttkus, 2000; Allen and Mills, 2004).

The lengths of the time windows in use are not changed between consecutive runs, so the filter coefficients, which are needed for the filter setup are calculated once during the first use and are then kept in memory. This leads to a significant decrease in computation time in comparison with the naive approach of a multiplicative window filtering in frequency domain. The routine for finding and applying the filtering are part of the `SCIPY.SIGNAL` module of Python (Jones et al., 2001).

Updating the correlation matrix C

In real data applications not always all data streams from all stations are available for inversion due to technical failure. Nevertheless, their contribution has already been included in the setup of the correlation matrix $\boldsymbol{C}$ (see sec. 5.1.2). So for each time step it has to be checked, which stations currently provide valid data. If no (or incomplete) data are detected, this information is used to update $\boldsymbol{C}$. As one can see in its definition (equation (5.11)), the stations' data enter additively; so for correction, their respective parts can simply be subtracted. If $\mathcal{N}_0$ is the number of stations without valid data, the updated matrix $\boldsymbol{C}_{up}$ is given by

$$(\boldsymbol{C}_{up})_{ij} = (\boldsymbol{C})_{ij} - \sum_{r_0=1}^{\mathcal{N}_0} \sum_{t} w_{r_0} \cdot G_i^{r_0} \cdot G_j^{r_0} \cdot \Delta t \,, \tag{5.21}$$

with the weighting factors w, the $G_i^{r_0} \in \mathbf{G}$, and their respective length T. This update has to be done for every setup, which does not correspond to the original set of stations and their respective weights. Thus the most general or most probable configuration is chosen for the first setup of $\boldsymbol{C}$.

6 Synthetic tests

The inversion method and its implementation (*ARCTIC* tools) has been tested under several considerations. In the following, these tests are explained and the results are shown, demonstrating the functionality and features of the software.

6.1 Setup

I split the synthetic data testing into different stages. At the first stage, I ensure the general functionality of the software (6.2). Therefore, I set up simple inversion schemes, where the underground model for generating and analysing the data is held constant. The second stage deals with the influence of different velocity models on the inversion result (6.3). At the third stage, the handling of a three dimensional geometry and its influence on the inversion result is examined (6.4). Finally, the ability of *ARCTIC* to work as an independent, continuously running analysing and detection algorithm is verified (6.5).

6.1.1 Generation of synthetic data

In order to carry out the following tests, a set of synthetic data is needed. This is calculated on the base of a previously generated set of GFs (elementary displacement seismograms). A focal point and focal mechanism is chosen to simulate a real seismic source. This mechanism is defined as

$$\mathbf{M} = (-9, 27, -18, 2, 18, 19) \cdot 10^{15} \text{ Nm} \ , \ \ M_0 = 3.54 \cdot 10^{16} \text{ Nm} \ , \ \ M_w = 5.00 \ , \quad (6.1)$$

representing a shear crack with strike 327°, dip 72°, slip-rake −117°. This geometry coincides with the inversion result in (Dahm et al., 2007) for the Rotenburg event (s. section 7.1.1).
The source time is set to 18.05.1983; 12:00:00 o'clock.

The $\mathbf{M}$ is multiplied with the appropriate components of $\mathbf{G}$, yielding synthetic data traces with the same time-length as the Green's function $\mathbf{G}$. In order to apply the concept of the moving time window, these traces are extended into both directions. For a suitable time span before the source time, the traces are set to zero. At the end the traces are extended with arrays of constant values equal to the respective last values of the original traces. This process is illustrated in figure 6.1. Finally these traces are tapered to suppress numerical artifacts.

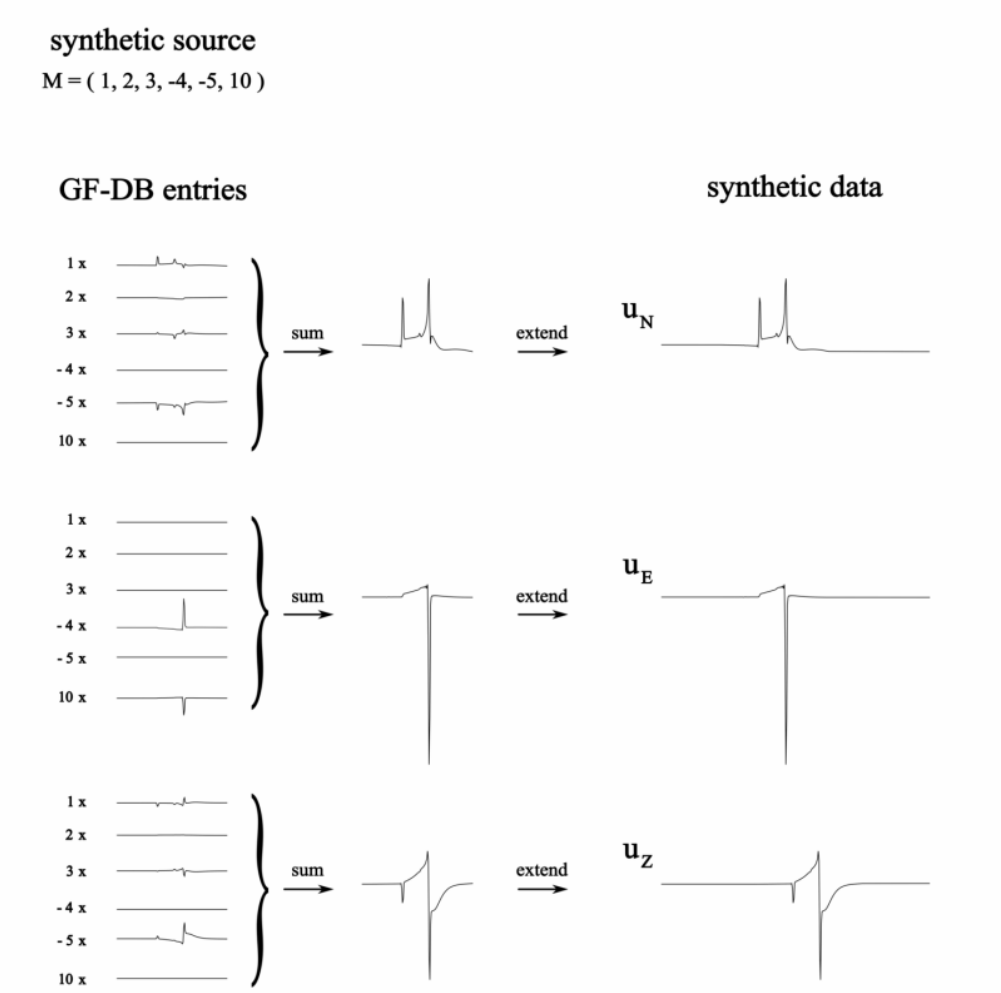

Figure 6.1:
Setting up synthetic data for one station. Traces $\boldsymbol{u}$ for 3 channels NEZ are built from a linear combination of 18 GFs (left). Weighting factors are defined by entries of the moment tensor $\mathbf{M}$ (see eq. (5.9)) – here $\mathbf{M}$ = (1,2,3,-4,-5,10)). Synthetic data are extended to arbitrary trace length, resulting in the final displacement data (right), overall scaling applies.

6.1.2 Spatial and temporal setup

The chronological and geometric setup for the synthetic tests in sections 6.2 and 6.3 is as follows:

- Sampling rate of data and GF is 2 Hz. Length of GF traces is 100 s, total length of data traces is 1 h.
- If frequency filtering is applied, data are filtered with a fourth order Butterworth bandpass between 0.05 Hz and 0.2 Hz.

- The wavelengths' total range for the used velocity models is given by: $\lambda_{\min} = 1.5$ km , $\lambda_{\max} = 50$ km.
- The source point grid is rectangular with a grid spacing of 500 m in horizontal directions and 2000 m in vertical direction, the latter beginning in a depth of 2000 m. This geometry suppresses spatial aliasing effects.
- The horizontal position of the grid's center is in the north eastern hemisphere at (50° N ; 10° E).
- The spatial extent of the grid is $11 \times 11 \times 5$ points.
- The stations' positions are set at the surface in concentrical circles around the epicenter in distances 1, 5, 25, and 100 km. On these circles the stations are located at the azimuths 0°, 45°, 90°, 135°, 180°, 225°, 270°, 315° as seen from the source location. This provides a regular coverage of different distances and angles, avoiding spurious influence of asymmetries on the outcome of the inversion.
- The artificial point source is located in the centre of the source grid in the depth of 6000 m (grid index 303).
- The moving time window has a length of 100 s. The data are analysed in the interval ±10 s around the correct source time in steps of 0.5 s. This interval reflects the extended support of the peak in time series of VR values in the case of an optimal solution (sec. 6.2.1). The analysis of the given interval enables the detailed study of the deviation from that optimal case. The large scale temporal evolution of the VR value time series is studied by the analysis of a continuous data set (sec. 6.5).

An overview of the station setup is given in figure 6.2. The source point grid and the location of the artificial source are illustrated in figure 6.3

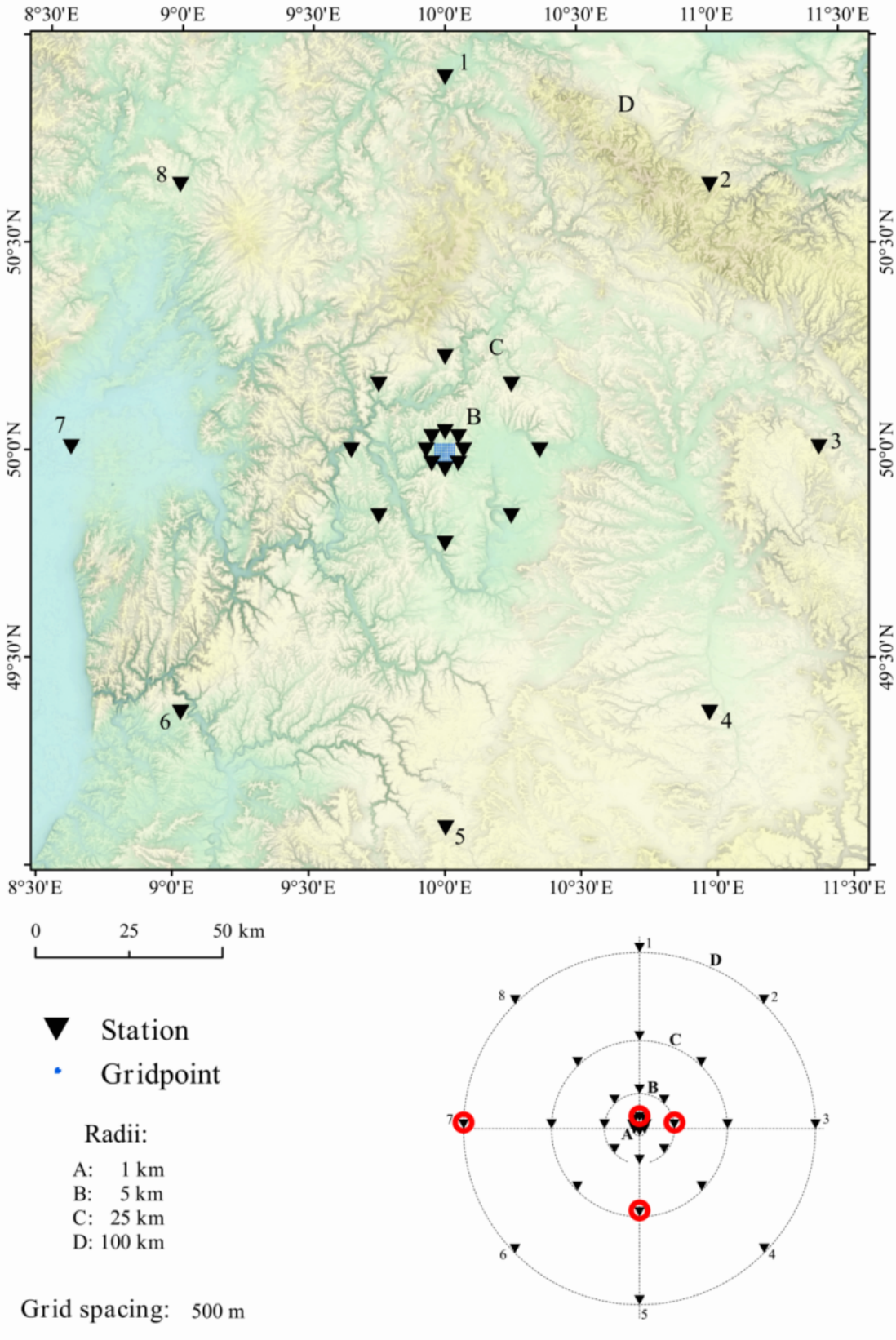

Figure 6.2:
Two dimensional planar overview of the source-receiver geometry. Stations are marked by black triangles. The innermost ring of stations is not marked for better visibility of the source point grid. The center of the concentrical setup is situated at the geographical coordinates 50° N, 10° E. **upper:** Map in correct scale. **lower:** Not to scale. Indication of rings (A-D) and stations providing example data (red circles).

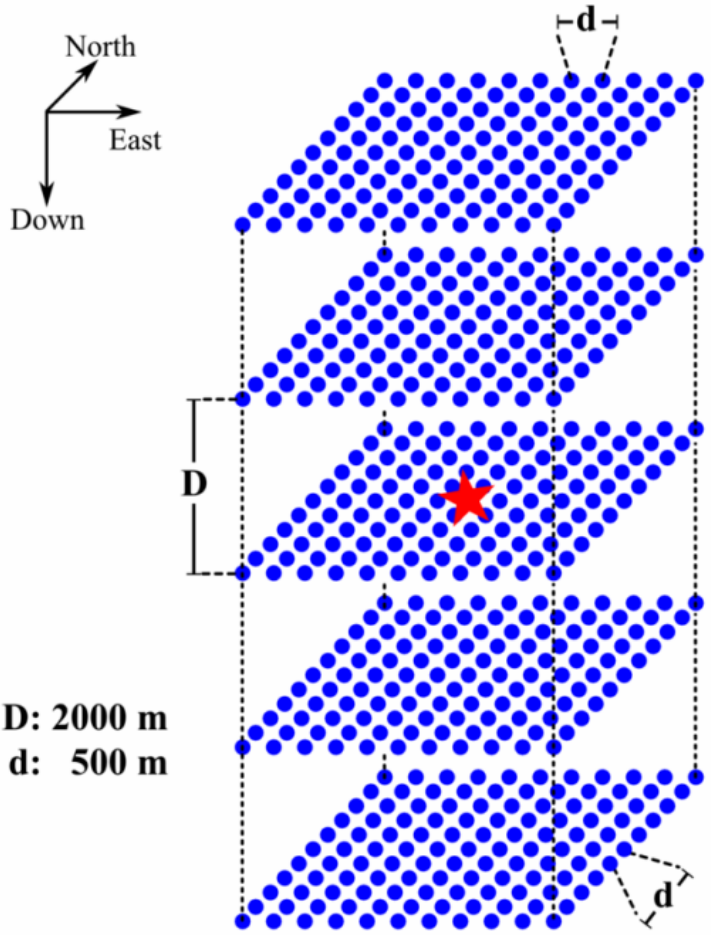

Figure 6.3:
Setup of the source point grid. Possible source points for the grid search are set by blue dot marks. The source of the synthetic signals is denoted by the red star.

6.2 Ensuring of general functionality

At this first stage of the test, a synthetic data set is generated (using QSEIS (Wang, 1999), s. sec. 3.2.2), assuming the homogeneous halfspace velocity model with the parameters

$$v_p = 5 \text{ km/s} \quad , \quad v_s = 3 \text{ km/s} \quad , \quad \rho = 2.5 \text{ g/cm}^3 \quad , \quad Q_p = 1000 \quad , \quad Q_s = 500.$$

Example data traces for four stations (locations indicated in figure 6.3) are shown in figure 6.4. Arrivals of different phases can hardly be distinguished for the nearest stations. At station A1, the influence of nearfield terms is slightly visible on channel E. For the large distance station D7, the onset of the P-phase can be observed approx. 20 s after the event. Some time later a superposition of Rayleigh- and S-wave is visible. Due to the homogeneous model, Love-waves are not generated, thus there is only an S-phase on the tangential component (N) at this station.

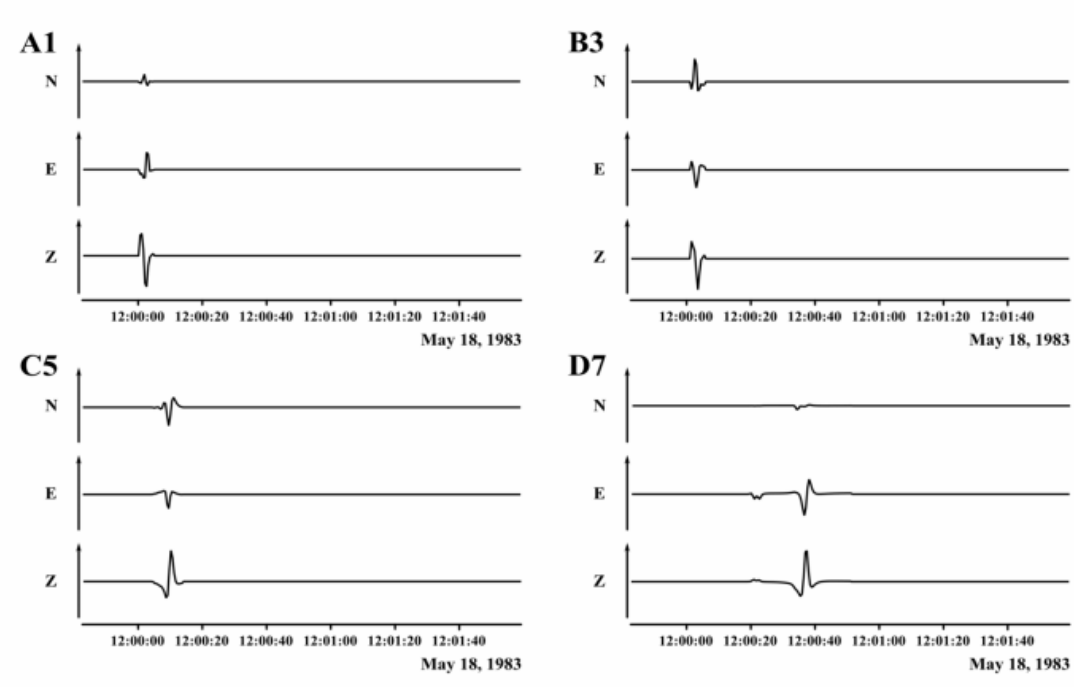

Figure 6.4:
Examples of synthetic data traces (homogeneous halfspace model). Three channels N, E, Z for four stations A1, B3, C5, D7. Displacement data, scaling by station – c.f. appendix A.1. Positions of stations are indicated in figure 6.2.

6.2.1 Handling of raw data

The generated synthetic data set is inverted directly; no further preprocessing is applied. A perfect agreement of inversion results and the setup parameters (see above) is expected.

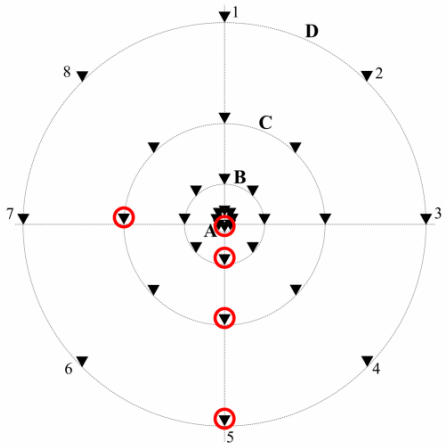

Figure 6.5:
Station geometry. Stations whose data are shown as examples in figure 6.6 are marked by red circles.

Results

The inversion for 21 time steps takes approximately 20 minutes. 96 data traces on 605 grid points are processed, each with 200 samples. The processing of each time step takes approximately 54 seconds, reading and preparing of the GFs array and correlation matrices adds another 10 seconds (Specification of computing machine given in appendix D.3).

The parameters of the inversion result coincide with the input values. The original source mechanism is obtained with a VR value of 100 %. It is located at the correct grid point and the correct source time. The grid search shows a clear maximum in time and space. Original data traces and synthetic traces generated with the parameters of the inversion result, match perfectly.

The final result of the inversion procedure is presented in figure 6.6. The numerical results of the inversion process are shown together with visualisations of the time- and space-dependency of the VR value, which defines the best estimator for source location and source time. Furthermore a graphical representation of the estimated source mechanism is shown. Finally a small set of example data traces is plotted in order to allow the visual comparison of the original data with synthetic data, that is build on the basis of the estimated source mechanism.

Four channels with same azimuth and varying distances together with the three channels of an arbitrary station with a different azimuth angle have been chosen for the comparative illustration of original data and synthetics reproduced from the inversion result. The locations of these stations are displayed in figure 6.5. The style of graphical presentation of the inversion results is used for all applications in the remainder of this thesis.

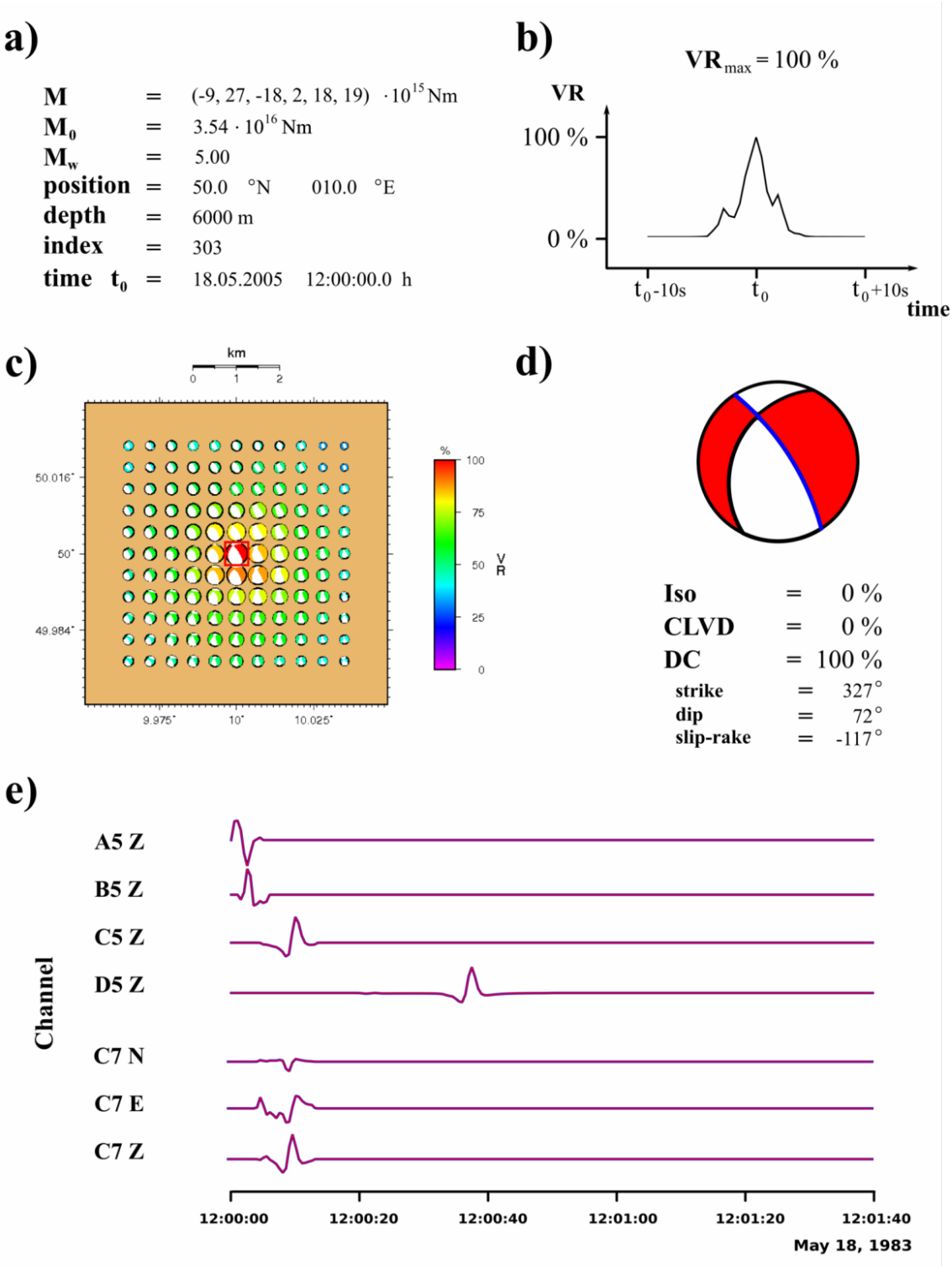

Figure 6.6:
Inversion result for synthetic raw data (sec. 6.2.1). **a)** Estimated numerical values for **M**, position (geographical and grid point index no.), and source time. **b)** Chronological evolution of VR. The position of the maximum defines the source time estimation. t_0 is the correct/reference source time. **c)** Geometrical overview with focal sphere diagrams on their spatial position on a horizontal section of the source point grid. The VR of the respective inversion solution on each point is coded by colour and size (linear w.r.t. best solution.). Best solution is marked by red square. **d)** Focal sphere diagram (stereographic projection) and source parameters of the estimated optimal source mechanism. Spatial parameters are given for one fault plane of the DC component (thick blue line). **e)** Comparison of original data traces (red) and reproduced synthetics (blue), scaling by station.

6.2.2 Handling of frequency filtered data

Since the filtering step is carried out internally after reading in the appropriate data set, these example data have been generated by applying the equivalent algorithm externally on the raw data traces.

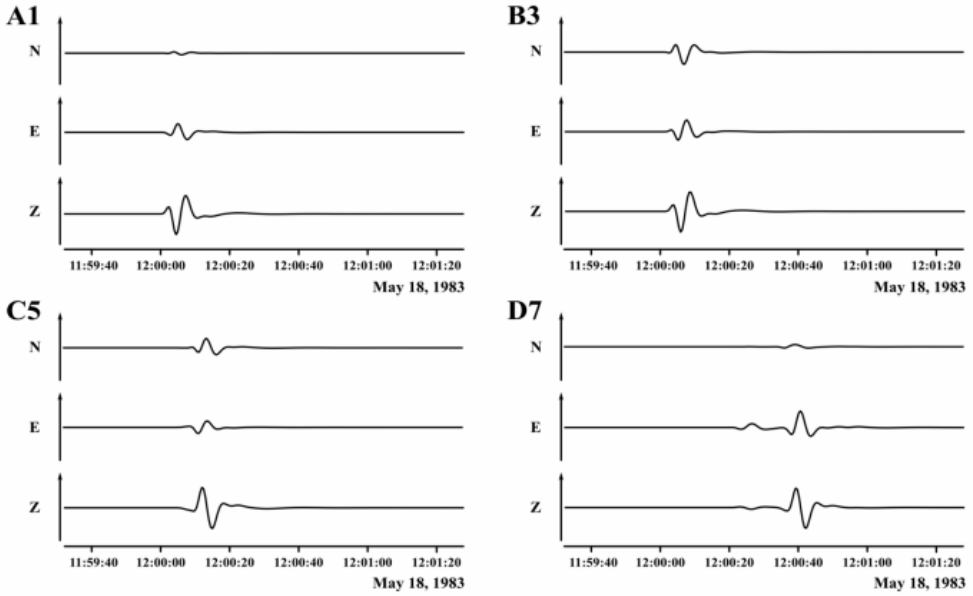

Figure 6.7:
Examples of frequency filtered (0.05 – 0.2 Hz) synthetic data traces. Three channels N, E, Z for four stations A1, B3, C5, D7. Displacement data, scaling by station. (Position of stations shown in figure 6.2)

Results

The inversion yields the correct mechanism, source time, and location. It shows a VR value of 100 %. Its spatial and temporal dependency is slightly smoothed out and shows small asymmetries. In opposite to the results of section 6.2.1, a smoother variation of the source mechanism around the source point is observed (compare figs. 6.6 c) and 6.8 c)). The inversion results in a perfect match of data and synthetics. The result of the inversion is presented in figure 6.8. (Example data from stations defined in figure 6.5.)

The data section shown in 6.8e) is the part of data used for the inversion, the time interval is the same as in 6.6e). It can be clearly seen, that signals can be unfavourably cut by the determination of the interval (trace A5 Z). This situation is handled by applying the same taper function and frequency filter parameters on both GFs and data in the same way. This leads to a consistent result.

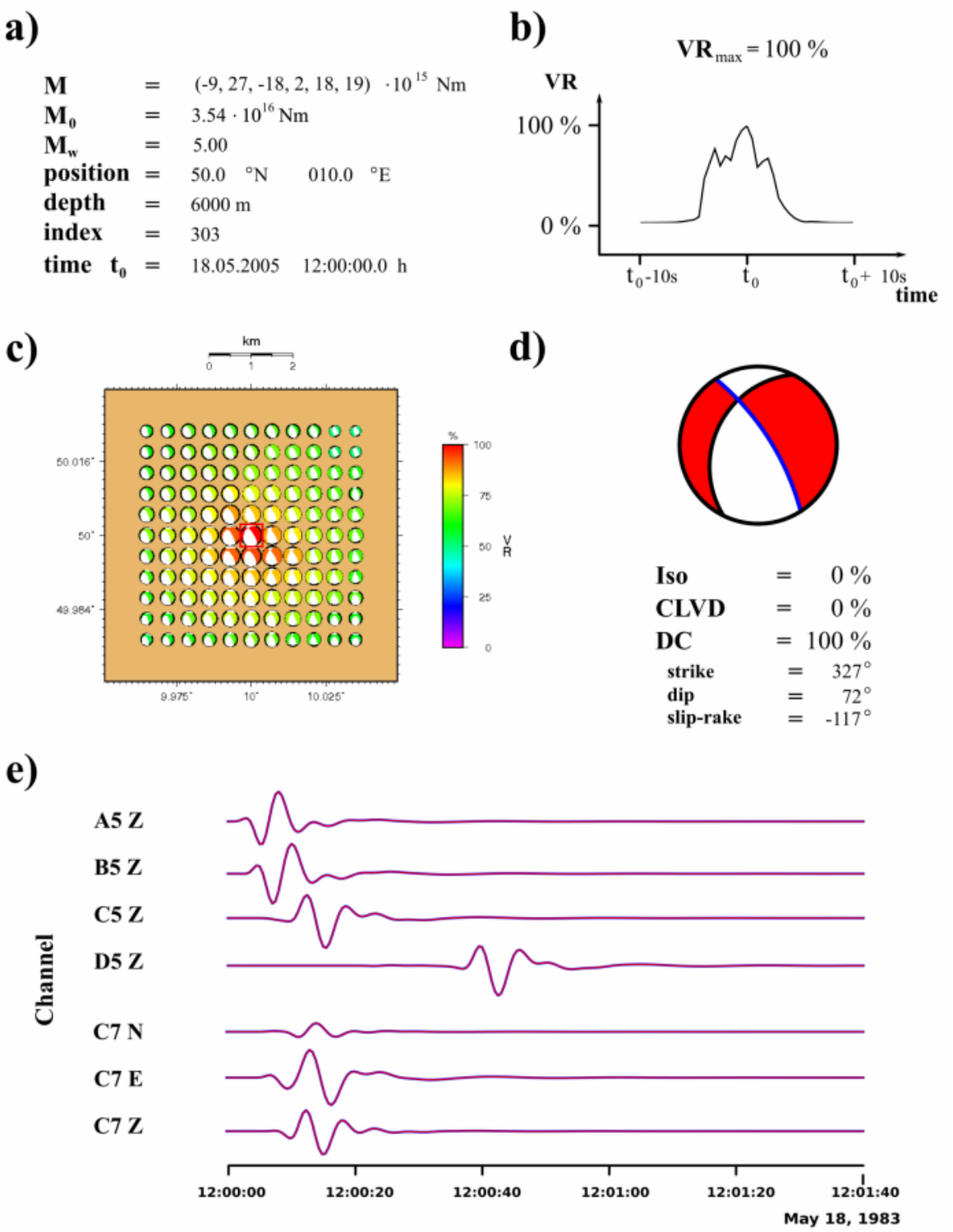

Figure 6.8:
Inversion result for frequency filtered data (sec. 6.2.2). **a)** Estimated numerical values. **b)** Chronological evolution of VR. **c)** Geometrical overview of a horizontal source grid section. Best solution is marked by the red square. **d)** Focal sphere diagram and source parameters of the estimated optimal source mechanism. **e)** Original data traces (red) and synthetics (blue), based on the estimated source mechanism (scaling by station).

6.2.3 Handling of data with noise

In reality one may not expect undisturbed data sets, so I test the robustness with respect to (white) noise. I generate data by adding white noise the data set from sec. 6.2.1, the standard deviation of the white noise process is set to a fixed percentage of the signal's maximal amplitude, i.e. noise is relative at each station. This is a very rigid condition, since in reality additional noise, independent from the signal amplitude, is more likely to be recorded. Here no data with a good signal-to-noise ratio is present.

The inversions have been carried out for varying noise amplitudes in order to estimate the reliability of the result under non-ideal circumstances. For low noise amplitudes ($< 20\,\%$), no significant deviation of the results can be detected. For showing possible deviations due to the influence of noise, I invert here a data set with an unrealistically high noise amplitude of $40\,\%$, the event can hardly be determined by manual picking. Example data traces are shown in figure 6.9.

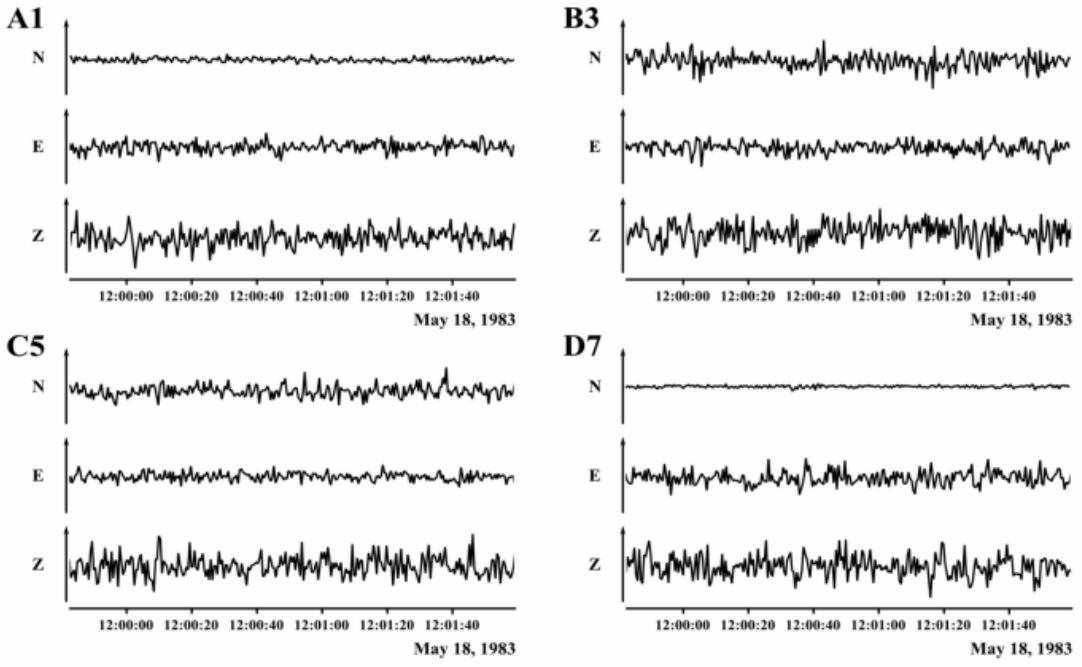

Figure 6.9:
Examples of raw synthetic data traces with added noise. White noise with mean amplitude $40\,\%$, relative to absolute maximum of the respective trace. Three channels N, E, Z for four stations A1, B3, C5, D7. Displacement data, scaling by station. Position of stations is shown in figure 6.2.

Results

Source time and location are determined correctly, even for very high relative noise amplitudes of $40\,\%$. The VR value has decreased to $80\,\%$, the variability of solutions

is smooth in time and space. The scalar seismic moment M_0 has increased by a factor of 1.5. The general geometry of the source mechanism is obtained, small variations in strike ($-3°$), dip ($-1°$), and rake ($-9°$) are observed. The decomposition of $\mathbf{M}$ yields noticeable isotropic (15 %) and CLVD (10 %) components. Internally generated synthetic data traces show only slight deviations from frequency filtered original data traces. the influence of (white) noise is strongly suppressed by the low frequency bandpass filter. The overview of the results is given in figure 6.10.

6.2.4 Ensuring functionality – summary

The functionality of the algorithm has been successfully tested. The inversion results are as expected and consistently. Perfect matches of input data and reproduced synthetics occur for the inversion of optimal raw or frequency filtered data. The confinement of the optimal source in space and time decreases consistently, if the low frequency bandpass filter is applied.

The inclusion of relative noise with high amplitude in the data provides rough conditions. The inversion result shows that the information can be recovered by inversion quite well for white noise. Deviations from the original parameters occur; consistently, they do not depend on the absolute amplitudes of the signals. Noticeable deviations occur in the determination of the slip-rake angle and the seismic moment. The latter one is over-estimated due to the additional energy contained in the noise.

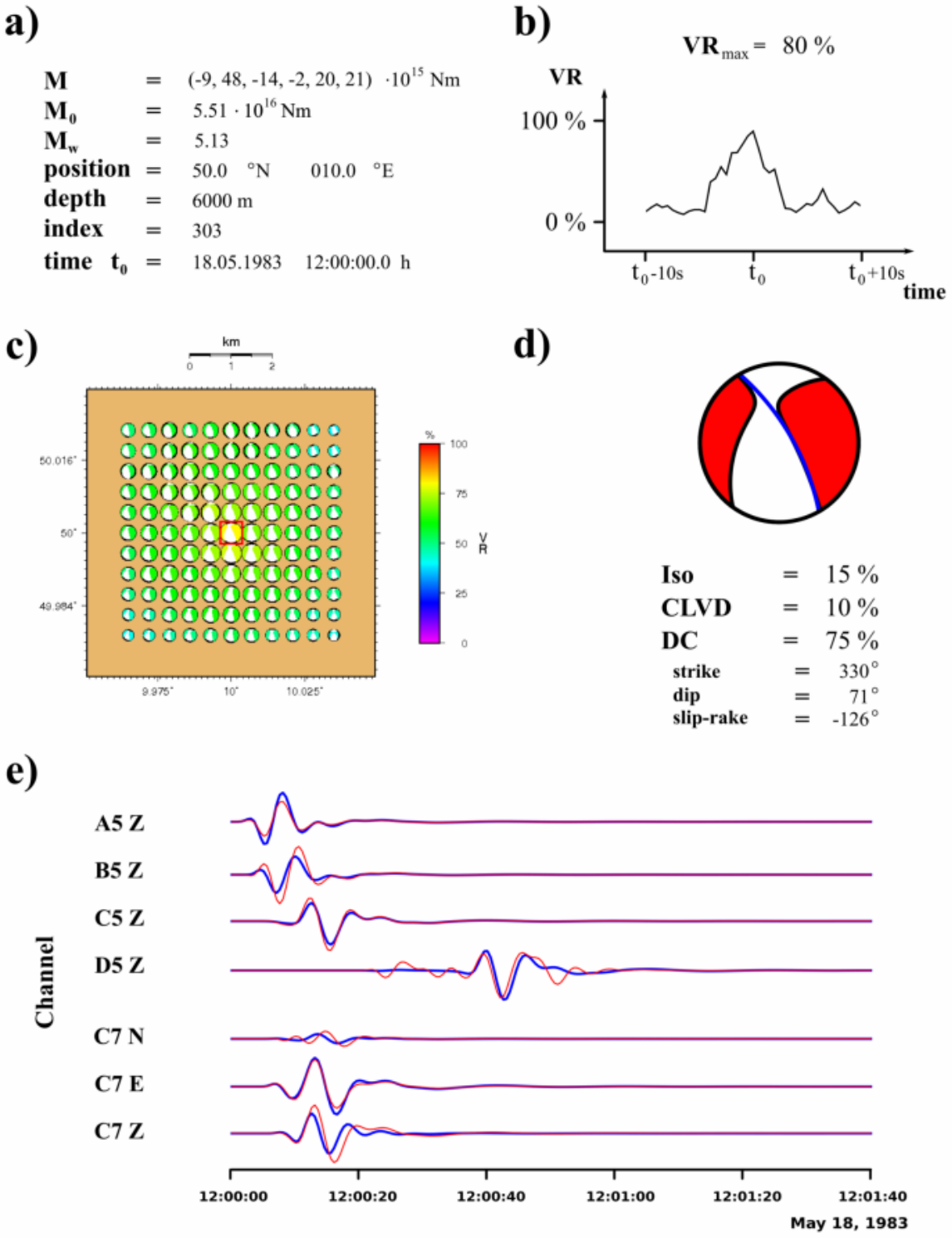

Figure 6.10:
Inversion result for frequency filtered noisy data (sec. 6.2.3). **a)** Estimated numerical values. **b)** Chronological evolution of VR. **c)** Geometrical overview of a horizontal source grid section. Best solution is marked by the red square. **d)** Focal sphere diagram and source parameters of the estimated optimal source mechanism. **e)** Original data traces (red) and synthetics (blue), based on the estimated source mechanism (scaling by station).

6.3 Sources of errors – qualitative appraisal

I qualitatively test the sensitivity of the algorithm with respect to different sources of errors in this stage. I investigate the influence of wrong velocity models in the inversion of noisy data traces. Additionally, the influence of the station distribution is evaluated. Except the velocity models for the generation of synthetic data and GFs, all parameters from the latter two sections are kept, including the geometry.

For all practical purposes, the correct model of the underlying medium is not known exactly. Therefore I show the influence of a wrong velocity model on the result of the inversion in this test section. Under the valid assumption, that the complexity in real Earth is rather under- than overestimated, synthetic data for this section are generated for a horizontally layered medium with several layers. The complex one-dimensional velocity model is shown in figure 6.11 (c.f. page 37). White noise with 10 % amplitude is added. Figure 6.12 shows a set of example data traces in overall scaling (correct relative scaling of amplitudes), figures 6.13 and 6.14 show the same data set (raw data and frequency filtered respectively) with scaling by station. The first plot makes clear, how the amplitudes decrease with distance, the latter two plots show the respective qualitative behaviour of the traces. Contrary to the homogeneous halfspace in the previous section, Love-waves are now present additionally to Rayleigh-waves (e.g. figure 6.13, station D7, channels N and E) In the following, the synthetic data set is inverted several times, each time using different velocity models or station geometries. By this I want to show how the deviations in the velocity model qualitatively change the inversion results

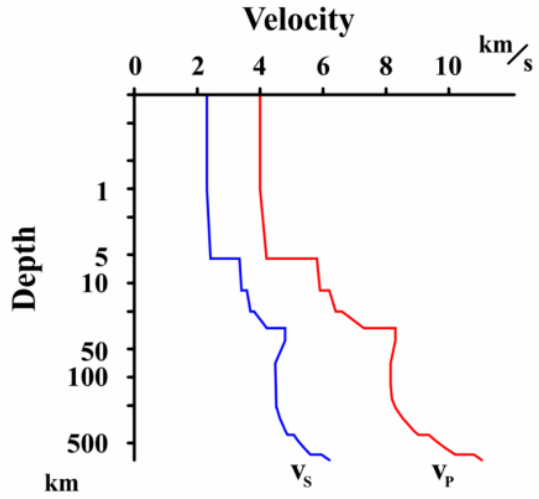

Figure 6.11:
Velocity model for generating GFs with QSEIS. The velocity curves v_p (red) and v_s (blue) are shown against a logarithmic depth scale (c.f. figure 3.9).

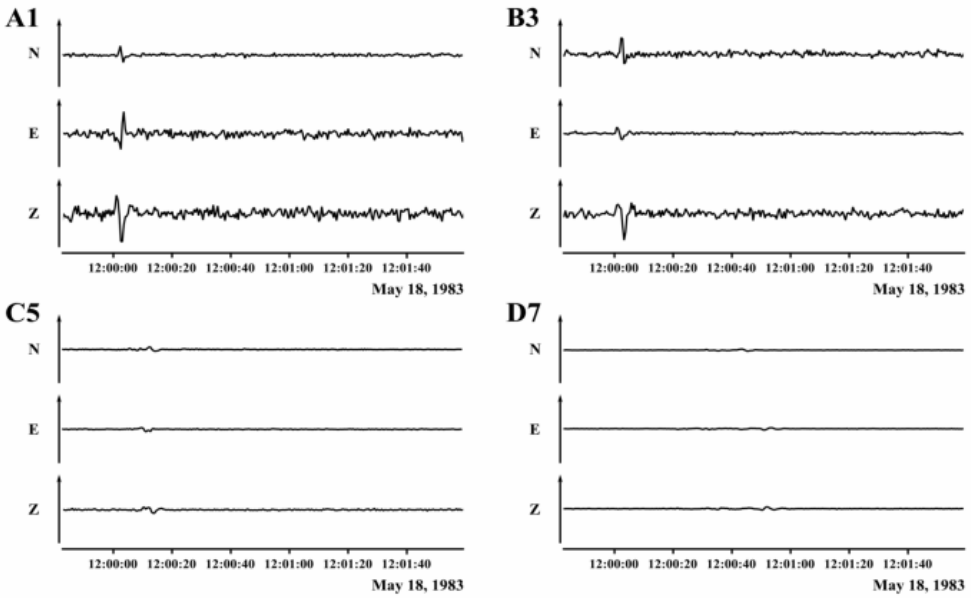

Figure 6.12:
Examples of synthetic data traces. Three channels N, E, Z for four stations A1, B3, C5, D7. Displacement data, overall scaling. Position of stations is shown in figure 6.2.

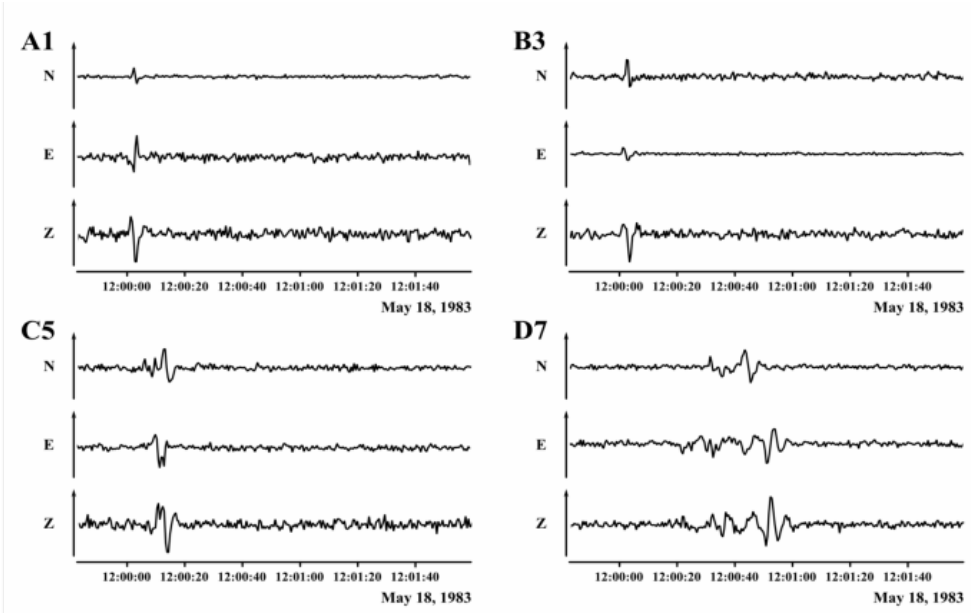

Figure 6.13:
Examples of synthetic data traces. Three channels N, E, Z for four stations A1, B3, C5, D7. Displacement data, scaling by station. Position of stations is shown in figure 6.2.

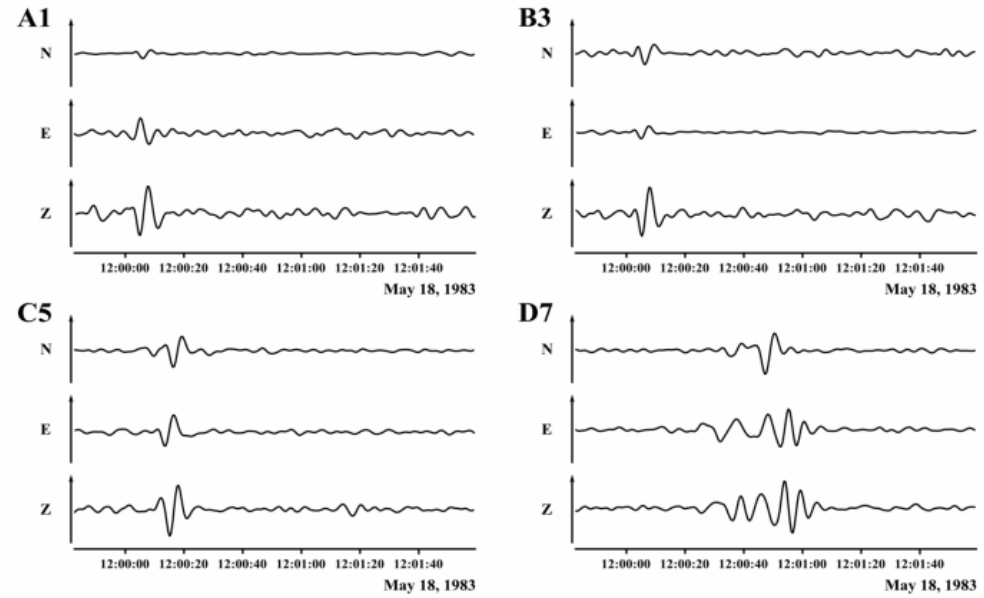

Figure 6.14:
Examples of synthetic data traces. Data are frequency filtered (BP 0.05 – 0.2 Hz). Three channels N, E, Z for four stations A1, B3, C5, D7. Displacement data, scaling by station. Position of stations is shown in figure 6.2.

6.3.1 Unknown velocity model 1 – halfspace with wrong average velocity

Assuming that the original velocity model is unknown, I need a first approximation to this *unknown* underground model. I take the homogeneous halfspace model which has been defined in section 6.2 as basis for the first inversion try. The geometry is simplified with respect to the *real* geometry and the average velocities of the model are set to wrong values by this choice. This is a very strong simplification. In reality, smaller deviations between true and assumed models are expected. The differences between the velocity models are shown in figure 6.15.

Results

Results of this inversion are shown in figure 6.16. The lateral source location (epicentre) is estimated correctly, the depth is estimated as being significantly deeper by 4000 m. The estimation of the source time shows deviation of one time step (0.5 s). The VR value is 78 %, its time dependence shows a broad maximum. The seismic moment is higher by a factor of 1.4. The spatial dependency is very smooth with only slightly varying mechanisms. The general geometry of the source mechanism is obtained, small variations in strike (3°) and dip (−1°) are observed. The decomposition of $\mathbf{M}$ yields small isotropic (6 %) and CLVD (6 %) components. Internally generated comparison data traces show strong deviations from frequency filtered original data traces, increasing with epicentral distances. For instance, Love-waves are excited (on component C7N), but cannot be represented in a half space model.

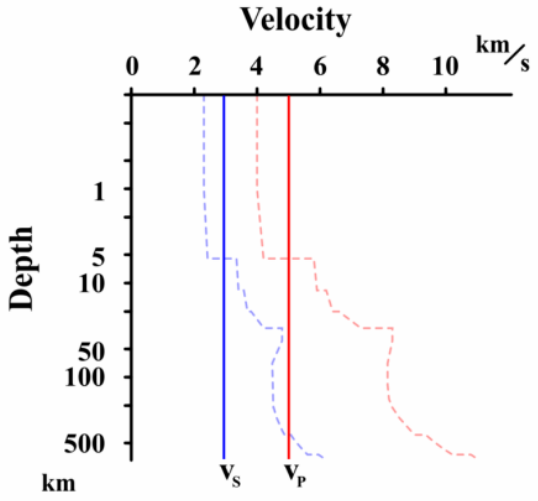

Figure 6.15:
Velocity model used for the inversion 6.3.1. The velocity curves v_p (red) and v_s (blue) are shown against a logarithmic depth scale. Dashed lines indicate the correct model.

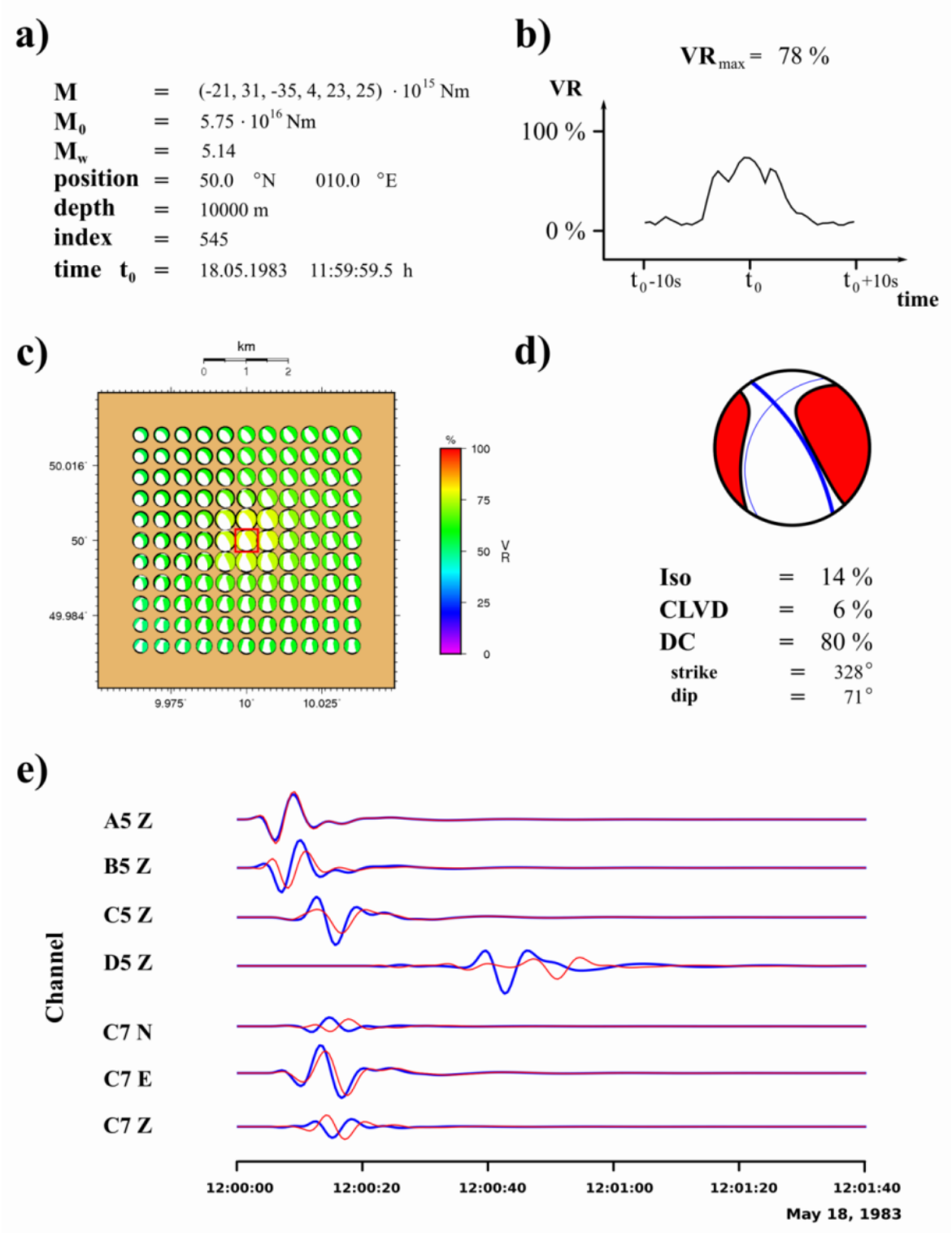

Figure 6.16:
Inversion result for test 6.3.1. Data inverted using a wrong underground model. Homogeneous halfspace with wrong velocities. **a)** Estimated numerical values. **b)** Chronological evolution of VR. **c)** Geometrical overview of a horizontal source grid section. **d)** Focal sphere diagram and source parameters of the estimated optimal source mechanism. **e)** Original data traces (red) and synthetics (blue), based on the estimated source mechanism, scaling by station.

6.3.2 Unknown velocity model 2 – halfspace with correct average velocity

As the next step I assume, that the average of the velocity model is known. The values

$$v_p = 6.01 \text{ km/s} \quad , \quad v_s = 3.47 \text{ km/s} \quad , \quad \rho = 2.75 \text{ g/cm}^3 \quad , \quad Q_p = 1033 \quad , \quad Q_s = 521$$

are the mean values of the correct underground model, taken for the depth range to approximately 30 km. The term *correct average velocity* has to be understood in a relative sense. The depth range considered in the averaging model depends on the dominant periods of the seismic signals. The depth range in this test has been chosen after preliminary studies. The velocities of this model differ by approximately 20 % from the values in the previous setup. The model is shown in figure 6.17.

Results

By using the given values for generating GFs in a halfspace model, I obtain inversion results as presented in figure 6.18.

The lateral source location is estimated correctly. Depth is determined as 8000 m, which is one gridpoint too deep. A time shift of 1 s occurs with respect to the correct source time. The magnitude is estimated being 5 % higher than the original source strength. All values are given obtained with a VR value of 81 %. The time dependency of this value shows a high variability within the analysed time interval. The spatial variation of VR shows a maximum around the correct source location and a symmetric decrease with distance. The source geometry varies only smoothly within the horizontal grid section, where a spatial asymmetry with respect to the respective mechanisms occur. The best source mechanism consists mainly of a pure shear component (92 %). Its main orientation is defined by a strike angle of 329° and a dip angle of 71°. This is only a small deviation from the correct values (2° and −1° respectively). The slip-rake shows a change in sign (179°), hence the FSD shows a polarity which is opposite to the correct one. The problem of polarity flipping of the the moment tensor solution, here occurring the first

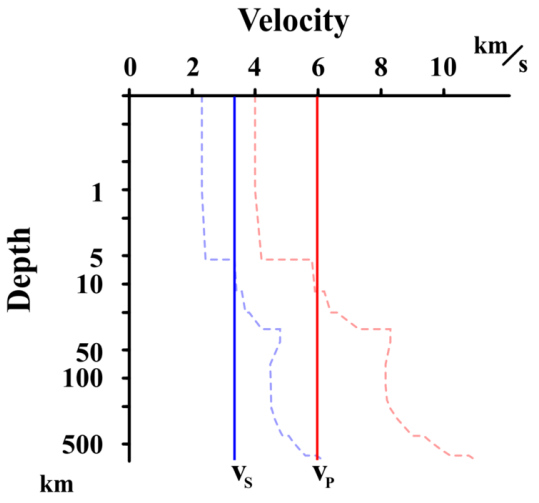

Figure 6.17:
Velocity model used for the inversion 6.3.2. The velocity curves v_p (red) and v_s (blue) are shown against a logarithmic depth scale. Dashed lines indicate the correct model.

time, is more severe and will be discussed in later chapters in detail. The comparison of input data and reproduced synthetics show good agreement of traces for the nearest stations (located on rings A and B) and for some channels of station in larger distances. Data appear to be tapered too early for stations with large epicentral distances due to a too high slowest velocity in the model parameters.

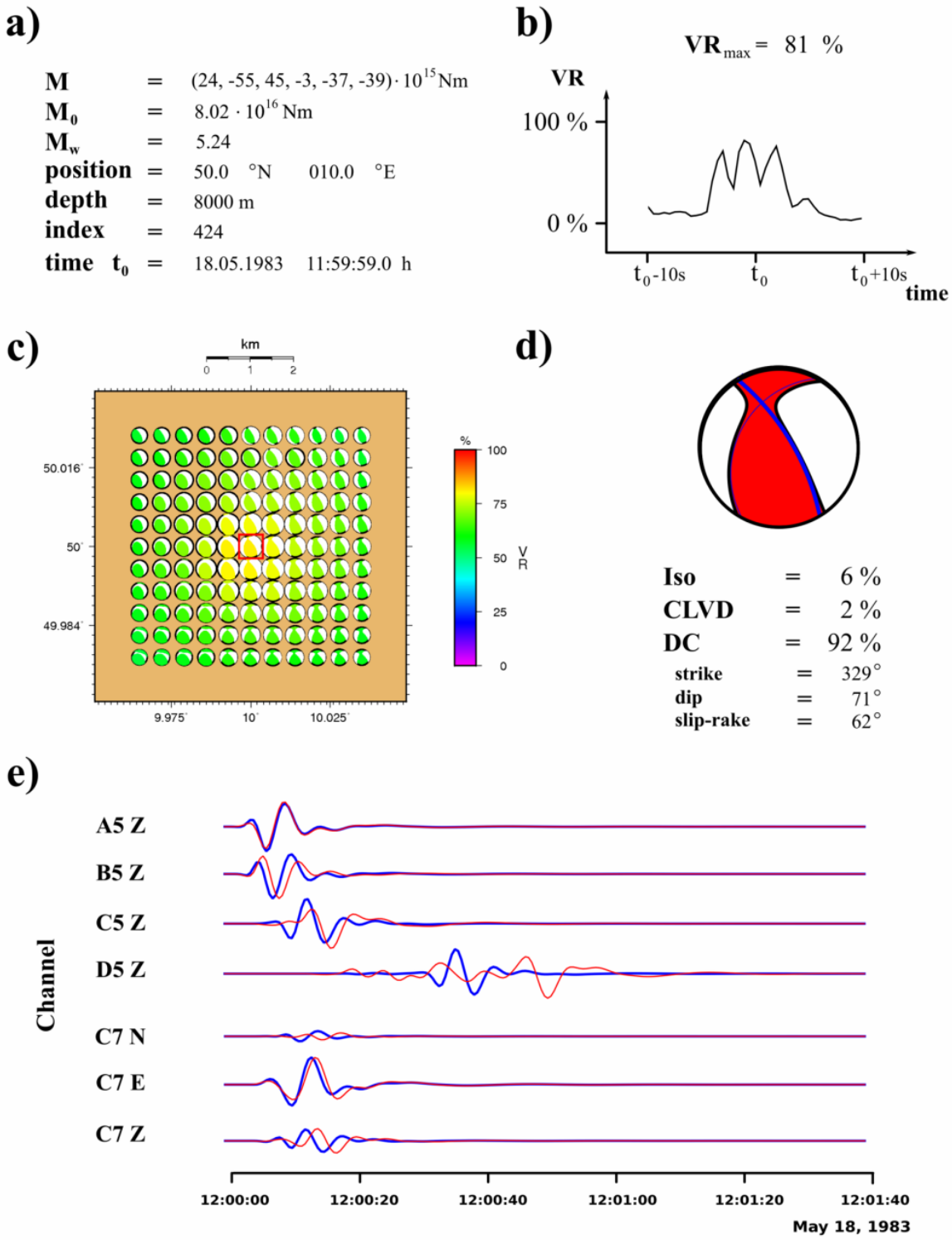

Figure 6.18:
Inversion result for test 6.3.2. Data inverted using a wrong underground model. Simple halfspace with correct average velocities. **a)** Estimated numerical values. **b)** Chronological evolution of VR. **c)** Geometrical overview of a horizontal source grid section. **d)** Focal sphere diagram and source parameters of the estimated optimal source mechanism. **e)** Original data traces (red) and synthetics (blue), based on the estimated source mechanism, scaling by station.

6.3.3 Unknown velocity model 3 – correct layer positions, wrong velocities

In order to test, if the knowledge of the correct layer boundaries in the model is essential, a model that contains the same layer positions is set up. The respective velocities vary in comparison with the original model by approx. 5 %. The model is sketched in figure 6.19.

Data generated from this model look similar to the original data traces. A set of example data traces is presented in figure 6.20

Results

The inversion of data on basis of this layered model yields the result shown in figure 6.21.

Source location and source time are estimated correctly. The VR value is 91 %, its time dependence shows a clear maximum. The seismic moment is estimated slightly too high (4 %). The spatial dependency is smooth with slightly varying mechanisms. Although the source-station geometry is concentric and the underground model is one-dimensional, an asymmetry in the spatial variation of the source occurs. The general geometry of the source mechanism is obtained, small variations in strike (4°), dip (−2°), and rake (1°) are observed. The decomposition of **M** yields isotropic (11 %) and small CLVD (8 %) components. Internally generated comparison data traces show partially deviations from frequency filtered original data traces. Love-waves are well reproduced by this model.

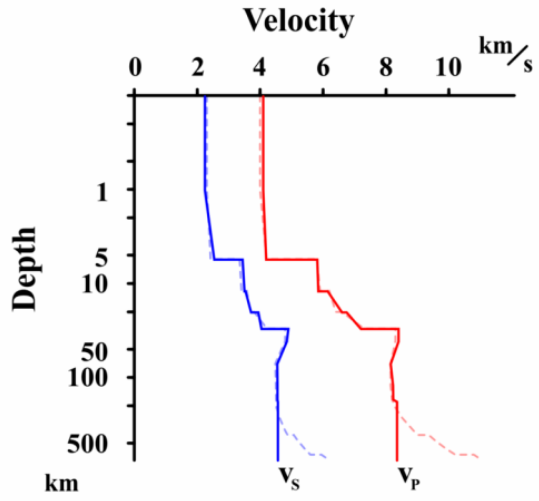

Figure 6.19:
Velocity model for the inversion in test 6.3.3. The velocity curves v_p (red) and v_s (blue) are plotted against a logarithmic depth scale. Slight velocity variations with respect to the model in figure 6.11 (dashed lines). Layer boundaries are in identical depths.

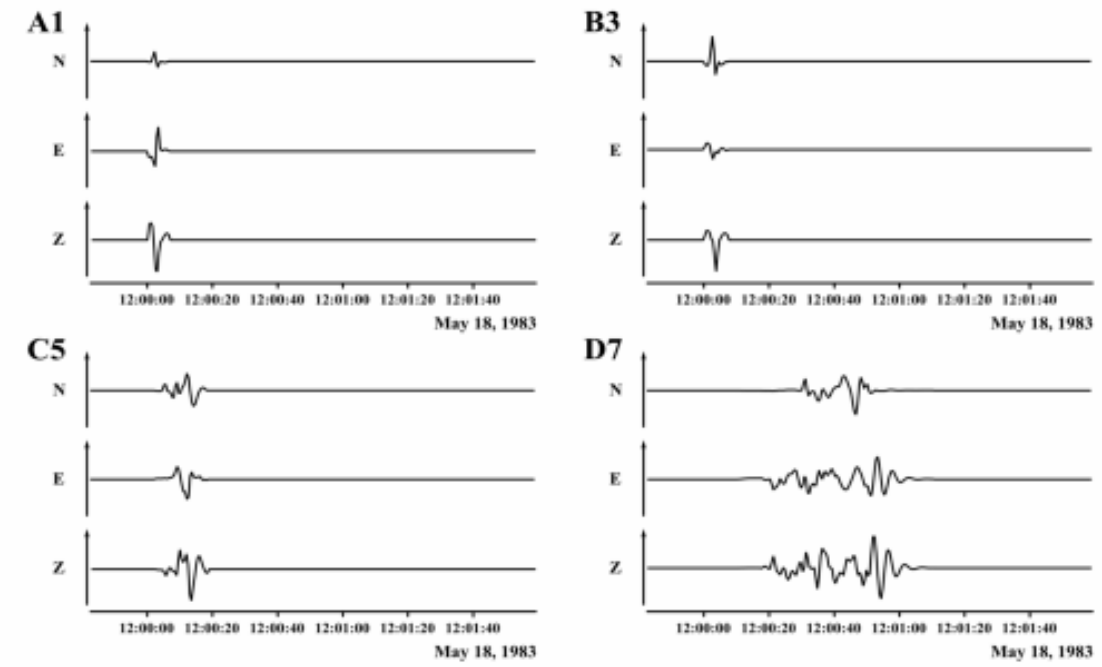

Figure 6.20:
Examples of synthetic data traces for test 6.3.3. Three channels N, E, Z for four stations A1, B3, C5, D7. Displacement data, scaling by station. Position of stations is shown in figure 6.2.

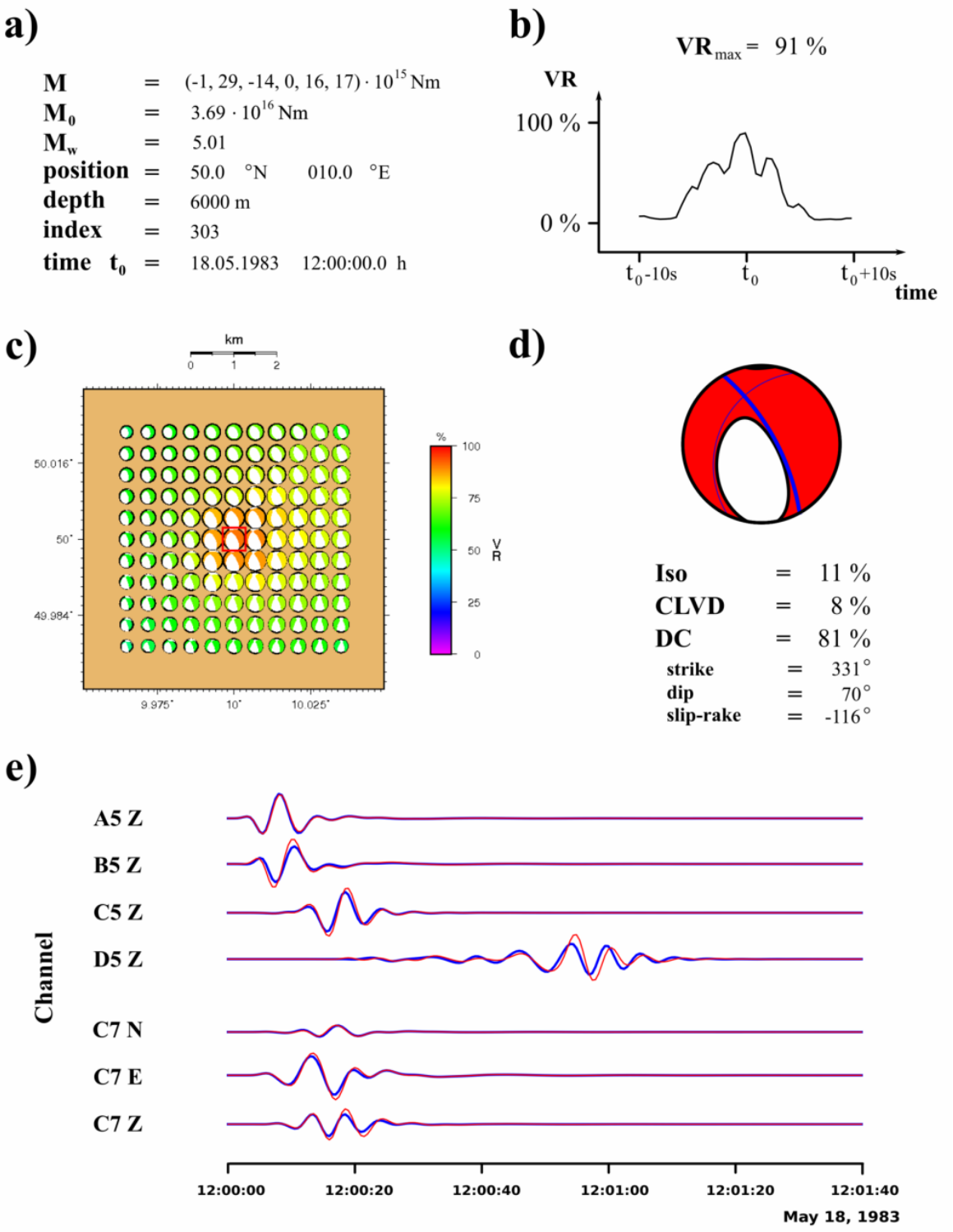

Figure 6.21:
Inversion result for test 6.3.3. Data inverted using a wrong underground model. Layered model, layer boundaries are in correct depth, velocities vary from original model. **a)** Estimated numerical values. **b)** Chronological evolution of VR. **c)** Geometrical overview o a horizontal source grid section. **d)** Focal sphere diagram and source parameters of the estimated optimal source mechanism. **e)** Original data traces (red) and synthetics (blue), based on the estimated source mechanism, scaling by station.

6.3.4 Unknown velocity model 4 – soft sediment layer

As shown in chapter 4.3.3, path effects can occur, if a low velocity layer is situated at the top of an underground model. This case is modelled here, illustrated in figure 6.22.

Data generated from this model show low frequency ringing at stations in large distances. This is a result of strong dispersion of Rayleigh-waves (station D7, channel N) and pronounced Airy phases (station D7, channels E and Z). A set of example data traces is presented in figure 6.23.

Results

The inversion results are presented in figure 6.24.

The lateral source location is estimated correctly. The depth is estimated as 8000 m, which is a deviation of one grid point. The result for the source time is one second too early (two time steps). The estimation of the seismic moment is too low (70 %). The best VR value is 78 %, its time dependence shows a clear maximum at the position of the aforementioned time shift. The spatial dependency of the VR value and the source mechanism varies very smoothly. The correct geometry of the source mechanism is generally obtained, small variations in strike (2°), dip (−3°) are observed. The decomposition of **M** yields additionally a small isotropic part (13 %) components. Internally generated comparison data traces show deviations from frequency filtered original data traces, especially for stations in large distances (due to path-effects, surface wave influence and dispersion effects increase with increasing distance).

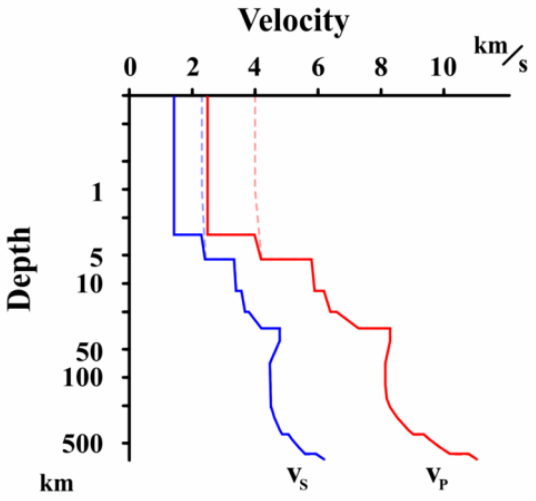

Figure 6.22:
Velocity model for the inversion in test 6.3.4. The velocity curves v_p (red) and v_s (blue) are shown against a logarithmic depth scale. A low velocity layer of thickness 3000 m is added on top of the original model in figure 6.11. Dashed lines indicate the correct model.

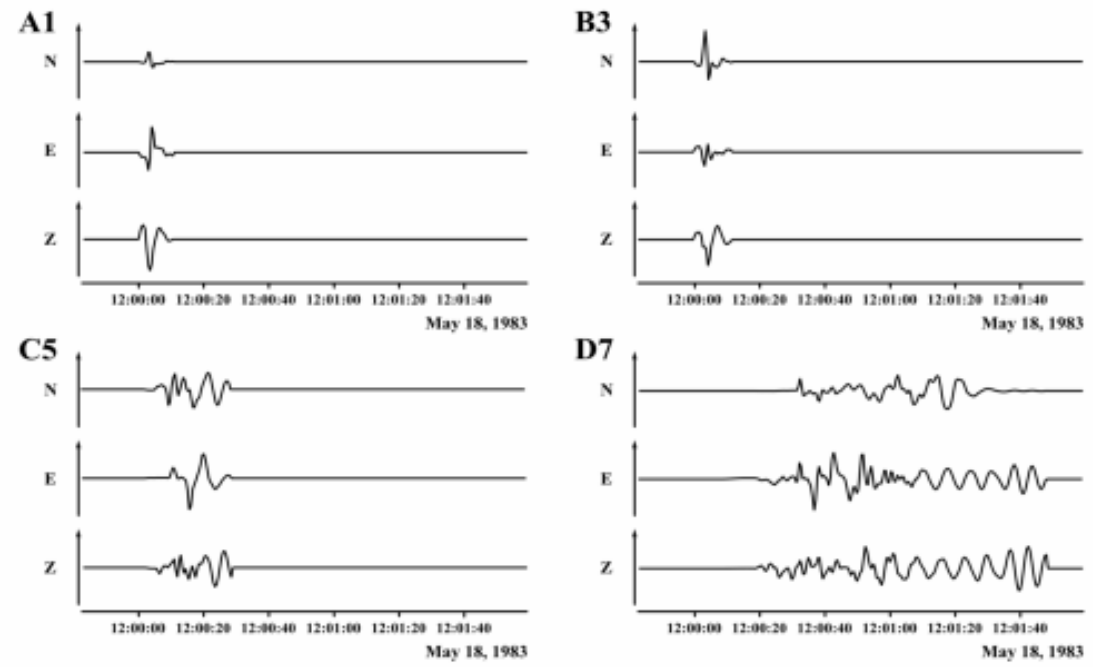

Figure 6.23:
Examples of synthetic data traces for test 6.3.4. Three channels N, E, Z for four stations A1, B3, C5, D7. Displacement data, scaling by station. Position of stations is shown in figure 6.2

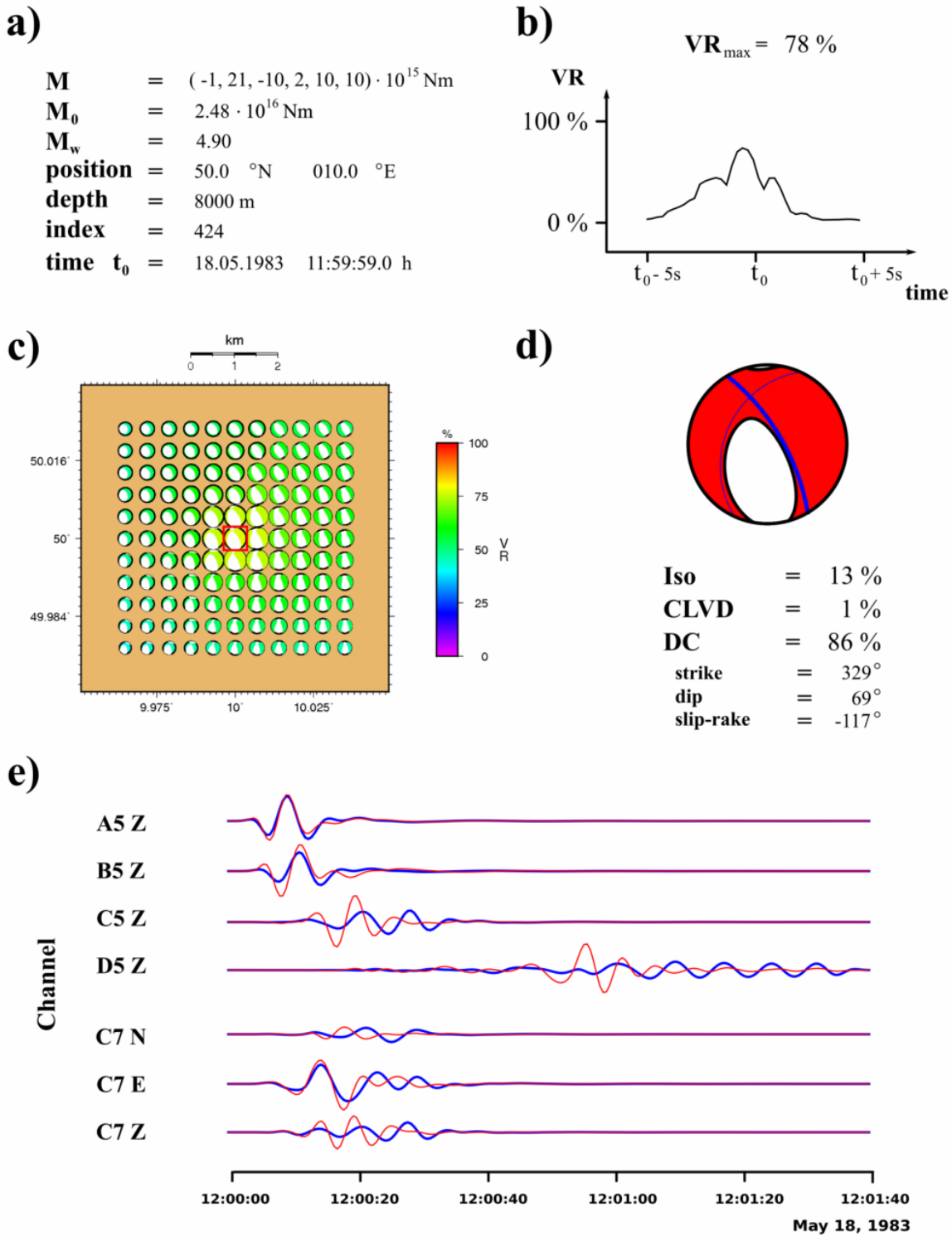

Figure 6.24:
Inversion result for test 6.3.4. Layered model, layers are correct, but an additional low-velocity layer is added on top. **a)** Estimated numerical values. **b)** Chronological evolution of VR. **c)** Geometrical overview of a horizontal source grid section. **d)** Focal sphere diagram and source parameters of the estimated optimal source mechanism. **e)** Original data traces (red) and synthetics (blue), based on the estimated source mechanism, scaling by station.

6.3.5 Station geometry 1 – soft sediment layer – only stations in far distances

The data generated with the velocity model from the latter section show strong deviation from the original data for the stations in the outer two circles of the station geometry. In sec. 6.3.4, the effect of these deviations has been suppressed by the high amplitudes of the well-fitting data from the stations on the two inner rings. Thus, I analyse here only data from the two outer rings. Figure 6.25 shows the spatial configuration. This setup yields very bad conditions for the inversion. On the one hand, it this is a general stress test for the robustness of the algorithm; on the other hand, this setup is similar to the configuration of the real data application in section 7.1.2.

Results

Figure 6.26 illustrates the results of this application. The comparison of data traces is visualised for data from stations marked in figure 6.25.

The lateral source location of the best inversion result is laterally shifted by one gridpoint to the East and to the North respectively. The estimation of depth also yields a deviation of on gridpoint (4000 m). The estimation of the source time shows a shift of 7 s, where the time series of the VR values does not show one clear single maximum. the best VR value is 33 %. The spatial dependence of VR is not confined. Additionally, the source mechanism varies very smoothly in space. The estimated source mechanism consistently has a high double-couple component (68 %), that shows again the correct main orientation, variations in strike ($-4°$) and dip ($0°$) are very small. The rake is shifted by ($171°$), so the polarity of the result is inverted with respect to the correct mechanism (polarity flipping of the source mechanism). Due to the intrinsic weighting by geometric damping, data from nearer stations (ring C) match better with the theoretical traces than data from the distant stations. However, even these relatively good agreement is worse than in previous tests.

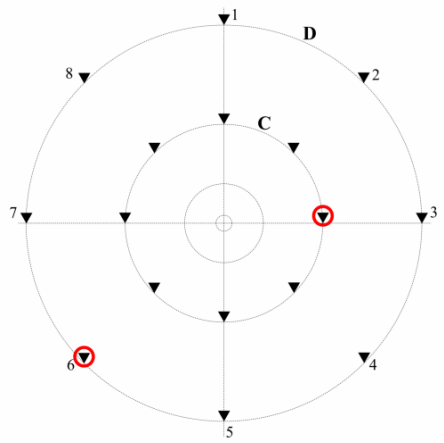

Figure 6.25:
Station geometry. Stations with epicentral distance < 25 km of the setup in figure 6.2 are removed. Data samples are from stations marked by red circles.

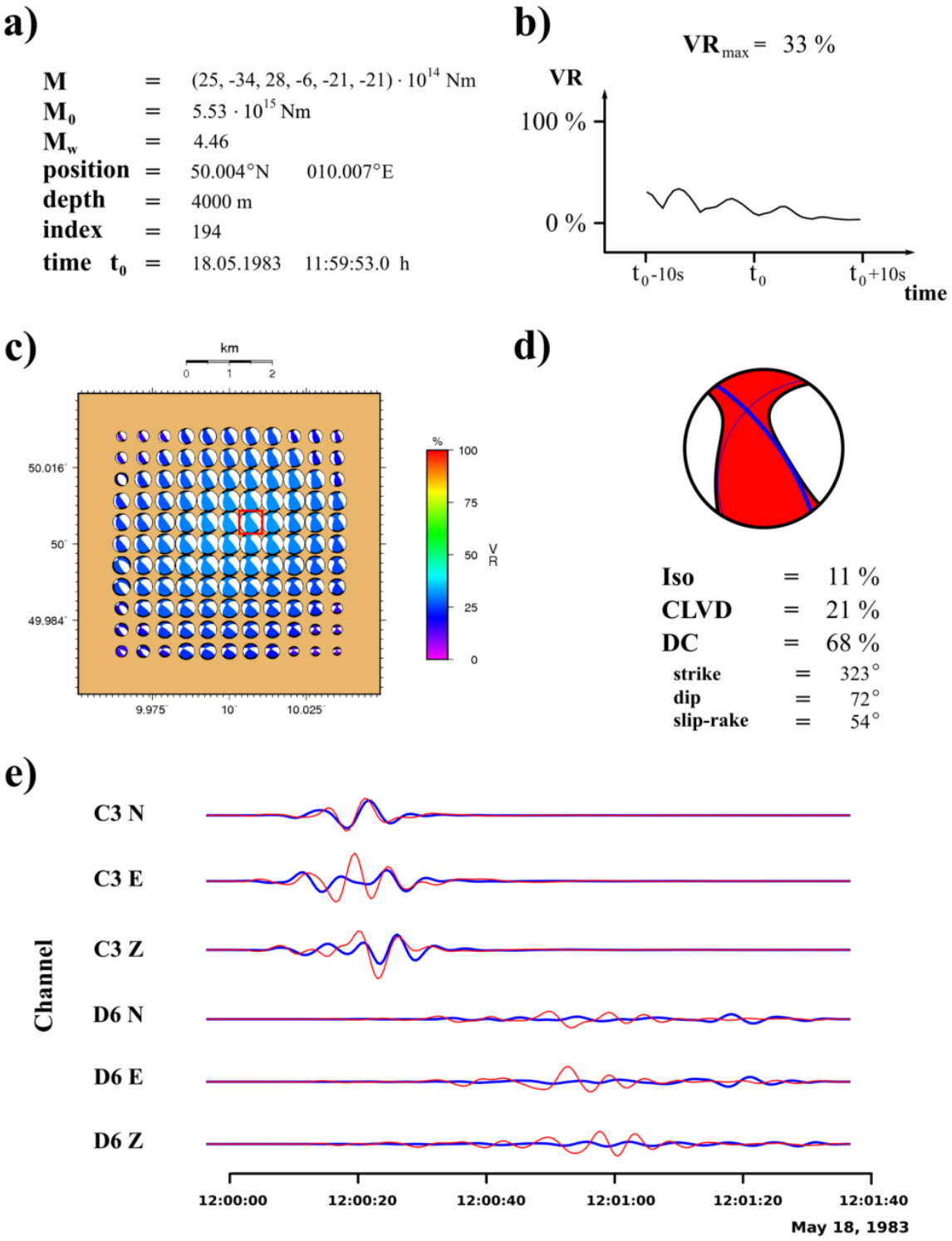

Figure 6.26:
Inversion result for test 6.3.5. Layered model, layers are correct, but an additional low-velocity layer is added on top. Only data from stations on the two outermost rings are considered. **a)** Estimated numerical values. **b)** Chronological evolution of VR. **c)** Geometrical overview of a horizontal source grid section. **d)** Focal sphere diagram and source parameters of the estimated optimal source mechanism. **e)** Original data traces (red) and synthetics (blue), based on the estimated source mechanism, overall scaling. Data from stations, defined in figure 6.25

6.3.6 Station geometry 2 – soft sediment layer – large azimuthal gap

Aside the epicentral distance of the stations, a significant azimuthal gap in the station coverage may have a significant influence on the inversion result. This effect is investigated here by removing the stations with indices {1,2,8}, hence no data radiated in North direction is included in the inversion. The configuration is sketched in figure 6.27. It qualitatively reflects the setup in section 7.1.1.

Results

The given setup leads to the result shown in figure 6.28.

The lateral source location is estimated correctly. The depth is estimated as 8000 m, which is a deviation of one grid point. The result for the source time is one second too early (two time steps) in a clear maximum of 73 % of the time series. The spatial dependency of the source mechanism varies noticeable but smoothly. The correct geometry of the source mechanism is generally obtained, small variations in strike ($-1°$), dip ($-2°$), and rake ($3°$) are observed. The decomposition of $\mathbf{M}$ yields small isotropic (11 %) and CLVD (5 %) components. The estimation of the seismic moment is too low.

Internally generated comparison data traces show good agreement with the original data traces for the near stations (on rings A and B), but strong deviations at larger distances (rings C and D). The high influence of the near stations result in the high VR value.

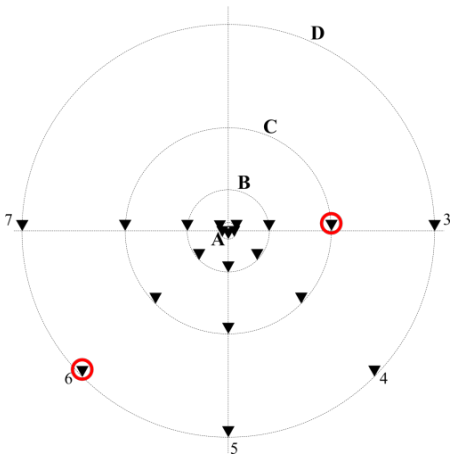

Figure 6.27:
Station geometry for test 6.3.5. Stations in the northern hemisphere of the setup in figure 6.2 are removed. Data samples in the result presentation (figure 6.28) are from stations marked by red circles.

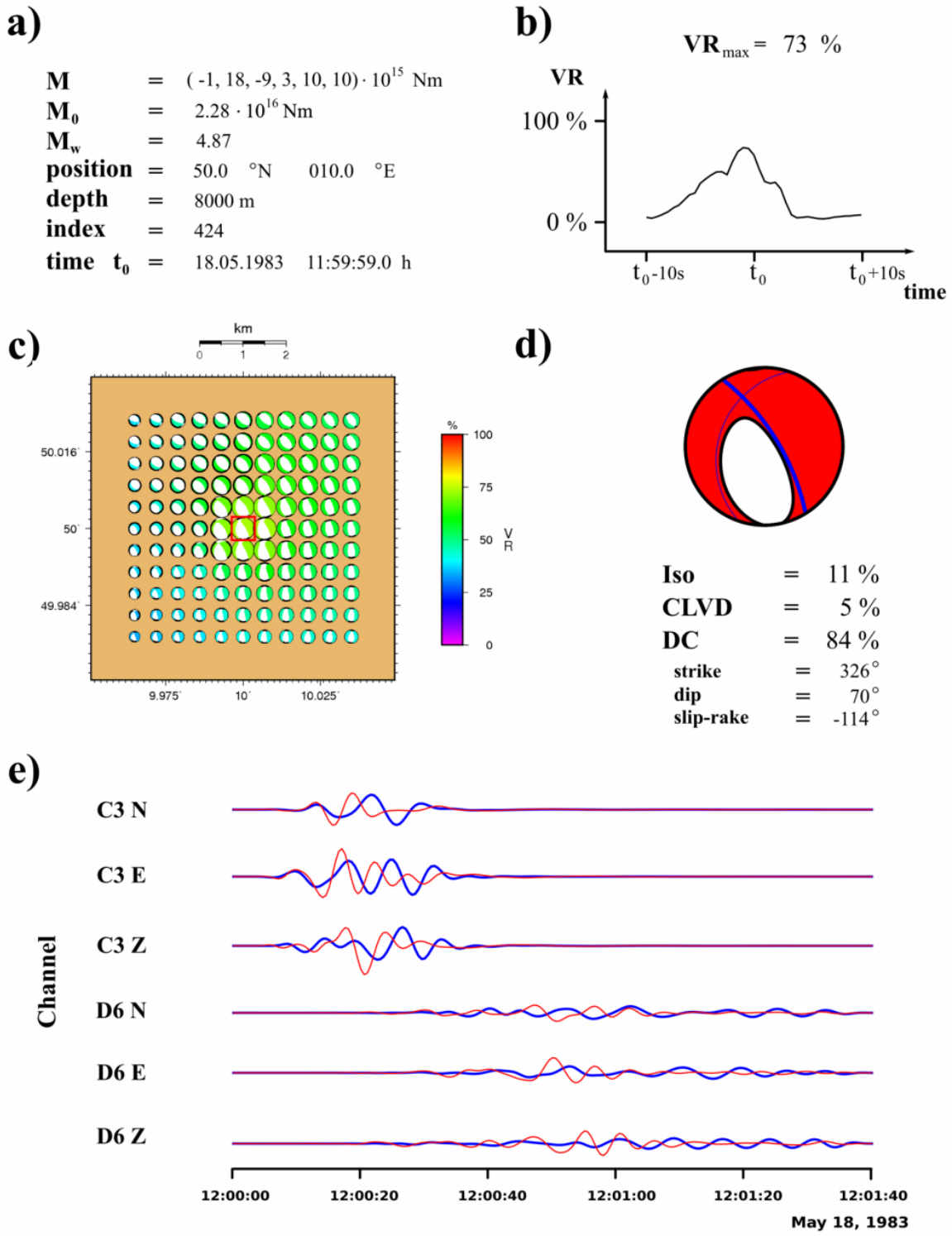

Figure 6.28:
Inversion result for test 6.3.6. Layered model, layers are correct, but an additional low-velocity layer is added on top. No stations in the northern hemisphere of the setup are considered. **a)** Estimated numerical values. **b)** Chronological evolution of VR. **c)** Geometrical overview of a horizontal source grid section. **d)** Focal sphere diagram and source parameters of the estimated optimal source mechanism. **e)** Original data traces (red) and synthetics (blue), based on the estimated source mechanism, overall scaling. Traces from stations, defined in figure 6.27.

6.3.7 Potential sources of errors – summary

The tests in this section demonstrate the qualitative influence of two main components of the inversion setup: the velocity model and the station geometry.

The synthetic data are generated with a complex layered model. The tests start with an inversion, based on a homogeneous halfspace model. This approach is very harsh, in reality one would start already with a layered model after a first evaluation of the data set (including Love-waves and characteristic dispersion features). However this first test yields already quite satisfactory results, mainly determined by data from stations in small epicentral distances. The estimated solution is qualitatively in the range of the inversion of noise data in sec. 6.2.3.

By changing the average velocity to the correct value (c.f. sec. 6.3.2), I slightly improve the VR value, the source depth is closer to the correct value, the double-couple content of the source mechanism is increased, and the solution seems to be better confined in space. This is the expected behaviour. Unfortunately, the polarity of the solution has switched, which is a first hint at some method inherent issue, which becomes important in the evaluation of the inversion results for real data cases (c.f. chapter 7.1): there is a trade-off between the velocity model, the source time, and the source depth in the determination of the overall solution. Depending on the dominating wavelengths of the signal, the best solution can be shifted by half of a wavelength in space or half of the respective period in time. This then leads to the wrong polarity of the inverted source mechanism.

The slight change of velocity values (by approx. 5 %) in the given layered model geometry leads to only small deviations in the inversion result, which is again consistent behaviour. One exception is the determination of the double-couple content (differs by 20 %), which seems to be most sensitive to this change in the setup.

If one assumes an underground model which is rather too complex than too simple, the satisfying inversion results stem mainly from the data from stations in small epicentral distances. This could be shown by only analysing data from stations in large distances. Signals measured at these stations were strongly influenced by a spurious low-velocity layer in the underground model. Their data show strong dispersion of surface waves, leading to persisting oscillating behaviour of the signal. These features are not contained in the input data set, so the inversion yields a solution with a very low VR value. It is obtained under shifts in source time and source depth, and the change of polarity. The only parameter, which is robustly determined in this setup is the general orientation, defined by strike and slip angle of the double-couple part.

The realistic scenario of a large azimuthal gap in the station coverage leads to no significant decrease of the quality of the solution. There is again a good match of synthetic traces and original data for the nearer stations, but a comparably poor match for stations in further distance. Systematic effects of the the lower absolute number of stations cannot be observed in the inversion result.

Under the aforementioned realistic geometrical influences it shows that the main orientation of the source mechanism in terms of strike and slip angle, and to a somewhat

lesser extent the magnitude, were the most stable parameters comparing all synthetic tests up to this point. The estimated source position varies by only few gridpoints in horizontal dimensions. The maxima of VR values over the horizontal positions, are quite broad. However, the VR values show one clear maximum in the time series for almost all test cases, hence the estimation of the source time seems to be well confined.

The results suggest to introduce an additional *smoothness parameter* which yields the overall confinement of the final VR value in space and time by analysing the width of the respective maxima.

6.4 Three-dimensional geometry

Volcanic seismic data could be inverted using one-dimensional GFs. This approach, justified by large wavelengths of the observed signals, simplifies the inner velocity structure and neglects topography. However, this concept has been used in real data analyses (e.g. Aster et al., 2003). The inclusion of the mentioned three-dimensional effects allows a more realistic modelling of the volcano, hence the inversion results will more likely reflect structural features.

I show here, that the presented inversion routine is capable of handling three-dimensional data by carrying out a self test with a set of synthetic data. Afterwards I show that the use of one-dimensional GFs lead to systematic differences.

A new set of synthetic data is generated from GFs, that are based on a three-dimensional velocity model, including topography. The geometry for this test, including topography information, is adopted from the case study of Mt. Erebus data in chapter 7.2. The topography is significant, the altitude varies by approx. 1600 m on a horizontal distance of 4000 m. An overview of the spatial setup is given in figure 6.29.

A regular source point grid is defined with the dimensions $9 \times 9 \times 9$ (1000 m grid spacing). The velocity model is a homogeneous halfspace model with parameters

$$v_p = 2.20 \text{ km/s} \quad , \quad v_s = 1.27 \text{ km/s} \quad , \quad \rho = 2.40 \text{ g/cm}^3 \quad , \quad Q_p = 1000 \quad , \quad Q_s = 500 \, .$$

The grid is laterally centred at (77.528°S, 167.140°E). Afterwards, the model is extended by information about the topography as shown in figure 3.8 (page 37). Depths in this model are defined with respect to surface level. Due to the stretching of the underground model, the former regular source point grid is distorted in vertical direction. The effective depths of the gridpoints are varying laterally. The source point depth of 6000 m is defined on the original (regular) grid, which is equivalent to a subsurface depth of 5700 m in the transformed source point grid. A vertical cross-section of the distorted source point grid is visualised in figure 6.30. The program ct3dtopo (Tessmer, 1995), c.f. chapter 3.2.1, is used for the generation of the GFs. Because the concept of reciprocity is applied in calculating the GFs, no correct absolute amplitude of the traces is given. Since the differences between vertical grid deformations at the stations' positions are negligible (see figure 6.30), the pairwise ratios of amplitudes of GFs are assumed to be correct.

Data, generated with the three-dimensional GFs for the given setup, are plotted in figure 6.31. Clear differences between data for a deep source and a near surface source position occur. Depending on the station, the data can show oscillatory behaviour. This feature results only from the inclusion of topography.

The data in these tests are representing velocity instead of displacement signals. This accommodates the native data format from the real data case study, additionally it is the generic format of the three-dimensional GFs used here. Data are sampled with 10 Hz. Source time and mechanism are the same as in the previous sections.

The two test cases are as follows:

1. Ensuring the general functionality by testing the handling of three-dimensional GFs. The synthetic data are inverted using the identical set of GFs. A perfect match of inversion results and input parameters is expected.

2. Applying the flat Earth approximation by using one-dimensional GFs for the inversion. The data are inverted by neglecting the topography information. The GFs are calculated with QSEIS (Wang, 1999), c.f. chapter 3.2.2. The arrival times in these GFs coincide with the times in the three-dimensional GFs, apart from that the waveforms of both sets differ. Due to the mentioned scaling issue for the three-dimensional GFs, no seismic moment can be calculated in this case.

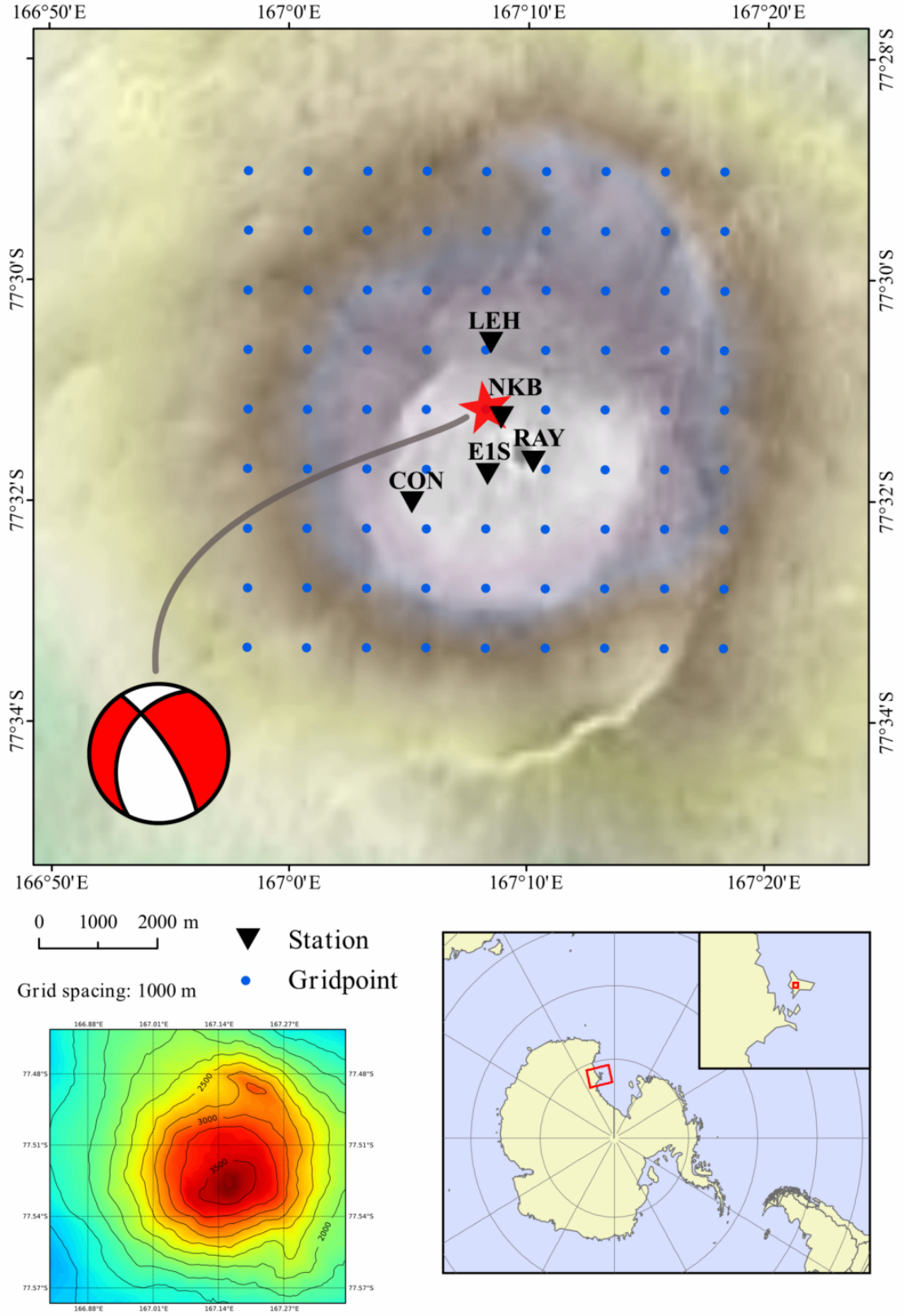

Figure 6.29:
Station geometry for testing the handling of a 3D model in sec. 6.4. **upper:** Geometry of the station-grid configuration. Stations are marked with black triangles. Blue dots are lateral positions of gridpoints. **lower left:** Topography (altitude from WGS84) is given in colour code. Contour lines in 500 m steps. **lower right:** Geographical overview of the source region.

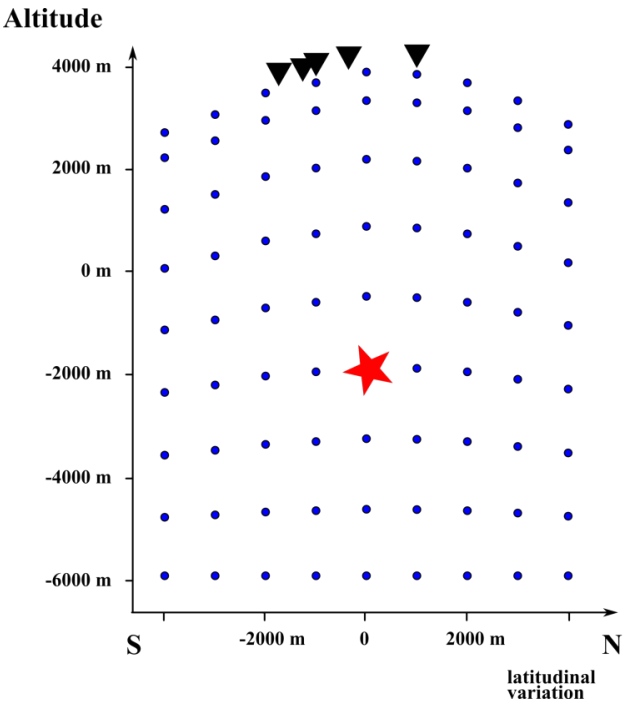

Figure 6.30:
Vertical cross section of the three-dimensional source point grid. Section is orientated South-North. Longitude of the section is 167.14°E. Grid points are given by blue dots, position of the artificial source is marked by the red star. Orthogonal projection of station locations indicated by black triangles.

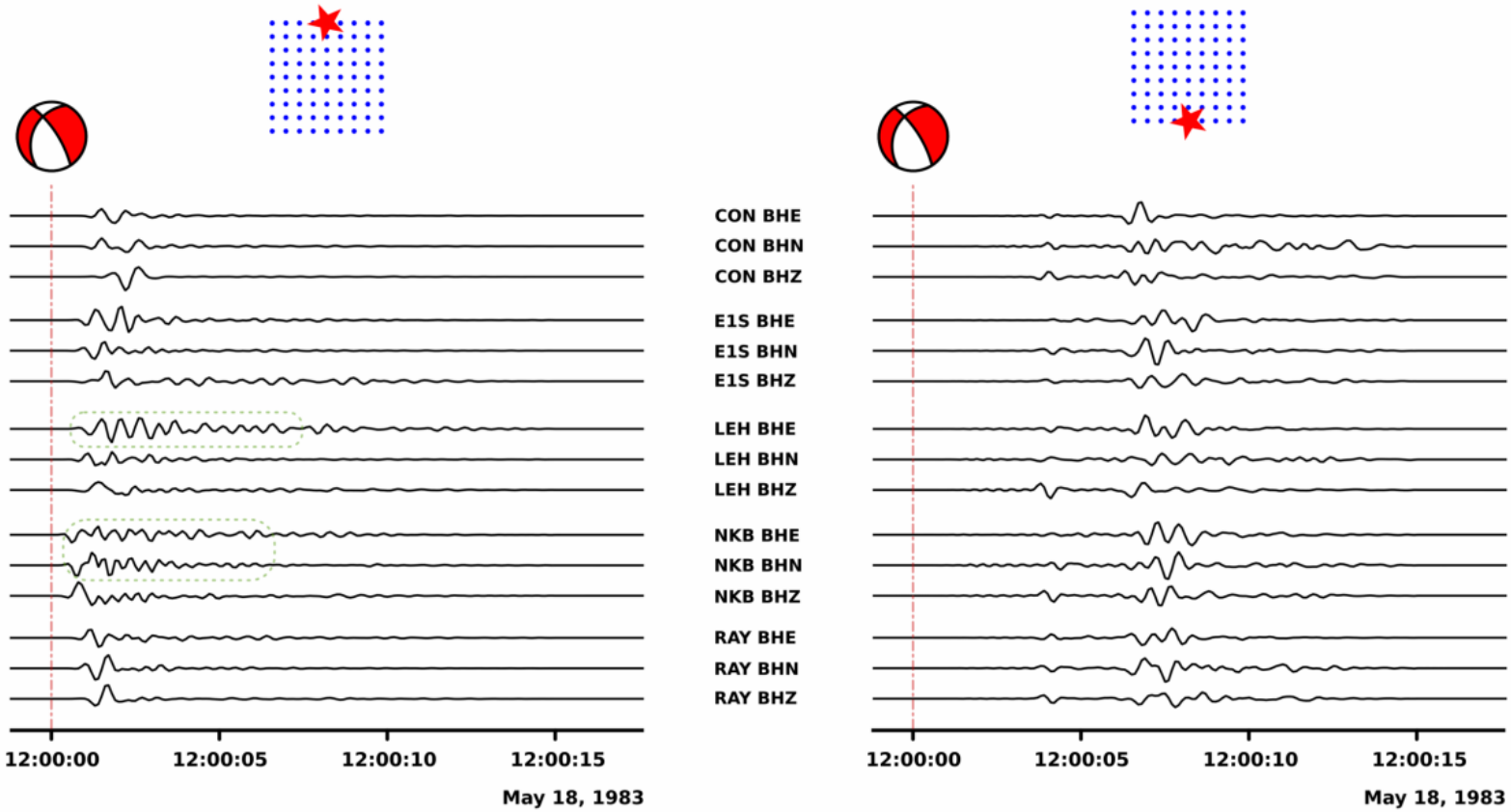

Figure 6.31:
Comparison of synthetic velocity data traces (overall scaling). Synthetic data are generated using 3D GFs. Source mechanism and source time are indicated by FSD and red line. Source positions are indicated by the red star on the relative grid (not including topography). **left:** Source position near the surface, topography related oscillatory content (green line) in some data at stations LEH and NKB. **right:** Source position at the bottom of the grid. Mainly P- and S-phases are visible, no clear influence of topography.

Results

1. **Ensuring general functionality**

   All source parameters are determined correctly. The VR value is 100 %. The time series of this value shows a clear maximum at the correct source time, the time series shows slight oscillatory behaviour at the flanks of the maximum peak. With respect to horizontal spatial variations, the solution is well confined (better than in the test case 6.2.1, consistent with the higher complexity of the waveforms). The overview of the results of this inversion can be found in figure 6.32.

2. **Flat Earth approximation**

   The inversion of data from a three-dimensional setup using one-dimensional GFs yields the results shown in figure 6.33.

   The lateral shift of the estimated source location is two gridpoints to the West and one gridpoint to the North; additionally, the depth is over-estimated as 8000 m. The variability of VR values on the horizontal grid section shows an annular symmetry with a comparably small value at the correct position. The source mechanism varies quite strongly. The best determined source mechanism consists mainly of an implosive isotropic component (50 %) and a double-couple (40 %). The orientation of the double-couple part does not reflect the correct source mechanism. A shift of the source time by 1 s is estimated, there is a distinct but broad maximum in the time series of VR values.

   The comparison of input data traces and the internally generated synthetic results shows a rather good agreement of traces, considering the harsh approximation of the used model (see figure 6.34). From the good match of the two sets of traces there results a high maximal VR value of 76 %.

3D geometry – summary

It is shown, that three-dimensional GFs can be handled without problems. The direct inversion of the synthetic raw data using the identical set of GFs yields the expected complete match of input parameters and inversion results.

The data set includes features, that reflect the influence of topography. The approach of inverting these data using a one-dimensional set of GFs yields an inversion result with a comparably high VR value and a well confined source time. However, all other parameters show strong deviations from the correct values. The annular horizontal symmetry of VR values suggests, that these deviations are rather systematically caused by the negligence of topography than being only numerical artifacts originating in the different generation softwares for the GFs. Furthermore, the source mechanism shows a decomposition, which is very different from the original.

Altogether, the occurring differences between the one-dimensional GFs and the three-dimensional GFs suggest, that only the latter can be used for inverting volcanic seismic data in presence of strong topography.

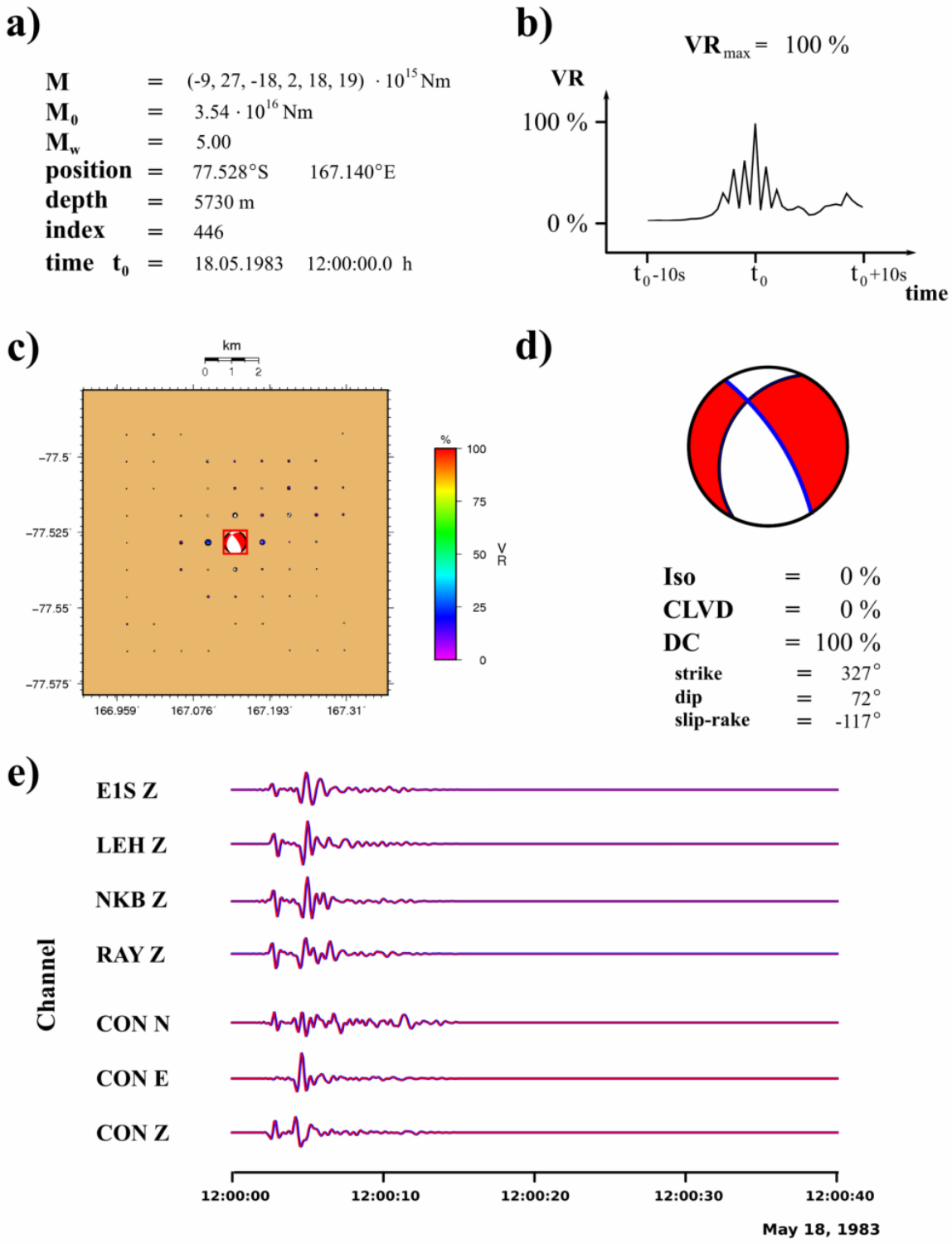

Figure 6.32:
Inversion result – 3D geometry – self test (6.4-case 1) **a)** Estimated numerical values. **b)** Chronological evolution of VR. **c)** Geometrical overview of a horizontal source grid section. **d)** Focal sphere diagram and source parameters of the estimated optimal source mechanism. **e)** Original data traces (red) and synthetics (blue), based on the estimated source mechanism.

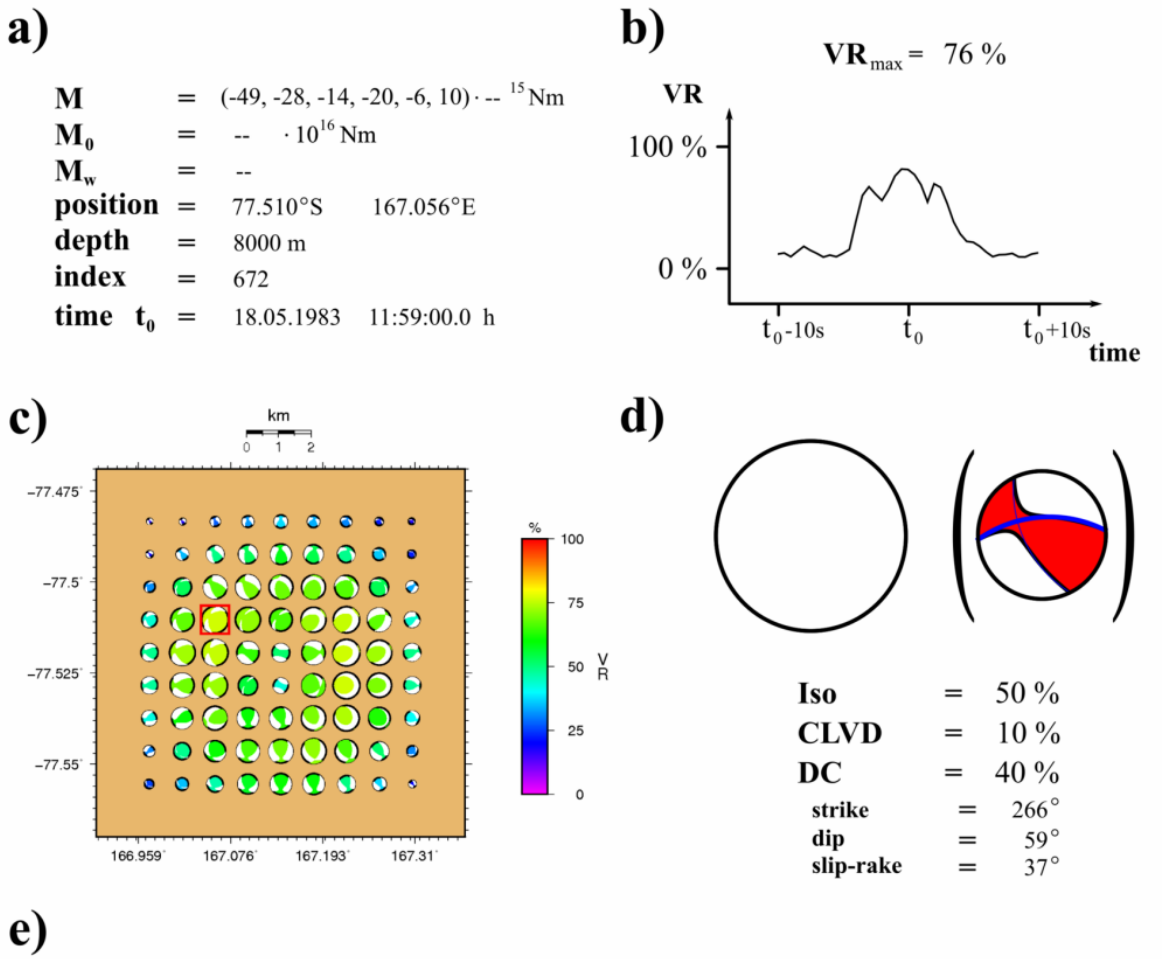

Figure 6.33:
Inversion result – 3D geometry – flat Earth approximation (6.4-case 2). **a)** Estimated numerical values. **b)** Chronological evolution of VR. **c)** Geometrical overview of a horizontal source grid section. **d)** Focal sphere diagram and source parameters of the estimated optimal source mechanism (deviatoric part given in parentheses) **e)** Original data traces (red) and synthetics (blue), based on the estimated source mechanism.

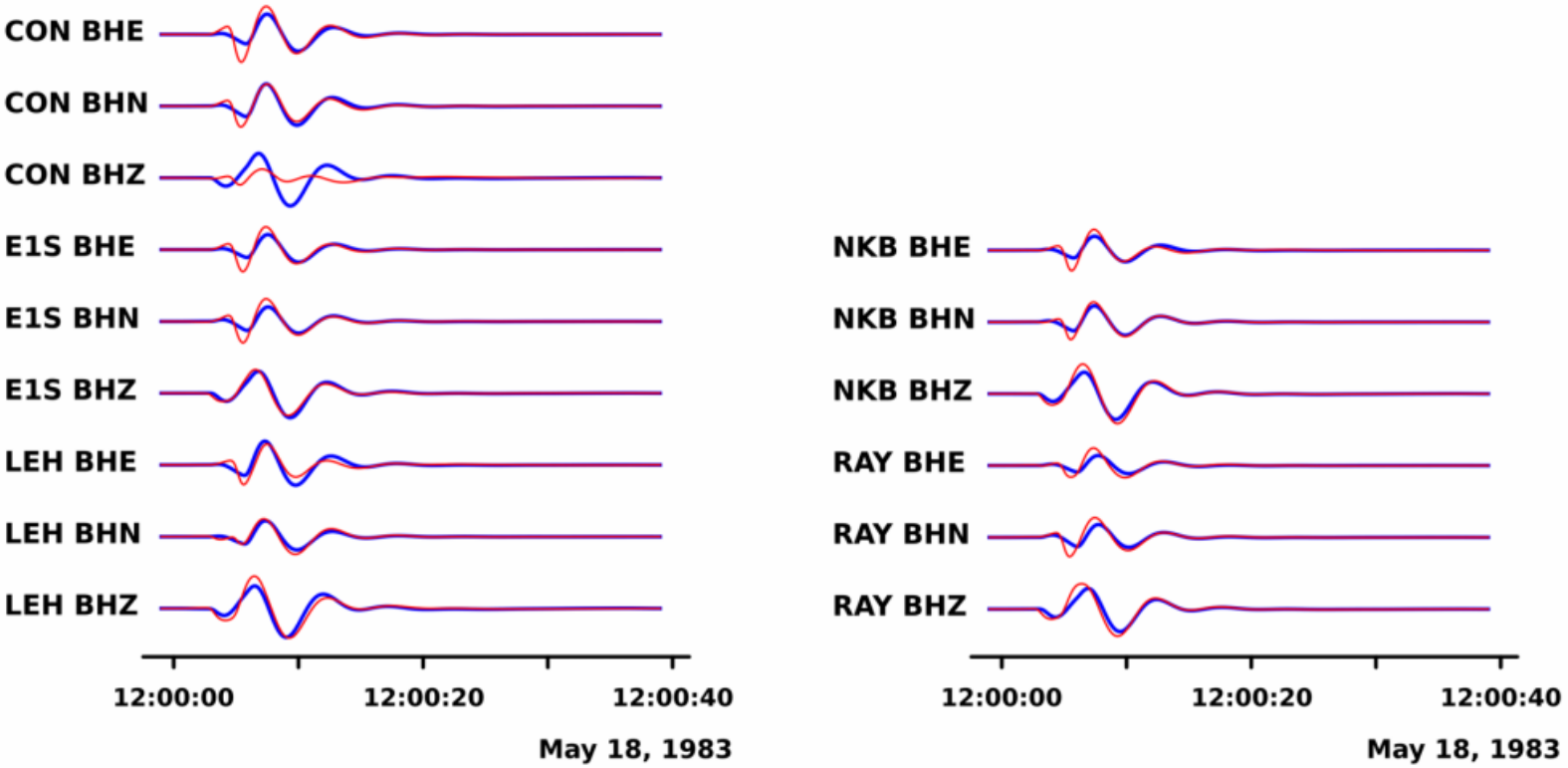

Figure 6.34:
Examples of synthetic data traces for test 6.4-case 2. All channels, stations CON, E1S, LEH, NKB, RAY. Velocity data, overall scaling, frequency bandbass 0.033-0.2 Hz. Positions of stations are shown in figure 6.29

6.5 Continuous analysis of synthetic data – inversion and event detection

In this last section of (synthetic) tests, I elucidate the capability of *ARCTIC* to act as an autonomous detection algorithm working on a continuous data stream. Following the idea, sketched in sections 5.3.2 and 5.4, a synthetic data set is set up, imitating continuous real data (anticipating the real case application in section 7.3). Data from 16 stations, three channels each, are used in this inversion procedure. Naturally, the data are not extended to infinity, but their length is chosen so that all the important features of the method are shown. A temporal section of the data is shown in figure 6.35. The data traces start on 20.10.2004, 00:00 h, and they end on 20.10.2004, 12:00 h, they do not contain gaps or non-numerical values. One event is contained in the data set, the source time is 20.10.2004, 06:59:15 h. The event parameter are the same as in the previous one-dimensional test cases (see section 6.1.1). The data are generated based on the one-dimensional velocity model used before in section 6.3 (shown in figure 6.11). White noise in amplitude ratio 10 % is added to the data. The processing of data includes frequency filtering.

The station geometry is set up on the basis of the case study in section 7.1.1. It is shown in figure 6.36. The source point grid is reduced by a lateral radius of 25 km around the centre point, which results in 63 grid points. The length of the moving time window is 240 s. Data are displacement traces, which have a sampling of 2 Hz. The threshold of the VR value for defining an event detection is set to 60 %.

Results

The simulation of continuous data inversion ran 12 hours without problems. Near real-time inversion has been simulated. Within this time frame, the data of 16 stations, each with 3 channels, have been analysed. After having finished loading the GFs and setting up the correlation matrix and its inverse, the moving time window has shifted in step sizes of 3.34 seconds on average. The highest VR value within the whole time frame coincides with the generated synthetic event and it has a value of 83 %. Only one clear maximum has been observed in the data. In the intervals without event, the mean value of VR is approximately 2 %. The important section of the time series of VR values (including the event) is presented in figure 6.37.

The VR value exceeded the threshold value for two successive time steps. Therefore two `.xml`-files have been generated in case of the detected event. These files have been successfully sent to an external event database. A graphical representation of the solution parameters for the detected event time is shown in figure 6.38.

The detected source time (first of the two time steps, belonging to this event) is 0.6 seconds before the correct event time. The solution has a VR value of 83 %.The correct source location has been determined. The seismic moment is estimated slightly too low (92 %). The spatial variation of VR values is high and symmetric, the solution is well confined. The geometry of the source mechanism shows the expected high shear-crack content of 96 %. The isotropic and CLVD components are negligible. The orientation of

the governing double-couple is only marginally deviating from the correct orientation in strike ($-2°$) and dip ($-1°$) angles; variations are found in the slip-rake angle ($-9°$).

The waveforms of original input data and the internally reproduced synthetics coincide very well, only small deviations occur.

Near real-time inversion of a continuous data stream – summary

It is shown by the test on a long synthetic data set, that it is possible to analyse a continuous stream of seismic data in near real-time with the *ARCTIC* tool. From a constantly low noise level of VR values, from the analysis of data in time windows without events, the event shows up in the time series very clearly. Thus the tool has the potential to act as a detection algorithm for LP-events.

Since the steps between consecutive time windows are of finite length and depend on the computational time for the inversion of a single window, the source time of the event is not matched exactly by an analysis window position. Although the correct time is missed by the very small time difference of only 0.7 s in the example, the inversion result showed a VR value of only 83 %. However the inverted source mechanism was correct and well confined with only minor deviations.

Small differences in the estimated source time seem to result in comparably large deviations from the correct source inversion result. Especially the essential VR value decreases very fast, but in the end this is the value which defines the detection of the event. Hence the limiting factor for obtaining a robust detection in the long run is mainly the time step between the successive windows. This must be far smaller than only half of the length of the dominating period in the signal. The number of source grid points enters linearly into the computational time. In order to obtain a sufficiently fast inversion within the analysis window, the number of grid points had to be significantly decreased down to approx. 10 % of the original grid in the setup of the example. A trade-off between maximum size of the source point grid and a reasonable step size of the moving window has to be found in advance for the application on real data sets, most likely by preliminary test runs on data sets with signals of known events.

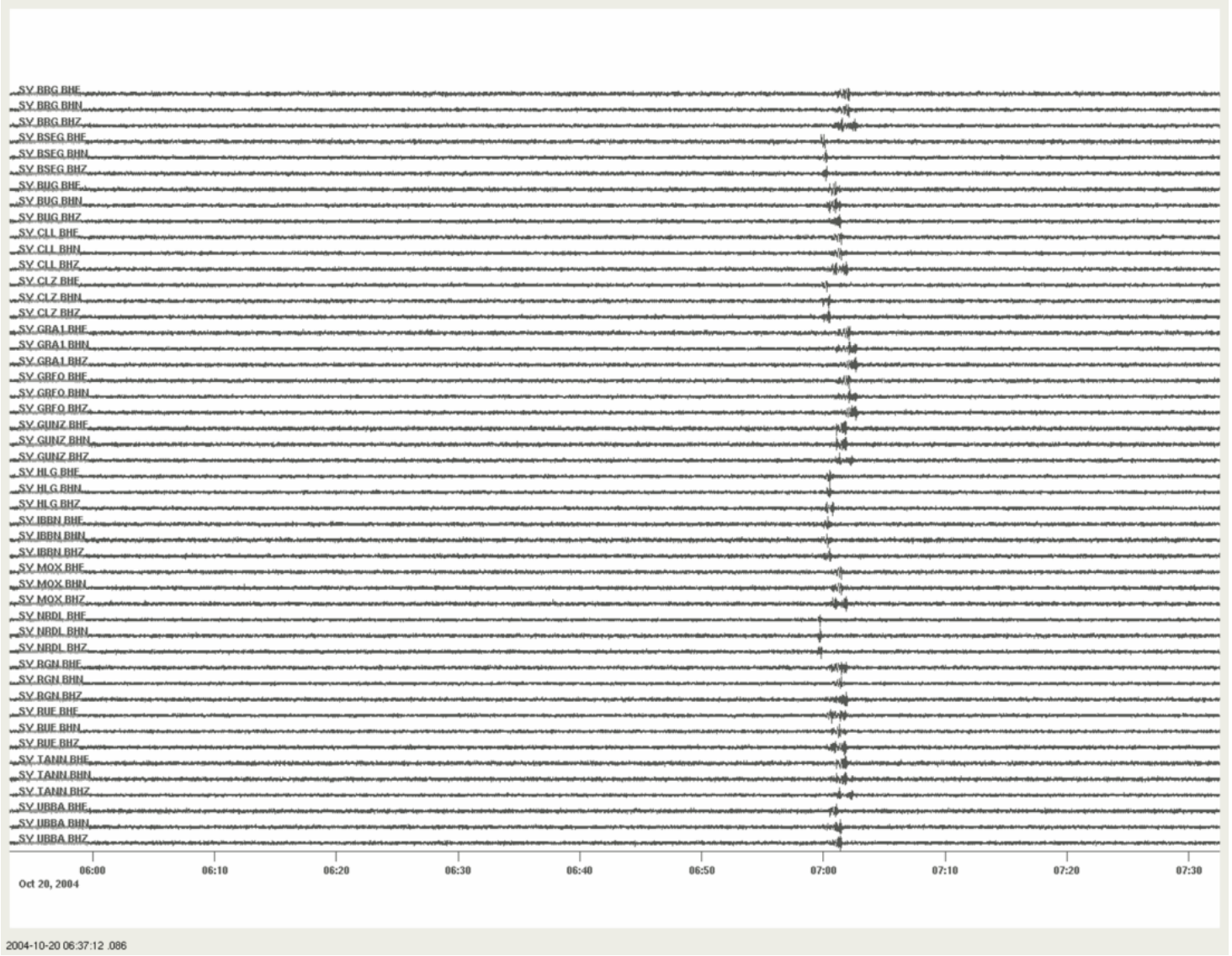

Figure 6.35:
Synthetic data traces for testing continuous application of *ARCTIC* (sec. 6.5). Showing an approximately 90 min. section of displacement data traces from 16 stations, each with three channels. Traces are individually scaled to unity to clearly show characteristics of data and varying onset times at different stations. Total data length is 12 hours.

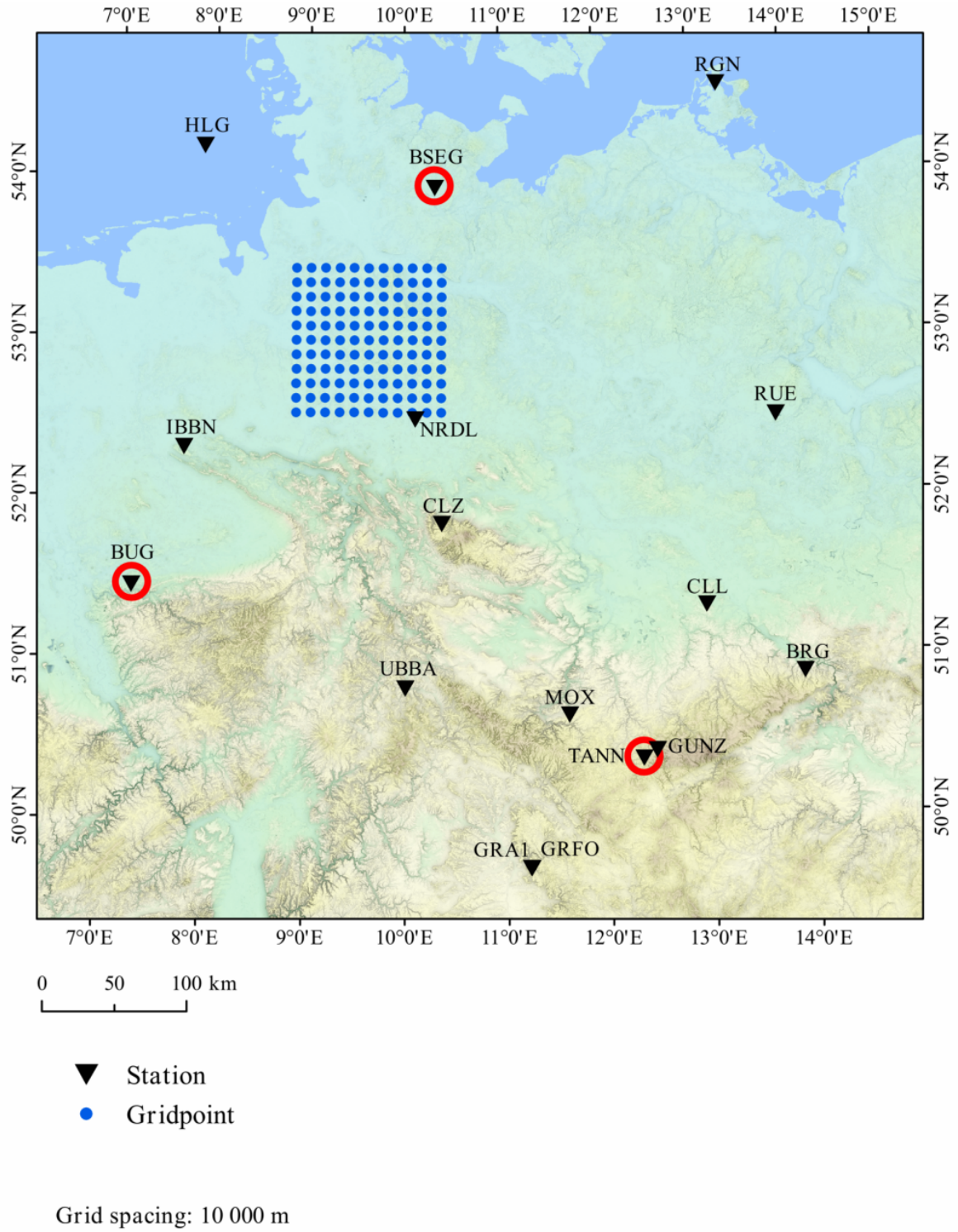

Figure 6.36:
Geometrical setup for synthetic test of continuous application (sec. 6.5). Horizontal projection of the source grid is given as blues dots. Seismic stations are indicated by black triangles. Red circles denote stations, whose data are shown in figure 6.38.

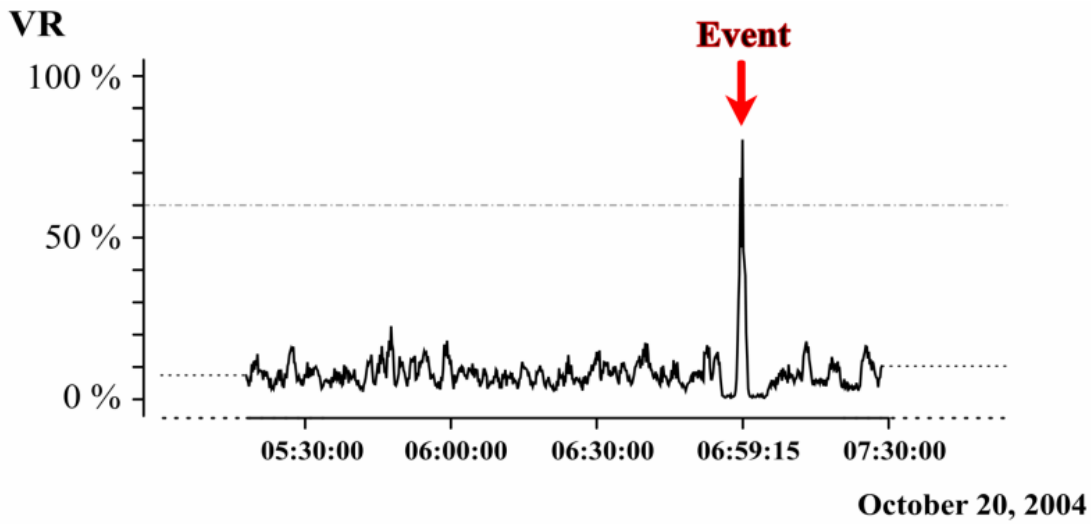

Figure 6.37:
Result of the continuous application on synthetic data traces (sec. 6.5). Section of the time series of VR values, containing one event at 06:59:15 UTC. The dash and dot line at VR = 60 % indicates the detection trigger threshold defined in this test.

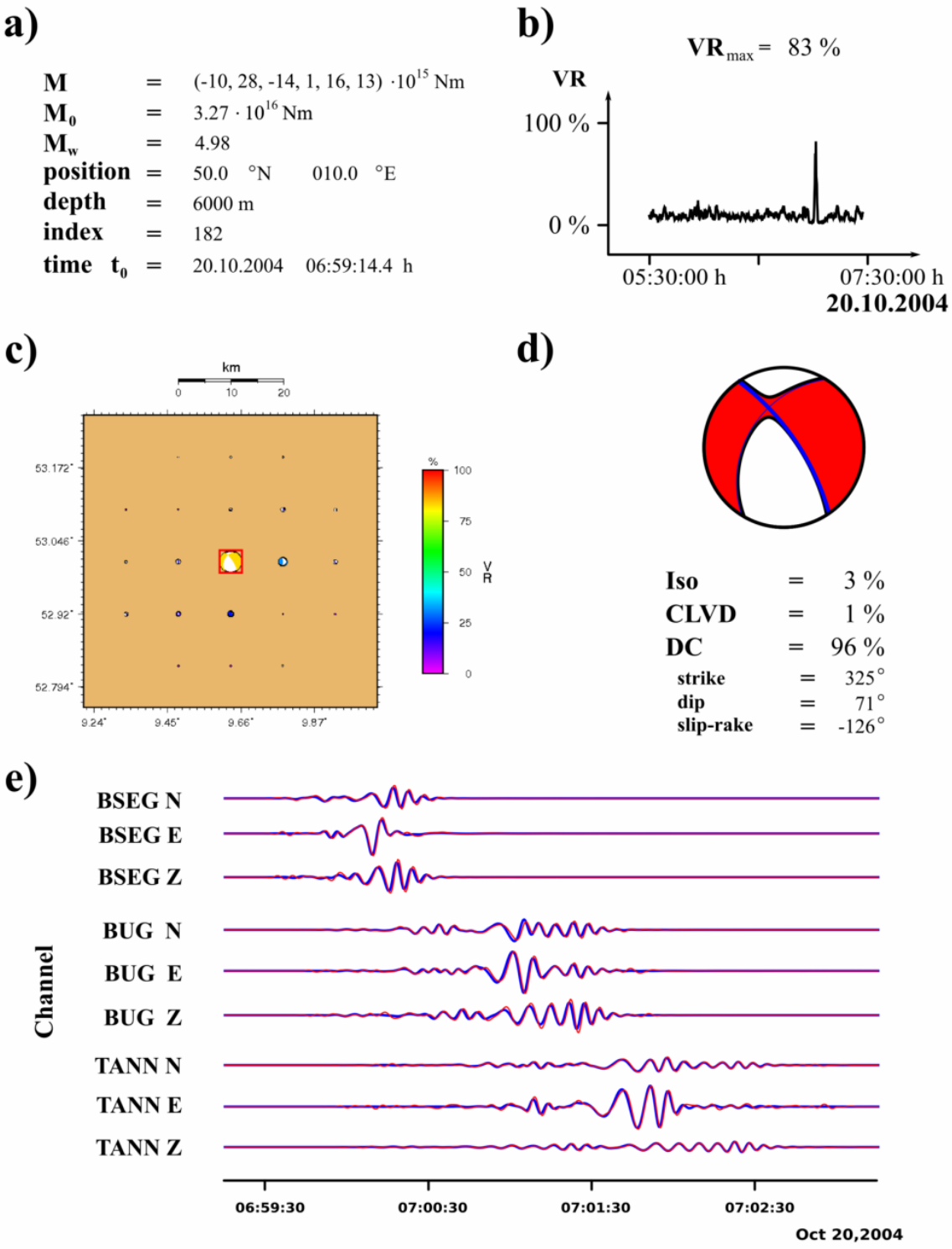

Figure 6.38:
Inversion result for the detected event in the continuous application (sec. 6.5). **a)** Estimated numerical values. **b)** Chronological evolution of VR. **c)** Geometrical overview of a horizontal source grid section. **d)** Focal sphere diagram and source parameters of the estimated optimal source mechanism. **e)** Original displacement data traces (red) and synthetics (blue), based on the estimated source mechanism. Data are scaled individually. Stations contributing data are defined in fig 6.36.

7 Case studies

7.1 Induced events

7.1.1 The Rotenburg 2004 M_w 4.4 earthquake

On 20.10.2004, at about 7:00 h (UTC), the north-western part of Germany was struck by an unusually strong earthquake. Its epicentre was situated in the vicinity of the town of Rotenburg (Wümme), near to a large gas field. This location suggested that the event was potentially induced by gas recovery. It gave rise to a detailed event study, the results been published in (Dahm et al., 2007). The authors have inverted seismic data for source time, location, and mechanism. They propose a source with:

- $M_w = 4.43$,
- centroid depth 5-7 km ,
- shear crack mechanism
  - strike angle $327°$,
  - dip angle $72°$,
  - slip-rake angle $-117°$,
- source time 20.10.2004, 06:59:15.1 UTC ,
- source location
  - latitude $53.01° \pm 0.05°$,
  - longitude $9.63° \pm 0.12°$.

These parameters are taken as reference values for the evaluation and validation of my inversion results. The availability of the results of this detailed study makes this (most likely induced) shallow seismic event an obvious test case for the application of *ARCTIC* on a real data set.

Data from 9 stations of the *German Regional Seismic Network* (*GRSN*) in epicentral distances < 400 km are used, 23 channels in total. Data are given as integrated raw data, reflecting displacement. The sampling of the data is 2 Hz. The available data traces are shown in figure 7.1 (data provided by S. Cesca).

The source point grid has the lateral dimensions 11×11 with a grid spacing of 10000 m. The vertical extension of the grid is given by 3 layers in depths 2000 m, 6000 m, and 10000 m. The grid is laterally centred at the source coordinates of the reference result.

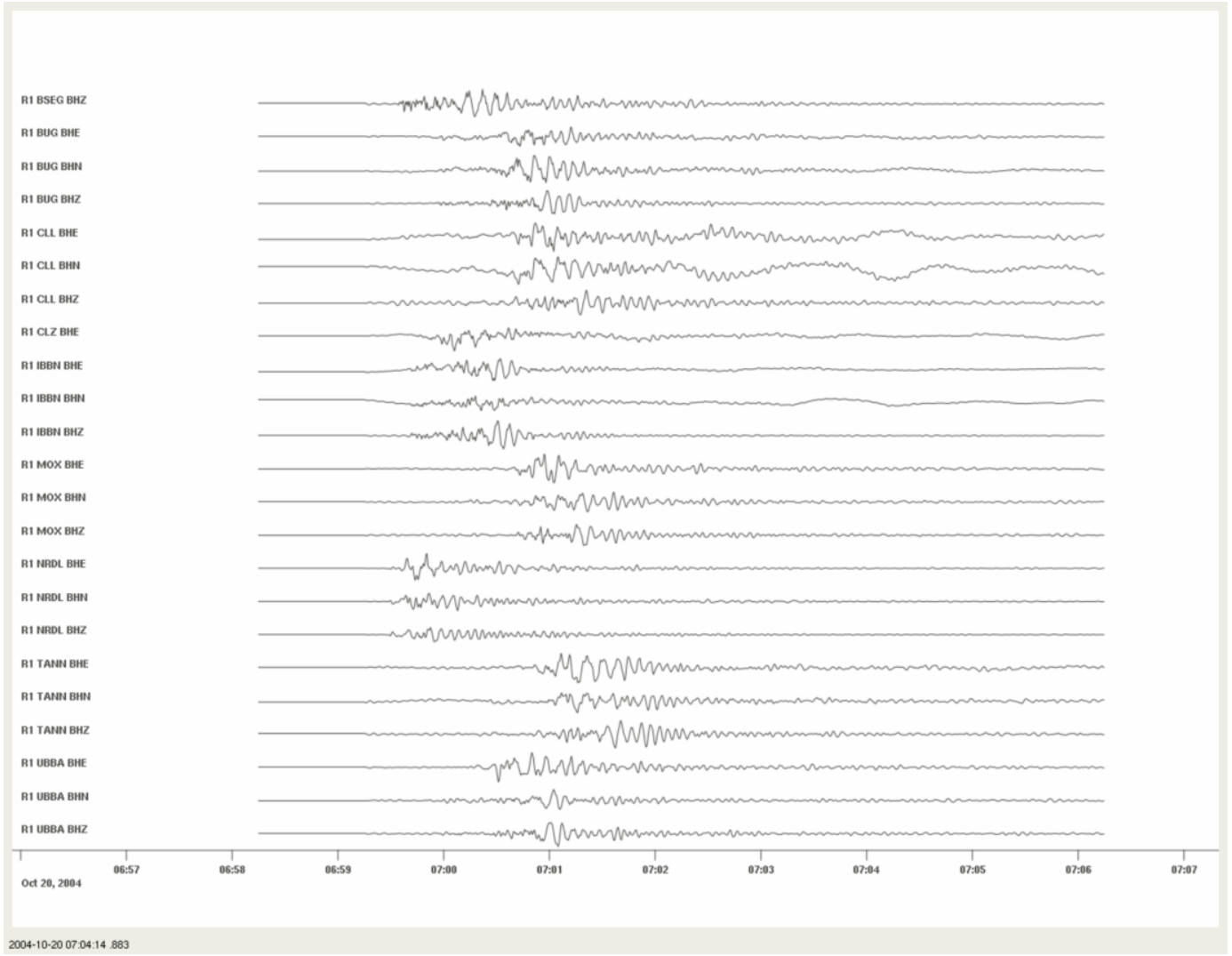

Figure 7.1:
Available restituted displacement data traces for the *Rotenburg* event (sec. 7.1.1). Approx. 8 minutes of displacement data for 23 channels of 9 stations of the *GRSN*. Individual scaling, sampling rate 2 Hz.

The velocity model for generating the GFs is shown in fig. 6.11. It is taken from (Dahm et al., 2007) and has already been used for the generation of synthetic data in section 6.3. The geometry of the inversion setup is shown in figure 7.2.

The data and GFs are frequency filtered with a bandpass from 0.04 Hz to 0.06 Hz. Data traces are analysed in time windows of length 210 s; the time window is moved $\pm 10s$ around the aforementioned source time in steps of 0.5 s.

In total, four inversions have been carried out for this data set:

1. full grid search in space and time,
2. given reference source time is assumed to be correct, only spatial grid search,
3. given reference (horizontal) source coordinates are assumed to be correct, grid search for source depth and source time,
4. inversion of data only for source mechanism, given reference source time and location are assumed to be correct.

Results

1. **Full grid search**

   The results for the full grid search are presented in figure 7.3.

   The estimated best solution of the inversion has a VR value of 68 %. The source location is estimated to be shifted one gridpoint to the East and to the North respectively. Additionally, the depth is over-estimated as 10000 m. The horizontal position seems well confined in North-South direction, higher uncertainty is given in East-West direction, still localised near the horizontal grid center. The source mechanism does not vary significantly among positions with high VR values. The estimated mechanism is dominated by a double-couple part (64 %). Its main orientation (defined by strike and dip angle) reflects only very roughly the reference mechanism, the strike vary by 26°, the dip by −21°. The slip-rake angle is rotated by 191°, so the polarities of the estimated mechanism and the reference mechanism are inverse.

   The determined source time is delayed by 5.5 s with respect to the reference value. However, the time series of VR values shows two not very pronounced maxima, the reference time marks a local minimum. The strength of the event is estimated as M_w 5.24, which is significantly higher than the reference result (M_w 4.43).

   A comparison of (frequency filtered) original data traces and synthetic traces, generated with the parameters of the inversion result, is shown in figure 7.4. The traces match well in general; some deviations occur, which do not systematically depend on stations but on single channels.

2. **Fixed source time – grid search on spatial grid**

   In figure 7.5, I show the results for the purely spatial grid search.

   The depth of the source location is again over-estimated as 10000 m. The lateral shift of the source location is determined to one gridpoint each to the South and the East. The source is confined there by one gridpoint variation in all directions. The source mechanism varies only slightly in the surrounding of that source point. It is dominated by a strong double-couple (64 %) and a CLVD part (20 %). Strike angle (14°) and dip angle (−22°) are in the range of the result of setup no. 1. Contrary, the slip-rake is similar to the reference value (−5°). The best source shows again a high magnitude (M_w 5.16). The match of original data traces and reference synthetics is satisfactory.

3. **Fixed horizontal source position – grid search in time and depth**

   Opposite to the former setup, I have taken the given reference source location as the correct one. The grid search yields the results, given in figure 7.6.

   The best estimation of the source time is shifted by 8 s, the depth is at 10000 m. The result has a VR-value of 62 %. The VR shows two maxima in the time series, the smaller one is located at the reference source time (additionally fixing the source depth yields the result for the slightly smaller maximum of 58 % at $t_0 - 1s$). The time span of 8 s is in the range of one half of the dominating signal period of approx. 13 s. The magnitude is similar to the result of the full grid search result (M_w 5.12). The source mechanism is again governed by a large double-couple part (87 %), the deviation (strike 21°, dip −11°) of its main orientation is comparable to the previous result. The slip-rake angle is 75°, so the polarity changed again (the solution of the second maximum does not show this change of polarity, it is similar to the following in case 4). The fit of data is of the same quality as for the previous inversion result (case 2).

4. **Fixed source time and location – inversion only**

   Assuming that the given source time, as well as the source location, are correct, I inverted the data fixing these parameters. This allows for a direct comparison with the reference result. The outcome of this inversion is presented in figure 7.7.

   The large double-couple part of the source mechanism (65 %) is accompanied by an isotropic component of 20 % and the CLVD (15 %). The orientation of the double-couple is similar to the reference result with small deviations in strike (9°) and dip (−2°), and a slightly larger deviation in the slip-rake (14°). The strength of the event is given as M_w 5.18, which is in the same range as the former results.

   The comparison of original and synthetic data traces is shown in figure 7.8. Most traces match well; deviations for channels with high amplitudes are the reason for the lower VR value of this solution.

Evaluation

The inversion of the *Rotenburg* event in four different setups yields satisfying results. All comparisons of the solution parameters are given with respect to the reference result.

In case 4, it is shown that the pure inversion result of the data sets yields an estimator for the source mechanism that is quite similar to the reference mechanism. Only small deviations occur in the main orientation, the mechanism is dominated by the double-couple component. The reference result originates from an inversion, which was restricted to the determination of the double-couple component of the source. Therefore I interpret the estimated source mechanism as being consistent with the reference result. The shapes of original data traces and reproduced synthetic traces match quite well in general, Some strong deviation for channels with a high absolute amplitude level influence the result by leading to a significant decrease of the VR value. Since the overall maximum of VR determines the final inversion solution, this local solution cannot be found by an unconfined full grid search.

The cases 2 and 3 (grid search in space and time respectively) show, that the search for the optimal source is governed by the trade-off between source location and time (c.f. chapter 6.3.7). Although the VR value of the best solution is similar for both cases, it seems that the correct determination of the source time has a higher weight than the exact position. Firstly, the polarity of the solution, obtained from the spatial gridsearch fits better the reference result. Secondly, the local maximum of the VR time series in case 2 around the correct source time determines a solution that is also very similar to the solution for fixed location and time.

The full free grid search (case 1) is the generic result of this algorithm. No preliminary assumptions are confining the solution. The original data and the reproduced synthetic traces coincide very well for most of the channels, more precisely for most of the channels with large amplitudes. The solution is shifted in time as well as depth. The time series shows two maxima, which may originate from solutions in different depths. The absolute difference between the maximal values is very small, thus the effective confinement of the source depth estimation is very low. With regard to the aforementioned problem of finding in internal trade-off for determining the solution, the wrong polarity of this optimal solution fits in consistently.

The study in case 4 shows, that the application of the inversion algorithm to real data yields results, that are consistent with the reference result. The issue of finding a best overall solution by the trade-off between spatial and temporal confinement, that is not consistent, is an inherent problem of the combination of full waveform analysis in time domain and a full gridsearch in space and time.

The quality of the best overall solution depends on the chosen frequency range of the internal bandpass. Analyses with a broader bandpass between 0.035 Hz and 0.08 Hz yielded results with VR values between 33 % and 47 % only. Many non event-related features were still present in the data within that frequent range. Other values for the appropriate frequency range have been evaluated in preliminary studies.

In case of the broader bandpass, the estimated magnitudes had systematically smaller values than in the present results. The chosen bandpass seems to have an influence on that parameter. However, the determined magnitude is quite robust, it is estimated as being in the interval [5.12, 5.24] in all four cases. In addition to the magnitude, the general orientation of the double-couple part of the mechanism (strike and dip angle) seems to be another robust parameter, it varies only little (strike 17°, dip 20°).

Data have been manually checked with respect to quality. Channels with a low signal-to-noise ratio or significant spurious signal content have been eliminated in advance from the inversion. A systematic study is needed in order to investigate to what extent the low quality of data outweighs the positive effect of a better statistical confinement simply by a by larger number of data traces.

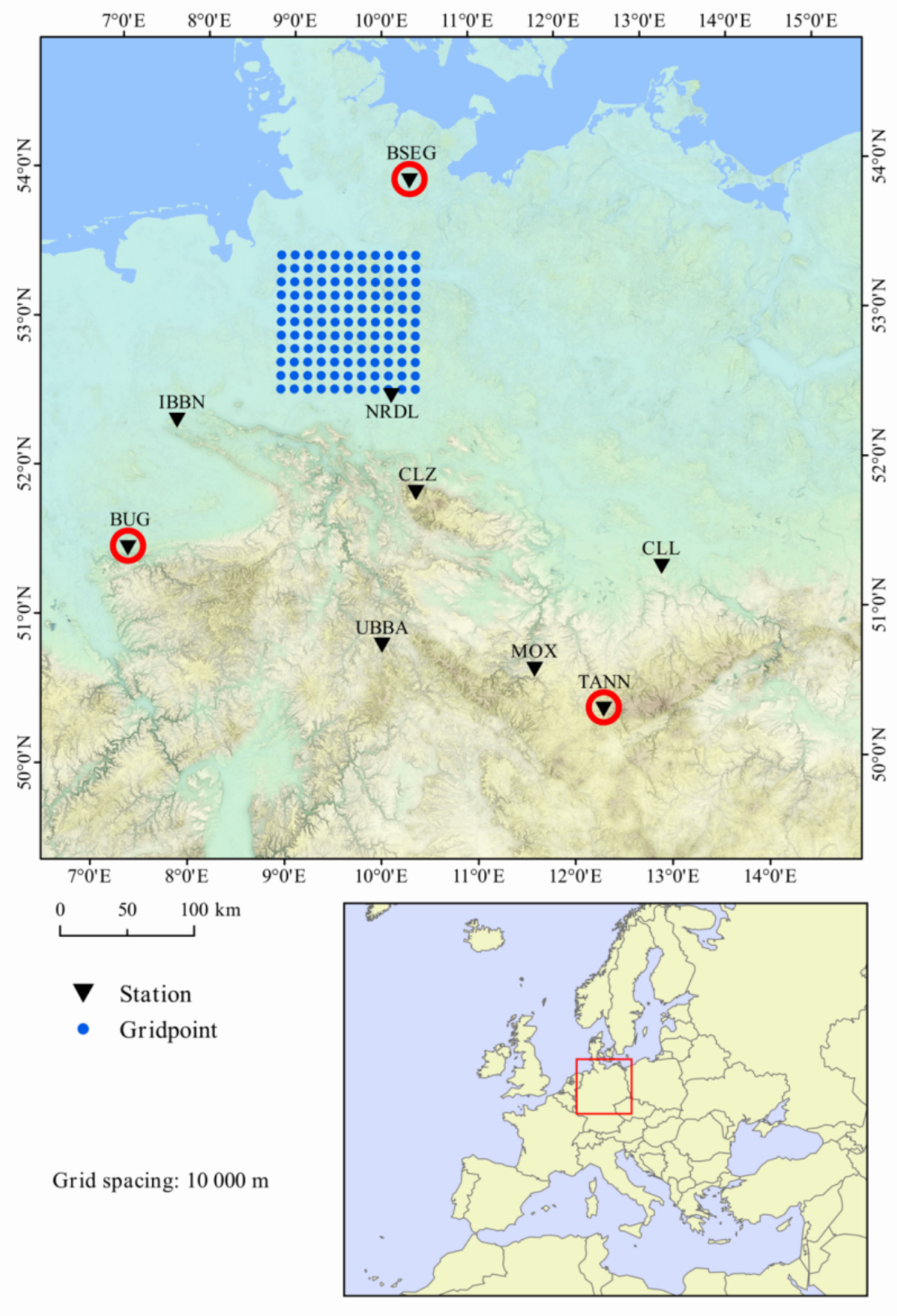

Figure 7.2:
Geometrical setup for analysis of Rotenburg event (sec. 7.1.1). **lower:** Geographical overview. **upper:** Map including the given setup. Horizontal projection of the source grid is given as blues dots. Seismic stations are indicated by black triangles. Red circles denote stations, whose data are shown in inversion result plots.

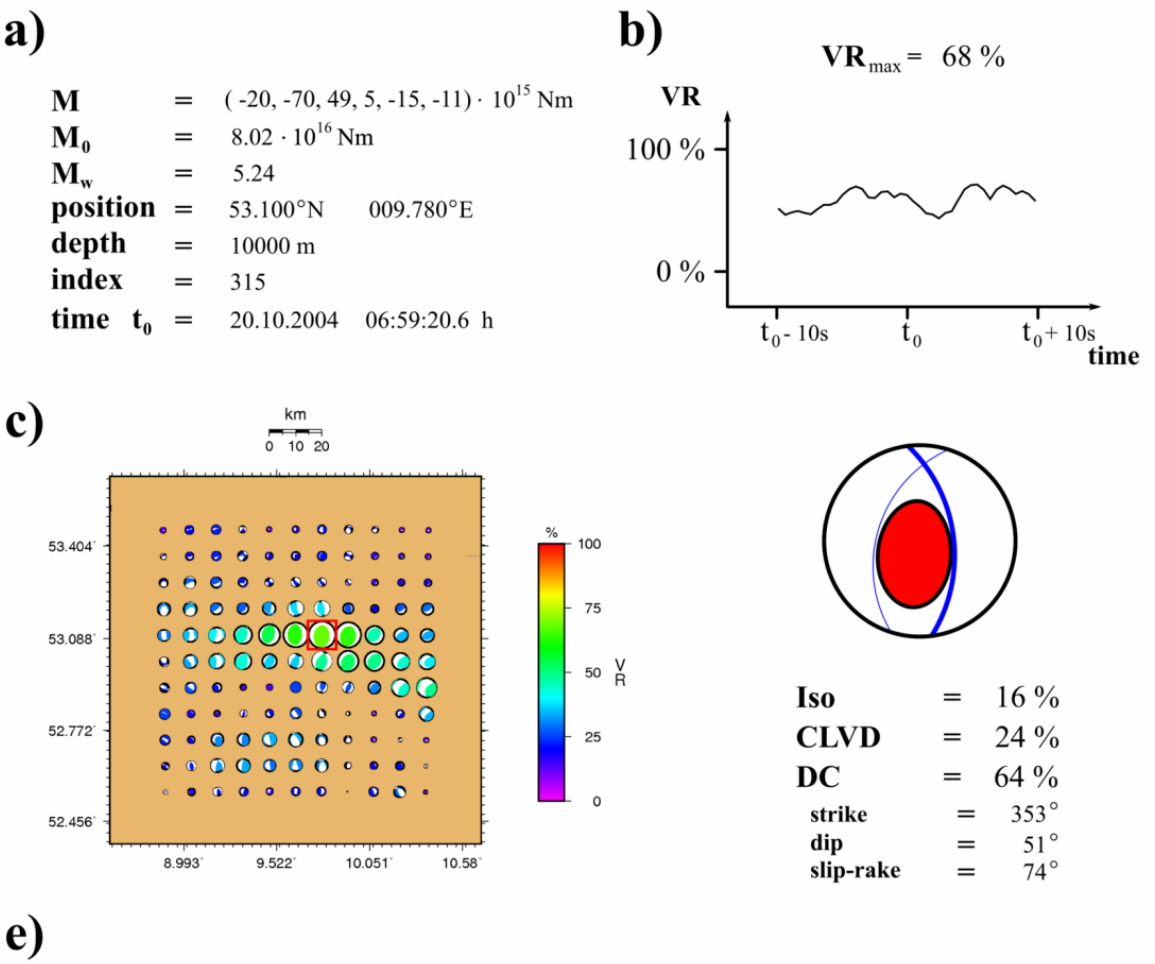

data comparison in external figure

Figure 7.3:
Rotenburg case 1 – inversion results – full grid search. **a)** Estimated numerical values. **b)** Chronological evolution of VR. **c)** Geometrical overview over a horizontal source grid section. **d)** Focal sphere diagram and source parameters of the estimated optimal source mechanism. **e)** Comparison of traces in figure 7.4

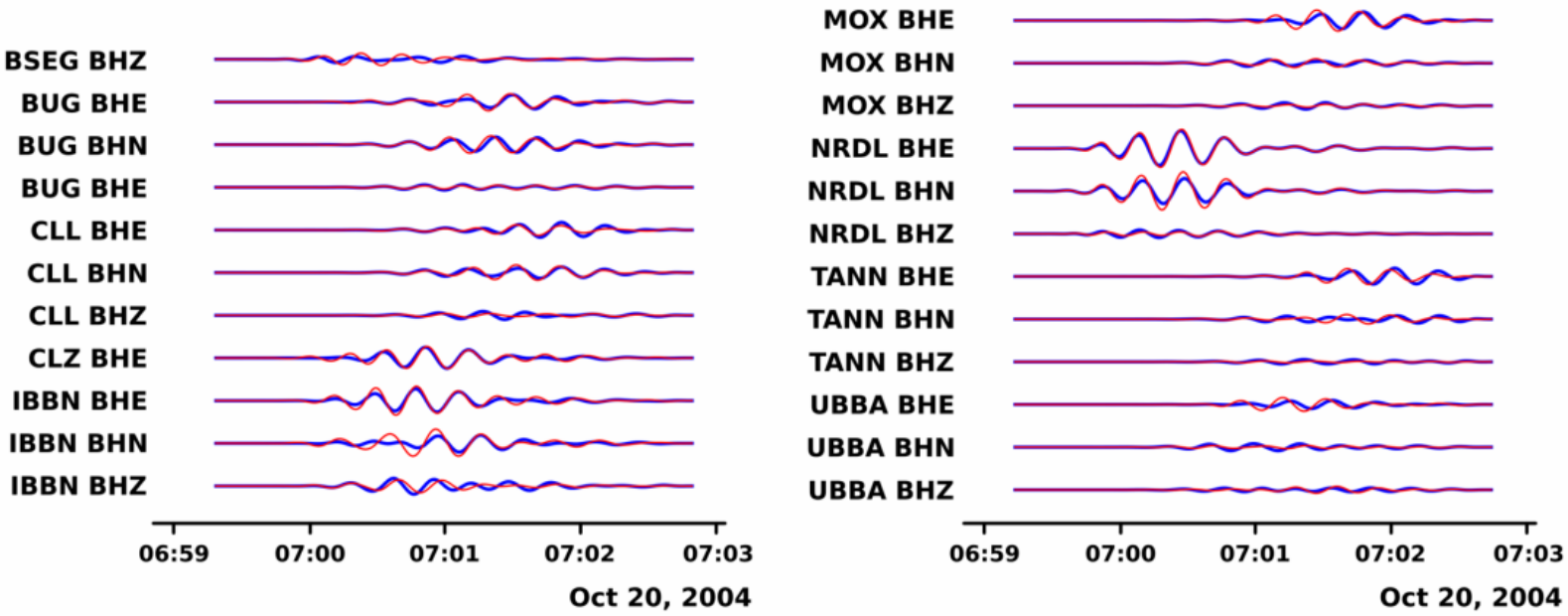

Figure 7.4:
Rotenburg case 1. Comparison of original data (red) and reproduced synthetics (blue). 210 s data with frequency bandpass 0.04 - 0.06 Hz, estimated source time at beginning of traces. Displacement traces, overall scaling. Positions of stations indicated in fig. 7.2.

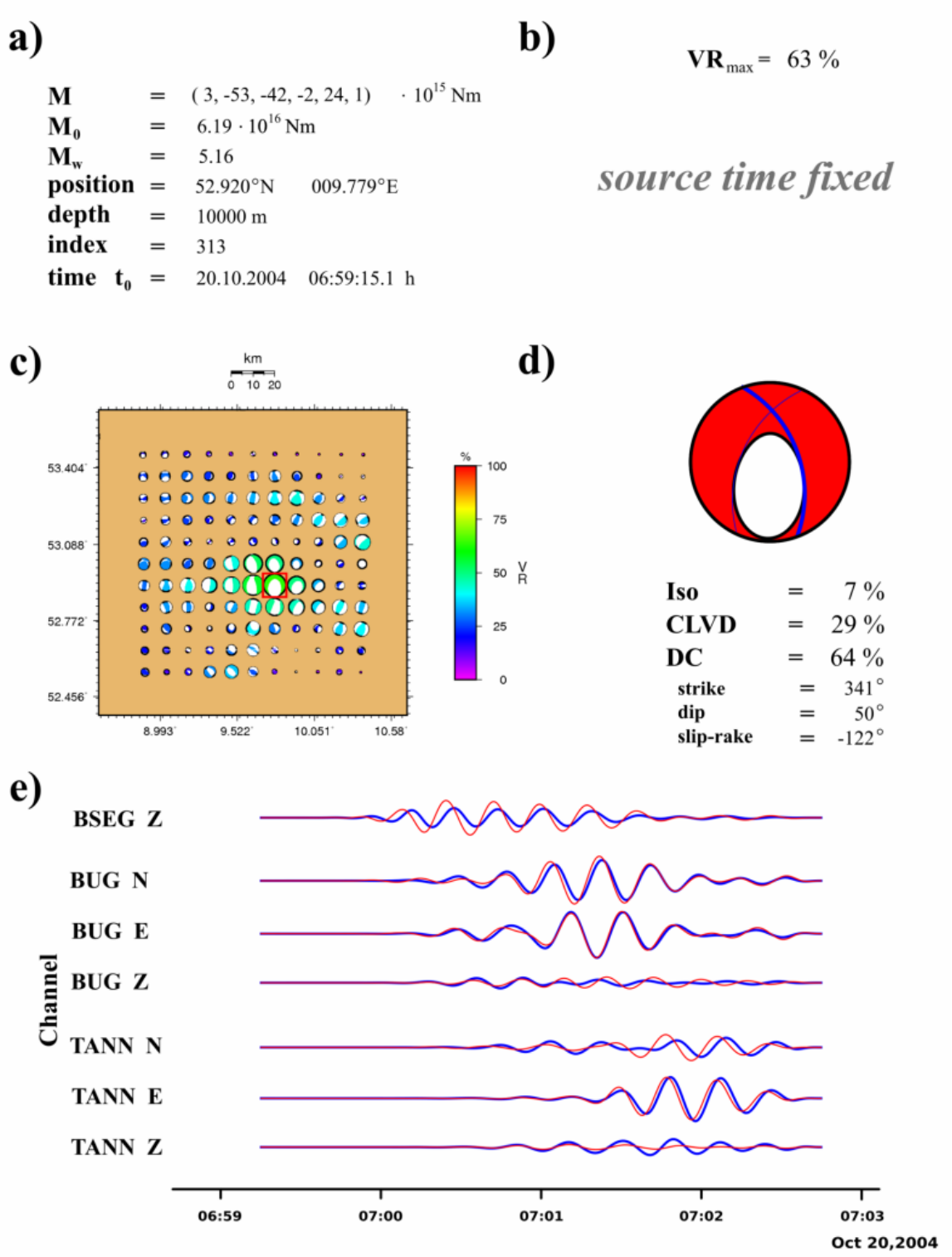

Figure 7.5:
Rotenburg case 2 – inversion results – grid search in space. **a)** Estimated numerical values. **b)** Chronological evolution of VR. **c)** Geometrical overview over a horizontal source grid section. **d)** Focal sphere diagram and source parameters of the estimated optimal source mechanism. **e)** Original data traces (red) and synthetics (blue), based on the estimated source mechanism. Displacement traces, scaling by station. Positions of stations indicated in fig. 7.2.

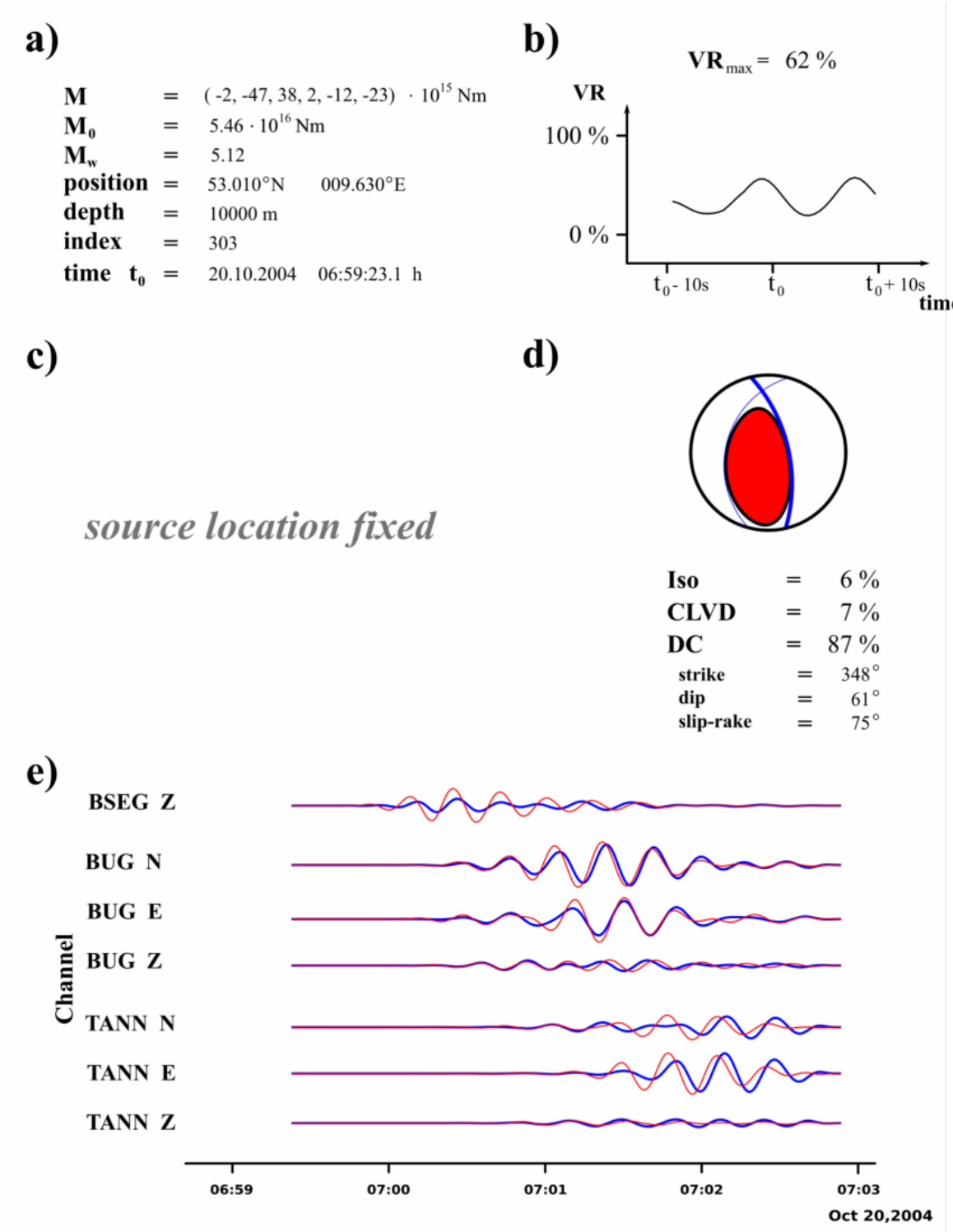

Figure 7.6:
Rotenburg case 3 – inversion results – grid search in time and depth. **a)** Estimated numerical values. **a)** Estimated numerical values. **b)** Chronological evolution of VR. **c)** Geometrical overview over a horizontal source grid section. **d)** Focal sphere diagram and source parameters of the estimated optimal source mechanism. **e)** Original data traces (red) and synthetics (blue), based on the estimated source mechanism. Displacement traces, scaling by station. Positions of stations indicated in fig. 7.2.

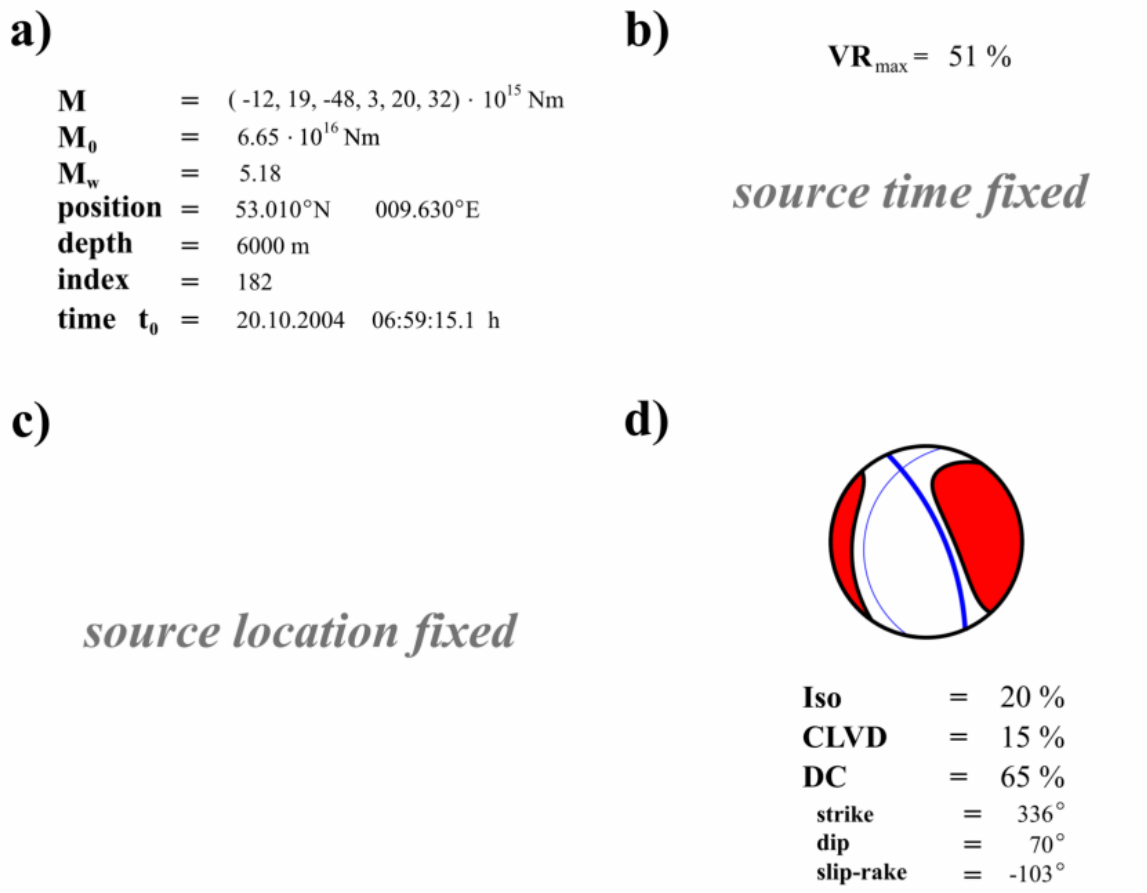

Figure 7.7:
Rotenburg case 4 – inversion results – fixed location and source time. **a)** Estimated numerical values. **a)** Estimated numerical values. **b)** Chronological evolution of VR. **c)** Geometrical overview over a horizontal source grid section. **d)** Focal sphere diagram and source parameters of the estimated optimal source mechanism. **e)** Comparison of traces in figure 7.8.

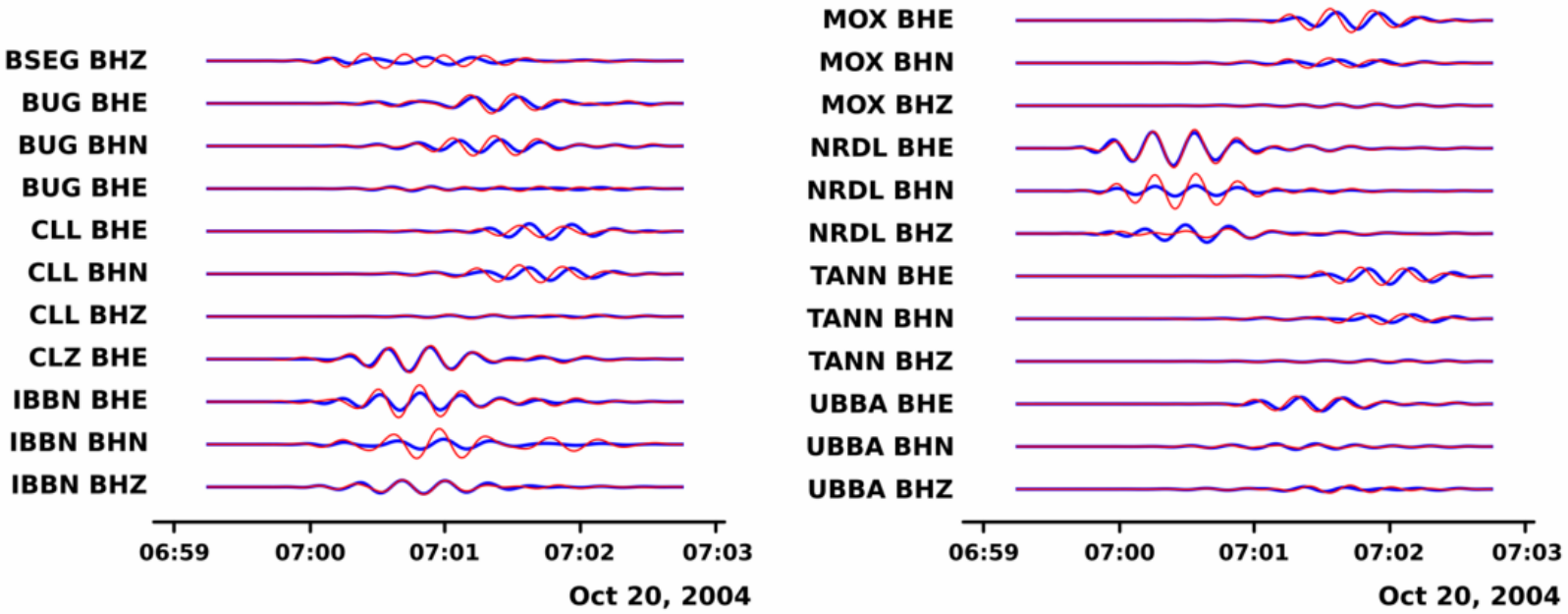

Figure 7.8:
Rotenburg case 4. Comparison of original data (red) and reproduced synthetics (blue). 210 s data with frequency bandpass 0.04 - 0.06 Hz, estimated source time at beginning of traces. Displacement traces, overall scaling. Positions of stations indicated in fig. 7.2.

7.1.2 The Ekofisk oilfield 2001 $\mathbf{M_w}$ $\mathbf{4.1 - 5.0}$ earthquake

In (Ottemöller et al., 2005), (Selby et al., 2005), and (Cesca et al., 2011) a shallow event is discussed, which is most likely induced by oil recovery. The event took place on the 07.05.2001, at 09:43 UTC. The source is located in the vicinity of the *Ekofisk* oilfield. The mentioned publications infer the following event parameters:

- M_w = 4.1 - 4.4 from (Ottemöller et al., 2005) / 4.99 from (Selby et al., 2005) ,
- centroid depth shallower than 7 km (approx. 2-3 km) ,
- source time 09:43:33.8 UTC ,
- shear crack mechanism from (Ottemöller et al., 2005)
  - strike angle 344° ,
  - dip angle 87° ,
  - slip-rake angle −97° ,
- shear crack mechanism from (Selby et al., 2005)
  - strike angle 170° ,
  - dip angle 90° ,
  - slip-rake angle −90° ,
- source location
  - latitude 56.567° N ,
  - longitude 3.179° E .

I analyse this event, using displacement data from 18 stations within the epicentral radius of 800 km, 31 channels in total (data provided by S. Cesca). Available data are shown in figure 7.10

The source point grid has the lateral dimensions 11×11 with a grid spacing of 10000 m. The vertical extension of the grid is given by 3 layers in depths 1000 m, 5000 m, and 9000 m. The grid is horizontally centred at the reference source position. The velocity model for generating the GFs is shown in fig. 7.9. The horizontal geometry of the inversion setup is shown in figure 7.11.

The data and GFs are frequency filtered with a bandpass from 0.01 Hz to 0.033 Hz. Data traces are analysed in time windows of length 900 s; the time window is moved ±10 s around the aforementioned source time in steps of 0.5 s. No weighting is applied.

Two inversions have been carried out for this data set:

1. full grid search in space and time,
2. inversion of data only for source mechanism, given reference source time and location are assumed to be correct.

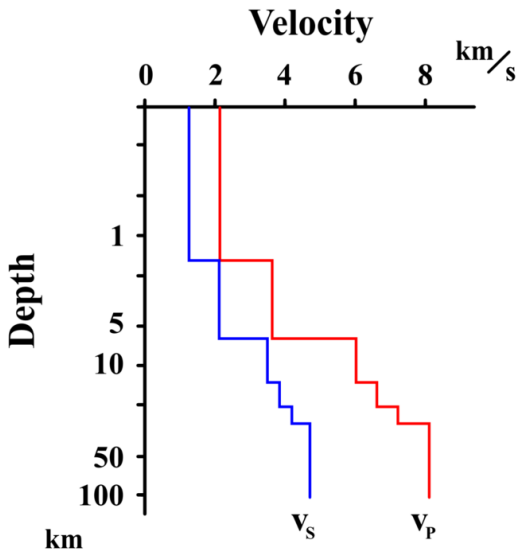

Figure 7.9:
Regional one-dimensional velocity model, based on values from (Selby et al., 2005). The velocity curcves v_p (red) and v_s (blue) are plotted against a logarithmic depth scale.

Results

1. **Full grid search**

   Results for the inversion in combination with the full grid search in space and time are presented in figure 7.12

   The source location is determined to be in the deepest grid layer at 9000 m. The lateral position is shifted by 0.09° to the North and by 0.657° (40 km) to the East with respect to the reference result(s). The magnitude is given as 4.43, which is in the range of reference results in (Ottemöller et al., 2005) and (Cesca et al., 2011). VR-value and source mechanism show high variation in space. The time series of VR-values is a very flat curve with no clearly peaking maximum The best solution has a VR-value of 25 %. The source geometry is dominated by an implosive isotropic part of 51 %. The double-couple part is negligible small (7%). Data traces and reproduced synthetics are in good agreement for stations, where the *ringing* part of the signal (coda of surface waves) is not dominant. The data show persistent oscillation due to strong dispersion of Rayleigh-waves. This cannot be reproduced with the given Earth model.

2. **Fixed source time and location – inversion only**

   The result for the inversion for the source mechanism is given in fig. 7.13 together with visualisations of the reference results. In addition to the solutions for source mechanisms mentioned above, a third inversion result from Cesca et al. (2011) is presented. My solution consists of a very large CLVD component of 64 %. The double-couple component is only 11 % of the full mechanism. Its orientation is in agreement with the result of (Selby et al., 2005). It coincides also with the third result obtained from Cesca et al. (2011). The strength of the event is estimated as M_w4.02, which is only slightly lower than the reference results. The VR-value

from this inversion is only 10 %. Data and reproduced synthetics match only very poorly.

Evaluation

The pure inversion, keeping the reference source time and location, yields a result with a very low VR value of 10 %. This is just four times the level expected for the analysis of white noise (c.f.6.5). However, the inversion result shows roughly the correct (main) geometry, compared with the reference result in (Cesca et al., 2011).

The comparison of waveforms, original data and reproduced synthetic traces, shows a qualitative mismatch. The oscillatory characteristics of the original signal, reflecting the strong dispersion of the surface waves, are not reproduced by the respective GFs, for some stations the same problem occurs vice versa.

By running the full grid search, the correct source time is only shifted by 1.5 s, which is a quite low value regarding the spatial extension and absolute time frame of the setup. However, the source location is clearly mis-estimated in depth and horizontal position. The source position is confined in a region to the North-East of the reference position; the correct source position shows a clear minimum of VR values. Thus the mis-estimation seems to be systematic. Due to the negligible double-couple component and the dominating isotropic pat, no information is reliably obtained about the main orientation of the source mechanism.

From the comparison of the waveforms one can see, why the VR value in the case of the full grid search is more than twice as high as in the other case. Parts of signals with high absolute amplitudes are far better matched; the persistent oscillation in later parts of the waveforms play a smaller role due to smaller amplitudes.

The moment magnitudes are estimated as being in realistic ranges for both cases. Together with the main orientation of the source mechanism of the result (case 2), it seems to be the most realistic and reliable value obtained in the inversion. Despite the low frequency range of the data, the model for creating the GFs does not sufficiently represent the true Earth. The dispersion of the surface waves influences the characteristics of the waveforms very strongly. This feature cannot easily be suppressed by frequency filtering. Inversions of the data using different corner frequencies for the bandpass filter did not yield qualitatively improved results.

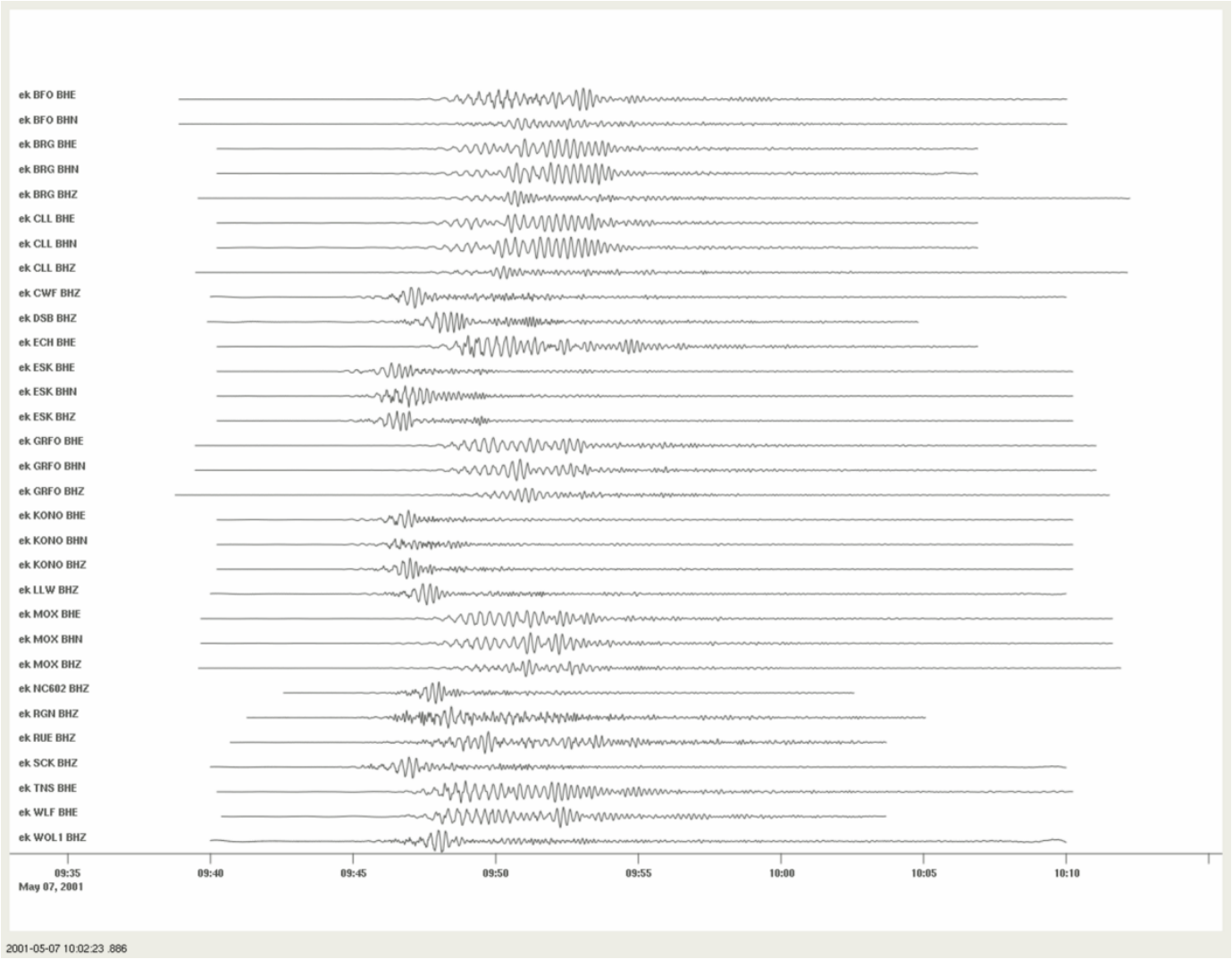

Figure 7.10:
Available restituted displacement data traces for the *Ekofisk* event (sec. 7.1.2). Approx. 30 minutes of displacement data for 31 channels of 18 stations. Scaling by station, sampling rate 2 Hz. Positions of stations shown in figure 7.11.

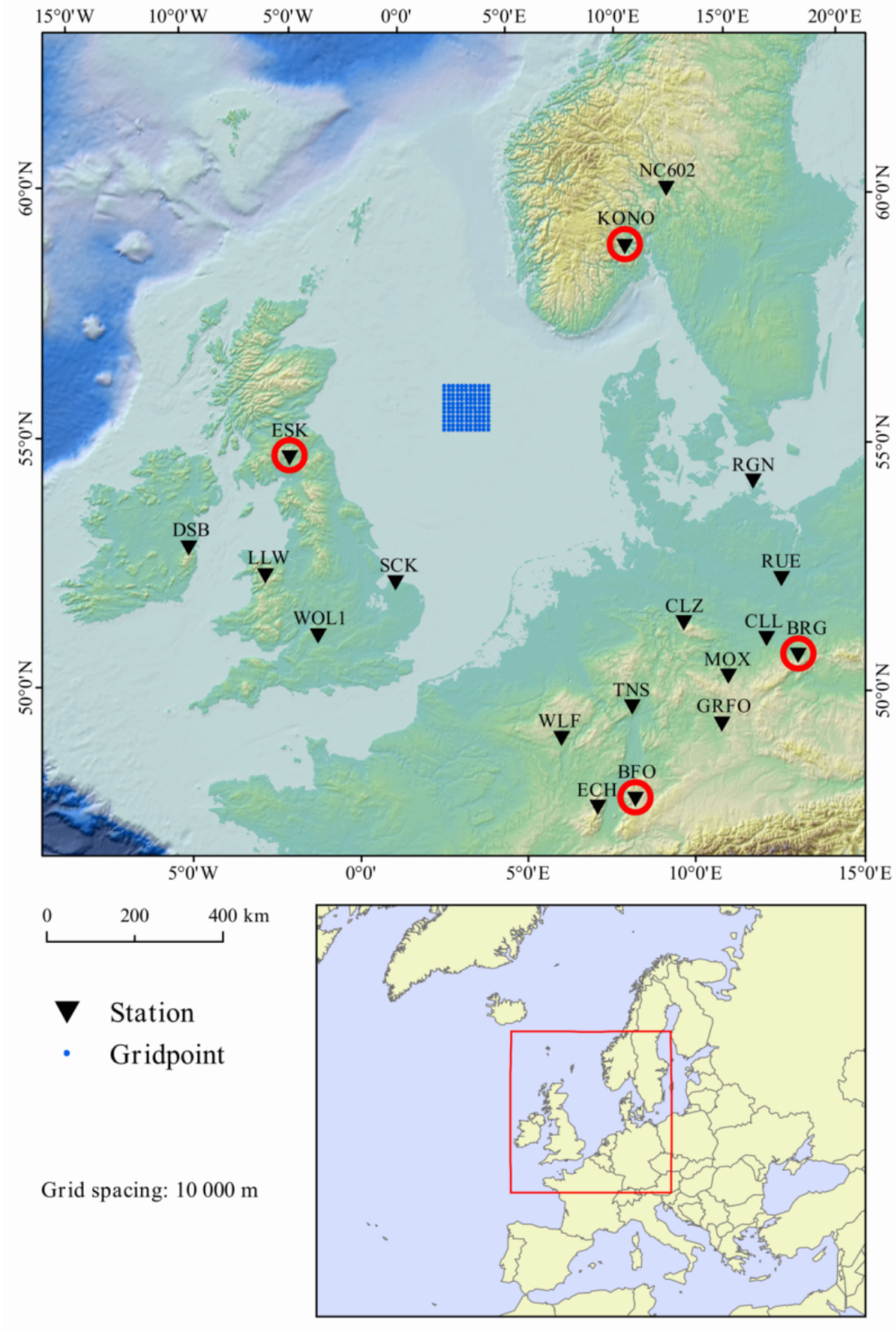

Figure 7.11:
Geometrical setup for analysis of Ekofisk event (sec. 7.1.2). **lower:** Geographical overview. **upper:** Map including the given setup. Horizontal projection of the source grid is given as blues dots. Seismic stations are indicated by black triangles. Red circles denote stations, whose data are shown in inversion result plots.

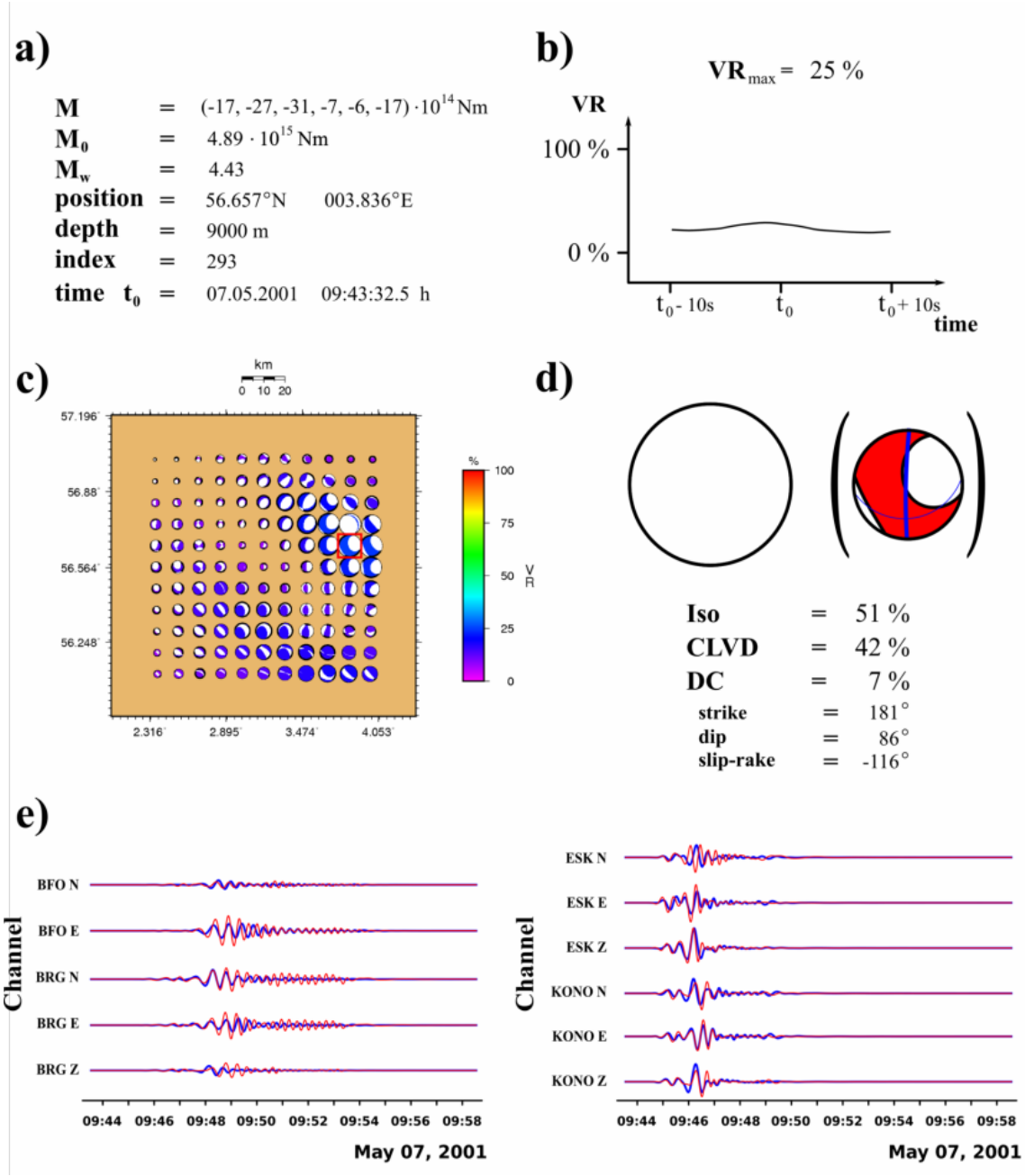

Figure 7.12:
Ekofisk – case 1 – inversion results – full grid search. **a)** Estimated numerical values. **b)** Chronological evolution of VR. **c)** Geometrical overview over a horizontal source grid section. **d)** Focal sphere diagram and source parameters of the estimated optimal source mechanism. FSD for deviatoric part of **M** is shown in parentheses. **e)** Original data traces (red) and synthetics (blue), based on the estimated source mechanism. Displacement traces, overall scaling.

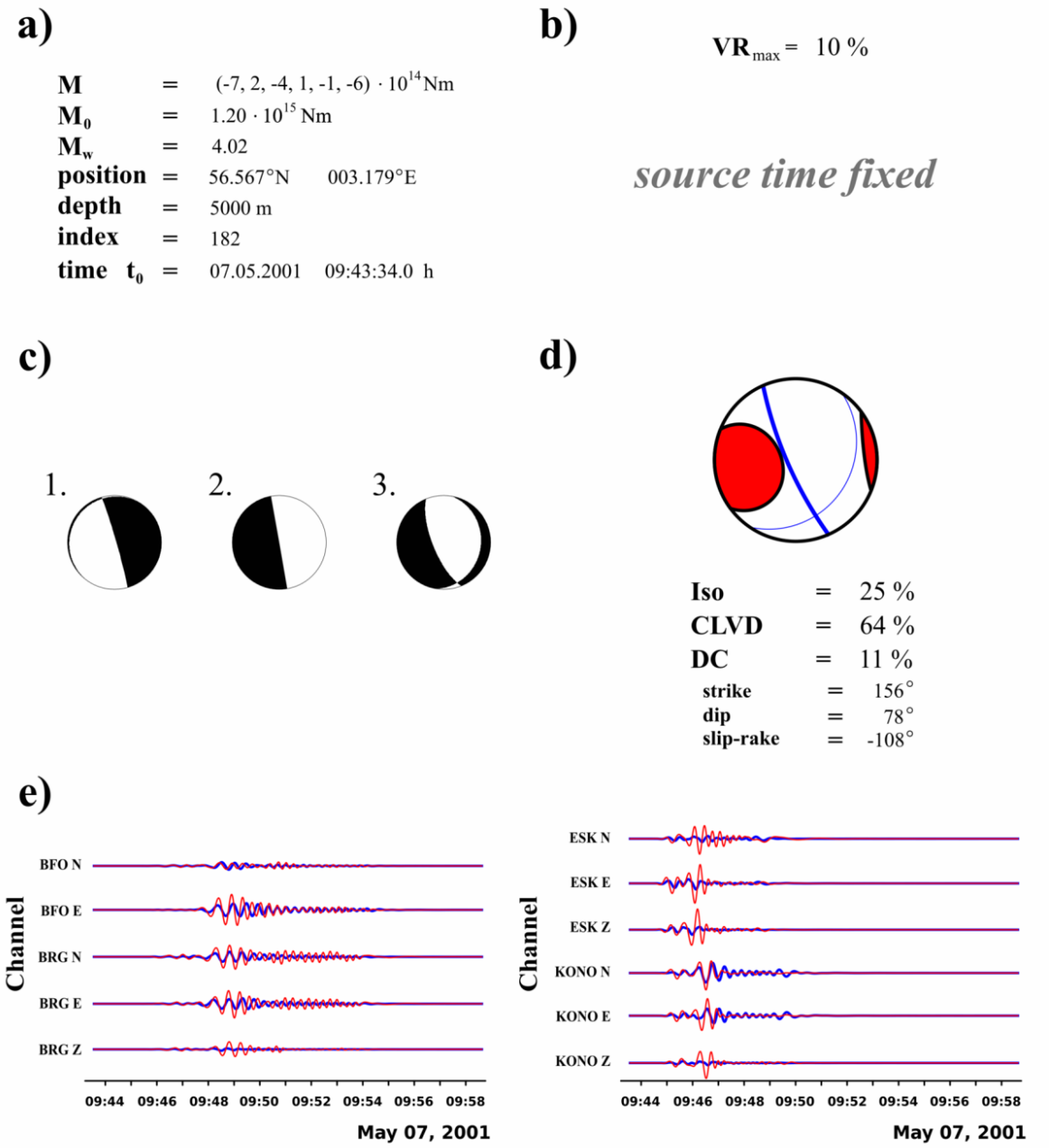

Figure 7.13:
Ekofisk – case 2 – inversion results – fixed location and source time. **a)** Estimated numerical values. **b)** – **c)** Plots of FSD for reference solutions 1.) (Ottemöller et al., 2005), 2.) (Selby et al., 2005), 3.) (Cesca et al., 2011). **d)** Focal sphere diagram and source parameters of the estimated optimal source mechanism. **e)** Original data traces (red) and synthetics (blue), based on the estimated source mechanism. Displacement traces, overall scaling.

7.2 Volcanic LP-event – Mt. Erebus 2005

Results from several analyses of LP-events at Mt. Erebus have been published (Rowe et al., 1998, 2000; Aster et al., 2003, 2008). These analyses mainly deal with the evaluation of the time history for specific events and the localisation of LP-sources by investigating stacked data sets with a collection of different events. All the investigations are based on multiple steps in the processing of data. So far, no approach to an analysis of volcanic seismic data in a single step inversion method has been applied on Mt. Erebus data.

Data of one event on the 31.12.2005 are analysed. The time span of data lies in the range within which detailed measurements have been carried out directly at the summit/crater (Gerst, 2010). Therefore the source of the signal is known as a bursting gas slug at the surface of the lava lake. Due to this source mechanism, a high CLVD component with a vertically orientated symmetry axis is expected in the estimated moment tensor solution. The event time is registered as 10:53:46.0 UTC.

Velocity data traces from 5 stations (3 channels each) are available, data sampling is 10 Hz. Data traces are plotted in figure 7.15 (data provided by IRIS Data Management System, 2010).

According to the test results in section 6.4, I use the three-dimensional modelling for the inversion, thus the correct topography is added to the homogeneous model (elevation model provided by K. Zaksek), as described in section 3.2.1. The GFs are the same as in section 6.4-case 1. Hence no absolute amplitude scale is available. The velocity structure is defined by a homogeneous halfspace model, based on the mean velocities in shallow depths, as proposed in (Aster et al., 2008) (mean value from velocity model in (Dibble et al., 1994), alternative model available in (Kaminuma, 1987)). This is justified by the large wavelengths of the signals under consideration, as well as the small epicentral distances of the stations.

The source point grid has the lateral dimensions 9×9 with a grid spacing of 1000 m. The vertical extension of the grid is given by 9 irregular layers in altitudes from 3800 m to −6000 m (c.f. fig. 6.30 on page 120). The grid is laterally centred at (77.528° S, 167.140° E), the position of the lava lake is (77.527° S, 167.165° E). The full transfer functions

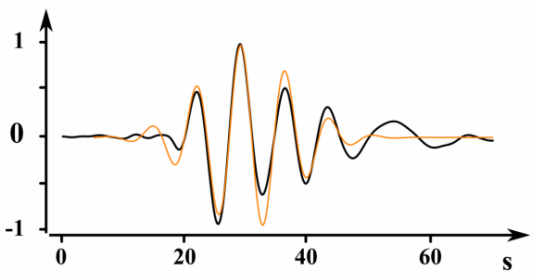

Figure 7.14:
Velocity data, recorded at station RAY for one single LP-event. This oscillatory function is assumed to reflect the original source time function. Source time is assumed to be at 7 s. The normalised data trace (black) is approximated by an analytical function (orange). The latter function is convolved with the GFs, yielding appropriate elementary seismograms.

are contained in the GFs, hence no further restitution has to be taken into account in the process of data handling. The geometry of the inversion setup has been presented in figure 6.29 (page 119).

Many LP-signals at Mt. Erebus show characteristic oscillations. These are most likely source generated signals, therefore they are not included in the GFs, that depend only on the underground model. Since the GFs are generated with an impulsive source time function, they are additionally convolved with an oscillatory source time function in order to obtain appropriate elementary seismograms (c.f. section 3.1.6). A function, fitted to data recorded at a station near the source location is taken as a first approximation to the real source time function of the signal. Data and fitted function are plotted in figure 7.14.

The data and GFs are frequency filtered with a bandpass from 0.033 Hz to 0.2 Hz. Data traces are analysed in time windows of length 60 s; the time window is moved in steps of 0.5 s. The temporal grid search spans 20 seconds, starting 20 s before reference event time (time shift based on preliminary evaluation).

Results

The inversion results are presented in figure 7.16.

The source time estimation shows a very high deviation of -9.5 s. A single maximum of 60 % in the time series of VR values determines this value. The depth of the optimal source is given as 520 m. This is a position on the second shallowest grid layer, hence a realistic value for the position of the lava lake. The lateral position of the source is determined 3 gridpoints to the East and 1 gridpoint to the South. The spatial distribution of VR-values shows an annular symmetry with low values at the centre point. The source position is confined only with respect to this symmetry. The source mechanism is qualitatively constant for positions with high values of VR. It is characterised by a large CLVD component (69 %). The isotropic component is unexpectedly small (10 %).

A comparison of traces from original data and reproduced synthetics is shown in figure 7.17. It can be seen, that except for three traces, both sets match very well. The oscillatory characteristic of the data is well reproduced by the GFs.

Evaluation

The result of the inversion does not allow an easy evaluation. The determination of the best solution with the help of the VR value alone proves being critical again. No clear maximum is present, the times series shows comaparably high values within a longer interval. Unfortunately, the curve shows the lowest value at the correct source time. This suggests that the assumed source time function introduces a spurious time shift to the elementary seismograms. The estimation of the source mechanism is satisfactory, the expected geometry is reproduced. One drawback is the double-couple content, which is higher than the isotropic component; this is an unrealistic outcome. However, the estimation of the geometry of the source mechanism seems to be robust with respect to the horizontal annular symmetry in comparably high VR values.

For source points in greater depth, the annular symmetry itself can be explained by the unfavourable station geometry. Due to the clustering of stations around the grid center, there is an ambiguity with respect to the azimuthal incident angle of the signal. The shallow source location in this present case should have lead to a better confinement of the correct source location (which is located in the inner part of the region of the annular symmetry).

The comparison of data and reproduced synthetics allows two conclusions. Firstly the relative scale of GFs for the different stations seems to coincide with the actual scaling of data traces (comparison with respect to the maximal amplitude at each station), furthermore the respective relative scaling of amplitudes within each station is not correct for every station. The latter may indeed be an effect of the specific radiation pattern determined here; but further study is needed to evaluate, if it is rather an effect of the GFs themselves. Secondly, the general shape of the waveforms is matched very well by the GFs, the oscillatory behaviour can be reproduced. The latter is not the case, if an impulsive source time function is assumed, or if one-dimensional GFs are applied.

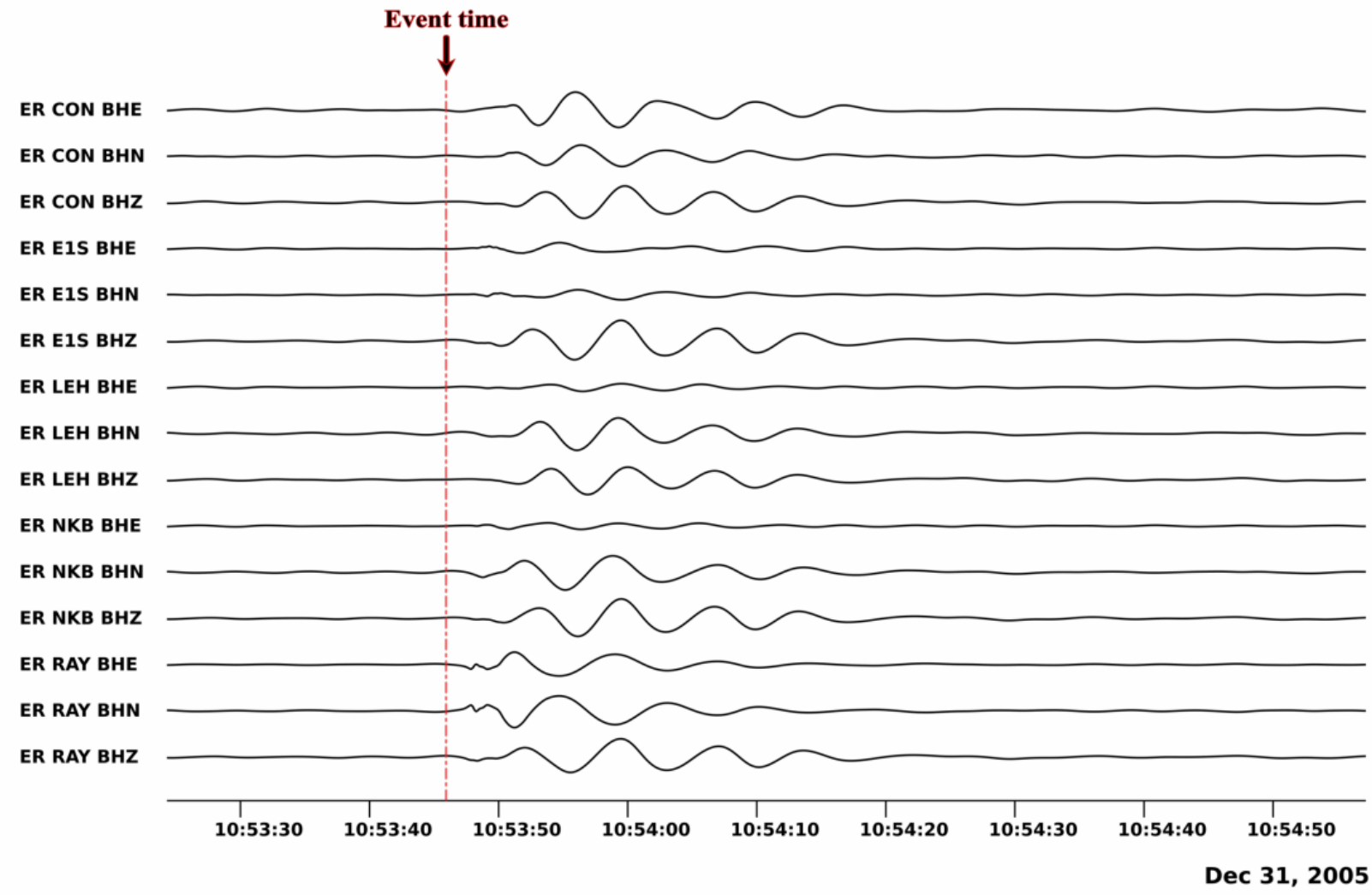

Figure 7.15:
Available data traces for the Erebus event. Approx. 5 minutes of velocity data for 15 channels from 5 stations with a frequency bandpass 0.033 - 0.2 Hz. Overall scaling. Positions of stations indicated in figure 6.29.

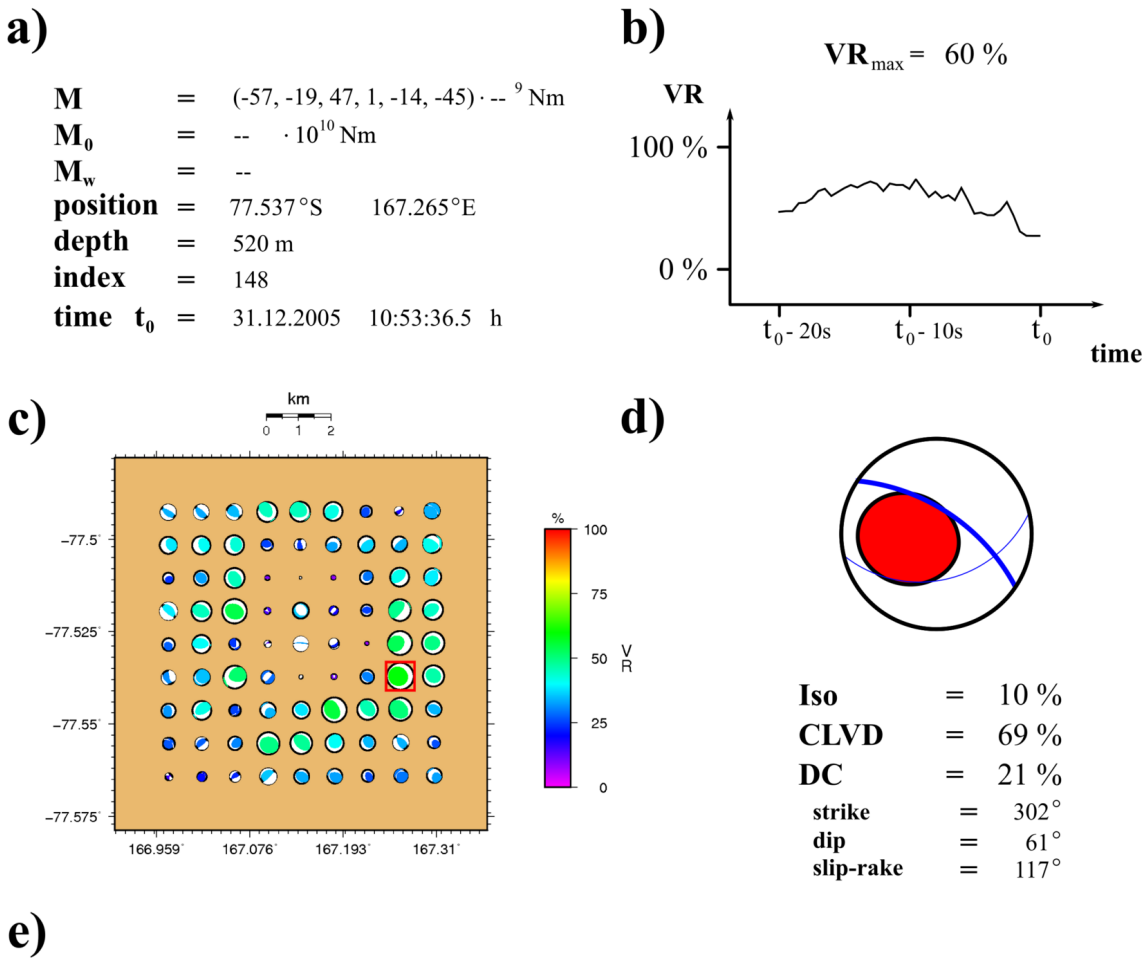

Figure 7.16:
Erebus – case 1 – inversion result – three-dimensional GFs. **a)** Estimated numerical values. No absolute scale available. **b)** Chronological evolution of VR. **c)** Geometrical overview over a horizontal source grid section. **d)** Focal sphere diagram and source parameters of the estimated optimal source mechanism. **e)** Comparison of data traces in fig. 7.17.

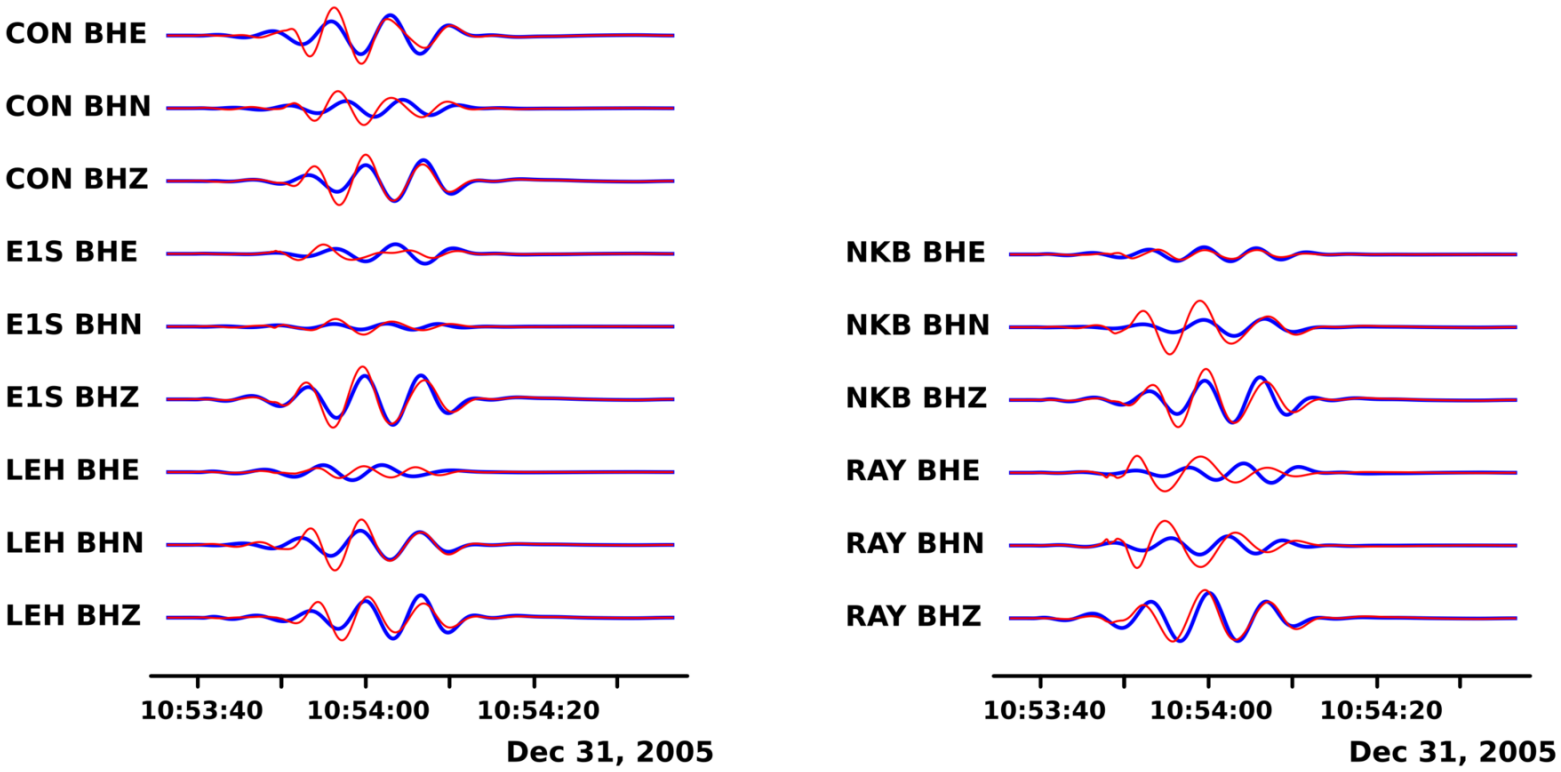

Figure 7.17:
Erebus case 1. Comparison of original data (red) and reproduced synthetics (blue). 60 s data with a frequency bandpass 0.033 - 0.2 Hz, estimated source time at the beginning of traces. Velocity traces, overall scaling. Positions of stations indicated in fig. 6.29.

7.3 Continuous data analysis – inversion and event detection

The concept of applying *ARCTIC* as a detection routine on a continuous data stream is tested on a real data set. The program runs for 12 hours on a continuous data stream of unrestituted raw velocity data. The chosen time span includes the *Rotenburg* event (c.f. section 7.1.1): data from the 20.10.2004, 00:00:00 UTC till 12:00:00, are analysed. The event shall be automatically detected, no further large events are known for this time interval.

The data set consists of 45 traces from 15 stations of the *GRSN* within the epicentral radius of 400 km. No data traces have been excluded in advance, some traces contain gaps. Data sampling is 20 Hz. A section of the data traces is shown in figure 7.18 (data provided by K. Stammler).

The source point grid from section 7.1.1 is adopted. It is horizontally reduced by a 25 km radius around the center point (53.01°N, 9.63°E), horizontal grid spacing is 1000m. The vertical extent of the grid is given by three layers in depths 2000 m, 4000 m, and 6000 m. The grid is set up by 63 points in total. An overview over the source-station geometry is plotted in figure 7.19.

For each time step, the raw data are successively read in, integrated and downsampled. These steps are equivalent to the preprocessing of the data samples used in section 7.1.1. The data and GFs are afterwards frequency filtered with a bandpass from 0.035 Hz to 0.08 Hz. Data traces are analysed in time windows of length 300 s. No weighting is applied.

Results

The continuous application of the *ARCTIC* ran 12 hours without technical problems, including the handling of data gaps. After having finished loading the GFs and setting up the correlation matrix and its inverse, the moving time window has shifted in step sizes of 11.5 seconds on average. The highest VR-value within the whole time frame coincides more or less with the source time of the Rotenburg event. A VR-value of 25 % has been calculated as the overall maximum at this instance. The average noise level of the VR-value is 2.1 %. The time series of VR-values is visualised in fig. 7.20. Only one event has been observed.

A graphical representation of the solution parameters for the detected event time is shown in figure 7.21.

The source time is given as 06:69:18.2, which is a time shift of 3.1 s with respect to the given reference result (c.f. sec.7.1.1). Source mechanisms vary noticeable in space, the best solution is shifted to both South and West, each by one grid point. The depth is given as 2000 m. The strength is estimated to M_w 4.4, which is in the range of the results of the static inversion, as well as the reference result (c.f. section 7.1.1). The source mechanism consists of significant implosive isotropic and CLVD components, as

well as a shear crack (41 %), which is orientated quite similar to the reference result. Strike-angle is 347°, dip-angle 63°, and slip-rake −90°. Comparison of data traces and reproduced synthetics show a low degree of matching in most cases (inversion included low quality traces).

Evaluation

The data set for the *Rotenburg* event has been stepwisely analysed in near real time. No numerical problems arose from the inclusion of stations with general bad data quality or even data gaps. The algorithm is functional for the application on real data.

In contrast to the fast operating in case of the synthetic data example in section 6.5, the effective computational speed is limited by further processing steps in the present case. Data are given in raw form, so they have to be preprocessed for every time step. Beside the frequency filtering, this processing consists of the the integration to displacement data, resampling, and the updating of the correlation matrix in case of data gaps. These steps work numerically stable, but they are time consuming.

Although the time steps have a length of only 4 % (11.5 s) of the analysis window length, they are significantly larger than in the synthetic test case. The danger that an event can been *overseen* is quite high. This can be seen from the fact, that the event is indeed clearly detected, but at a time, shifted by 3 s with respect to the correct source time. The VR value decreases (compared to 68% of the result from the inversion in sec. 7.1.1) only 25 % within this short period. Thus one has to define a very low threshold value for automatically detecting the event.

The results obtained from the inversion for the automatically detected event consist of a realistic shallow depth and a slight lateral shift of the source position with respect to the reference results (see sec. 7.1.1). Furthermore the mechanism is roughly in agreement with the result from the *static* inversion (see above). The polarity is correct, and a realistic value is estimated for the magnitude.

Although the geometrical setup is reduced to a smaller source point grid (to 10 %), the computational time for every time step seems to be still too large, therefore parts of the processing steps should be excluded from the inversion scheme. However, the processing worked well in this case study, the detection of the event shows to be robust; several applications of the algorithm detected the event with varying VR values due to different time shifts of the windows.

A general quality check seems to be necessary, to exclude stations with general bad data in advance, by this not only improving the average data quality but also restraining the number of stations to the necessary minimum. The length of the analysis windows can perhaps be shortened. This has to be optimised for each specific case.

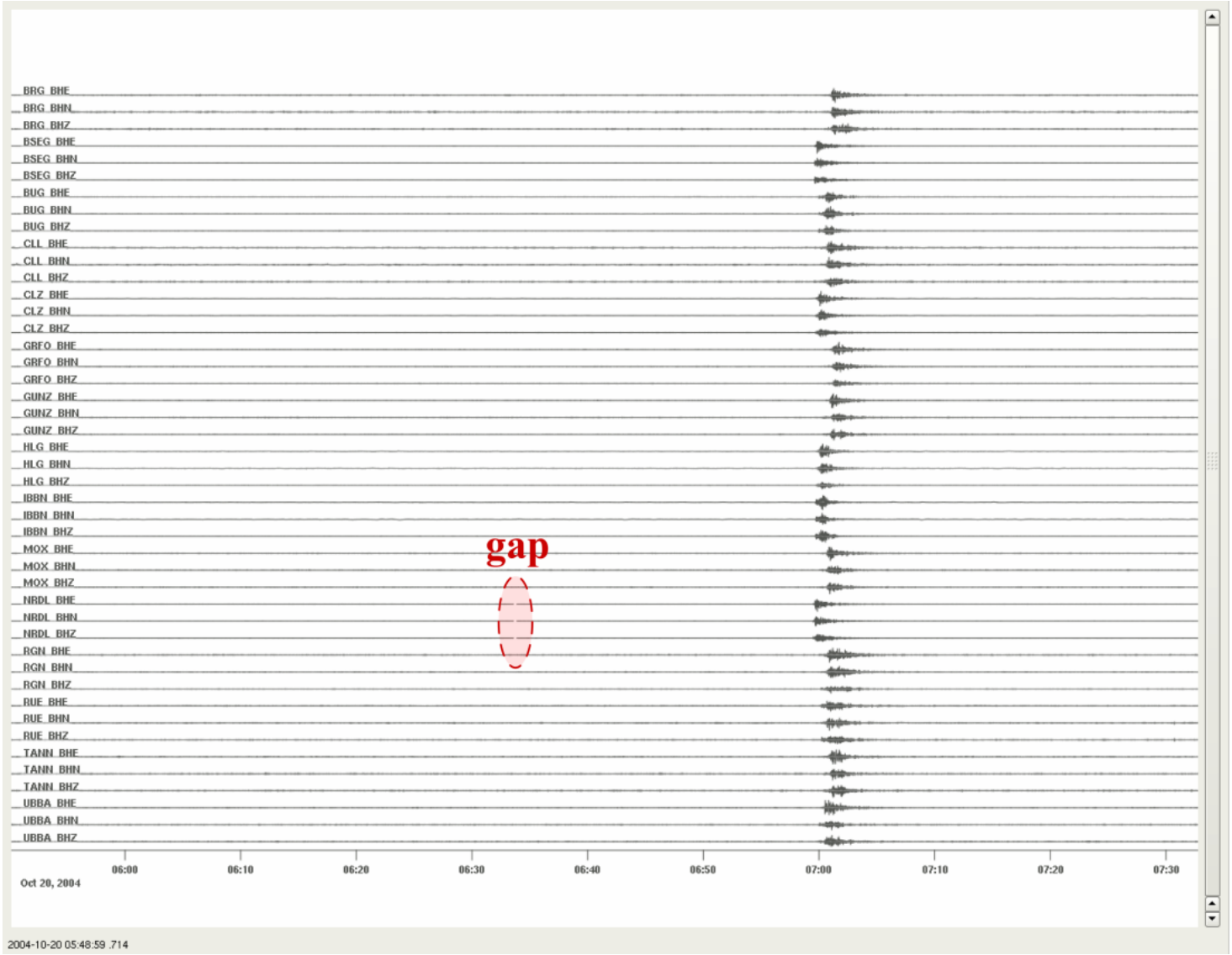

Figure 7.18:
Available data traces for the continuous application on the Rotenburg event (sec. 7.3). Data gaps within the marked red area. Approx. 90 minutes of displacement data for 45 channels from 15 stations, scaling by station.

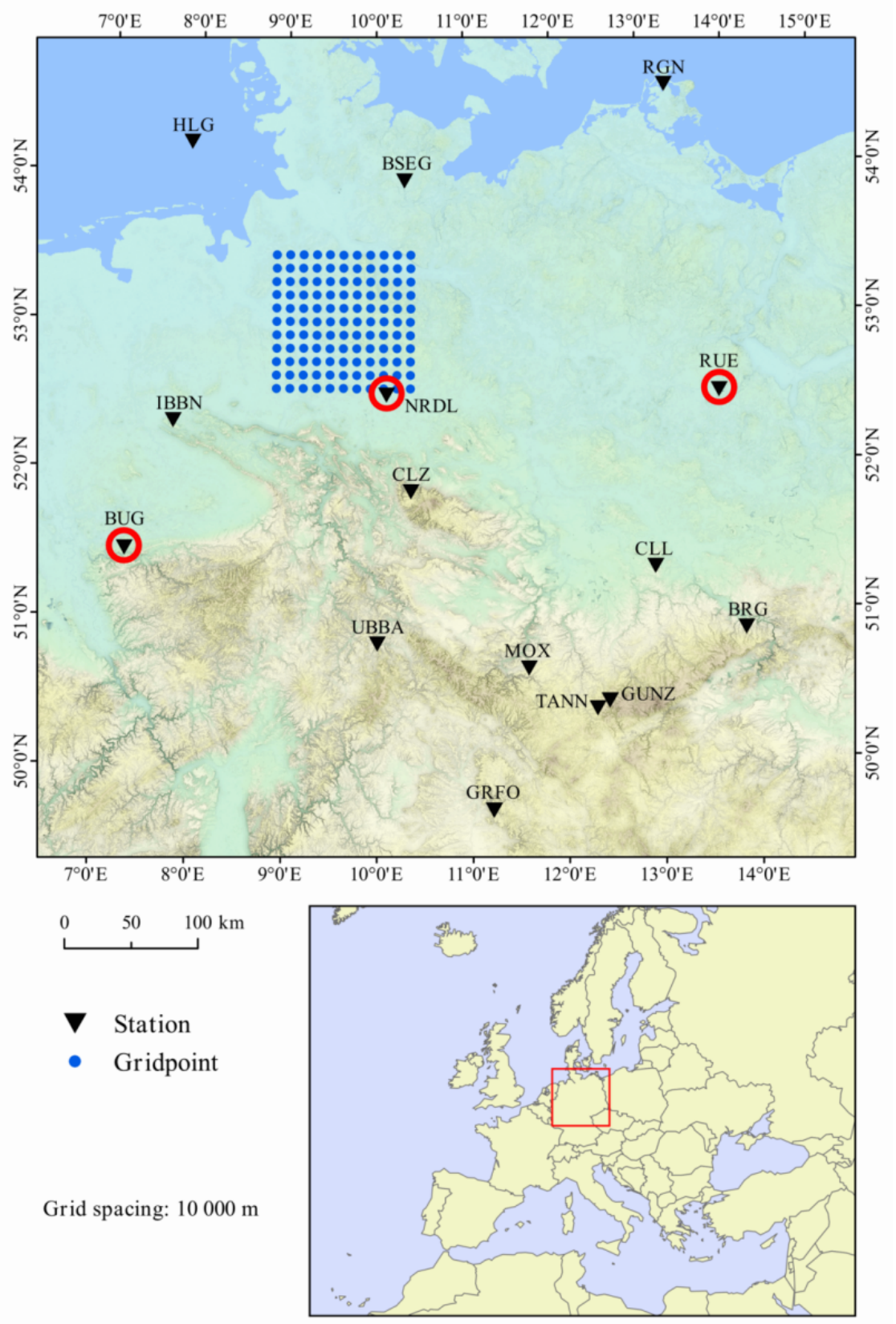

Figure 7.19:
Continuous inversion – geometrical setup (sec. 7.3). **lower:** Geographical overview. **upper:** Map including the given setup. Horizontal projection of the source grid is given as blues dots. Seismic stations are indicated by black triangles. Red circles denote stations, whose data are shown in inversion result plots.

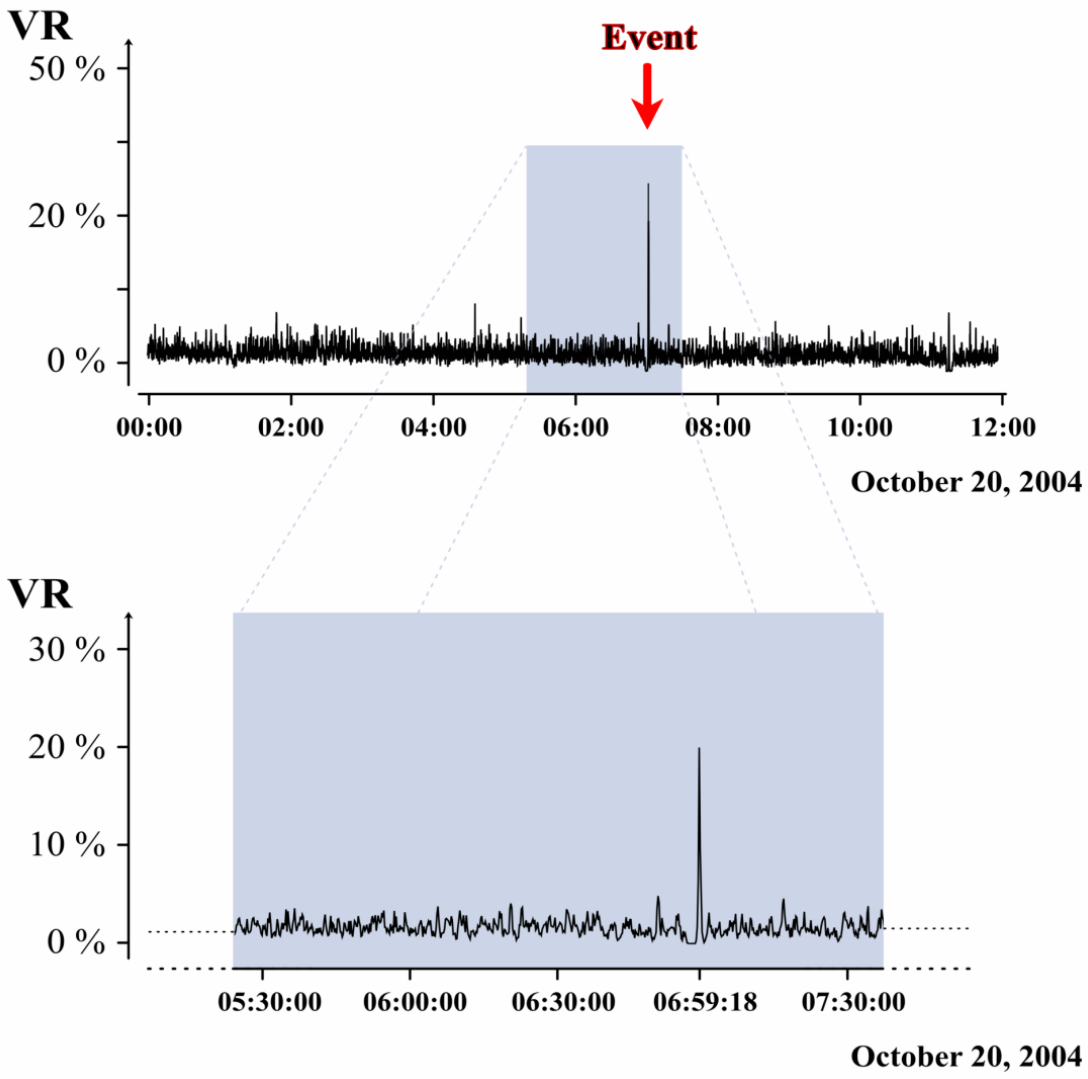

Figure 7.20:
Result of the continuous application on real data traces. **upper:** Time series of VR-value, containing one event at 06:59:15 UTC. The *Rotenburg* event is marked by the red arrow. The grey box denotes the section shown in the lower part of the plot. **lower:** Section of full time series (magnified), clearly indicating the peak position.

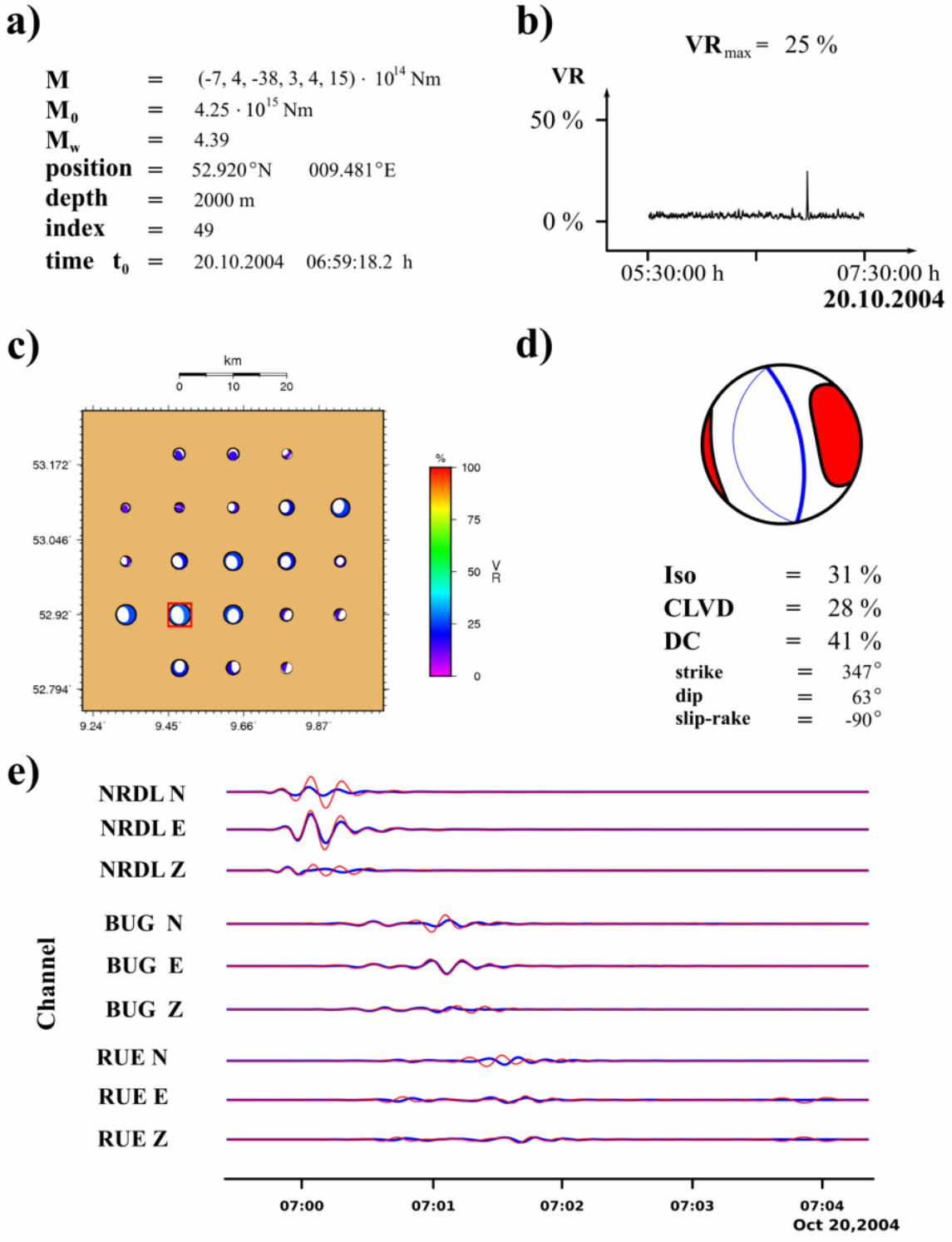

Figure 7.21:
Inversion result *Rotenburg* event – detected by continuous data analysis (sec. 7.3). **a)** Estimated numerical values. **b)** Chronological evolution of VR. **c)** Geometrical overview over a horizontal source grid section. **d)** Focal sphere diagram and source parameters of the estimated optimal source mechanism. **e)** Original data traces (red) and synthetics (blue), based on the estimated source mechanism. Displacement traces, overall scaling.

8 Discussion and conclusion

8.1 Discussion

8.1.1 Implementation of the algorithm

One of the critical requirements that I was aiming to address is the near real-time analysis of seismic data. To achieve this high performance of the numerical algorithm I chose a fast single-step inversion scheme as suggested by (Sipkin, 1982) and (Kawakatsu, 1989). By doing so, time-consuming back and forth transformations are omitted by carrying out all processing steps in time domain rather than in spectral domain. Reducing the application of the software to LP-events, it is possible to analyse full waveforms directly, neglecting effects on small time scales within the signals. This approach allows a simple linear formulation of the numerical problem that, as an additional optimisation, allows to obtain the inversion result in a single computational step.

The one-step inversion is a distinguishing feature of the method I have presented in this thesis. In contrast, analysis methods that use the information of amplitude spectra in order to invert for source parameters (Bukchin, 1995; Ottemoller and Havskov, 2003; Cesca et al., 2010a), face the problem of a non-linear inversion setup, which always require time-consuming multi-step inversion schemes. Their advantage over the method I have developed, however, is their robustness with respect to relative time shifts of the data traces. A possible way to overcome this problem in time-domain-based methods is to use correct the data for the mentioned time shifts using a sophisticated multi-step method during the preprocessing (Pondrelli et al., 2002; Bernardi et al., 2004; Ford et al., 2009). This is not yet implemented in the developed algorithm but can be subject to future improvement.

In contrast to *ARCTIC*, other time domain based inversion methods (Dreger and Woods, 2002; Tsuruoka et al., 2009) suffer from strong a-priori limitations. they are for instance restricted to a flat geometry and apply a far-field approximation. This does only allow for the inversion of large scale tectonic events (Tajima et al., 2002). In addition, these tools are often further restricted to purely deviatoric source mechanisms, or only the fault plane solutions (Braunmiller et al., 2002).

ARCTIC does not have the aforementioned restrictions and is able to use the general information about the geometry in order to invert for full moment tensor solutions. It can analyse point source events on all spatial and magnitude scales, as long as long-periodic signals are emitted.

The use of pre-calculated Green's functions (GFs) for a case specific source-station geometry allows for a fast spatial gridsearch for the source location. From these GFs, synthetic seismograms are calculated internally, which are correlated with frequency filtered

real data traces within a distinct time interval. The synthetic traces are parametrised by the six entries of the seismic moment tensor. The latter is finally obtained for every position on the grid of possible source points by a least squares estimation. Every estimated parameter set is evaluated and characterised by one specific value, the variance reduction (VR), which marks the quality of the match of real data and internally calculated synthetic traces. The grid point corresponding to the highest VR value is taken as the most probable source location.

There are two different modes for handling the determination of the source time. On the one hand a pre-defined interval in time can be searched for the best source time estimation in arbitrary time steps. This extends the three-dimensional spatial grid search to a four-dimensional one. Again the point in space and time with the highest VR value is taken as estimator for the correct source. On the other hand, the method can be used for a continuous data analysis, hereby acting as a detection routine at the same time. The inversion and spatial grid search are stepwisely applied on data from successive overlapping time windows. A seismic event is assumed to have occurred if the best VR value that has been found in one temporal inversion step, exceeds some pre-defined threshold.

The inversion results of the respective time step are stored or sent to an event data base. Afterwards, the analysis of the data stream continues. The ability to work as a static analysis algorithm on a fixed time interval in addition to being an automatic detection routine on a continuous data set, distinguishes the newly developed code from other inversion codes that work in time domain (e.g. Dreger and Helmberger, 1993).

The algorithm works with GFs that hold the full three-dimensional information on the modelled underground medium as 18 elementary seismograms. Their calculation is done independently with external software. Hence special needs and specifications, as for instance the inclusion of topography or anisotropy, can be easily considered case by case. This variability is a new concept, which is an extension to the methods of existing near real-time inversion codes (e.g. Kawakatsu, 2003). GFs that are generically generated from one-dimensional underground models contain only eight (in the far-field approximation) or ten components, which have to be extended to the number of 18 by geometrical corrections.

The software implementation of the algorithm is an open source code, written in Python. The case specific parameters are provided to the program by a configuration file. GFs are handled as NetCDF data, where seismic data is taken in miniSEED format.

8.1.2 Applications of the algorithm to synthetic and real data

I have shown the general functionality of the algorithm by the application on one-dimensional and three-dimensional setups. I pointed out the effects of the inclusion of topography into the GFs. Furthermore, I have studied the influences of wrong underlying velocity models and disadvantageous station geometries on the inversion result. I demonstrated, that it is possible to use the developed tool for the near real-time inversion of continuous data. All these tests have been carried out on synthetic data sets. In these synthetic data tests, it turned out the inversion algorithm finds a best solution by a trade-off between optimal source location, source time, and polarity of the source

mechanism. This trade-off can hardly be described properly by only the VR value. Since the latter, however, is the value that determines the optimal solution, the results contain the impact of this internal trade-off on different occasions.

From this it follows that an additional regularisation parameter is needed in order to determine a stable and well confined solution. One proposition for such an parameter is a value that describes the smoothness of the local confinement in space and time (perhaps several values are preferable here). Again, even the evaluation of the local smoothness alone may not be sufficient. On the one hand, a very smooth behaviour of values in the surrounding of a local maximum may be interpreted as a bad confinement; on the other hand it seems reasonable that a quasi non-continuous behaviour in that region indicates rather statistical spread than a realistic well defined solution. More studies are necessary in order to reveal the optimal solution to this problem.

In addition to the synthetic tests, I applied the *ARCTIC* code to several sets of real data. Two examples of shallow induced seismic events and one volcanic seismic event have been analysed. Furthermore, I tested the capability of the tool to work as an independent detection routine on a real data set.

Induced seismic events

The events *Rotenburg* (section 7.1.1) and *Ekofisk* (sec. 7.1.2) are shallow induced seismic events. I chose them as reference events in order to test *ARCTIC* on real data and to compare the results with reviewed solutions.

The first event has been studied in greater systematic detail. The comparison of two analyses – the full grid search in space and time, as well as the pure inversion with fixed source time and location – demonstrated the influence of the above mentioned trade-off problem on the overall result. The pure inversion yielded a result, that is comparable to the reference result, the full gridsearch yielded a combination of mis-estimations in time, space and polarity of the source mechanism. Hence the necessity of further regularisation parameters became clearly apparent. Significant differences between results showed up, if the degrees of freedom of the setup had been reduced, i.e. the grid search had been restrained. By confining the source time to the reference value, the polarity of the source mechanism changed. In the case of a grid search only in the time domain, the main orientation of the source mechanism is comparable to the reference solution in terms of strike and dip angle. The estimation of the source time showed a shift of 8 s, and the polarity of the mechanism had the wrong sign (consistent for several tests not shown here).

All things considered, the latter result demonstrated the functionality of *ARCTIC* inverting real data. However it elucidated the problems of the free four-dimensional grid search as well. There is intrinsically no way to find out, if the provided best numerical solution coincides with the physically meaningful true solution. Theoretically the only final solution to this problem is the optimisation of the applied Earth model. For all practical purposes, at least an improvement could be achieved by the introduction of boundary conditions or regularisation parameters, as for instance the mentioned smooth-

ness parameter. It seems to be adequate to apply the latter rather to the time domain than to the spatial grid search, because the examples have shown hitherto that the general orientation of the source mechanism is mainly correct, if only the source time is determined correctly.

The analysis of the *Ekofisk* event consisted of two qualitative setups, the full grid search in space and time, and the pure inversion. The full grid search yielded a result that was qualitatively worse than the result of the *Rotenburg* case study. Estimated values of source location and time differed systematically from all available reference solutions. The obtained mechanism did not contain shear components, which is a very unlikely result. Only the estimated magnitude was within the (wide) range of given reference values. The horizontal distribution of VR values was asymmetric and showed even a minimum at the correct source location.

In contrast to the former grid search, the pure inversion of the data for fixed source time and position resulted in values for magnitude and source orientation, which were similar to two of the three reference results. Although the source mechanism consisted mainly of a CLVD-part with only a small fraction of a (expected) double couple, the strike, dip, and slip-rake angles of the latter were in good agreement, especially with the solution in (Cesca et al., 2011). The overall VR value was very low (10 %), only by a factor of 4-5 larger than the background result for inverting white noise. Considering only this value for evaluating the reliability of the solution, it can most probably be concluded that the result has to be dismissed. The results of the synthetic test cases showed indeed that the VR value can decrease rapidly under several influences, but it is not clear, if it is systematically possible to obtain good and stable solutions in ranges of low VR values. This is a vital topic for further systematic studies.

Volcanic seismic event

The analysis of synthetic data from a three-dimensional geometry using one-dimensional GFs showed, that the effects of topography cannot be neglected, not even if a low frequency bandpass filtering is applied. According to this outcome of the synthetic test, I used three-dimensional GFs in order to analyse real volcanic seismic data from an LP-event at Mt. Erebus. Contrary to the former real data case studies, no reference result was present for this analysis. However the source time and mechanism (bursting gas bubble at the lava lake surface) were known by complementary information.

In addition to the topography, already included within the GFs, I took into account, that the source time function of the event cannot be simplified to an impulsive step function. Seismic signals, recorded near to the summit, are assumed to provide a good approximation to the real source time function. Such a function has been convolved with the GFs. By using these modified elementary seismograms for the analysis of the seismic data, I obtained an ambivalent result. Mainly the source depth and the source mechanism turned out to be consistent with the correct source. Despite estimations of source position and time, which are quite unlikely to reflect the real source coordinates in space and time (although again results in (Ohminato, 2008) suggest the possibility

of a horizontally shifted source location for greater depths), the comparably high VR value simulateted a good solution. This conclusion was supported by a good agreement of original data and reproduced synthetic traces.

The result cannot be compared with any reference, and the narrow station geometry, in combination with the small absolute number of stations, does not allow an estimation of a possible localisation error by means of statistical evaluation (e.g. a bootstrap test). However, according to (Panza and Saraò, 2000) more comprehensive synthetic tests are needed in order to analyse the quality of the result. Therefore, a final evaluation of the inversion result cannot be given in this case.

Continuous application

The real data case study for the continuous application of the *ARCTIC* code (sec. 7.3) demonstrated the general ability to invert a stream of seismic data in near real-time. The inversion procedure detected the *Rotenburg* event in a data stream of 12 hours by successively analysing data in consecutive overlapping time windows of 300 seconds length. The inversion of the background noise yielded a constantly low value of VR values, hence the global confinement in time is very strong. A detection occurred, for VR values exceeding a threshold of 20 %. In case of an event detection – only one detection with a VR value of 25 % occuered in the case study – the inversion result for this respective time is stored, and the analysis continues. However, it has been shown in the former parts of this work, that a time shift of a few seconds can lead to varying results, especially with respect to the polarity of the source mechanism (e.g. Ford et al., 2009). The detection time of the event depends on the exact position of the analysis window, but the temporal process of the successive window positions is non-deterministic. In order to obtain robust inversion results for one and the same event with this automatic method, a second processing step must be introduced. If an event is detected in the continuous inversion, an additional refined local gridsearch must be applied around the detected source time. Thus the continuous application should be combined with the static configuration, which has been applied throughout this work. Furthermore, the restitution of data should be handled independently by an external tool, that can work parallel to the inversion.

By allowing too large time steps between the consecutive overlapping analysis windows, the detection method can only yield robust results, if the analysis is carried out in a far lower frequency range. Hence it would be restricted to events with magnitudes, which are too large for induced events (c.f. Tajima et al., 2002). Thus the processing time for each single analysis window must be reduced in order to omit the danger of spuriously skipping events. Beside the reduction of the grid size, as already applied in this work, there is the possibility to reduce the amount of data by downsampling of the incoming data stream. Additionally one could skip data from stations in large epicentral distances, if possible. On the one hand I showed in the synthetic tests that the influence of wrong velocity models is largest at them, so they provide most likely data with the intrinsically worst quality; on the other hand, the data could be handled in shorter time windows then, again reducing the amount of absolute data. In (Tsuruoka et al., 2009), an example can be found, where short, low sampled, data traces are used. In combination with the

reduction of the GFs to only eight components in the far-field approximation (c.f. sec. 3.2.3), this is sufficient to allow very small time steps.

The aforementioned configurations restrict the applicability of the inversion routine significantly. It would not be possible to apply it to source regions with more complex geometries, e.g. volcanoes. In order to circumvent this significant drawback, a more technical approach is favourable: extending the code to a parallel working inversion scheme in combination with a larger number of processors. The single source grid points are handled completely independently, therefore this is an approach that has no need of a special geometrical setup and does not influence the inversion itself. Hence it is a worthwhile step in the future optimisation of *ARCTIC*.

8.1.3 Interpretation

It has been demonstrated that the developed tool is operational for the inversion of LP-signals on synthetic and real data. It can be applied as a static inversion routine or for the near real-time analysis of a continuous data set. The successful application to the continuous data stream can be contrued as a first feasibility study for the further development of a generalised monitoring system for volcanic areas, as well as fluid reservoirs and mining areas.

The underlying method seems to be very sensitive with respect to the determination of the correct source time, small uncertainties in this parameter can lead to large variation of the estimated source mechanism. This means a systematic problem for the usage of a free grid search: the best numerical solution is not inevitably the most meaningful one. The inclusion of boundary conditions is necessary, especially for the determination of the polarity. On the one hand it has been shown in the evaluation of synthetic tests and real data case studies that this parameter shows a high variability. On the other hand, it could be confined comparatively simple by the parallel application of a first motion analysis (using a different frequency band) for the respective data set.

Even if the correct maximum is determined in the time series of VR values, the high sensitivity leads to very fast deviation from the correct inversion result around this maximum. Hence it is necessary to analyse data successively at a high processing step rate. In case of the continuous analysis of data with large steps of the analysis window, a local gridsearch with high sampling around a detected event must be additionally conducted to refine the result. Due to the fact that the present high computational speed is mainly achieved by refining the source point grid to a much smaller sub grid, there is demand of further computational optimisation.

8.1.4 Error estimation

A system inherent error estimation for the four-dimensional grid search is limited by the design of the grid, the accuracy cannot exceed one half of the respective grid spacing. In order to allow an estimation of an upper boundary for the parameters of the grid search, which is below the extent of the whole grid, an extension of the setup by one or more of the aforementioned smoothness parameters is advisable. This allows for the

definition of confidence intervals. No additional processing steps would be required for their calculation, hence no loss of computational speed is suffered.

An investigation of the stability of the solution with regard to source mechanism and magnitude must be carried out using a statistical approach. After introducing slight time shifts in the data and small variations in the source mechanism, a statistical connection between the *wrong* data traces and changes in the inversion results can be obtained. Beside the analysis of this general data-mechanism relation, also the systematic errors from the application of wrong velocity models can be quantified by statistical approaches. The elaboration of these improved error estimations is beyond the scope of this thesis.

It is shown in (Barth, 2007), that the choice of the corner frequencies for the applied bandpass filter can influence the result to a certain extent. A detailed study about this influence or the inclusion of a statistical confinement of the solution by applying several frequency ranges for each inversion are worth a second thought.

Furthermore, the informative value of VR is restricted by the ambiguity of local maxima from different depths, and in addition the determination of the correct source depth is a complex issue (Romanowicz, 1982). Therefore it seems that is not sufficient to take the overall VR alone for the evaluation of the solution quality but information about the respective source position (especially depth) should be added and evaluated.

The occurrence of high non-double-couple components in both synthetic test cases (section 6.3.5) and real data case studies (section 7.1) must be further analysed. It has to be clearified, if this effect occurs due to the instable inversion of surfaces waves or systematically reflects subsurface structures (Kuge and Kawakatsu, 1993; Kuge and Lay, 1994; Henry et al., 2002).

Aside the mentioned sources of errors and uncertainties (mainly the time shift sensitivity), other minor issues occurred in the evaluation of the test results. For example the tapering of data on the basis of the velocities within the underlying Earth model leads to problems and even wrong results, if the velocities are significantly under-estimated. Then the data are cut off too early and after the frequency filtering, systematically wrong waveforms are inverted, potentially leading to results with spuriously high VR values. This again may lead to wrong source times (and consequently to wrong polarities). An additional, but by far smaller, potential source of numerical errors is the internally handled in-time preprocessing of raw input data in case of the continuous application. This processing step has only been applied on the test data set, presented here, further systematic study is necessary for this topic.

8.1.5 Optimisations

Beside the error estimation, other parts of the algorithm provide opportunity for improvement. The most time consuming processing step is the full grid search, therefore the above mentioned parallelisation of the code holds a large potential for increasing the computational speed significantly.

If the gain of speed is sufficient, one could think about including one further processing step, which includes the determination of the first arrival polarities in the data. Furthermore, the linear grid search could be extended by more sophisticated algorithms, for

instance a non-linear localisation algorithm (Lomax et al., 2000). This is a multi-step method which demands too large time for including it in the present stage of the software. Parallelised code in combination with larger computational power in future times will potentially allow its application.

The inclusion of stationwise time shifts aims to correct first order effects from wrong velocity models (three-dimensional heterogeneities) (Giardini, 1992; Ford et al., 2009). It is a common technique, which is included in many time-domain inversion algorithms (e.g. Dreger and Woods, 2002). Since it is a very time consuming approach, it has not been considered so far in the developed algorithm. It must be evaluated, if the potentail gain in robustness of the inversion solutions outweighs the loss in computational speed.

For most of the processing steps, as for instance the tapering, the frequency filtering, and the determination of the VR values, standard methods have been implemented. Each of these methods must be systematically tested against possible faster or more robust alternatives. Especially the implementation of another norm in the definition of VR value may improve the confinement of the results.

8.2 Conclusions

The first and main objective of this thesis has been to develop and implement a numerical algorithm that allows a fast and automated inversion of low frequency seismic data for source-time, -location, -mechanism, and -strength. The algorithm should be applicable for event-based analysis of data sets and be capable of handling one- and three-dimensional GFs. Furthermore, the software should be applicable for the near real-time analysis of continuous data sets, which additionally enables an independent event detection.

The second objective was the application of the new algorithm to synthetic data sets with the aim to find its capabilities as well as restrictions. Real data from volcanic and other shallow induced seismic LP-events were also used to test the algorithm.

8.2.1 Technical development and innovations

I implemented a new software code for analysing signals from seismic LP-events. The handling of seismic data in miniSEED format, the inversion, based on pre-calculated Green's functions (GFs), and the storage of the output are combined within a single Python software tool (*ARCTIC*).

The inversion algorithm is an extension of the well-tested concept of a one-step time-domain inversion of full waveform data in combination with a gridsearch in space and time. The inversion is event-based in that the source time has to be provided by an external detection routin. The source time can be refined using a temporal gridsearch around the provided time stamp. In contrast to other existing inversion codes, the algorithm I have developed in this thesis can also be applied to a continuous data set, where it operates as an automated inversion and event detection routine.

Another innovative advantage of the development is the consideration of arbitrary geometries of source regions and velocity structures. Near- and far-field terms of a full

three-dimensional Green's function can be considered in the inversion so that no restrictions to specific source regions or scales apply.

8.2.2 Test applications and case studies

The software has been tested on synthetic data sets for varying geometric configurations. Aside the demonstration of general functionality of the algorithm, the synthetic tests have shown consistent results. The inversion results depend critically on the underlying GFs.

The algorithm is capable of working on a continuous data stream, which allows to analyse seismic data in near real-time. This is carried out by a successive inversion of data in moving time windows of fixed length. Applying this concept enables *ARCTIC* to act as an independent detection routine. The source point grid has to be chosen properly in order to allow sufficiently small time steps for the moving inversion window.

ARCTIC has been applied to several real data sets from shallow induced seismic LP-events. The inversion of real data sets yields results that are comparable to reference values from reviewed publications where available. However, the accuracy of the results depends on the degrees of freedom in the gridsearch, where different parameters show different robustness. For instance the general orientation of the source mechanism, as well as the moment magnitude seem to be quite stable results. The focal time was poorly confined since spurious time shifts occurred consistently in case of real data sets.

In contrast to other approaches, complete three-dimensional GFs are the basis of the inversion algorithm. Therefore *ARCTIC* itself is independent of the respective source-station geometry and it can handle GFs with arbitrary topographies or anisotropies.

The handling of both one-dimensional and three-dimensional GFs has been tested. Topography effects included in the three-dimensional GFs can be significant and cannot be reproduced by one-dimensional GFs. Consequently, three-dimensional GFs have been used for inverting volcanic seismic data from Mt. Erebus, where topography effects cannot be neglected. The outcome of this inversion was a reasonable source mechanism in combination with an arguable source location. However, more comprehensive comparison of the one-dimensional and three-dimensional GFs is highly necessary.

The continuous inversion of a set of real raw data included preprocessing steps for partial restitution (integration, scaling, downsampling). Data of bad quality were included as well as data gaps, which had to be handled automatically. The general applicability of *ARCTIC* on a realistic setup has been demonstrated. The tool is in a functional state and works on synthetic and real data, either event-based or continuous and yields satisfying results in almost all cases.

The development is a supplement to existing seismic analysis tools, which are either restricted to the analysis of large scale events or are based on time consuming multi-step methods.

The aforementioned systematic tests aimed to quantify the influence of several parameters on the inversion results. In general the inversion results of the first version of the software can be interpreted as a fast way to estimate source parameters, which af-

terwards can be improved by further processing. Here either a statistic evaluation of the parameters or an external multi-step method can be used for optimisation.

8.2.3 Error estimation

The tests yielded evidence that the general method of the single step inversion of full waveforms in combination with a free gridsearch contains inherent sources of errors. Polarities of estimated source mechanisms are in general not reliable as they change in combination with spurious shifts in the estimated source time. Consequently, the inversion results require further confinement to suppress this type of instability.

An error estimation in terms of a quantification could not be carried out in the scope of this thesis. Several potential sources of errors have been identified and partially analysed. Further studies by means of statistical methods are required in order to obtain reliable values for confidence intervals. In addition an implementation of further parameters as part of future work may allow the simple definition of confidence intervals for grid search results.

8.2.4 Summary

A software tool has been developed, which allows the fast and simple analysis of seismic LP-events. The developed tool is in a functional state. It works on synthetic and real data, either event-based or continuous, in almost all cases yielding satisfying results.

The development is a supplement to the existing seismic analysis tools, which are mainly either restricted to the analysis of large scale events or are based on time consuming multi-step methods.

Aside from the aforementioned prospective systematic studies with regard to the influence of several parameters, the inversion results of the first version of the software can be interpreted as fast available estimations of source parameters, which have to be further processed. Either they can be statistically evaluated or they can serve as optimised starting values for sophisticated external multi-step inversion methods.

8.2.5 Outlook and future work

As pointed out in the discussion, there are many possibilities for improvement of the software in terms of stability and performance. Furthermore the precise influence of every single processing step on the inversion result has to be analysed systematically in order to finally evaluate the *ARCTIC* code. The specified topics for these analyses and improvements were beyond the scope of this work. Addressing these open questions will allow to benefit from the above mentioned advantages of *ARCTIC* and will make this software a useful tool for the fast analysis of low frequency seismic data.

Bibliography

K. Aki and P.G. Richards. Quantitative seismology. *Univ. Science Books*, 2002.

K. Aki, M. Fehler, and S. Das. Source mechanism of volcanic tremor: Fluid-driven crack models and their application to the 1963 Kilauea eruption. *Journal of volcanology and geothermal research*, 2(3):259–287, 1977. ISSN 0377-0273.

R.L. Allen and D.W. Mills. Signal Analysis: time, frequency, scale, and structure. *Wiley-IEEE Press*, 2004.

D.N. Anderson, G.E. Randall, R.W. Whitaker, S.J. Arrowsmith, M.D. Arrowsmith, D.K. Fagan, S.R. Taylor, N.D. Selby, F.R. Schult, G.D. Kraft, et al. Seismic event identification. *Wiley Interdisciplinary Reviews: Computational Statistics*, 2(4):414–432, 2010. ISSN 1939-0068.

A. Arciniega-Ceballos, B.A. Chouet, and P. Dawson. Very long-period signals associated with vulcanian explosions at Popocatepetl Volcano, Mexico. *Geophysical Research Letters*, 26(19):3013–3016, 1999.

A. Arciniega-Ceballos, B. Chouet, and P. Dawson. Long-period events and tremor at Popocatepetl volcano (1994-2000) and their broadband characteristics. *Bulletin of Volcanology*, 65(2):124–135, 2003. ISSN 0258-8900.

R. Aster, S. Mah, P. Kyle, W. McIntosh, N. Dunbar, J. Johnson, M. Ruiz, and S. McNamara. Very long period oscillations of Mount Erebus Volcano. *J. geophys. Res*, 108: 2522, 2003.

R. Aster, B. Beaudoin, J. Hole, M. Fouch, J. Fowler, and D. James. IRIS Seismology Program marks 20 years of discovery. *Eos Trans. AGU*, 86:171, 2005.

R. Aster, D. Zandomeneghi, S. Mah, S. McNamara, DB Henderson, H. Knox, and K. Jones. Moment tensor inversion of very long period seismic signals from Strombolian eruptions of Erebus Volcano. *Journal of Volcanology and Geothermal Research*, 177(3):635–647, 2008. ISSN 0377-0273.

G. Backus and M. Mulcahy. Moment tensors and other phenomenological descriptions of seismic sources – I. Continuous displacements. *Geophysical Journal of the Royal Astronomical Society*, 46:341–361, 1976a.

G. Backus and M. Mulcahy. Moment tensors and other phenomenological descriptions of seismic sources – II. Discontinuous displacements. *Geophysical Journal of the Royal Astronomical Society*, 47(2):301–329, 1976b. ISSN 1365-246X.

G.E. Backus. Interpreting the seismic glut moments of total degree two or less. *Geophysical Journal of the Royal Astronomical Society*, 51(1):1–25, 1977. ISSN 1365-246X.

D. Bame and M. Fehler. Observations of long period earthquakes accompanying hydraulic fracturing. *grl*, 13:149–152, 1986. doi: 10.1029/GL013i002p00149.

R. Barsch. *Web-based technology for storage and processing of multi-component data in seismology.* PhD thesis, 2009.

A. Barth. Frequency sensitive moment tensor inversion for light to moderate magnitude earthquakes in eastern Africa and derivation of the regional stress field. Frequenzabhängige Momententensorinversion für schwache bis mittelstarke Erdbeben im östlichen Afrika und Ableitung des regionalen Spannungsfeldes. *Unpublished PhD thesis, Institute of Geophysics, University of Karlsruhe, 149 pp.(Barth, 2006 check in text)*, 2007.

J. Battaglia, J.L. Got, and P. Okubo. Location of long-period events below Kilauea Volcano using seismic amplitudes and accurate relative relocation. *Journal of Geophysical Research*, 108(B12):2553, 2003. ISSN 0148-0227.

J. Battaglia, C.H. Thurber, J.L. Got, C.A. Rowe, and R.A. White. Precise relocation of earthquakes following the 15 June 1991 eruption of Mount Pinatubo (Philippines). *Journal of Geophysical Research*, 109(B7):B07302, 2004. ISSN 0148-0227.

C. Bean, I. Lokmer, and G. O'Brien. Influence of near-surface volcanic structure on long-period seismic signals and on moment tensor inversions: Simulated examples from Mount Etna. *J. geophys. Res*, 113, 2008.

J.P. Benoit and S.R. McNutt. New constraints on source processes of volcanic tremor at Arenal Volcano, Costa Rica, using broadband seismic data. *Geophysical Research Letters*, 24(4):449–452, 1997.

H.M. Benz, B.A. Chouet, P.B. Dawson, J.C. Lahr, R.A. Page, and J.A. Hole. Three-dimensional P and S wave velocity structure of Redoubt Volcano, Alaska. *Journal of Geophysical Research*, 101(B4):8111–8128, 1996. ISSN 0148-0227.

H. Berckhemer. Einführung in die geophysik. *Wiss. Buchges. Darmstadt*, 1990.

F. Bernardi, J. Braunmiller, U. Kradolfer, and D. Giardini. Automatic regional moment tensor inversion in the European-Mediterranean region. *Geophysical Journal International*, 157(2):703–716, 2004. ISSN 1365-246X.

M. Beyreuther and J. Wassermann. Continuous earthquake detection and classification using discrete Hidden Markov Models. *Geophysical Journal International*, 175(3):1055–1066, 2008. doi: 10.1111/j.1365-246X.2008.03921.x.

M. Beyreuther, R. Barsch, L. Krischer, T. Megies, Y. Behr, and J. Wassermann. ObsPy: A Python Toolbox for Seismology. *Seismological Research Letters*, 81(3):530, 2010. ISSN 0895-0695.

M.A. Biot. Propagation of elastic waves in a cylindrical bore containing a fluid. *Journal of Applied Physics*, 23(9):997–1005, 1952. ISSN 0021-8979.

M. Bischoff. Ruhr-Universität Bochum, personal communication, 2010.

D. Bowers and J.A. Hudson. Defining the scalar moment of a seismic source with a general moment tensor. *Bulletin of the Seismological Society of America*, 89(5):1390, 1999. ISSN 0037-1106.

M.B.C. Brandt and I. Saunders. New Regional Moment Tensors in South Africa. *Seismological Research Letters*, 82(1):69, 2011. ISSN 0895-0695.

J. Braunmiller, T. Dahm, and K.P. Bonjer. Source mechanism of the 1992 Roermond earthquake from surface-wave inversion of regional data. *Geophysical Journal International*, 116(3):663–672, 1994. ISSN 1365-246X.

J. Braunmiller, U. Kradolfer, M. Baer, and D. Giardini. Regional moment tensor determination in the European-Mediterranean area–initial results. *Tectonophysics*, 356 (1-3):5–22, 2002. ISSN 0040-1951.

I.N. Bronstein, K.A. Semendjajew, G. Musiol, and H. Mühlig. Handbuch der Mathematik. *Verlag Harri Deutsch*, 1989.

M.J. Buckingham and M.A. Garcés. Canonical model of volcano acoustics. *Journal of geophysical research*, 101(B4):8129–8151, 1996. ISSN 0148-0227.

B.G. Bukchin. Determination of stress glut moments of total degree 2 from teleseismic surface wave amplitude spectra. *Tectonophysics*, 248(3-4):185–191, 1995. ISSN 0040-1951.

R. Burridge and L. Knopoff. Body force equivalents for seismic dislocations. *Bulletin of the Seismological Society of America*, 54:1875–1888, 1964.

B. Buttkus. Spectral analysis and filter theory in applied geophysics. *Springer Verlag*, 2000.

A. Cannata, M. Hellweg, G. Di Grazia, S. Ford, S. Alparone, S. Gresta, P. Montalto, and D. Patanč. Long period and very long period events at Mt. Etna volcano: Characteristics, variability and causality, and implications for their sources. *Journal of Volcanology and Geothermal Research*, 187(3-4):227–249, 2009. ISSN 0377-0273.

S. Cesca. University of Hamburg, personal communication, 2010.

S. Cesca. Mining Environments (MINE) – BMBF/DFG-project – University of Hamburg, personal communication, 2011.

S. Cesca, E. Buforn, and T. Dahm. Amplitude spectra moment tensor inversion of shallow earthquakes in Spain. *Geophysical Journal International*, 166(2):839–854, 2006. ISSN 1365-246X.

S. Cesca, J. Battaglia, T. Dahm, E. Tessmer, S. Heimann, and P. Okubo. Effects of topography and crustal heterogeneities on the source estimation of LP event at Kilauea volcano. *Geophysical Journal International*, 172(3):1219–1236, 2008. ISSN 1365-246X.

S. Cesca, S. Heimann, and T. Dahm. Rapid directivity detection by azimuthal amplitude spectra inversion. *Journal of seismology*, pages 1–18, 2010a. ISSN 1383-4649.

S. Cesca, S. Heimann, K. Stammler, and T. Dahm. Automated procedure for point and kinematic source inversion at regional distances. *Journal of Geophysical Research*, 115 (B6):B06304, 2010b. ISSN 0148-0227.

S. Cesca, T. Dahm, C. Juretzek, and D. Kühn. Rupture process of the 7 may 2001 mw 4.2 ekofisk induced earthquake. *Geophys. J. Int., submitted*, 2011.

B. Chouet. Excitation of a buried magmatic pipe: a seismic source model for volcanic tremor. *Journal of geophysical research*, 90(B2):1881–1893, 1985. ISSN 0148-0227.

B. Chouet. Dynamics of a fluid-driven crack in three dimensions by the finite difference method. *Journal of geophysical research*, 91(B14):13967–13, 1986. ISSN 0148-0227.

B. Chouet. Resonance of a fluid-driven crack: radiation properties and implications for the source of long-period events and harmonic tremor. *Journal of geophysical research*, 93(B5):4375–4400, 1988. ISSN 0148-0227.

B. Chouet. Volcano seismology. *Pure and Applied Geophysics*, 160(3):739–788, 2003. ISSN 0033-4553.

B. Chouet and B.R. Julian. Dynamics of an expanding fluid-filled crack. *Journal of Geophysical Research*, 90(B13):11187, 1985. ISSN 0148-0227.

B. Chouet, P. Dawson, T. Ohminato, M. Martini, G. Saccorotti, F. Giudicepietro, G. De Luca, G. Milana, and R. Scarpa. Source mechanisms of explosions at Stromboli Volcano, Italy, determined from moment-tensor inversions of very-long-period data. *Journal of Geophysical Research*, 108(B1):2019, 2003. ISSN 0148-0227.

B.A. Chouet. Long-period volcano seismicity: its source and use in eruption forecasting. 1996.

S.D. Conte and C.W.D. Boor. Elementary numerical analysis: an algorithmic approach. *McGraw-Hill Higher Education*, 1980.

R.S. Crosson and D.A. Bame. A spherical source model for low frequency volcanic earthquakes. *Journal of geophysical research*, 90(B12):10237, 1985. ISSN 0148-0227.

F.G. Cruz and B.A. Chouet. Long-period events, the most characteristic seismicity accompanying the emplacement and extrusion of a lava dome in Galeras Volcano, Colombia, in 1991. *Journal of Volcanology and Geothermal Research*, 77(1-4):121–158, 1997. ISSN 0377-0273.

T. Dahm. Relative moment tensor inversion based on ray theory: theory and synthetic tests. *Geophysical Journal International*, 124(1):245–257, 1996. ISSN 1365-246X.

T. Dahm and F. Krüger. Higher-degree moment tensor inversion using far-field broadband recordings: theory and evaluation of the method with application to the 1994 Bolivia deep earthquake. *Geophysical Journal International*, 137(1):35–50, 1999. ISSN 1365-246X.

T. Dahm, G. Manthei, and J. Eisenblätter. Relative moment tensors of thermally induced microcracks in salt rock. *Tectonophysics*, 289(1-3):61–74, 1998. ISSN 0040-1951.

T. Dahm, G. Manthei, and J. Eisenblätter. Automated moment tensor inversion to estimate source mechanisms of hydraulically induced micro-seismicity in salt rock. *Tectonophysics*, 306(1):1 – 17, 1999. ISSN 0040-1951. doi: DOI:10.1016/S0040-1951(99)00041-4.

T. Dahm, F. Kruger, K. Stammler, K. Klinge, R. Kind, K. Wylegalla, and J.R. Grasso. The 2004 Mw 4.4 Rotenburg, Northern Germany, Earthquake and Its Possible Relationship with Gas Recovery. *Bulletin of the Seismological Society of America*, 97(3): 691, 2007. ISSN 0037-1106.

T. Dahm, S. Heimann, and W. Bialowons. A seismological study of shallow weak microearthquakes in the urban area of Hamburg city, Germany, and its possible relation to salt dissolution. *Natural Hazards*, pages 1–24, 2010. ISSN 0921-030X.

R. Davi, GS O'Brien, I. Lokmer, C.J. Bean, P. Lesage, and M.M. Mora. Moment tensor inversion of explosive long period events recorded on Arenal volcano, Costa Rica, constrained by synthetic tests. *Journal of Volcanology and Geothermal Research*, 2010. ISSN 0377-0273.

P.B. Dawson, B.A. Chouet, P.G. Okubo, A. Villasenor, and H.M. Benz. Three-dimensional velocity structure of the Kilauea Caldera, Hawaii. *Geophysical Research Letters*, 26(18):2805–2808, 1999. ISSN 0094-8276.

L. De Barros, C.J. Bean, I. Lokmer, G. Saccorotti, L. Zuccarello, G.S. O'Brien, J.P. Métaxian, and D. Patanè. Source geometry from exceptionally high resolution long period event observations at Mt Etna during the 2008 eruption. *Geophysical Research Letters*, 36(24):L24305, 2009. ISSN 0094-8276.

R.R. Dibble, B. O'Brien, and C.A. Rowe. The velocity structure of Mount Erebus, Antarctica, and its lava lake. *Volcanological and Environmental Studies of Mount Erebus, Antarctica*, pages 1–16, 1994.

D.J. Doornbos. Seismic source spectra and moment tensors. *Physics of The Earth and Planetary Interiors*, 30(2-3):214–227, 1982. ISSN 0031-9201.

H. Dragert, K. Wang, and T.S. James. A Silent Slip Event on the Deeper Cascadia Subduction Interface. *Science*, 292(5521):1525–1528, 2001. doi: 10.1126/science.1060152.

D. Dreger and A. Kaverina. Seismic remote sensing for the earthquake source process and near-source strong shaking: a case study of the October 16, 1999 Hector Mine earthquake. *Geophys. Res. Lett*, 27(13):1941–1944, 2000.

D. Dreger and B. Woods. Regional distance seismic moment tensors of nuclear explosions. *Tectonophysics*, 356(1-3):139–156, 2002. ISSN 0040-1951.

D.S. Dreger and D.V. Helmberger. Determination of source parameters at regional distances with three-component sparse network data. *Journal of Geophysical Research*, 98(B5):8107–8125, 1993. ISSN 0148-0227.

A.M. Dziewonski, T.A. Chou, and J.H. Woodhouse. Determination of earthquake source parameters from waveform data for studies of global and regional seismicity. *Journal of Geophysical Research*, 86(B4):2825–2852, 1981. ISSN 0148-0227.

A.M. Dziewonski, G. Ekström, and N.N. Maternovskaya. Centroid-moment tensor solutions for July-September 1999. *Physics of the Earth and Planetary Interiors*, 119(3-4): 311–319, 2000. ISSN 0031-9201.

Earth Data. Edl pr6-24. URL `http://www.earthdata.co.uk/pr6-24.html`.

M. Fehler. Observations of volcanic tremor at Mount St. Helens volcano. *Journal of geophysical research*, 88(B4):3476–3484, 1983. ISSN 0148-0227.

B. Feignier and R.P. Young. Moment tensor inversion of induced microseisnmic events: Evidence of non-shear failures in the $-4 < M < -2$ moment magnitude range. *Geophysical Research Letters*, 19(14):1503–1506, 1992. ISSN 0094-8276.

V. Ferrazzini and K. Aki. Slow waves trapped in a fluid-filled infinite crack: implication for volcanic tremor. *Journal of Geophysical Research*, 92(B9):9215–9223, 1987. ISSN 0148-0227.

A.M.G. Ferreira and J.H. Woodhouse. Long-period seismic source inversions using global tomographic models. *Geophysical Journal International*, 166(3):1178–1192, 2006. ISSN 1365-246X.

M.G. Ferrick, A. Qamar, and W.F.S. Lawrence. Source mechanism of volcanic tremor. *Journal of geophysical research*, 87(B10):8675–8683, 1982. ISSN 0148-0227.

R.P. Feynman. Feynman lectures on physics. Volume 2: Mainly electromagnetism and matter. 1964.

T. Forbriger. Inversion of shallow-seismic wavefields: I. Wavefield transformation. *Geophysical Journal International*, 153:719–734, June 2003a. doi: 10.1046/j.1365-246X.2003.01929.x.

T. Forbriger. Inversion of shallow-seismic wavefields: II. Inferring subsurface properties from wavefield transforms. *Geophysical Journal International*, 153(3):735–752, 2003b. ISSN 1365-246X.

S.R. Ford, D.S. Dreger, and W.R. Walter. Identifying isotropic events using a regional moment tensor inversion. *Journal of Geophysical Research*, 114(B1):B01306, 2009. ISSN 0148-0227.

W. Friederich and J. Dalkolmo. Complete synthetic seismograms for a spherically symmetric earth by a numerical computation of the Green's function in the frequency domain. *Geophysical Journal International*, 122(2):537–550, 1995. ISSN 1365-246X.

S. Gambino. High precision locations of LP events on Mt. Etna: Reconstruction of the fluid-filled volume. *Studia Geophysica et Geodaetica*, 50(4):663–674, 2006. ISSN 0039-3169.

M.A. Garcés and S.R. McNutt. Theory of the airborne sound field generated in a resonant magma conduit. *Journal of volcanology and geothermal research*, 78(3-4):155–178, 1997. ISSN 0377-0273.

M.A. Garcés, M.T. Hagerty, and S.Y. Schwartz. Magma acoustics and time-varying melt properties at Arenal Volcano, Costa Rica. *Geophysical research letters*, 25(13): 2293–2296, 1998. ISSN 0094-8276.

A. Gerst. *The First second of a strombolian volcanic eruption.* PhD thesis, University of Hamburg, PhD thesis, 2010.

D. Giardini. Moment tensor inversion from Mednet data (1) large worldwide earthquakes of 1990. *Geophysical research letters*, 19(7):713–716, 1992. ISSN 0094-8276.

S.J. Gibowicz. Seismicity Induced by Mining: Recent Research. *Advances in Geophysics*, pages 1–53, 2009. ISSN 0065-2687.

F. Gilbert. Excitation of the normal modes of the Earth by earthquake sources. *Geophysical Journal of the Royal Astronomical Society*, 22(2):223–226, 1971. ISSN 1365-246X.

J.S. Gilbert and S.J. Lane. The consequences of fluid motion in volcanic conduits. *Geological Society, London, Special Publications*, 307(1):1, 2008. ISSN 0305-8719.

G.H. Golub and C. Reinsch. Singular value decomposition and least squares solutions. *Numerische Mathematik*, 14(5):403–420, 1970. ISSN 0029-599X.

S. Hainzl, T. Kraft, J. Wassermann, H. Igel, and E. Schmedes. Evidence for rainfall-triggered earthquake activity. *Geophysical Research Letters*, 33(19):L19303, 2006. ISSN 0094-8276.

C. Hammer. Universität Potsdam, Diplomarbeit: Wellenformeigenschaften seismischer Signale vulkanischen Ursprungs im Nah- und Fernfeld, 2007.

A. Hasegawa, D. Zhao, S. Hori, A. Yamamoto, and S. Horiuchi. Deep structure of the northeastern Japan arc and its relationship to seismic and volcanic activity. *Nature Publishing Group*, 1991.

H.S. Hasegawa, R.J. Wetmiller, and D.J. Gendzwill. Induced seismicity in mines in Canada—an overview. *Pure and Applied Geophysics*, 129(3):423–453, 1989. ISSN 0033-4553.

J. Havskov, S. De la Cruz-Reyna, SK Singh, F. Medina, and C. Gutierrez. Seismic activity related to the March-April, 1982 eruptions of El Chichon Volcano, Chiapas, Mexico. *Geophysical Research Letters*, 10(4):293–296, 1983. ISSN 0094-8276.

S. Heimann. Universität Hamburg, Diplomarbeit: Numerische Modellierung der Nachgiebigkeit des Meeresbodens mit einer Tschebyscheff-Fourier-Methode, 2005.

S. Heimann. "*Snuffler* – a python tool for the graphical representation of data – university of hamburg, personal communication", 2009.

S. Heimann. *A Robust Method To Estimate Kinematic Earthquake Source Parameters*. PhD thesis, University of Hamburg, PhD thesis, 2011.

C. Henry, J.H. Woodhouse, and S. Das. Stability of earthquake moment tensor inversions: effect of the double-couple constraint. *Tectonophysics*, 356(1-3):115–124, 2002. ISSN 0040-1951.

D. Hidayat, B. Voight, C. Langston, A. Ratdomopurbo, and C. Ebeling. Broadband seismic experiment at Merapi Volcano, Java, Indonesia: very-long-period pulses embedded in multiphase earthquakes. *Journal of Volcanology and Geothermal Research*, 100(1-4):215–231, 2000. ISSN 0377-0273.

D. Hidayat, B. Chouet, B. Voight, P. Dawson, and A. Ratdomopurbo. Source mechanism of very-long-period signals accompanying dome growth activity at Merapi volcano, Indonesia. *Geophysical Research Letters*, 29(23):2118, 2002. ISSN 0094-8276.

D.P. Hill, F. Pollitz, and C. Newhall. Earthquake-volcano interactions. *Physics Today*, 55(11):41–47, 2002. ISSN 0031-9228.

S. Ide, D.R. Shelly, and G.C. Beroza. Mechanism of deep low frequency earthquakes: Further evidence that deep non-volcanic tremor is generated by shear slip on the plate interface. *Geophysical Research Letters*, 34(3):L03308, 2007. ISSN 0094-8276.

A.M. Ionov and G.A. Maximov. Propagation of tube waves generated by an external source in layered permeable rocks. *Geophysical Journal International*, 124(3):888–906, 1996. ISSN 1365-246X.

IRIS Data Management System. Iris data management center, 2010. URL `http://www.iris.washington.edu/data`. This is an electronic document. Date retrieved: December 5, 2010.

R. M. Iverson, D. Dzurisin, C. A. Gardner, T. M. Gerlach, R. G. Lahusen, M. Lisowski, J. J. Major, S. D. Malone, J. A. Messerich, S. C. Moran, J. S. Pallister, A. I. Qamar, S. P. Schilling, and J. W. Vallance. Dynamics of seismogenic volcanic extrusion at Mount St Helens in 2004-05. *Nature*, 444:439–443, November 2006. doi: 10.1038/nature05322.

J.D. Jackson and R.F. Fox. Classical electrodynamics. *American Journal of Physics*, 67: 841, 1999.

J. Johnson, R. Aster, K.R. Jones, P. Kyle, and B. McIntosh. Acoustic source characterization of impulsive Strombolian eruptions from the Mount Erebus lava lake. *Journal of Volcanology and Geothermal Research*, 177(3):673–686, 2008. ISSN 0377-0273.

E. Jones, T. Oliphant, P. Peterson, et al. SciPy: Open source scientific tools for Python, 2001. URL `http://www.scipy.org/`.

M.L. Jost and R.B. Herrmann. A student's guide to and review of moment tensors. *Seism. Res. Lett*, 60(2):37–57, 1989.

P. Jousset, J. Neuberg, and S. Sturton. Modelling the time-dependent frequency content of low-frequency volcanic earthquakes. *Journal of Volcanology and Geothermal Research*, 128(1-3):201 – 223, 2003. ISSN 0377-0273. doi: DOI:10.1016/S0377-0273(03)00255-5. Putting Volcano Seismology in a Physical Context. In memory of Bruno Martinelli.

J. Julia, A.A. Nyblade, R. Durrheim, L. Linzer, R. Gok, P. Dirks, and W. Walter. Source Mechanisms of Mine-Related Seismicity, Savuka Mine, South Africa. *Bulletin of the Seismological Society of America*, 99(5):2801, 2009. ISSN 0037-1106.

B.R. Julian. Volcanic tremor: nonlinear excitation by fluid flow. *Journal of Geophysical Research*, 99(B6):11859, 1994. ISSN 0148-0227.

Y.Y. Kagan. Universality of the seismic moment-frequency relation. *Pure and Applied Geophysics*, 155(2):537–573, 1999. ISSN 0033-4553.

K. Kaminuma. Seismic activity of Erebus volcano, antarctica. *Pure and Applied Geophysics*, 125(6):993–1008, 1987. ISSN 0033-4553.

H. Kanamori. Synthesis of Long-Period Surface Waves and Its Application to Earthquake Source Studies Kurile Islands Earthquake of October 13, 1963. *Journal of Geophysical Research*, 75:5011–5027, 1970. doi: 10.1029/JB075i026p05011.

H. Kanamori. The energy release in great earthquakes. *Journal of Geophysical Research*, 82(20):2981–2987, 1977. ISSN 0148-0227.

H. Kanamori and J.W. Given. Use of long-period surface waves for rapid determination of earthquake-source parameters. *Physics of the Earth and Planetary interiors*, 27(1): 8–31, 1981. ISSN 0031-9201.

H. Kawakatsu. Centroid single force inversion of seismic waves generated by landslides. *Journal of Geophysical Research*, 94(B9):12363, 1989. ISSN 0148-0227.

H. Kawakatsu. Automated near-realtime CMT inversion. *Geophysical Research Letters*, 22(19):2569–2572, 1995. ISSN 0094-8276.

H. Kawakatsu. On the realtime monitoring of the long-period seismic wavefield. *Methods and Applications of Signal Processing in Seismic Network Operations*, pages 251–257, 2003.

H. Kawakatsu and J.P. Montagner. Time-reversal seismic-source imaging and moment-tensor inversion. *Geophysical Journal International*, 175(2):686–688, 2008. ISSN 1365-246X.

M. Kirchdörfer. Analysis and quasistatic FE modeling of long period impulsive events associated with explosions at Stromboli volcano (Italy). *Annals of Geophysics*, 42(3), 1999. ISSN 1593-5213.

L. Knopoff and A.F. Gangi. Seismic reciprocity. *Geophysics*, 24(4):681–691, 1959. doi: 10.1190/1.1438647.

L. Knopoff and M.J. Randall. The compensated linear-vector dipole: a possible mechanism for deep earthquakes. *Journal of Geophysical Research*, 75(26):4957–4963, 1970. ISSN 0148-0227.

R. Köthe. Was ist was – band 057: Vulkane. *Tessloff Verlag Ragnar Tessloff GmbH & Co. KG*, 2010.

Y.A. Kozlovsky. The superdeep well of the Kola Peninsula. *Springer-Verlag New York Inc., New York, NY*, 1986.

L. Krieger and S. Heimann. MoPaD – Moment tensor Plotting and Decomposition. *Seismological Research Letters (revised)*, 2011.

K. Kuge and H. Kawakatsu. Analysis of a deep non double couple earthquake using very broadband data. *Geophysical Research Letters*, 17(3):227–230, 1990. ISSN 0094-8276.

K. Kuge and H. Kawakatsu. Significance of non-double couple components of deep and intermediate-depth earthquakes: implications from moment tensor inversions of long-period seismic waves. *Physics of the Earth and Planetary Interiors*, 75(4):243–266, 1993. ISSN 0031-9201.

K. Kuge and T. Lay. Data-dependent non-double-couple components of shallow earthquake source mechanisms: Effects of waveform inversion instability. *Geophysical research letters*, 21(1):9–12, 1994.

H. Kumagai and B.A. Chouet. The complex frequencies of long-period seismic events as probes of fluid composition beneath volcanoes. *Geophysical Journal International*, 138 (2):F7–F12, 1999. ISSN 1365-246X.

H. Kumagai and B.A. Chouet. Acoustic properties of a crack containing magmatic or hydrothermal fluids. *Journal of Geophysical Research*, 105(B11):25493, 2000. ISSN 0148-0227.

H. Kumagai, K. Miyakawa, H. Negishi, H. Inoue, K. Obara, and D. Suetsugu. Magmatic dike resonances inferred from very-long-period seismic signals. *Science*, 299(5615): 2058, 2003.

H. Kumagai, B.A. Chouet, and P.B. Dawson. Source process of a long-period event at Kilauea volcano, Hawaii. *Geophysical Journal International*, 161(1):243–254, 2005. ISSN 1365-246X.

J.C. Lahr, B.A. Chouet, C.D. Stephens, J.A. Power, and R.A. Page. Earthquake classification, location, and error analysis in a volcanic environment: implications for the magmatic system of the 1989-1990 eruptions at Redoubt Volcano, Alaska. *Journal of Volcanology and Geothermal Research*, 62(1-4):137–151, 1994. ISSN 0377-0273.

S. Larsen and J. Grieger. Elastic modeling tive, Part III: 3-D computational modeling. *SEG*, 2005.

S. Larsen and D. Harris. Seismic wave propagation through a low-velocity nuclear rubble zone. Technical report, Lawrence Livermore National Lab., CA (United States), 1993.

E. Larson, G. Ekström, and M. Nettles. Global cmt web page, 2010. URL `http://www.globalcmt.org`. This is an electronic document. Date of publication: [Date unavailable]. Date retrieved: July 24, 2010. Date last modified: May 28, 2010.

S. Lasocki and B. Orlecka-Sikora. Seismic hazard assessment under complex source size distribution of mining-induced seismicity. *Tectonophysics*, 456(1-2):28–37, 2008. ISSN 0040-1951.

J.H. Latter and N. Zealand. *Volcanological Observations at Tongariro National Park: 2. Types and Classification of Volcanic Earthquakes, 1976-1978*. Geophysics Division, Dept. of Scientific and Industrial Research, 1979.

T. Lay and T.C. Wallace. Modern global seismology. *Academic Press*, 1995.

D. Legrand, S. Kaneshima, and H. Kawakatsu. Moment tensor analysis of near-field broadband waveforms observed at Aso Volcano, Japan. *Journal of Volcanology and Geothermal Research*, 101(1-2):155–169, 2000. ISSN 0377-0273.

P. Lesage, F. Glangeaud, and J. Mars. Applications of autoregressive models and time-frequency analysis to the study of volcanic tremor and long-period events. *Journal of Volcanology and Geothermal Research*, 114(3-4):391–417, 2002. ISSN 0377-0273.

J. Li, H. Zhang, H.S. Kuleli, and M.N. Toksöz. Focal Mechanism Determination using High Frequency, Full Waveform Information. *SEG*, 2010.

I. Lokmer, C.J. Bean, G. Saccorotti, and D. Patanè. Moment-tensor inversion of LP events recorded on Etna in 2004 using constraints obtained from wave simulation tests. *Geophysical Research Letters*, 34(22):L22316, 2007. ISSN 0094-8276.

I. Lokmer, G. Saccorotti, B. Di Lieto, and C.J. Bean. Temporal evolution of long-period seismicity at Etna Volcano, Italy, and its relationships with the 2004-2005 eruption. *Earth and Planetary Science Letters*, 266(1-2):205–220, 2008. ISSN 0012-821X.

I. Lokmer, G.S. O'Brien, D. Stich, and C.J. Bean. Time reversal imaging of synthetic volcanic tremor sources. *Geophysical Research Letters*, 36(12):L12308, 2009. ISSN 0094-8276.

A. Lomax. seisgram2k - version 5.0, 2008. URL `http://alomax.free.fr/seisgram/SeisGram2K.html`.

A. Lomax, J. Virieux, P. Volant, and C. Berge. Probabilistic earthquake location in 3D and layered models: Introduction of a Metropolis-Gibbs method and comparison with linear locations. *Advances in Seismic Event Location*, pages 101–134, 2000.

M. Lutz. Programming python. *O'Reilly Media, Inc.*, 2006.

D.A. Malovichko. Study of "low-frequency" seismic events sources in mines of the Verkhnekamskoye potash deposit. In *Controlling seismic risk. Proceedings of the Sixth International Symposium on Rockbursts and Seismicity in Mines*, pages 9–11, 2005.

D.A. Malovichko, O.I. Kadebskaya, D.Y. Shulakov, and P.G. Butyrin. Local seismologic observations of karst processes. *Izvestiya Physics of the Solid Earth*, 46(1):57–73, 2010. ISSN 1069-3513.

A. McGarr. Seismic moments and volume changes. *Journal of Geophysical Research*, 81 (8):1487–1494, 1976. ISSN 0148-0227.

A. McGarr, D. Simpson, and L. Seeber. Case histories of induced and triggered seismicity. *International Geophysics Series*, 81(A):647–664, 2002. ISSN 0074-6142.

S.R. McNutt. Seismic monitoring and eruption forecasting of volcanoes: a review of the state-of-the-art and case histories. *Monitoring and mitigation of volcano hazards*, pages 99–146, 1996.

S.R. McNutt. Volcanic seismology. *Annual Review of Earth and Planetary Sciences*, 33 (1):461–491, 2005. doi: 10.1146/annurev.earth.33.092203.122459.

S.E. Minson and D.S. Dreger. Stable inversions for complete moment tensors. *Geophysical Journal International*, 174(2):585–592, 2008. ISSN 1365-246X.

P. Moczo, J. Kristek, and L. Halada. The finite-difference method for seismologists. *Comenius University*, 2004.

I. Molina, H. Kumagai, and H. Yepes. Resonances of a volcanic conduit triggered by repetitive injections of an ash-laden gas. *Geophysical Research Letters*, 31(3):L03603, 2004. ISSN 0094-8276.

I. Molina, H. Kumagai, A. García-Aristizábal, M. Nakano, and P. Mothes. Source process of very-long-period events accompanying long-period signals at Cotopaxi Volcano, Ecuador. *Journal of Volcanology and Geothermal Research*, 176(1):119–133, 2008. ISSN 0377-0273.

G. Müller. The reflectivity method: a tutorial. *J. geophys*, 58(1-3):153–174, 1985.

V. Muñoz, S. Cloetingh, A. Muñoz-Martín, O. Campos, A. José, D. Stich, R. Vegas, J. Galindo-Zaldívar, and J. Fernández-Lozano. Inversion of moment tensor focal mechanisms for active stresses around the microcontinent Iberia: Tectonic implications. *Tectonics*, 27(TC1009):1–22, 2008. ISSN 0278-7407.

A. Nabyl, J. Dorel, and M. Lardy. A comparative study of low-frequency seismic signals recorded at Stromboli volcano, Italy, and at Yasur volcano, Vanuatu. *New Zealand Journal of Geology and Geophysics*, 40(4):549–558, 1997. ISSN 0028-8306.

M. Nakano, H. Kumagai, and B.A. Chouet. Source mechanism of long-period events at Kusatsu-Shirane Volcano, Japan, inferred from waveform inversion of the effective excitation functions. *Journal of Volcanology and Geothermal Research*, 122(3-4):149–164, 2003. ISSN 0377-0273.

A.G. Neeman. Visualizing 3D Symmetric Moment Tensors In Oil. 2004. URL `http://www.soe.ucsc.edu/classes/cmps290b/Fall04/projects/aneeman/alisa_tensor_final.pdf`.

J. Neuberg. Characteristics and causes of shallow seismicity in andesite volcanoes. *Philosophical Transactions: Mathematical, Physical and Engineering Sciences*, pages 1533–1546, 2000. ISSN 1364-503X.

J. Neuberg. preprint, Leeds University, personal communication, 2011.

J. Neuberg and R. Luckett. Seismo-volcanic sources on stromboli volcano. *Annali di Geofisica*, 39(2):377–391, 1996. Cited By (since 1996): 14.

J. Neuberg, R. Luckett, M. Ripepe, and T. Braun. Highlights from a seismic broadband array on Stromboli volcano. *Geophysical Research Letters*, 21(9):749–752, 1994. ISSN 0094-8276.

J. Neuberg, R. Luckett, B. Baptie, and K. Olsen. Models of tremor and low-frequency earthquake swarms on Montserrat. *Journal of Volcanology and Geothermal Research*, 101(1-2):83–104, 2000. ISSN 0377-0273.

I. Newton. 1687 Philosophiae naturalis principia mathematica. *Translation by Andrew*, 1687.

T. Nishimura, H. Nakamichi, S. Tanaka, M. Sato, T. Kobayashi, S. Ueki, H. Hamaguchi, M. Ohtake, and H. Sato. Source process of very long period seismic events associated with the 1998 activity of Iwate Volcano, northeastern Japan. *Journal of Geophysical Research*, 105(B8):19135, 2000. ISSN 0148-0227.

R.C. Nolen-Hoeksema and L.J. Ruff. Moment tensor inversion of microseisms from the B-sand propped hydrofracture, M-site, Colorado. *Tectonophysics*, 336(1-4):163–181, 2001. ISSN 0040-1951.

G.S. O'Brien and C.J. Bean. Seismicity on volcanoes generated by gas slug ascent. *Geophys. Res. Lett*, 35:10–50, 2008.

T. Ohminato. Source mechanisms of vulcanian eruptions at Mt. Asama, Japan, inferred from volcano seismic signals. *Geological Society, London, Special Publications*, 307(1): 189, 2008. ISSN 0305-8719.

T. Ohminato, B.A. Chouet, P. Dawson, and S. Kedar. Waveform inversion of very long period impulsive signals associated with magmatic injection beneath Kilauea Volcano, Hawaii. *Journal of Geophysical Research*, 103(B10):23839, 1998. ISSN 0148-0227.

M. Ohrnberger. *Continuous automatic classification of seismic signals of volcanic origin at Mt. Merapi, Java, Indonesia.* PhD thesis, Universität Potsdam, 2001.

T.E. Oliphant. Guide to numpy. March 2006. URL `http://numpy.scipy.org`.

L. Ottemoller and J. Havskov. Moment magnitude determination for local and regional earthquakes based on source spectra. *Bulletin of the Seismological Society of America*, 93(1):203, 2003. ISSN 0037-1106.

L. Ottemöller, H.H. Nielsen, K. Atakan, J. Braunmiller, and J. Havskov. The 7 May 2001 induced seismic event in the Ekofisk oil field, North Sea. *J. geophys. Res*, 110, 2005.

G.F. Panza and A. Saraò. Monitoring volcanic and geothermal areas by full seismic moment tensor inversion: are non-double-couple components always artefacts of modelling? *Geophysical Journal International*, 143(2):353–364, 2000. ISSN 1365-246X.

M.E. Pasyanos, D.S. Dreger, and B. Romanowicz. Toward real-time estimation of regional moment tensors. *Bulletin of the Seismological Society of America*, 86(5):1255, 1996. ISSN 0037-1106.

I.S. Pearsall. The velocity of water hammer waves. In *ARCHIVE: Proceedings of the Institution of Mechanical Engineers, Conference Proceedings 1964-1970 (vols 178-184), Various titles labelled Volumes A to S*, volume 180, pages 12–27. Prof Eng Publishing, 1965.

W.A. Peppin and C.G. Bufe. Induced versus natural earthquakes: Search for a seismic discriminant. *Bulletin of the Seismological Society of America*, 70(1):269, 1980. ISSN 0037-1106.

A.M. Pitt and D.P. Hill. Long-period earthquakes in the Long Valley Caldera Region, eastern California. *Geophysical Research Letters*, 21(16):1679–1682, 1994. ISSN 0094-8276.

S. Pondrelli, A. Morelli, G. Ekström, S. Mazza, E. Boschi, and A.M. Dziewonski. European-Mediterranean regional centroid-moment tensors: 1997-2000. *Physics of the Earth and Planetary Interiors*, 130(1-2):71–101, 2002. ISSN 0031-9201.

W.H. Press, B.P. Flannery, S.A. Teukolsky, W.T. Vetterling, et al. Numerical recipes. *Cambridge university press*, 3, 2007.

M.J. Randall. Elastic multipole theory and seismic moment. *Bulletin of the Seismological Society of America*, 61(5):1321, 1971. ISSN 0037-1106.

P. A. Reasenberg and D. Oppenheimer. Fpfit, fpplot, and fppage:fortran computer programs for calculating and displaying earthquake fault-plane solutions. *U.S. Geological Survey, Open-File Reports 85-739*, 1985.

R. Rew and G. Davis. NetCDF: an interface for scientific data access. *Computer Graphics and Applications, IEEE*, 10(4):76–82, 2002. ISSN 0272-1716.

M.A. Riedesel and T.H. Jordan. Display and assessment of seismic moment tensors. *Bulletin of the Seismological Society of America*, 79(1):85, 1989.

J. Ritsema and T. Lay. Long-period regional wave moment tensor inversion for earthquakes in the western United States. *Journal of Geophysical Research*, 100(B6):9853–9864, 1995. ISSN 0148-0227.

I.V. Rodriguez, M.D. Sacchi, and Y.J. Gu. Continuous hypocenter and source mechanism inversion via a Green's function-based matching pursuit algorithm. *The Leading Edge*, 29:334, 2010.

B.A. Romanowicz. Moment tensor inversion of long period Rayleigh waves: a new approach. *Journal of Geophysical Research*, 87(B7):5395–5407, 1982. ISSN 0148-0227.

D. Rößler. *Retrieval of earthquake source parameters in Inhomogeneous anisotropic media with application to swarm events in West Bohemia in 2000*. PhD thesis, 2006.

C.A. Rowe, R.C. Aster, P.R. Kyle, J.W. Schlue, and R.R. Dibble. Broadband recording of Strombolian explosions and associated very-long-period seismic signals on Mount Erebus volcano, Ross Island, Antarctica. *Geophysical Research Letters*, 25:2297–2300, 1998. ISSN 0094-8276.

C.A. Rowe, R.C. Aster, P.R. Kyle, R.R. Dibble, and J.W. Schlue. Seismic and acoustic observations at Mount Erebus Volcano, Ross Island, Antarctica, 1994-1998. *Journal of Volcanology and Geothermal Research*, 101(1-2):105–128, 2000. ISSN 0377-0273.

C.A. Rowe, C.H. Thurber, and R.A. White. Dome growth behavior at Soufriere Hills Volcano, Montserrat, revealed by relocation of volcanic event swarms, 1995-1996. *Journal of Volcanology and Geothermal Research*, 134(3):199–221, 2004. ISSN 0377-0273.

A.C. Rust, N.J. Balmforth, and S. Mandre. The feasibility of generating low-frequency volcano seismicity by flow through a deformable channel. *Geological Society, London, Special Publications*, 307(1):45, 2008. ISSN 0305-8719.

G. Saccorotti, B. Chouet, and P. Dawson. Wavefield properties of a shallow long-period event and tremor at Kilauea Volcano, Hawaii. *Journal of Volcanology and Geothermal Research*, 109(1-3):163–189, 2001. ISSN 0377-0273.

G. Saccorotti, I. Lokmer, C.J. Bean, G. Di Grazia, and D. Patanč. Analysis of sustained long-period activity at Etna Volcano, Italy. *Journal of volcanology and geothermal research*, 160(3-4):340–354, 2007. ISSN 0377-0273.

SEED, manual. The (mini)seed data format, 2010. URL `http://www.iris.washington.edu/manuals/SEEDManual_V2.4.pdf`. This is an electronic document. Date retrieved: December 5, 2010.

P. Segall. Earthquakes triggered by fluid extraction. *Geology*, 17(10):942, 1989. ISSN 0091-7613.

N.D. Selby, E. Eshun, H.J. Patton, and A. Douglas. Unusual long-period Rayleigh wave radiation from a vertical dip-slip source: The 7 May 2001 North Sea earthquake. *Journal of Geophysical Research*, 110(B10):B10304, 2005. ISSN 0148-0227.

C.E. Shannon. Communication in the presence of noise. *Proceedings of the IRE*, 37(1): 10 – 21, 1949. ISSN 0096-8390. doi: 10.1109/JRPROC.1949.232969.

P.M. Shearer. Introduction to seismology. *Cambridge Univ. Press*, 1999.

D.R. Shelly, G.C. Beroza, S. Ide, and S. Nakamula. Low-frequency earthquakes in Shikoku, Japan, and their relationship to episodic tremor and slip. *Nature*, 442(7099): 188–191, 2006. ISSN 0028-0836.

J. Šílení and A. Milev. Seismic moment tensor resolution on a local scale: Simulated rockburst and mine-induced seismic events in the kopanang gold mine, south africa. *Pure and Applied Geophysics*, 163:1495–1513, 2006. ISSN 0033-4553. URL `http://dx.doi.org/10.1007/s00024-006-0089-z`. 10.1007/s00024-006-0089-z.

J. Sílenı and A. Milev. Source mechanism of mining induced seismic events–Resolution of double couple and non double couple models. *Tectonophysics*, 456(1-2):3–15, 2008. ISSN 0040-1951.

J. Šílení, G.F. Panza, and P. Campus. Waveform inversion for point source moment tensor retrieval with variable hypocentral depth and structural model. *Geophysical journal international*, 109(2):259–274, 1992. ISSN 1365-246X.

S.A. Sipkin. Estimation of earthquake source parameters by the inversion of waveform data: synthetic waveforms. *Physics of the Earth and Planetary Interiors*, 30(2-3): 242–259, 1982. ISSN 0031-9201.

S.A. Sipkin. Rapid determination of global moment-tensor solutions. *Geophysical Research Letters*, 21(16):1667–1670, 1994. ISSN 0094-8276.

A.T. Smith, C. Schultz, and JJ Zucca. Aftershocks and on-site inspections under a test ban: A progress report. Technical report, Lawrence Livermore National Lab., CA (United States), 1995.

T. Spies and J. Eisenblätter. Acoustic emission investigation of microcrack generation at geological boundaries. *Engineering Geology*, 61(2-3):181–188, 2001. ISSN 0013-7952.

S. Stein and M. Wysession. An introduction to seismology, earthquakes, and earth structure. *Wiley-Blackwell*, 2003.

D. Stich, R. Martín, and J. Morales. Moment tensor inversion for iberia-maghreb earthquakes 2005-2008. *Tectonophysics*, 483(3-4):390 – 398, 2010. ISSN 0040-1951. doi: DOI:10.1016/j.tecto.2009.11.006. URL `http://www.sciencedirect.com/science/article/B6V72-4XNF3XP-2/2/56deb667ddeb2870d7a8f6c17eaa6014`.

W.S. Stump and L.R. Johnson. Higher-degree moment tensors-the importance of source finiteness and rupture propagation on seismograms. *Geophys. JR Astr. Soc*, 69:143, 1982. ISSN 1365-246X.

S. Sturton and J. Neuberg. The effects of conduit length and acoustic velocity on conduit resonance: Implications for low-frequency events. *Journal of Volcanology and Geothermal Research*, 151(4):319–339, 2006. ISSN 0377-0273.

F. Tajima, C. Megnin, D.S. Dreger, and B. Romanowicz. Feasibility of real-time broadband waveform inversion for simultaneous moment tensor and centroid location determination. *Bulletin of the Seismological Society of America*, 92(2):739, 2002. ISSN 0037-1106.

T. Takanami, G. Kitagawa, and H. Kawakatsu. On the realtime monitoring of the long-period seismic wavefield. In *Methods and Applications of Signal Processing in Seismic Network Operations*, volume 98 of *Lecture Notes in Earth Sciences*, pages 251–257. Springer Berlin / Heidelberg, 2003. URL `http://dx.doi.org/10.1007/BFb0117707`. 10.1007/BFb0117707.

Y. Takei and M. Kumazawa. Why have the single force and torque been excluded from seismic source models? *Geophysical Journal International*, 118(1):20–30, 1994. ISSN 1365-246X.

Y. Takei and M. Kumazawa. Phenomenological representation and kinematics of general seismic sources including the seismic vector modes. *Geophysical Journal International*, 121(3):641–662, 1995. ISSN 1365-246X.

E. Tessmer. 3-D seismic modelling of general material anisotropy in the presence of the free surface by a Chebyshev spectral method. *Geophysical Journal International*, 121 (2):557–575, 1995. ISSN 1365-246X.

C.I. Trifu and M. Radulian. Predicted near-field ground motion for dynamic stress-drop models. *Pure and Applied Geophysics*, 123(2):173–198, 1985. ISSN 0033-4553.

C.I. Trifu, D. Angus, and V. Shumila. A fast evaluation of the seismic moment tensor for induced seismicity. *Bulletin of the Seismological Society of America*, 90(6):1521, 2000. ISSN 0037-1106.

H. Tsuruoka, H. Kawakatsu, and T. Urabe. GRiD MT (grid-based real-time determination of moment tensors) monitoring the long-period seismic wavefield. *Physics of the Earth and Planetary Interiors*, 175(1-2):8–16, 2009. ISSN 0031-9201.

H. Tuffen and D. Dingwell. Fault textures in volcanic conduits: evidence for seismic trigger mechanisms during silicic eruptions. *Bulletin of Volcanology*, 67(4):370–387, 2005. ISSN 0258-8900.

H. Tuffen, D.B. Dingwell, and H. Pinkerton. Repeated fracture and healing of silicic magma generate flow banding and earthquakes? *Geology*, 31(12):1089, 2003. ISSN 0091-7613.

A. Udıas. Principles of seismology. *Cambridge University Press, Cambridge*, 1999.

T.I. Urbancic, C.I. Trifu, R.A. Mercer, A.J. Feustel, and J.A.G. Alexander. Automatic time-domain calculation of source parameters for the analysis of induced seismicity. *Bulletin of the Seismological Society of America*, 86(5):1627, 1996. ISSN 0037-1106.

USGS. Usgs earthquake catalog, 2010. URL `http://earthquake.usgs.gov/earthquakes/catalogs/`. This is an electronic document. Date of publication: September 13, 2010. Date retrieved: January 21, 2011. Date last modified: January 21, 2011.

G. Van Rossum. The python language reference manual. *Network Theory Ltd.*, September 2003. URL `http://docs.python.org`.

N.R. Varley, R. Arámbula-Mendoza, G. Reyes-Dávila, J. Stevenson, and R. Harwood. Long-period seismicity during magma movement at Volcán de Colima. *Bulletin of Volcanology*, pages 1–15, 2010. ISSN 0258-8900.

S. Vergniolle, G. Brandeis, and J.C. Mareschal. Strombolian explosions. 2. Eruption dynamics determined from acoustic. *Journal of geophysical research*, 101(B9):20–449, 1996.

D. "Deezer" W. Copyright ©1997-2011, 2001. URL `http://themushroomkingdom.net/images/mlss/mlss_luigi-hammer.jpg`.

G.P. Waite, B.A. Chouet, and P.B. Dawson. Eruption dynamics at Mount St. Helens imaged from broadband seismic waveforms: Interaction of the shallow magmatic and hydrothermal systems. *Journal of Geophysical Research*, 113(B2):B02305, 2008. ISSN 0148-0227.

D. Wang. Some topics on weighted Moore-Penrose inverse, weighted least squares and weighted regularized Tikhonov problems. *Applied Mathematics and Computation*, 157 (1):243–267, 2004. ISSN 0096-3003.

R. Wang. A simple orthonormalization method for stable and efficient computation of green's functions. *Bulletin of the Seismological Society of America*, 89(3):733–741, 1999.

B. Weber, J. Becker, W. Hanka, A. Heinloo, M. Hoffman, T. Kraft, D. Pahlke, J. Reinhardt, J. Saul, and H. Thoms. SeisComP3—automatic and interactive real-time data processing. In *Geophysical Research Abstracts*, volume 9, page 09219, 2007. URL `http://www.seiscomp3.org`.

P. Wessel and W.H. Smith. F, 1998. New, improved version of the Generic Mapping Tools released. *EOS, Trans. Am. geophys. Un*, 79:579.

P. Wessel and W.H.F. Smith. Generic Mapping Tools Graphics. *School of Ocean and Earth Science and Technology University, ol Hawaii, Hawaii, USA*, 1999.

M. Withers, R. Aster, C. Young, J. Beiriger, M. Harris, S. Moore, and J. Trujillo. A comparison of select trigger algorithms for automated global seismic phase and event detection. *Bulletin of the Seismological Society of America*, 88(1):95, 1998. ISSN 0037-1106.

C.J. Wolfe, P.G. Okubo, and P.M. Shearer. Mantle fault zone beneath Kilauea volcano, Hawaii. *Science*, 300(5618):478, 2003.

R.P. Young, S. Talebi, D.A. Hutchins, and T.I. Urbancic. Analysis of mining-induced microseismic events at Strathcona Mine, Subdury, Canada. *Pure and Applied Geophysics*, 129(3):455–474, 1989. ISSN 0033-4553.

Appendix A

Conventions and abbreviations

A.1 Conventions

- Bold faced letters denote multi dimensional values
- If not stated explicitly, entries of $\mathbf{M}$ are given in Nm.
- Stations are abbreviated and named $\boldsymbol{r}$, for *receiver*.
- Formally, $\mathbf{G}$ is one function with set of variables. However, the entries of $\mathbf{G}$ are interpreted as single time series, thus they are seen as functions of time. This justifies the usage of the plural when referring to $\mathbf{G}$.
- Arguments/parameters of $\mathbf{G}$ are *point of observation* r, *source position* s, *time of observation* t, *source time* t_0 in the order $(r, s; t, t_0)$
- Indices ji of $\mathbf{G}$ are *component of source mechanism* i and *component of observed signal* j
- Functions and graphs of discrete values are plotted with connecting lines between single points in order to improve the human readability.
- If not stated otherwise, the source time is set to $t = 0$.
- Scaling of data is described by the following terms:
  - *scaling by station*: the maximum absolute amplitude of each station is scaled to unity. All channels of each station keep the correct amplitude ratios.
  - *overall scaling*: the maximum absolute amplitude of all traces is scaled to unity. All traces keep the correct amplitude ratios.
  - *individual scaling*: the maximum absolute amplitude of each trace is scaled to unity.
- Stations are marked by black triangles
- Source locations are marked by red stars

.

A.2 Abbreviations and symbols

- V
  source volume
- τ
  total source time
- $\boldsymbol{\xi}$, $\boldsymbol{\xi_0}$,
  source point
- S
  full set of source points
- $\mathcal{N}_S$
  number of source points
- $\boldsymbol{x}$, $\boldsymbol{x_0}$,
  observation point
- R
  full set of stations
- $\mathcal{N}_R$
  number of stations
- $\mathrm{stf}(t)$
  source time function
- $\boldsymbol{u}(\boldsymbol{x}, t)$
  displacement signal (generated by an impulsive source, if not stated otherwise)
- $\boldsymbol{v}(\boldsymbol{x}, t)$
  velocity signal (generated by an impulsive source, if not stated otherwise)
- $\mathrm{stf}^{\mathrm{alt}}(t)$
  alternative arbitrary source time function
- $\boldsymbol{u}^{\mathrm{alt}}(\boldsymbol{x}, t)$
  displacement signal (generated by the arbitrary source time function)$\mathrm{stf}^{\mathrm{alt}}(t)$
- $\Theta(t)$
  Heaviside step function (distribution)
- $\delta(x)$
  Dirac delta distribution
- δ_{ik}
  Kronecker symbol

- $\mathbf{F_i}$
  single force in i-direction
- $*$
  temporal convolution
- $\otimes$
  outer product
- Tr
  trace of a matrix
- Diag
  diagonal matrix
- (λ_i^*), λ_i
  (reduced) eigenvalue of $\mathbf{M}$
- $\hat{}$
  symbol for the estimator of a value
- $\dot{x}$
  temporal derivative of x
- $x_{a,v}(u, v, w)$
  spatial derivative of component x_a of x w.r.t. v
- $\mathbb{M}_{3\times3}^{\mathrm{sym}}(\mathbb{R})$
  space of real valued symmetric 3×3 matrices
- $\mathbf{G}$
  general Green's tensor
- G^*
  general Green's function
- $\tilde{G}_{ji}$
  GF for signal in j-direction for single force excitation in i-direction
- $\tilde{G}_{ji,k}$
  spatial derivative of GF in k-direction - transfer function for source $\mathbf{M} \in \mathbb{M}_{3\times3}^{\mathrm{sym}}(\mathbb{R})$
- $\bar{G}_{ji}$
  equivalent to $\tilde{G}_{ji;k}$ for $\mathbf{M} \in \mathbb{R}^6$
- G_{ji}
  elementary seismogram for source excitation $\Theta(t)$
- $\check{G}_{ji}$
  elementary seismogram for other source excitations

- $\breve{G}_{ji}$
  elementary seismogram for $\dot{M}$ in far-field approximation
- G'_{ji}
  time shifted and chronologically weighted form of $\bar{G}_{ji}$ – used for numerical convolution
- $\mathbf{M}$
  general seismic moment tensor
- M_0
  scalar seismic moment
- $\mathbf{M}^{\text{devi}}$
  deviatoric part of $\mathbf{M}$
- $\mathbf{M}^{\text{iso}}$
  isotropic part of $\mathbf{M}$
- $\mathbf{M}^{\text{DC}}$
  pure shear part of $\mathbf{M}$
- $\mathbf{M}^{\text{CLVD}}$
  CLVD (pure non-shear deviatoric) part of $\mathbf{M}$
- $\tilde{M}$
  mechanical torque
- M_{ik}
  seismic moment with force components in i- and k-direction
- M^*
  seismic moment tensor, expressed in $\mathbb{R}^6$
- m
  moment tensor density
- m_{il_2}
  torque/rotational moment density
- M'
  rotational moment of arbitrary order

Appendix B

LP-events
–
more models and a short history

There are several models for the generation of volcanic LP-events, only two of them have been presented in chapter 4.3.1. Here I give a comprehensive listing of the respective source geometries.

Although showing different geometries, all models have in common that they are built up by a resonator and some exciting impulse. However, it is not surprising that varying source models have been developed for the different volcanoes.

Source models

- Turbulent magma flow
  (Ferrick et al., 1982; Julian, 1994)
- Stick-slip movement in combination with local friction
  (Iverson et al., 2006)
- Buried magma pipe
  (Chouet, 1985)
- Dike resonance
  (Kumagai et al., 2003)
- Excitation of fluid filled conduits
  (Neuberg, 2000; Jousset et al., 2003; Molina et al., 2004; Sturton and Neuberg, 2006; Gambino, 2006; Gilbert and Lane, 2008)
- Static rectangular crack
  (Chouet and Julian, 1985; Chouet, 1986, 1988; Kumagai and Chouet, 2000; Hidayat et al., 2002)
- Extending crack
  (Aki et al., 1977; Chouet, 1988; Molina et al., 2008)

- Bubble burst
  (Gerst, 2010)
- Oscillating fluid chamber
  (Crosson and Bame, 1985)
- Opening valve between magma reservoirs or cavities
  (Nishimura et al., 2000; Gilbert and Lane, 2008)
- Gas slug ascent dynamics
  (Gilbert and Lane, 2008)
- Excited organ-pipe modes
  (Garcés and McNutt, 1997)
- Slow waves trapped in a boundary layer
  (Ferrazzini and Aki, 1987)
- Flow through deformable channel
  (Rust et al., 2008)

Excitation mechanisms

- Magmatic brittle failure
  (Tuffen et al., 2003; Tuffen and Dingwell, 2005)
- Degassing processes
  (Hidayat et al., 2002)
- Inherent excitations
  (Nakano et al., 2003; Tuffen and Dingwell, 2005)
- Water-hammer effect
  (Pearsall, 1965)
- Crack opening
  (Aki et al., 1977)
- Triggerring by earthquakes
  (Hill et al., 2002)

Event studies

- Popocatepetl
  (Arciniega-Ceballos et al., 1999, 2003)
- Mt. Erebus
  (Johnson et al., 2008)

- Kilauea
(Ohminato et al., 1998; Dawson et al., 1999; Saccorotti et al., 2001; Wolfe et al., 2003; Battaglia et al., 2003; Kumagai et al., 2005; Cesca et al., 2008)
- Pinatubo
(Battaglia et al., 2004)
- Mt. Etna
(Gambino, 2006; Lokmer et al., 2007; Saccorotti et al., 2007; Lokmer et al., 2008; Bean et al., 2008; Cannata et al., 2009; De Barros et al., 2009)
- Redoubt volcano
(Benz et al., 1996)
- Galeras volcano
(Cruz and Chouet, 1997)
- Arenal volcano
(Benoit and McNutt, 1997; Garcés et al., 1998; Davi et al., 2010)
- Mt. Merapi
(Hidayat et al., 2000)
- Stromboli
(Neuberg et al., 1994; Neuberg and Luckett, 1996; Kirchdörfer, 1999; Chouet et al., 2003)
- Aso volcano
(Legrand et al., 2000)
- Soufrière Hills
(Neuberg et al., 2000; Rowe et al., 2004)
- Shikoku
(Shelly et al., 2006)
- Mt. St. Helens
(Iverson et al., 2006; Waite et al., 2008)
- Colima
(Varley et al., 2010)
- Non-volcanic sources
(Ide et al., 2007; Muñoz et al., 2008)

Appendix C

Numerical methods

C.1 SVD

An extending possibility for the computation of the least squares solution is the wide spread and well known method of *singular value decomposition* of the matrix $\boldsymbol{A}$ (Golub and Reinsch, 1970).

There are two orthogonal matrices $\boldsymbol{U}$ and $\boldsymbol{V}$ so that $\boldsymbol{A}$ can be transformed into a diagonal matrix $\boldsymbol{\Sigma}$ by

$$\boldsymbol{A} = \boldsymbol{U} \cdot \boldsymbol{\Sigma} \cdot \boldsymbol{V}^T \,, \tag{C.1}$$

where $\boldsymbol{V}$ is built by the eigenvectors of $\boldsymbol{A^T A}$, and $\boldsymbol{U}$ by the eigenvectors of $\boldsymbol{A A^T}$. This systematic is a generalisation of the eigenvector decomposition of regular matrices. The unique diagonal matrix $\boldsymbol{\Sigma}$ contains the ordered singular values of $\boldsymbol{A}$.

Lets assume the general optimisation problem

$$\min\{\, \boldsymbol{x} \,|\, ||\boldsymbol{A}\boldsymbol{x} - \boldsymbol{b}||_w\} \tag{C.2}$$

in the w-norm

$$||\boldsymbol{x}||_w = ||\boldsymbol{W}^{1/2}\boldsymbol{x}||_2 \,, \tag{C.3}$$

which is defined by the station weighting diagonal matrix $\boldsymbol{W}$. Under the additional condition that the $\boldsymbol{U}$ has to be chosen in a way that

$$\boldsymbol{U}^T \boldsymbol{M} \boldsymbol{U} = \boldsymbol{1} \tag{C.4}$$

holds, this problem is solved in the sense of least squares by the estimator $\hat{\boldsymbol{x}}$

$$\hat{\boldsymbol{x}} = \mho^{-1} \cdot \boldsymbol{V} \cdot \boldsymbol{\Sigma}^{-1} \cdot \boldsymbol{U}^T \cdot \boldsymbol{W} \cdot \boldsymbol{b} \,, \tag{C.5}$$

with $\hat{\boldsymbol{x}}$ having minimal ϖ-norm $||\boldsymbol{x}||_\varpi$ at the same time.

The partition of $\boldsymbol{A}$ by the SVD has been standardised, therefore many numerical libraries exist for this step. But finding the appropriate decomposition is not that trivial, so in our case of a weighted optimisation problem, I decided to use the Moore-Penrose inverse instead of the SVD decomposition. The SVD is numerically slightly more robust, but on the other hand it shows small loss with regard to the computation time.

C.2 Alternative numerical codes for calculating Greens's functions

GEMINI – an alternative code for generating 1D-GFs

Aside from QSEIS, there are further tools for handling the problem of generating GFs for a one-dimensional velocity model. As one interesting example I would like to mention here the program *GEMINI* (Friederich and Dalkolmo, 1995), that is focussed on a different geometric approach; it takes the spherical symmetry of the Earth for using its normal modes as internal basis solutions. this decomposition and recombination of spherical harmonic functions for generating seismic signals is not a-priori suited for regional or even local applications.

E3D – a finite differences method for generating 3D-GFs

In contrast to the ct3dtopo code (s. chapter 3.2.1), the program *E3D* (Larsen and Harris, 1993; Larsen and Grieger, 2005) solves the wave equation purely by applying finite difference methods in time and space, so that no transformations between domains are carried out. *E3D* uses a regular spatial and temporal grid, from which a staggered sub grid is formed, on which the derivatives are calculated at every time step. The code returns simulated seismic traces with an accuracy of fourth order in space and second order in time. By this means the result is not as accurate as the one from ct3dtopo.

The boundary conditions include free surfaces and absorbing bounds; nothing can be said here about the possibility of implementing a topography. Its design allows for an application in parallel computing. An appropriate use of this feature allows the direct generation of the desired $\mathbf{G}$, thus skipping the additional processing step of spatial inversion of sources and stations as needed in the application of

C.3 Inversion in frequency domain

As a further popular systematic approach for solving the given inversion problem, the transformation into the frequency domain shows up. Although it has not been my final choice, it shall be briefly presented here.

Solution scheme

Looking at equation (5.5), one can see that the convolution theorem can be very beneficial at this point. Using the Fourier transformation $\mathcal{FT}\{\}$ one obtains:

$$\boldsymbol{u}(\boldsymbol{x},t) = \mathbf{G}(\boldsymbol{x},t) * \mathbf{M}(t) = \mathcal{FT}^{-1}\left\{\mathcal{FT}\{\mathbf{G}(\boldsymbol{x},t)\}(\boldsymbol{x},\omega) \cdot \mathcal{FT}\{\mathbf{M}(t)\}(\omega)\right\} \tag{C.6}$$

So the convolution reduces the problem to the product

$$\tilde{\boldsymbol{u}}(\boldsymbol{x},\omega) = \tilde{\mathbf{G}} \cdot \tilde{\mathbf{M}}\,, \tag{C.7}$$

(Fourier transformed values are denoted by the "$\sim$") that can potentially be solved with direct methods as described before, so it seems to be a crucial simplification on the first view. Additionally the frequency bandpass filtering for the reduction to the desired low frequency regime seems to be a simple process of devision by a given window function, excluding the source of error potentially inherited by time domain filtering.

On the second glance, one may notice that the absolute size of the numerical arrays occurring in this product are of the same dimensions as in the numerical convolution in eq. (5.7): The time steps therein are replaced by a regular spacing in frequency, which depends on the Nyquist frequency of the discretised time series. Having in mind, that a complex equation has to solved here, the absolute amount of values does not change, so no gain in speed or accuracy can be expected.

Although the numerical fast Fourier transformation (FFT) is an optimised method in our days, it still takes significant computing time. In the given setup we face the transformation of our data and the Green's function matrix on the one way, and the back transformation of the solution vector $\mathbf{M}$ on the way back.

Keeping in mind, that in the final inversion routine shall be applied in a continuous setup, a forward- and backward transformation for every time step is intuitively not appreciable.

When taking a closer look on the mentioned filter routines, it turns out that a recursive butterworth filter in time domain (Allen and Mills, 2004) performs faster than a forward- and backward-transformation including the multiplication with a frequency window function, of a data set via the FFT. The results from comparing these methods equalise in the range of numerical precision! So no advantages arise at this point from the use of a transformation to the frequency domain, if no further assumptions can be included.

Amplitude spectra inversion

To reduce the numerical size of the problem and to suppress the errors occurring in the phase values, one can simplify the problem by only taking into account the amplitude information of the signal. So in frequency domain, only the amplitude spectra of the different data sets are inverted to obtain an estimator of $\mathbf{M}$. This approach shows to be stable w.r.t. noise and especial to time shifts in the data. Small phase variations, not covered by the modelling in the Green's functions do not enter the inversion result at all, in opposite to a pure time domain inversion.

This property is a big advantage of the method, nearly weighing out the effects arising from the missing phase information for our needs.

The crucial disadvantageous point is here, that the reduction of the full signal to only the amplitude information is a non linear process. So the original setup has to be changed to

$$|\tilde{\boldsymbol{u}}(\boldsymbol{x},\omega)| = \sqrt{\Re\{\tilde{\mathbf{G}}\cdot\tilde{\mathbf{M}}\}^2 + \Im\{\tilde{\mathbf{G}}\cdot\tilde{\mathbf{M}}\}^2}\,, \tag{C.8}$$

the occurring non-linearities may either be handled in terms of using a numerical iterative solution method, which collides again with my needs for a systematically fast algorithm; or one uses a linearised version of eq. (5.1), which induces another significant simplification.

Appendix D

Miscellaneous

D.1 Funding

This work has been funded by a federal grant in the framework of a project bundle from the German BMBF/DFG *Geotechnologien* program (Project no. 03G0646H)
URL: `http://www.exupery-vfrs.de/`

D.2 External presentations of the work

- **Oral presentation**
  L. Krieger, T. Dahm, U. Wegler; Entwicklung und Test eines Algorithmus' zur Echtzeitbestimmung von Centroid-Momententensorloesungen fuer langperiodische vulkanische Ereignisse (LP-Events); DGG Annual conference; 2008; Freiberg

- **Poster**
  L. Krieger, T. Dahm; Anwendung eines Algorithmus' zur Bestimmung von Centroid-Momententensorlösungen auf vulkanische und induzierte seismische Daten; DGG Annual conference; 2010; Bochum

- **Poster**
  L. Krieger, T. Dahm; Inverting for centroid moment tensors for volcanic and induced seismic events; Poster; EGU General Assembly 2010; Wien

- **Oral presentation**
  L. Krieger and T. Dahm; Inverting for centroid moment tensor solutions - full waveform analysis for induced (and volcanic) seismic events; Vortrag; ESC General Assembly; 2010; Montpellier

D.3 Computer specifications

Personal computer (32Bit), 2007

- CPU : Intel(R) Core(TM)2 Duo CPU – E8500 3.16 GHz
- Ram : 3107604 kB

D.4 Data sources

- The facilities of the IRIS Data Management System, and specifically the IRIS Data Management Center, were used for access to waveform and metadata required in this study.

  The IRIS DMS is funded through the National Science Foundation and specifically the GEO Directorate through the Instrumentation and Facilities Program of the National Science Foundation under Cooperative Agreement EAR-0552316.

- Bundesanstalt für Geowissenschaften und Rohstoffe (BGR); Hannover; 2011
- Dr. S. Cesca; University of Hamburg; personal communication
- C. Hammer; University of Potsdam; personal communication
- K. Meier; University of Hamburg; personal communication

D.5 Comments

- Geographical maps and topography information provided by Dr. K. Zakšek, University of Hamburg
- Representation of seismic data by the application of *Snuffler* (Heimann, 2009)
- Visualisations of focal sphere diagrams created with *MoPaD* (Krieger and Heimann, 2011) and *GMT* (Wessel and Smith, 1999)

Danksagungen

Eine Dissertation kann nur in seltenen Ausnahmefällen vollständig ohne Hilfe erstellt werden. Diese Hilfe besteht neben Literatur und Technik vornehmlich aus vielen Personen, ohne die es nicht möglich wäre, sich über mehrere Jahre hinweg eingehend mit einem wissenschaftlichen Thema zu befassen. Meine Dissertation stellt dahingehend keine Ausnahme dar, und so möchte ich an dieser Stelle den Menschen danken, die es mir auf vielen Ebenen ermöglicht haben, die vorliegende Arbeit anzufertigen.

An erster Stelle danke ich meinem Betreuer Professor Torsten Dahm, der mir nicht nur die Möglichkeit gegeben hat, die dieser Dissertation zugrundeliegende Fragestellung wissenschaftlich zu bearbeiten, sondern mich auch über den gesamten Zeitraum von fast vier Jahren sehr gut betreut hat. Seine Fragen und Anregungen waren stets weiterführend und sehr hilf- und lehrreich. Neben dem Thema meiner Forschungsarbeit hat er mir umfassend die Möglichkeit gegeben, theoretische und praktische Aspekte der Seismologie kennenzulernen, sowie Erfahrungen in der Durchführung von seismologische Feld- und See-Experimenten zu sammeln. Ich bin Torsten besonders dankbar für einen wissenschaftlichen und immer freundlichen Arbeitsstil. Nicht zuletzt dadurch bestand in seiner Arbeitsgruppe immer eine sehr angenehme Arbeitsatmosphäre, geprägt von gegenseitiger Hilfe und vielen fruchtbaren wissenschaftlichen Diskussionen. Von Dirk Becker und Simone Cesca konnte ich so sehr viel über Seismologie lernen. Martin Hensch danke ich neben allem anderem für den positiven ersten Eindruck vom Institut. Ohne diesen hätte es diese Arbeit wahrscheinlich nicht gegeben. Er hat mir durch seine begeisterten, geduldigen und fundierten Erklärungen den Einstieg in die Seismologie sehr erleichtert.

Weiterhin bin ich enorm dankbar dafür, daß Sebastian Heimann mit einem unglaublich großen Maß an Geduld ausgestattet ist. Es ist mir unbegreiflich, wie er meine dilettantischen Kicker-Anfänge und meine Fragen zum Programmieren ertragen hat und in beiden Disziplinen für starke Verbesserungen meiner Fähigkeiten sorgen konnte. Meine Weiterentwicklungen haben schließlich dazu geführt, daß ich sowohl einmal gegen Mikhail Baykulov gewinnen als auch diese Dissertation fertigstellen konnte. Danke, Sebastian!

Celia Rios danke ich unter anderem für die jahrelange Büronachbarschaft und eine einzigartige Atlantikkreuzfahrt, inklusive stundenlanger Gespräche. Auch Stefan Trabs hat es sehr lange auf engstem Raum mit mir ausgehalten und kann wohl recht gut beschreiben, wie ich in seekrankem Zustand aussehe. Nicole Hettrich danke ich für maritime nichtfachliche Gespräche und den mittelfristig vergeblichen Versuch, meine Fensterbank mit neuen Pflanzen zu versehen. Nicht zuletzt möchte ich hier *meine* HiWis erwähnen, denen ich einerseits sehr dankbar für Ihre Hilfe auf See und an Land bin, andererseits auch für die Stunden außerhalb der Arbeitszeiten: Carina Juretzek und Friederike von Schlippe.

Natürlich möchte ich auch Barbara, Nicky, Jessica, Franzi, Barbara, Eleonora, Francesco (Bud Spencer), Alexander, Samira, Francesco, Luigi, Elias, die Lurche und ihre Musik, Meike, sowie meinen neuen Büromitbewohner Tolga nicht vergessen.

Weiterer Dank gebührt dem Zweitgutachter meiner Arbeit, Professor Matthias Hort. Neben vielen langen Diskussionen über die wissenschaftlichen Inhalte der Dissertation bin ich Matthias besonders für die sehr angenehme Zusammenarbeit beim Feldexperiment und die von ihm ermöglichten Einblicke in die hohe Kunst des wissenschaftlichen Projekt-Managements dankbar. Nicht nur im Zusammenhang mit der schwierigen Organisation unseres Forschungsprojekts geht auch ein großer Dank an Klemen Zakšek.

Mit Iris Ehlert, Alexander Gerst, Kristina Meier und Mi-Kyung Yoon habe ich gerne ein paar nette Jahre – mit oder ohne Bier und Kicker – auf unserem Flur verbracht, mit Lea Scharff und Jörg Hasenclever zusätzlich noch zu wenig Zeit beim Grillen, Eisessen, Hutbauen und bei anstrengenden Kilometern auf dem Fahrrad.

Ohne Ekkehart Teßmer (Ekki) hätte ich weder einen modellierten Vulkan für meine Arbeit zur Verfügung gehabt, noch hätte ich meinen Segelschein gemacht. Von Christian habe ich einiges über marine Seismik und See-Experimente gelernt. Alis Meßmethoden wirkten dagegen vergleichsweise beschaulich, was wiederum im Gegensatz zu seiner eigenen Dynamik bei Ballsportarten steht.

So, wie Christel Mynarik mir mit allem Analogen weiterhelfen konnte, habe ich mich als digital abhängig vom CIS erwiesen. Letzteres ist wahrscheinlich sehr froh, daß es meine computer- und netzwerkbezogenen Fragen nicht mehr beantworten muß. Lambert verdient hierbei noch einen speziellen Dank (!) Das Arbeiten mit Sven "Wissenschaft" Winter und Joachim Bülow war großartig, wenngleich die beiden deutlich weniger linke Hände als ich zu haben scheinen.

Auch wenn ich mich durch die geringen fachlichen Überschneidungen selten im 14. Stock aufgehalten habe, seien Dirk Gajewski, Claudia Vanelle, Bärbel Langmann und der Rest des Instituts hier natürlich nicht vergessen.

Außerhalb Hamburgs waren Matthias Ohrnberger, Frank Krüger, Joachim Wassermann, Robert Barsch und Arturo Montalvo Garcia eine große wissenschaftliche Hilfe.

Conny Hammer und Moritz Beyreuther: Mit Euch zusammen würde ich das Ganze vielleicht noch einmal machen!

Für fachliche Hilfen, Abendessen, Urlaub, Kommentare, gemeinsame Frustration, die konsequente Verschonung meiner Biervorräte und die häufigen Versuche, mich zum Verlassen meines Arbeitsplatzes zu bewegen, geht hiermit mein allerherzlichster Dank an Florian Ziemen! Sandra Busl, Jörg Schwöbel, Philipp Knake und Johannes Mundhenk verdanke ich vier Jahre erfolgreicher Freizeitgestaltung in und um Hamburg. Meine Mitbewohner und Mitbewohnerinnen Bernhard, Martin, Kerstin und Maren haben es nicht nur während des Anfertigens dieser Arbeit fast klaglos mit mir ausgehalten, was sicher nicht immer leicht war.

Es gibt weitere nette Menschen, die mir dehr dabei geholfen haben, unerfreuliche Zeiten zu verarbeiten: Julia Daumann, Dorle Michaelis, Veronika Bierbaum, Arndt Böhm, Inga Wolters, Thies Ehrich, Helmut Rathgen (Helmi), Sven Schumacher, Johannes Mundhenk, Falco Knapp, Hans-Peter Doerr, Johannes Wohlmuth, Philip Mundhenk, Tim Mundhenk, Martin Christner, Maren Klein, Timo Kritzokat, Jan Erler.

Erwähnen möchte ich noch Linus Viezens, Philipp Thurn, Lothar Gend, Robert Pietzker, Sophie Bruns, Sonja Knake, Christof Prahl, Mette Schmeling, Andreas Kleine, Leif Vogel, Patrick Weber, Daniel Stichtenoth, Tina Winter, Maggan, Pi, Maggus, Suz und alle, die mir durch die Korrektur dieser Arbeit geholfen haben.

Einen besonderen Dank an Philipp Knake und Johannes Mundhenk für alles innerhalb und außerhalb der Uni in den letzten 11.5 Jahren.

Das letzte und größte Dankeschön geht an Rebecca und meine Familie! Meine Eltern haben mir das Studium ermöglicht und meine Entscheidung für das Anfertigen einer Doktorarbeit in jeder Form unterstützt. Ich danke meiner Mutter für die vielfältige Hilfe, insbesondere in komplizierten Dingen des Alltags, sowie meiner Schwester für gegenseitige Hilfestellungen bei den unterschiedlichsten Themen und für interessante Einblicke in das Leben außerhalb der Universität. Rebecca war meine größte Motivation! Vor allem danke ich ihr dafür, daß sie die letzten Jahre all das Chaos und meine mangelnde Aufmerksamkeit ertragen hat.

Ich hatte in den letzten Jahren weniger Zeit für Euch als Ihr für mich. Das wird sich jetzt hoffentlich ändern!

DANKE !!